Hydrogen Production from Crude Oil using Microwave-Initiated Catalytic Technology

Saud A Aldrees

St Hilda’s College, University of Oxford

Supervisors

Prof. Peter P. Edwards FRS ML

Prof. Simon J. Clarke

A thesis submitted to the Department of Chemistry, University of Oxford

for the Degree of *Doctor of Philosophy in Inorganic Chemistry*

2022

Dedication

To the spirit of my ***Father****, may Allah have mercy on him, my role model in this life.*

To my dear beloved ***Mother****, may Allah bless her, the light of my life.*

This thesis is wholeheartedly dedicated to my beloved wife, ***Reem Alroumih****, who has been a source of strength, support, patience, and motivation for me throughout this entire experience. I am so lucky to have a woman who loves me so much and stands beside me the way you have!*

To my lovely children, ***Abdulaziz****,* ***Ashry****,* ***Waleed****, and* ***Sarah****, …*⊙
I hope the sacrifices you have endured for me to pursue this dream will be repaid to you with many opportunities for joy and success in your future.

Saud

Oxford, 7 October 2022

Acknowledgements

All the praise goes to Allah for his generous blessings, without which I would not have completed this work.

Looking back through the past 4 years, which have been full of challenges arising from the COVID-19 pandemic and others, I notice that this DPhil thesis could not have been possible without the support and encouragement of the people who are sincerely appreciated and gratefully acknowledged.

I gratefully acknowledge King Abdulaziz City for Science and Technology (KACST), Saudi Arabia, for providing the funding for my DPhil scholarship, and for an invaluable moral and financial support. I give special thanks to His Excellency **Dr Munir Eldesouki** -KACST president, Professor **Hamid Almegren**, and **Dr Saeed Alshihri**, who have always encouraged me to complete my DPhil, for all the support they gave me during my study.

My utmost deep and sincere gratitude to **Professor Peter P. Edwards**, my supervisor, teacher, and friend. I am grateful to have been part of your group. Thank you for trust and freedom in doing the research but also for keeping me on track. You always took care about me and my family, not only on professional but also personal level.

I would like to express my thanks to my supervisor **Professor Simon J. Clarke**, for the smooth supervision transition after Prof. Edwards's retirement, and for all his help and support throughout the last year of my DPhil.

I would like to express my sincere gratitude to **Professor Jon Dilworth** for his invaluable advice, encouragement, and guidance. Your support is greatly appreciated.

I would like to thank my college advisor **Professor Lorna Smith**, for all her help, advice, and support.

My special thanks and appreciation go to **Dr Sergio Gonzalez-Cortes**, my daily supervisor, and friend, for his unlimited help and support from the day one in ICL. thank you for all formal and informal discussions; they were always fruitful and encouraging me for further work.

I am grateful for the invaluable help of **Dr. Mohammad Al-Kinany**, my mentor, and friend, for all his advice, support, and helpful discussions.

I would like to thank a team of analytical experts in Oxford University who supported me with variety of analysis, **Dr Simon Cassidy**, **Dr Patrick Bergstrom Mann**, **Dr Robert Jacobs**, and **Dr Nick Rees**.

Mrs. Linda Webb and **Mrs. Alison Chesworth-Wing**, thank you so much for the continued assistance.

Thanks to all the member of the **Edward's group** for many interesting discussions.

Our stay in *Sandstones* would not be so enjoyable without our neighbours in Botley, **Mr. Steven** and **Mrs. Diane Braggs**. Thank you very much for the invaluable help, advice, and for creating a nice atmosphere. We always felt as being one family!

I would like to thank all my **brothers** and **sisters** for all the support and encouragement.

Last and not least, I would like to express my gratitude from the bottom of my heart to my wife **Reem** and **children**, this research work would not be successful and so cheerful without you All!! Excited to start a new chapter of our beautiful life together…

Saud Aldrees

Oxford, 2022

Thesis contents

Chapter2 Experimental Methods

Chapter3 The Production of Hydrogen through the Microwave-Initiated Catalytic Dehydrogenation of Model Hydrocarbon Compounds without Significant CO_2 Emissions

Chapter4 Influence of Metal Catalyst Particle Size and Loading on the Microwave-Initiated Deep-dehydrogenation of Light Crude Oil

Chapter5 Effective Conversion of Light Crude Oil to Syngas through Microwave-Initiated Catalysis

Chapter6 Conclusions and Future Work

List of Figures

List of Tables

Glossary

AAPG	American Association of Petroleum Geologists
AC	Activated carbon
Alkylation	Transferring an alkyl group from one molecule to another
API	American Petroleum Institute
ASTM	American Society for Testing and Materials
ATR	Autothermal reforming
BET	Brunauer-Emmett-Teller surface area analysis
Bragg's Law	Gives the angles of coherent scattering of waves from a crystal lattice
Btu	British thermal unit
BTX	Benzene, Toluene, and Xylene
CAGR	Compound Annual Growth Rate
CCE	Circular carbon economy
CCS	Carbon capture and storage
CCUS	Carbon capture, utilisation and storage
CE	Circular economy
CL-SRM	Chemical looping steam reforming of methane
Conversion	Describe how much of reactant was consumed in reaction
CPOX	Catalytic partial oxidation
CSDRM	Combined steam and dry reforming of methane
CSI	Catalyst selectivity index
Dark fermentative	Process carried out by anaerobes in the absence of light and oxygen
Dielectric constant	Measuring the ability of a substance to store electrical energy in an electric field.
DRM	Dry reforming of methane

DSC	Differential scanning calorimetry
EDS	Energy dispersive X-Ray analysis
EJ	Exajoul, or 10^{18} joules
FID	Flame ionization detector
Flexicoking	Converting high boiling petroleum fraction into valuable light hydrocarbons
FWHM	Full width at half maximum
GC	Gas chromatography
GC/MS	Gas chromatography-mass spectrometry
GHG	Greenhouse gases
Gt	Gigatonnes
GW	Gigawatts
HFCs	Hydrofluorocarbons
Hydroprocessing	Processes of hydrocracking and hydrotreating
IR	Infrared
Isomerization	Transferring of a molecule into a different isomer
LCO	Saudi Arabian Light Crude Oil
LHSV	Liquid-hourly space velocity
Loss tangent	Measuring the ability of a material to convert electromagnetic energy into heat energy
MFM	Mass flow meter
MW	Microwave
MWCNTs	Multi-wall carbon nanotubes
NEB	Net energy balance
NEOM	Stand for New Future – Saudi city
NMR	Nuclear magnetic resonance spectroscopy
PEM	Proton exchange membrane

PFCs	Perfluorocarbons
POM	Partial oxidation of methane
Photofermentation	Microbial process in which electrons and protons generated through oxidation of organic compounds
POX	Partial oxidation
Selectivity	Describe how much desired product was formed in relation to the undesired product(s)
SEM	Scanning electron microscopy
SE-SRM	sorption-enhanced steam reforming of methane
SF_6	Sulphur hexafluoride
SG	Specific gravity
SIMIT	Size-Induced Metal-Insulator Transition
Skin depth	The distance from the surface of material to the level at which microwaves pervade into the material
SOES	Solid oxide electrolysis cells
SPE	Society of Petroleum Engineers
SR	Steam reforming
SRM	Steam reforming of methane
SWOT	Strengths, weaknesses, opportunities, and threats
Syngas	Synthesis gas
TCD	Thermal conductivity detector
TEM	Transition electron microscopy
TGA	Thermogravimetric analysis
TM010	Mode within a waveguide creates only uniform electric field
TRL	Technology readiness levels
Visbreaking process	A mild form of a non-catalytic thermal cracking
XRD	X-ray powder diffraction
Yield	Describe how much desired product was formed

Hydrogen Production from Crude Oil using Microwave-initiated Catalytic Technology

Saud A Aldrees, St Hilda’s College

A thesis submitted to the Department of Chemistry, University of Oxford for the Degree of Doctor of Philosophy in Inorganic Chemistry

Abstract

The current target of limiting global warming to 2 °C above pre-industrial levels is recognised as a demanding task. Should renewable technologies, for example, wind and solar, be not able to decarbonise the energy industry sufficiently in the near future, other approaches are needed to generate energy without the emission massive amounts of CO_2.

Hydrogen as an energy vector or fuel of the future has many advantageous properties compared to the current fuels. At the present, hydrogen production relies on fossil fuels and this trend will continue in the foreseeable future. As a result, hydrogen plants are and will remain a major source of CO_2 emissions to the atmosphere. Decarbonisation is rapidly becoming a pressing but attractive challenge for worldwide fossil fuel utilization.

Here, we present an application of this new approach to the deep-dehydrogenation of Saudi Arabian light crude oil (LCO) - a liquid petroleum that has a low density and flows freely-. Hydrogen from fossil LCO - without significant CO_2 production - is realized through microwave-initiated catalysis on activated-carbon-supported inexpensive Fe catalysts. Further optimisation can make the new process potentially competitive with current H_2 production technologies, typically involving the steam reforming of methane, which invariably involves the release of significant amounts of CO_2 to the atmosphere.

This environmentally - acceptable approach - to clean hydrogen production directly from fossil fuels and having near - to - zero CO_2 production can make this new process potentially competitive with the current hydrogen production technologies, particularly through the portal of a carbon tax on energy producers. It, therefore, ushers in a new era …. The decarbonization of fossil fuels.

Chapter1

Introduction

Fossil fuels still accounted for more than 80% of the world's primary energy consumption in 2019 and remain one of the major sources of energy for humanity and will continue to do so for the foreseeable future [1-4]. This is due to fossil energy's intrinsic high energy content, its large resource base, its general availability at a reasonable cost, and the large investment in accessible technology and infrastructure which utilize fossil fuels.

With the continuity rapid increase in fossil fuel consumption and its environmental impact, developing clean and renewable energy is of the highest priority. Hydrogen offers the prospect of a highly effective fuel for future sustainable energy [5-7]. The Paris Agreement paved the way for the use of hydrogen as an energy source to keep global warming below the expected 2 degrees Celsius above pre-industrial levels. To reach this target, the world will need to cut energy-related CO_2 emissions by 60% by 2050 [9]. Considering this, a clear commitment to hydrogen and a circular carbon economy has been made on the global level. There is unprecedented momentum for hydrogen as new strategies, policies, and incentives have been put in place by different countries to push toward realizing the hydrogen economy.

Hydrogen is most commonly used in petroleum refining and fertilizer production. It can be produced using several different processes and a range of primary energy sources, including renewable and non-renewable sources. 95% of the global production of hydrogen is from fossil fuels, with the most significant contemporary technologies being the steam reforming of hydrocarbons (e.g., natural gas) [7-10].

1.1 Global Greenhouse Gas Emissions

Greenhouse gases (or GHG as acronym) are found in the atmosphere, and they are characterised by their ability to absorb the infrared radiation emitted by the earth and raise the temperature of the air, thus reducing heat loss from the earth to space, which makes it contribute to heating the earth's atmosphere, and thus leading to global warming. The main challenge lies in the increase of greenhouse gases, the most important of which is CO_2, resulting from the combustion of fossil fuels, whether from industrial facilities, power stations or means of transportation, and more than twenty billion tons of it are released annually into the earth's atmosphere.

Prior to the Industrial Revolution, the proportions of greenhouse gases in the atmosphere remained more or less constant. Human activity since the beginning of the Industrial Revolution around 1750 has led to a 45% increase in the concentration of CO_2 in the atmosphere; From 280 ppm to 419 ppm in 2021 [11, 12], with global energy-related CO_2 emissions around 31.5 Gt (**Figure 1.1**).

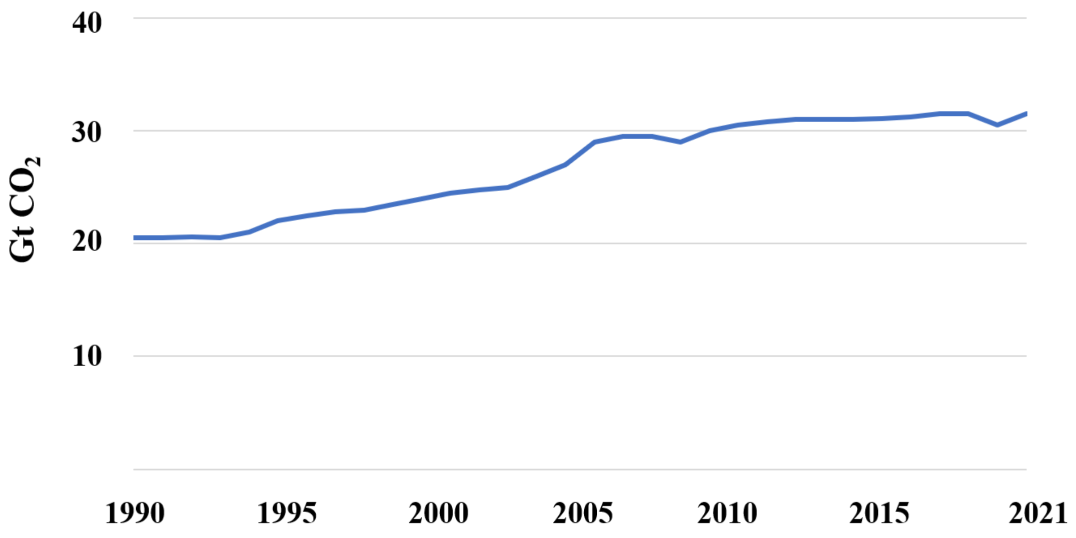

Figure 1.1 The global change in CO_2 emissions (1990-2021). (Adapted from Ref.[13]).

In the last few decades, climate change and global warming have received a lot of attention from policymakers and scientific researchers. Today, the effects of global warming are becoming noticeable to everybody, and greenhouse gases have been identified as one of the strongest influencing factors in these processes. The warming of the climate system is unequivocal, and since the 1950s, many of the observed changes are unprecedented. The atmosphere and ocean have warmed, the amounts of snow and ice have diminished, sea level has risen, the concentrations of greenhouse gases have increased, mostly due to human activities. The four major GHGs tied to human activities and their sources are listed in **Table 1.1** [14-16].

Table 1.1 The major greenhouse gases tied to human activities [14-16].

GHG	Sources
Carbon dioxide (CO_2) (76 %)	- Combustion of fossil fuels, wood, and solid waste. - Land-use changes, such as deforestation, road construction, and mining. - Industrial processes.
Methane (CH_4) (16 %)	- Combustion of fossil fuels. - Livestock and agricultural practices. - Landfills.
Nitrous oxide (N_2O) (6 %)	- Agricultural and industrial activities. - Combustion of fossil fuels and solid waste.
Fluorinated gases (F-gases) (HFCs, PFCs, SF_6) (2 %)	- Industrial processes.

The main culprit of global warming is CO_2 which is emitted from the combustion of fossil fuels like coal, oil, and gas. Coal is incredibly polluting and the single biggest source of global temperature rise, and responsible for 46% of global CO_2 emissions.

In 2019, CO_2 accounted for about 80% of all U.S. greenhouse emissions [14], and also it is globally the most abundant greenhouse gas emitted through human activities (**Figure 1.2**).

Burning fossil fuels is a major source of greenhouse gases, and it is included in most economic activities, from the industry sector and transportation to electricity production.

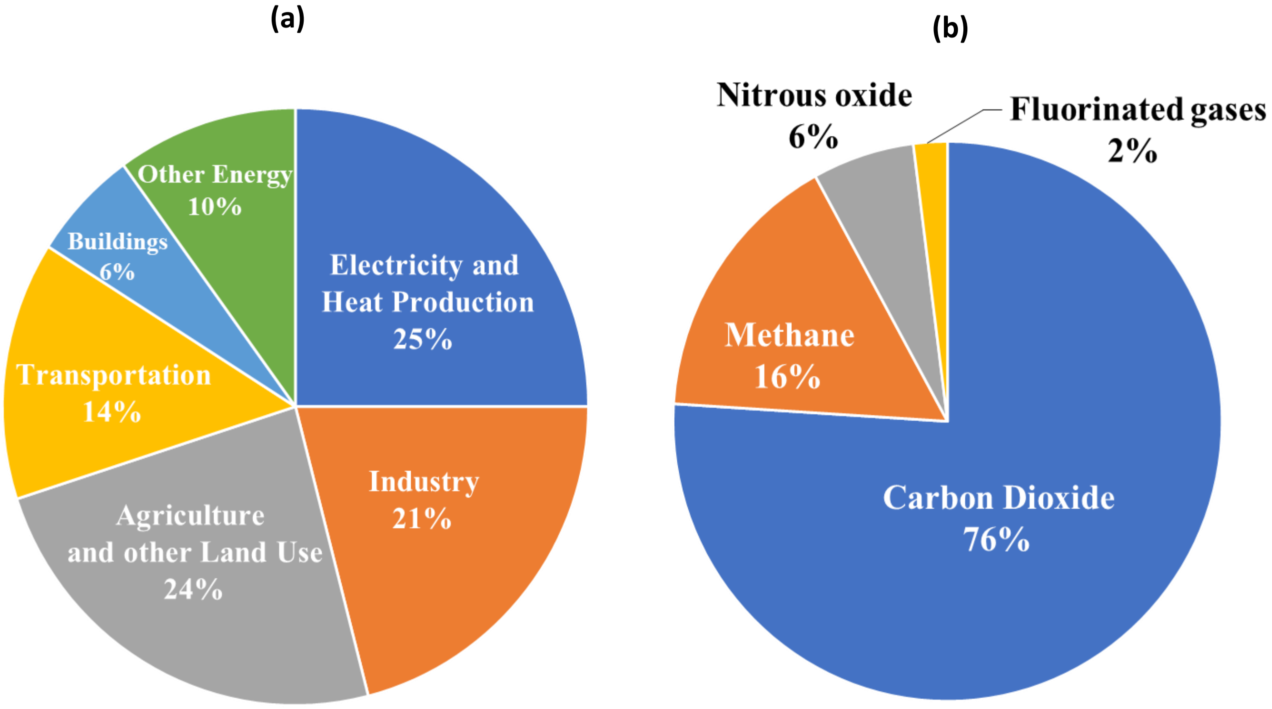

Figure 1.2 The global greenhouse gases emission by (a) economic sector and (b) gases. (Adapted from Ref. [17]).

In recent decades, climate change has become one of the most important challenge afflicting societies at the international, national, and local levels. Where scientists are unanimously agreed is that increasing temperatures and sudden climatic changes will generate immediate and long-term risks to societies. The world needs to focus now on the scientific fundamentals of climate change and on the actions otherwise the risks we run will be irreversible.

The Paris Agreement charted a new course in the effort to combat global climate change, requiring countries to make commitments to decarbonise and progressively strengthen any action taken. 194 countries signed the Paris Climate Agreement, which was adopted in Paris on 12 December 2015 [9]. It aims to reduce global greenhouse gas emission significantly and limit the increase in global temperature to below 2° C. Considering this, clear commitments to hydrogen and the circular carbon economy have been made. There is no doubt that we are living in an era of unprecedented momentum for implementing a hydrogen economy as new strategies, policies, and incentives are put in place globally.

1.2 The Circular Carbon Economy (CCE)

The circular economy (CE) is defined as “an economic system that replaces the ‘end-of-life’ concept with reducing, alternatively reusing, recycling, or recovering materials in production/distribution and consumption processes” [18]. This concept is not new, the roots of the circular economy arose toward the end of the 1960s, and it has since evolved through several stages (**Figure 1.3**). In 1965, the US economist Kenneth Boulding developed the concept of resource “circulation”, when he called for a shift from the "Cowboy economy", where there were no limitations in the use of resources or waste disposal, to a "Space economy" where everything must be recycled continuously. Going through the mid-1970s, Walter Stahel sketched the vision of “Economy in loops”, and its impact on job creation, economic competitiveness, resource savings and waste prevention. The CE concept has been described in extensive research and reports, and since 2010 the concept has been increasingly referred to by policymakers and businesses [19-21].

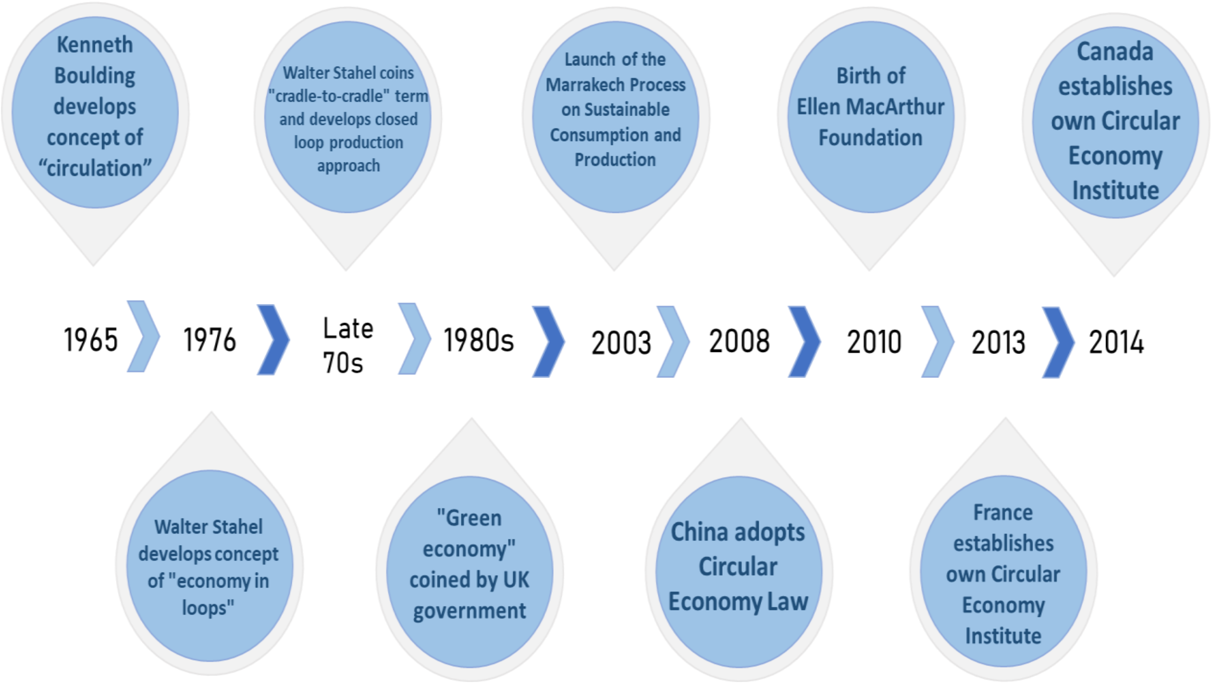

Figure 1.3 The key milestones of the circular economy. (Adapted from Ref. [19, 21]).

In the current dominant linear economy, considerable amounts of CO_2 are released to the atmosphere by burning fossil fuels for energy production. This is contrary to the international efforts on climate change and the increase of resource usage efficiency [22, 23]. Therefore, the transformation from a linear to a circular carbon economy has become an urgent necessity.

Unlike the linear economy where products in a “single-use” pattern, the circular carbon economy (CCE) is about closing the loop for managing and reducing emissions (i.e.waste) of carbon from all sectors involving 4Rs; namely, reduce, reuse, recycle and remove.

The CCE framework shows us that we can “Reduce” global CO_2 emissions, “Reuse” the captured CO_2 as useful products, “Recycle” the captured CO_2 by transforming it into new products, and “Remove” the CO_2 that is emitted in the atmosphere using technology to capture and store (**Figure 1.4**) [24-27].

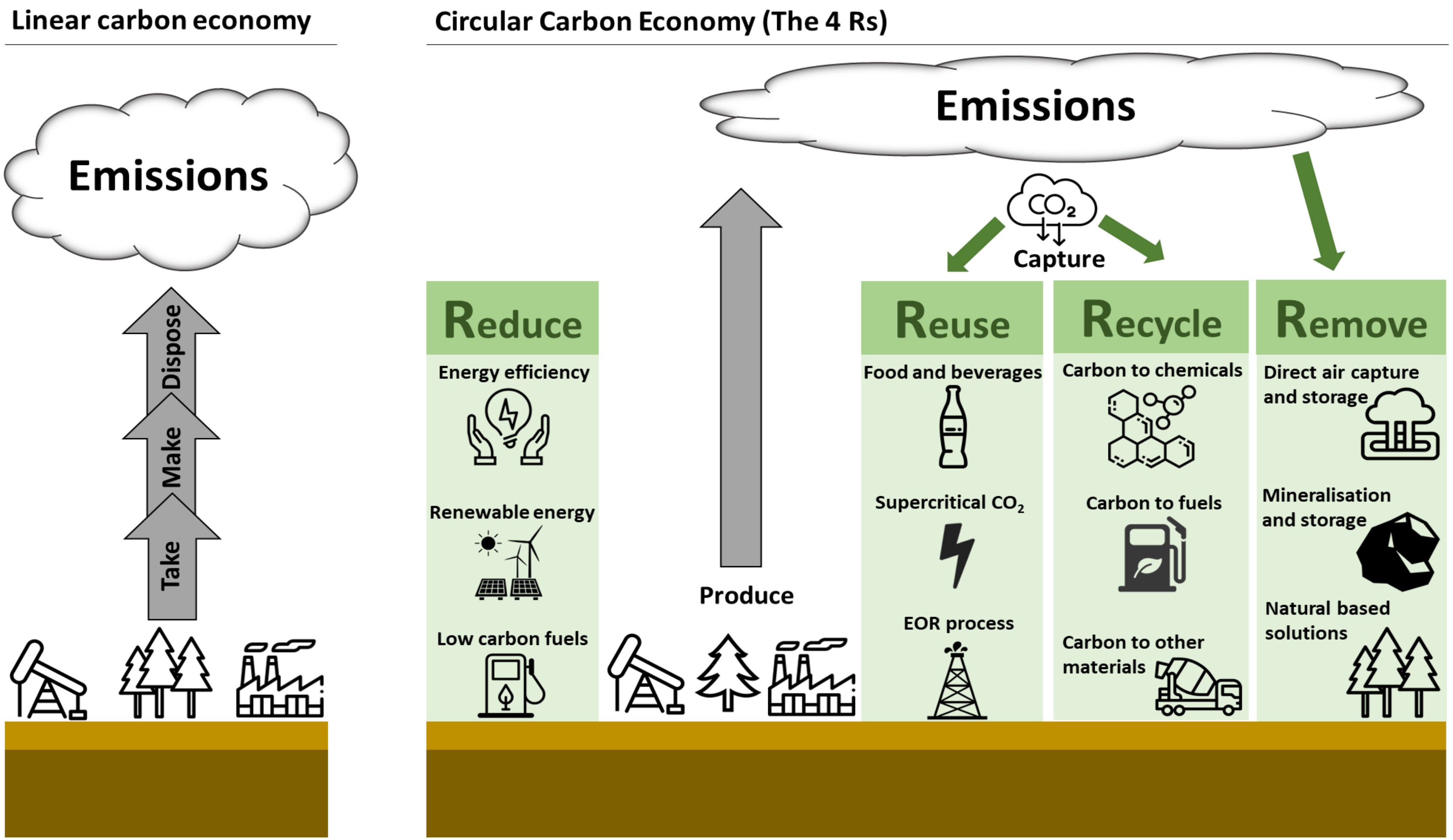

Figure 1.4 Schematic of CCE elements. (Adapted from Ref. [22, 24]).

1.3 Introduction to Crude Oil

Crude oil is considered one of the most important non-renewable energy sources, on which all aspects of our modern life are based. It was formed from decaying dead animals and plants as a result of geological conditions that have persisted for millions of years [28, 29].

1.3.1 Chemical Composition of Crude Oil

Crude oil is defined as “a mixture of hydrocarbons that existed in the liquid phase in natural underground reservoirs and remains liquid at atmospheric pressure after passing through surface separating facilities” (joint API, AAPG, and SPE definition) [30] (**Figure 1.5**), largely of the general formula C_nH_{2n+2}, containing paraffins, naphthenic and aromatic compounds, with a composition of 83-87% carbon, 10-14% hydrogen, 0.05-1.5% oxygen, 0.1-2% nitrogen, and 0.05-6% sulphur [29, 31-33]. Therefore, crude oils are classified as: paraffin based, naphthene based, or aromatic based.

Figure 1.5 A sample of crude oil. [Wikipedia].

Paraffins, also known as alkanes, are saturated compounds characterised by the rule that the carbon atoms are connected with another carbon or hydrogen atoms through single bonds. **Figure 1.6** shows some examples of paraffins which occur abundantly in crude oil [30, 34].

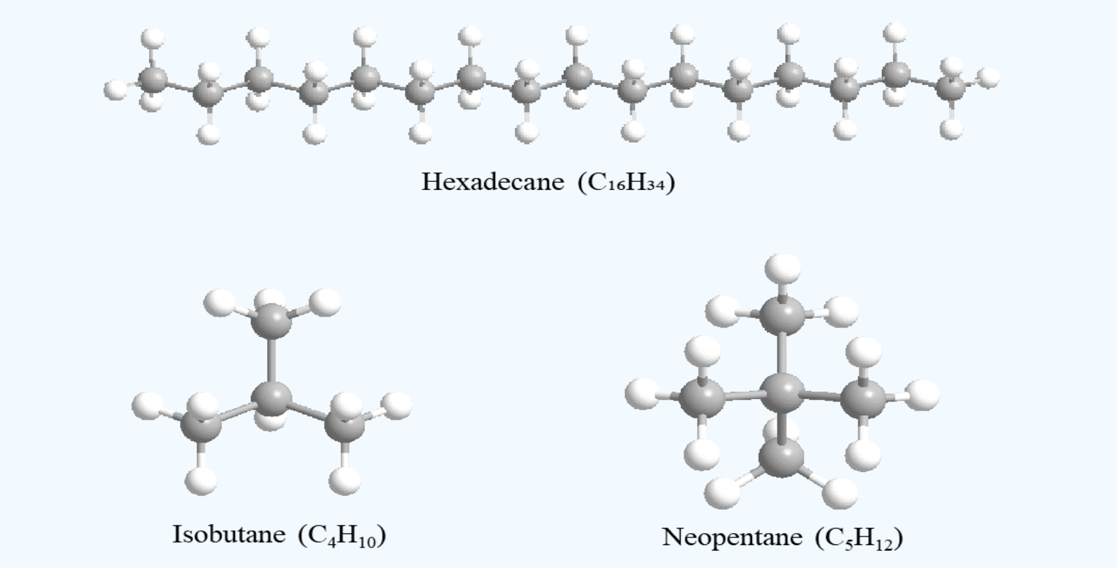

Figure 1.6 Paraffins in crude oil, the general formula is C_nH_{2n+2} where n is the number of carbons.

Naphthenes (Cycloparafins) are the second major group of hydrocarbons found in crude oil, in which all of the carbon atom bonds are saturated with hydrogen (**Figure 1.7**) [30, 35].

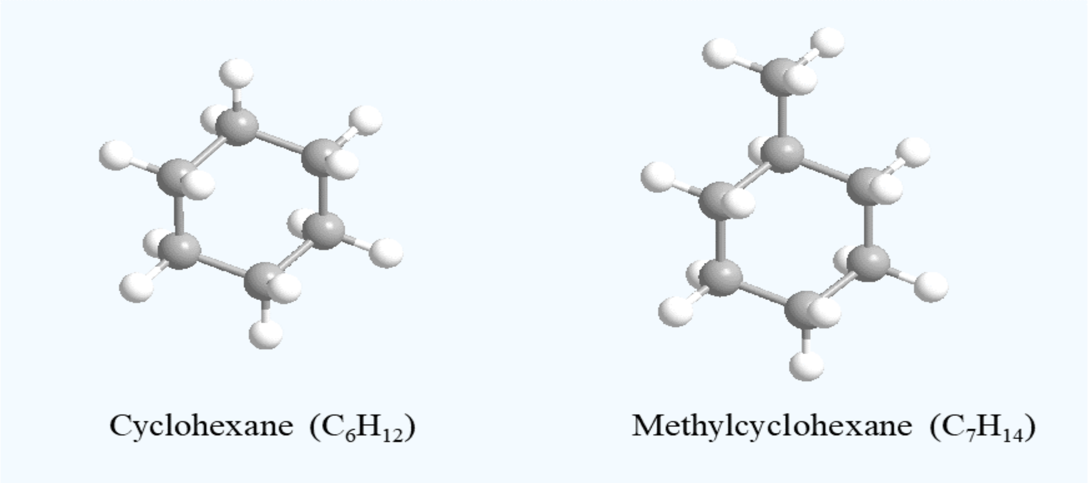

Figure 1.7 Naphthenes in crude oil, the general formula is C_nH_{2n} where n is the number of carbons.

Aromatic compounds are the third major group of hydrocarbons commonly found in crude oil. Depending upon the number of fused benzene rings presence in their molecules, they can be basically classified into three main groups, including monocyclic aromatic hydrocarbons (MAHs), polycyclic aromatic hydrocarbons (PAHs), and linear fusion of aromatic rings (**Figure 1.8**) [30, 36].

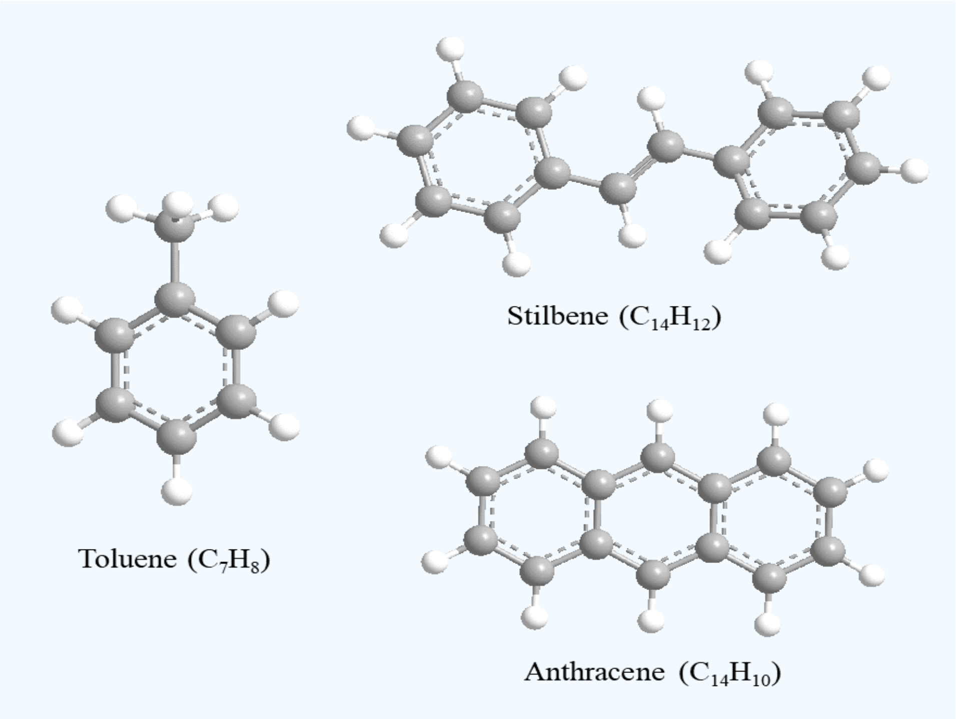

Figure 1.8 Aromatics in crude oil, the general formula is C_nH_{2n-6m} where *n* is the number of carbon atoms and *m* is the number of rings.

Based on the composition of crude oil, there are several types of analysis to determine composition [33, 37]:

- PONA (**p**araffins, **o**lefins, **n**aphthenes, and **a**romatics).
- PNA (**p**araffins, **n**aphthenes, and **a**romatics).
- PIONA (**p**araffins, **i**soparaffins, **o**lefins, **n**aphthenes, and **a**romatics).
- SARA (**s**aturates, **a**romatics, **r**esins, and **a**sphalthenes).
- Elemental analysis (C, H, S, N, O).

1.3.2 Physical Properties of Crude Oil

The physical properties of crude oil reflect its chemical composition and can vary widely depending on where the oil is found, and depend on reservoir temperatures and pressures [38, 39].

1.3.2.1 Density

Crude oil is referred to as either light, medium, or heavy, based on its density. Two density related properties of crude oil are used in industry to assess its quality: Specific gravity (SG), and American Petroleum Institute (API) gravity. Specific gravity (or relative density) is the ratio, at specified temperature, of the oil density to the density of the pure water [33, 39-42]. The API gravity is a commonly used index of how light or heavy a crude oil compared to water (**Equation 1.1**) [32, 43]. **Figure 1.9** indicate the most common ranges used.

$$\text{API gravity } (°) = \frac{141.5}{SG\ (at\ 60°F)} - 131.5 \qquad \textbf{Equation 1.1}$$

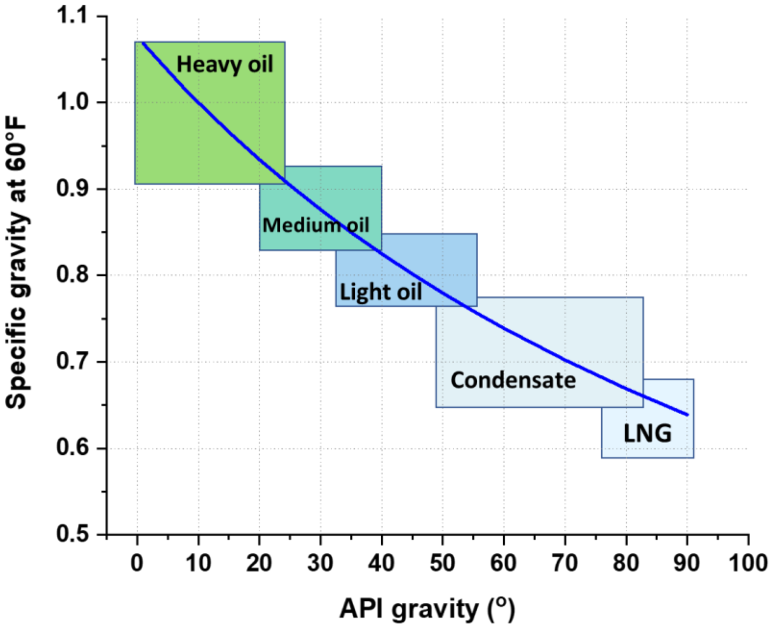

Figure 1.9 Different classes of crude oil based on the density.
[API Gravity, www.engineeringtoolbox.com].

1.3.2.2 Sulphur Content

Crude oil can also be referred to as sour or sweet, based on the sulphur content. Sweet crude oil contains less than 0.5 wt.% sulphur. Sour crude oil has a total sulphur content greater than 0.5 wt.%. Determining the sulphur content in crude oil is an important assessment of quality. Sulphur must be removed via hydroprocessing when refining crude. If it is not, when released into the atmosphere, it can cause pollution and acid rain, and harm some of the chemical equipment in the refinery [34, 42, 44-46].

1.3.2.3 Pour Point

The pour point is the minimum temperature in which the oil is able to pour down (still behaves as a fluid). The pour point of crude oils relates to their paraffin content: If the paraffin molecules are 18 carbon atoms or longer in length, they are waxes that are solid at surface temperature. A crude oil that contains a significant amount of wax is called a *waxy crude oil*. the higher the paraffin content, the higher the pour point [34, 42, 46].

1.3.2.4 Colour

The colour of crude oils can vary from nearly colourless through greenish-yellow, reddish, and brown to black, depending upon the hydrocarbon composition. In general, the darker the crude oil, the lower the °API gravity [47, 48].

The properties of crude oil determine its quality and price commercially. Crude oils that are higher API and lower sulphur content (sweet) are usually priced higher than heavy, sour crude oils. Crude quality classes are classified in **Table 1.2** and **Figure 1.10** [34, 49, 50].

Table 1.2 Crude quality classes [50].

	API (°)	Sulphur content (wt. %)
Light sweet	≥ 35	< 0.5
Light sour	≥ 35	≥ 0.5
Medium sweet	26 ≥ API > 35	< 0.5
Medium sour	26 ≥ API > 35	≥ 0.5
Heavy sweet	< 26	< 0.5
Heavy sour	< 26	≥ 0.5

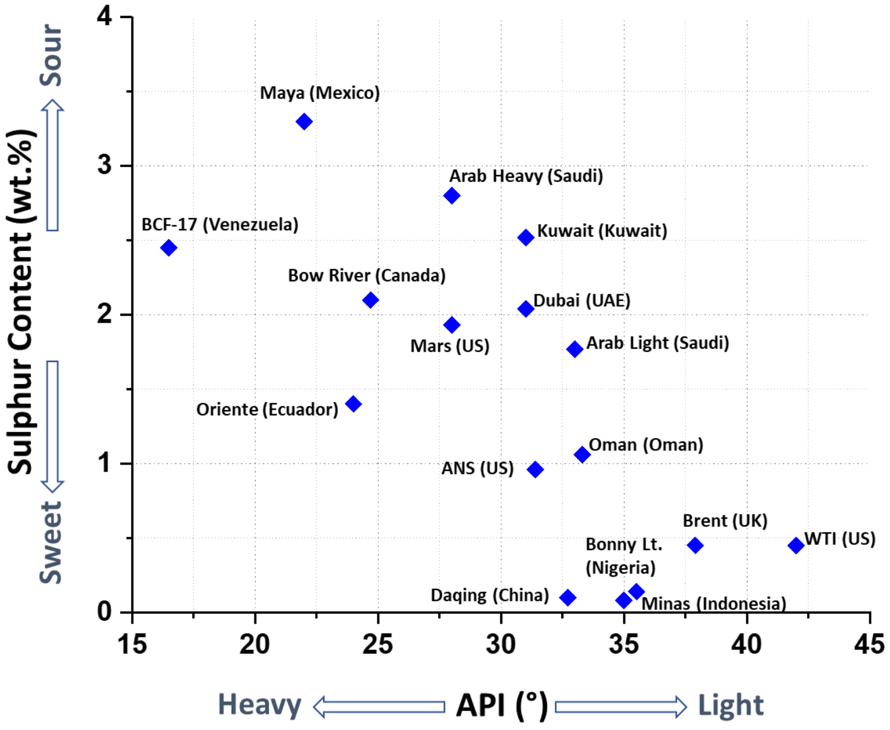

Figure 1.10 API gravity and sulphur content of selected crude oils. (Adapted from Ref.[49]).

Crude oil refining is one of the important processes that can be used to treat crude oil, extract the desired products, and convert it into a number of useful hydrocarbon products for use as fuels for transportation, heating, generating electricity and as feedstocks for petrochemical industries. All refineries have three basic steps: Separation, conversion and treatment [51].

Petroleum refining starts with crude oil distillation to separate crude oil in atmospheric and vacuum distillation column towers into different products based on their boiling points, called “fractions” or “cuts”. Crude oil is first desalted (dissolved brine is removed by washing) and heated to around 600 °C and then the heated crude is injected into to the distillation column. Lighter fractions (less-dense), such as butane and other liquid petroleum gases (LPG), gasoline blending components, and naphtha, are recovered at higher points in the distillation column. Mid-range products include jet fuel, kerosene, and distillates. The heaviest products such as residual fuel oil are recovered at temperatures sometimes over 500 °C (**Figure 1.11**) [42, 48, 51, 52].

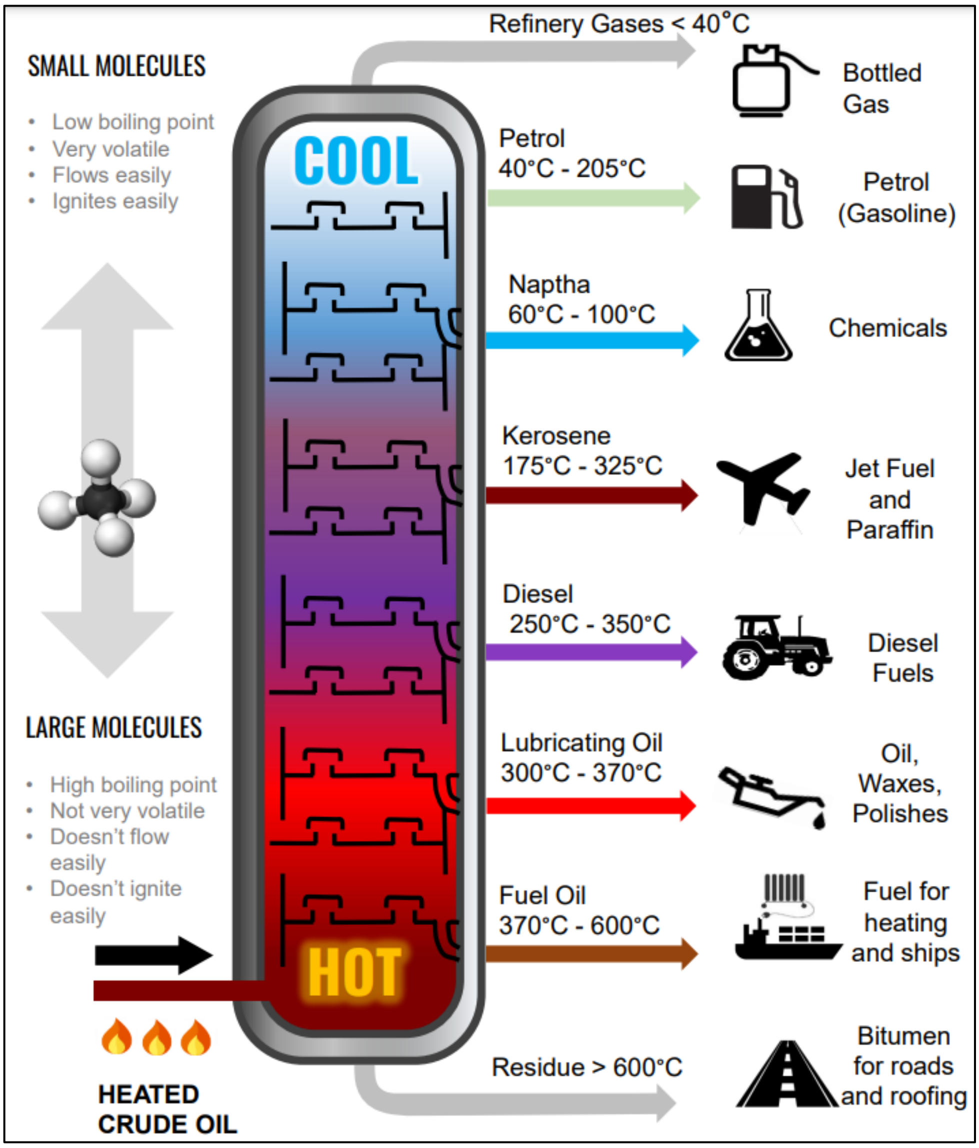

Figure 1.11 Crude oil distillation column and products. (Reproduced from Ref. [52]).

After distillation, large hydrocarbon fractions such as residual oils, fuel oils, and light ends can be processed further and converted into lighter, higher-value products such as gasoline, jet fuel, and diesel fuel. Cracking, coking, and visbreaking processes (a mild form of thermal cracking) are used to crack heavy hydrocarbon molecules into lighter ones. Polymerization and alkylation processes are used to combine small hydrocarbon molecules into larger ones [53].

Isomerization and reforming processes are applied to rearrange the structure of hydrocarbon molecules to produce higher-value molecules of a similar molecular size [51, 54].

The third step is the treatment (purification) process, which involves reducing and removing undesirable elements such as sulphur, nitrogen, and oxygen by hydrodesulfurization, hydrotreating, chemical sweetening, and acid gas removal [54, 55]. **Table 1.3** summarises the most common physical and chemical processes used in oil refineries.

Table 1.3 Physical and chemical processes used in oil refineries [54].

Physical	**Chemical**	
	Thermal	**Catalytic**
Distillation	Visbreaking	Hydrotreating
Solvent extraction	Delayed coking	Catalytic reforming
Propane deasphalting	Flexicoking	Catalytic cracking
Solvent dewaxing		Hydrocracking
Blending		Catalytic dewaxing
		Alkylation
		Polymerization
		Isomerization

1.4 Hydrogen Production

Hydrogen is the simplest and most abundant element in the universe and is also possesses the highest energy content per unit of weight compared to any other fuels (with the exception of nuclear fuel) (**Table 1.4**). Looking to a future clean energy source, it has long been recognised that hydrogen offers the prospect of a highly effective fuel or energy source for humankind's future sustainable energy. This is indeed reflected in a burgeoning interest in the use of hydrogen as a clean energy vector. Unlike fossil fuels, hydrogen gas burns cleanly, without emitting any environmental pollutants (**Figure 1.12**) [56, 57].

Table 1.4 Heat values of hydrogen and common fossil fuels [58].

Fuel type	**Heat value*** **(MJ/kg)**
Hydrogen (H_2)	120-142
Methane (CH_4)	50-55
Gasoline fuel	44-46
Diesel fuel	42-46
Crude oil	42-47
Liquefied petroleum gas (LPG)	46-51
Natural gas	42-55
Coal	17.4-25

*The amount of heat released during the combustion of a specified amount of the fuel.

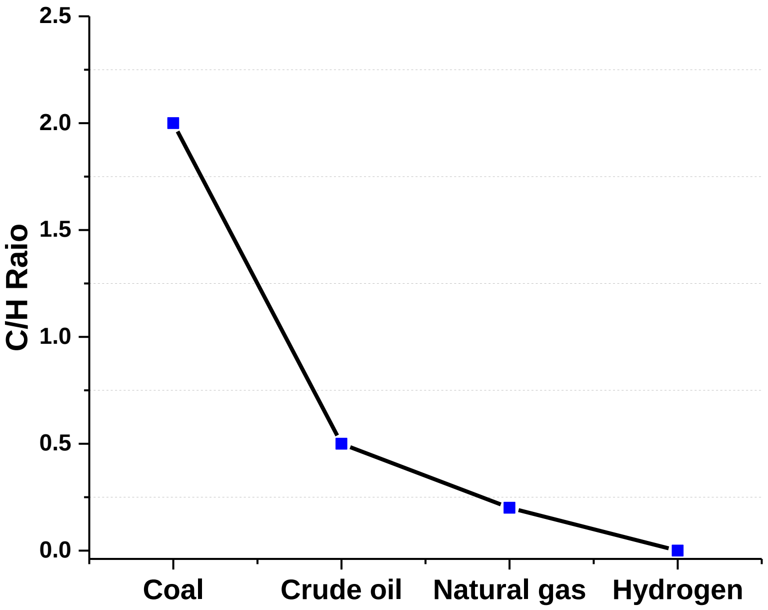

Figure 1.12 Variation of carbon/hydrogen ratio for various fuels. (Adapted from Ref.[59]).

Hydrogen can be produced by various technical processes using renewable or non-renewable sources and is used in important industrial processes. Thus, hydrogen is a fundamental building block in the large-scale manufacture of ammonia, and hence fertilizers, and of methanol, used in the manufacture of many polymers. Refineries where hydrogen participates in the processing of intermediate oil products, are another area of widespread use [60, 61]. Nowadays, over 70 million metric tons of hydrogen are produced and consumed worldwide [9]. The largest volumes are consumed in the ammonia production (47%), petroleum refining (27%), methanol production (18%), synthesis of other chemicals (3%), steel (0.5%) and other uses (4.5%) [62, 63]. Hydrogen consumption is forecasted to grow exponentially in the coming period and its uses to diversify across the power generation, transportation, industry and building heating sectors, in addition to its current use as a chemical feedstock [63]. **Figure 1.13** shows the forecasted hydrogen consumption breakdown through year 2050 from the Hydrogen Council [64].

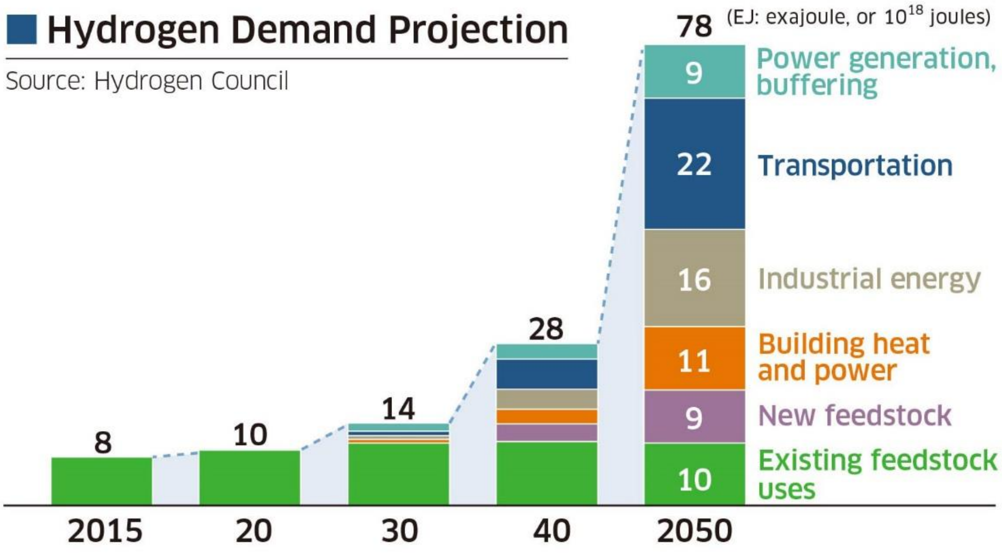

Figure 1.13 Hydrogen demand projection. (Reproduced from Ref. [64]). Original units in EJ converted to tonnes H_2, 1 EJ = 7,000,000 tonnes H_2.

1.4.1 Hydrogen Production from Non-Renewable Sources (Fossil Fuel-Based)

Fossil hydrocarbons still remain one of the major sources of energy for hydrogen gas production. “Grey” hydrogen is produced from natural gas or other fossil fuels via steam methane reforming (SMR) or coal gasification. This also produces huge amounts of CO_2 contributing to more than 2% of global CO_2 emissions [65-69]. It is called “Blue” hydrogen when CO_2 is captured, stored, and utilized (CCUS). Both Grey and Blue (including CCUS) technologies are mature and well-proven technologies. Over 96% of hydrogen produced today is Grey hydrogen [65] (**Figure 1.14**).

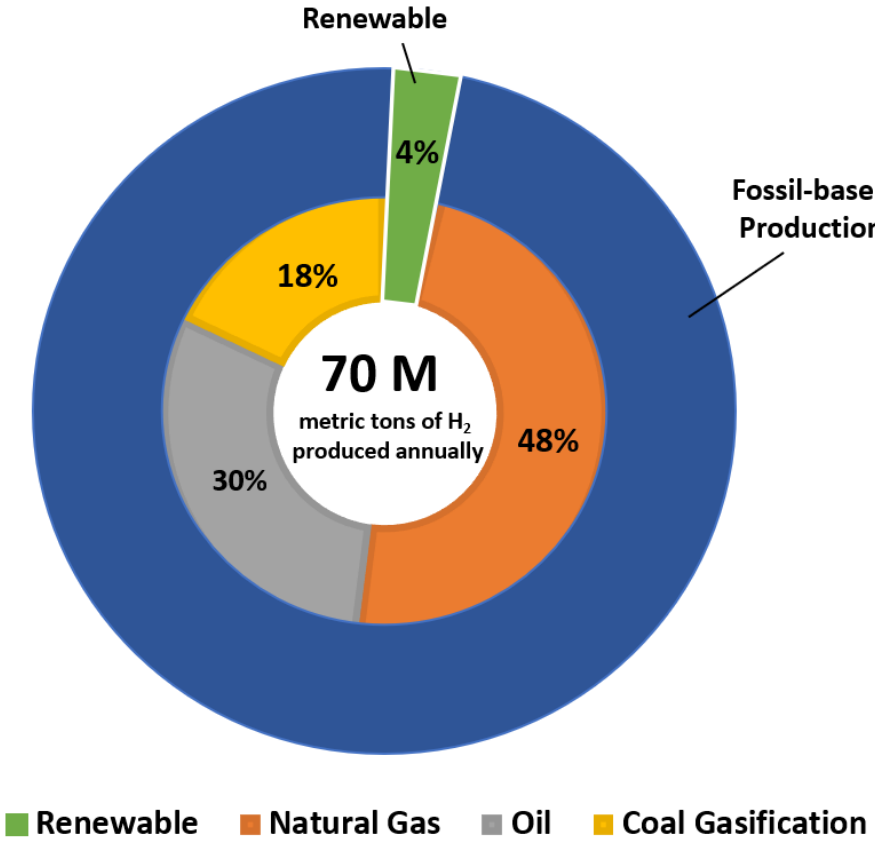

Figure 1.14 Hydrogen production and resources in % of total metric tonnes. (Adapted from Ref. [65]).

1.4.1.1 Hydrogen Reforming

Steam reforming (SR), partial oxidation (POX), and autothermal reforming (ATR) are the three main processes used to produce hydrogen from hydrocarbon fuels. In the reforming process, hydrogen is produced on an industrial scale by generating a gas stream composed primarily of hydrogen, carbon monoxide and CO_2. The reaction is endothermic and thermal energy is required to extract hydrogen from the hydrocarbon fuels (i.e. natural gas, methane, or naphtha) (**Equation 1.2)**. Subsequently, the water-gas shift reaction takes place and the stream react with carbon monoxide to produce CO_2 and more hydrogen. In the purification process, CO_2 and other impurities are removed from the gas stream (**Figure 1.15**) [69-74].

$$\mathrm{C}_m\mathrm{H}_n + m\mathrm{H_2O}\ (+\mathrm{heat}) \rightarrow m\mathrm{CO} + (m + \tfrac{1}{2}n)\mathrm{H}_2 \qquad \textbf{Equation 1.2}$$

ΔH= Hydrocarbon dependent, endothermic

For steam reforming of methane (SRM)

$$\mathrm{CH_4} + \mathrm{H_2O} \leftrightarrow \mathrm{CO} + 3\mathrm{H_2} \qquad \textbf{Equation 1.3}$$

$\Delta H^{\circ}_{298K} = +\ 206.8\ \mathrm{kJ\ mol^{-1}}$

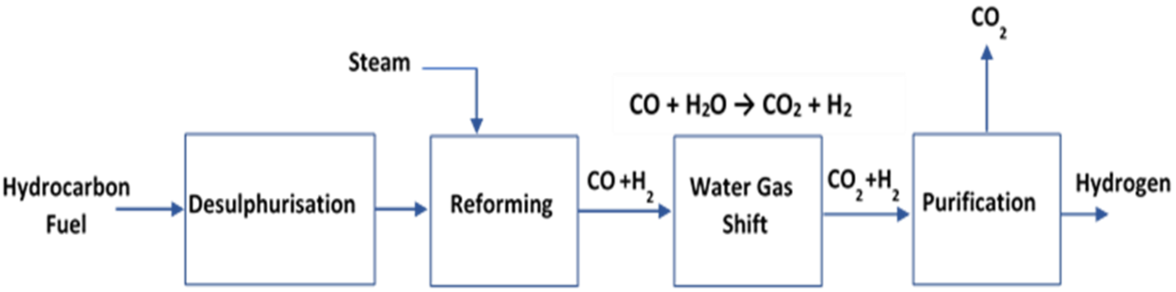

Figure 1.15 Hydrogen production by steam reforming process.

Partial oxidation (POX) and catalytic partial oxidation (CPOX) are an alternative process for hydrogen production with reduced energy cost, since the reaction is exothermic (**Equation 1.4)**, the hydrocarbon fuels react with a sub-stoichiometric amount of oxygen, producing a syngas stream (**Figure 1.16**) [69, 75-78].

$$C_mH_n + \frac{1}{2}mO_2 \rightarrow mCO + \frac{n}{2}H_2$$ **Equation 1.4**

ΔH= Hydrocarbon dependent, exothermic

For Partial oxidation of methane (POM); the syngas product has a H_2/CO molar ratio of 2, according to **Equation 1.5**, which is then increased thought the water gas-water shift reaction.

$$CH_4 + \frac{1}{2}O_2 \rightarrow CO + 2H_2$$ **Equation 1.5**

$\Delta H^{\circ}_{298K} = - 35.6\ kJ\ mol^{-1}$

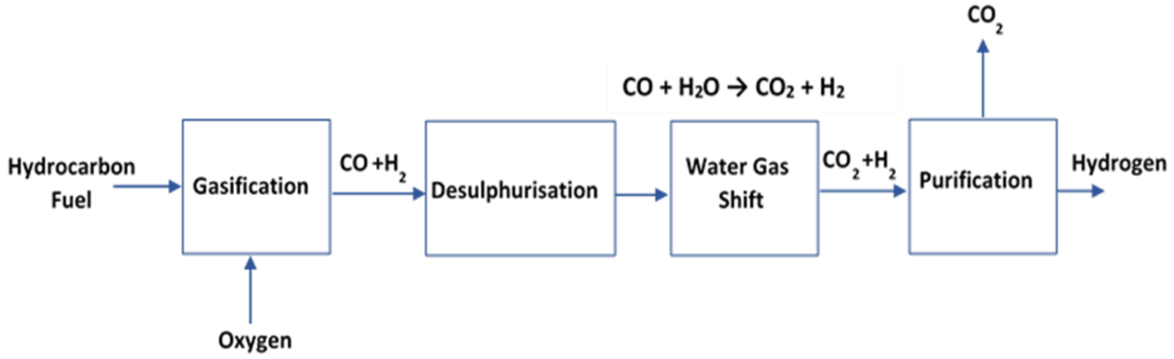

Figure 1.16 Hydrogen production by the partial oxidation process.

Autothermal reforming (ATR) is a combination of both steam reforming (endothermic) and partial oxidation (exothermic) reactions (**Equation 1.6)**, where steam is added in the partial oxidation process to form syngas (**Figure 1.17**) [79-81].

$$C_mH_n + \frac{1}{2}mH_2O + \frac{1}{4}mO_2 \rightarrow \frac{1}{2}nH_2 + mCO$$ **Equation 1.6**

ΔH= Hydrocarbon dependent, thermally neutral.

For Autothermal reforming of methane (ATRM):

$$4CH_4 + 2H_2O + O_2 \rightarrow 10H_2 + 4CO$$ **Equation 1.7**

$\Delta H^{\circ}_{298K} = 0$

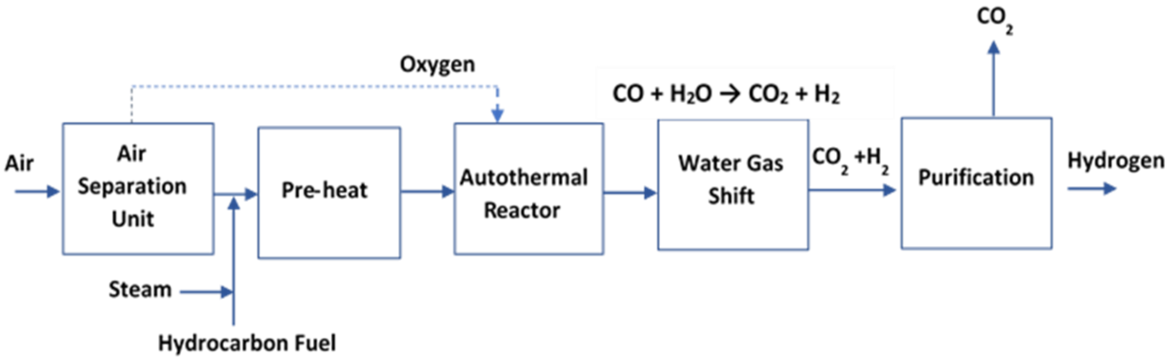

Figure 1.17 Hydrogen production by autothermal reforming process.

1.4.1.2 Hydrogen Pyrolysis

Pyrolysis (or decomposition) is an alternative process conducted in inert atmosphere able to convert hydrocarbon fuels into hydrogen and carbon without the presence of steam or oxygen, and as a result, no carbon oxides are formed during the process (**Equation 1.8**). One of the challenges with pyrolysis process is the fouling or coking by the carbon formed (**Figure 1.18**) [69, 82, 83].

$$C_mH_n \rightarrow mC + \frac{1}{2}\,nH_2 \qquad \textbf{Equation 1.8}$$

ΔH= Hydrocarbon dependent, endothermic

For methane pyrolysis:

$$CH_4 \rightarrow C + 2H_2 \qquad \textbf{Equation 1.9}$$

$\Delta H^{\circ}_{298K} = + 74.91$ kJ mol^{-1}

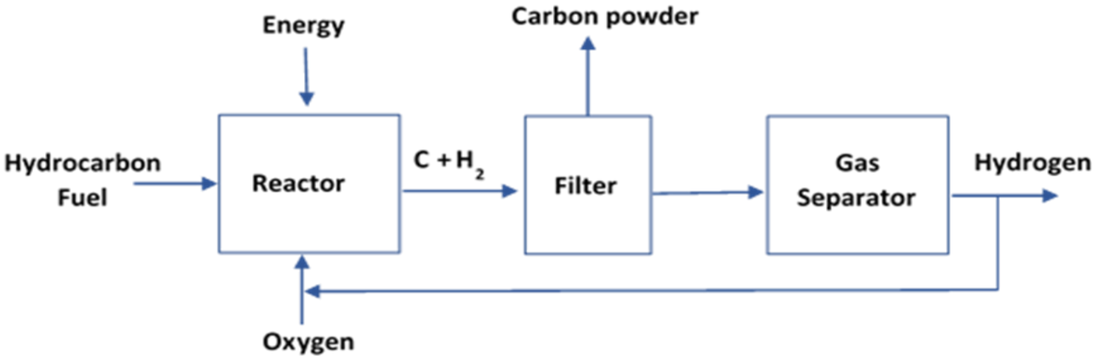

Figure 1.18 Hydrogen production by pyrolysis process.

1.4.1.3 Coal Gasification

In the gasification process (**Figure 1.19**), coal feedstock is converted thermochemically into mainly syngas (hydrogen and carbon monoxide) in the presence of steam and oxygen (or air) at high temperatures and pressures through two steps reactions [69, 70];

$$\mathrm{C + H_2O \rightarrow H_2 + CO} \qquad \textbf{Equation 1.10}$$

$$\mathrm{CO + H_2O \rightarrow H_2 + CO_2} \qquad \textbf{Equation 1.11}$$

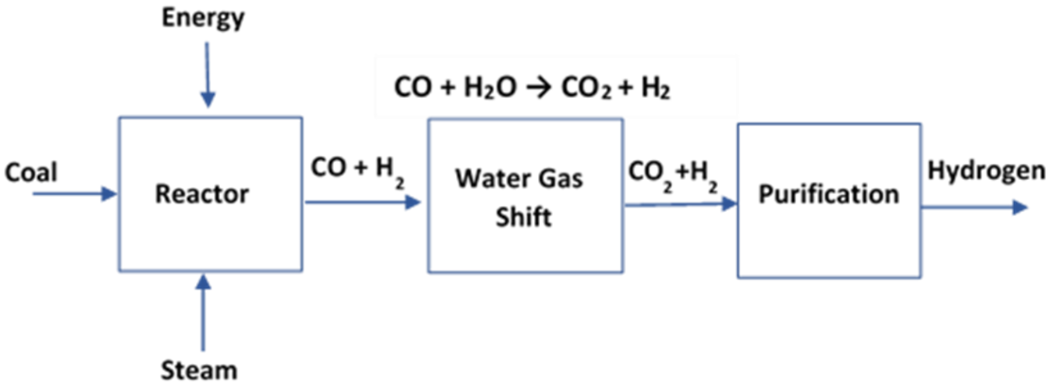

Figure 1.19 Hydrogen production by coal gasification process.

Table 1.5 summarises the different processes used to produce hydrogen at a commercial level. Note that among these technologies, the gasification is a particular energy intensive process that produces larger amount of CO_2 emissions compared to the other processes.

Table 1.5 Comparison of hydrogen production technologies from fossil fuels [69, 70].

Technology		Feedstock	Operation conditions	Pros	Cons
Reforming	Steam reforming	Light hydrocarbons	800–1000 °C	• Most extensive industrial experience. • Oxygen not required. • Lowest process temperature. • Best H_2/CO ratio.	Highest air emissions particularly CO_2.
	Partial oxidation	Hydrocarbons, heavy fuel oil, and coal	>1000 °C	• Desulfurization unit not required. • No catalyst required. • Low methane slip.	• Low H_2/CO ratio. • Very high processing temperatures. • Soot formation/handling.
	Autothermal reforming	Light hydrocarbons	>1000 °C	• Lower process temperature than POX. • Low methane slip.	• Limited commercial experience. • Requires air or oxygen.
Pyrolysis		Hydrocarbons	500–800 °C	• Oxygen not required. • No carbon oxides formed. • Reduce harmful emissions.	Fouling by the carbon formed.
Gasification		Coal	700–1200 °C	• Lower feedstock costs.	• Very high processing conditions. • Highest CO_2 emissions.

1.4.2 Hydrogen Production from Renewable Sources

As previously mention in this chapter, non-renewable sources (fossil-based fuels) have been widely used for hydrogen production and are projected to remain the dominant energy sources until at least 2050 [84, 85] (**Figure 1.20**). Nowadays, the renewable sources only contribute 4% to the total hydrogen production (**Figure 1.14**).

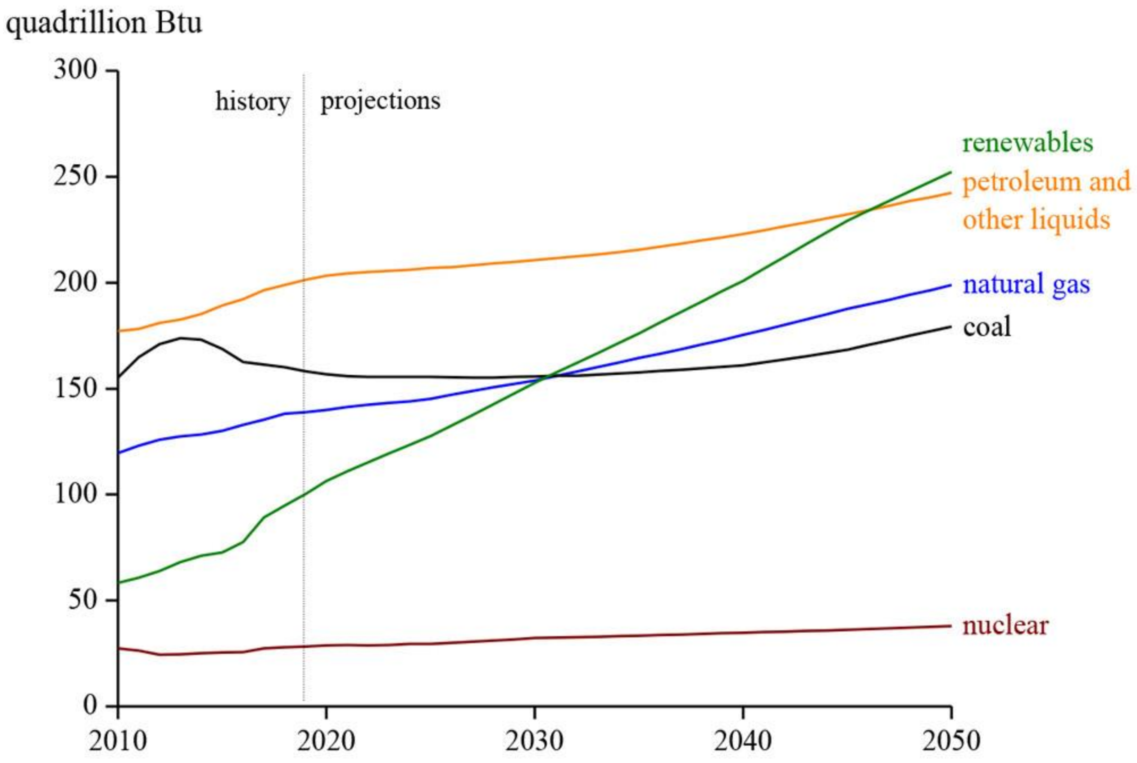

Figure 1.20 World primary energy consumption by energy source. (Adapted from Ref. [84]).

Although most hydrogen is produced from fossil fuels, renewable resources have attracted the attention to produce "Green" hydrogen and reduce energy-related CO_2 emissions. In this context, hydrogen could also be produced from water (e.g. electrolysis, thermolysis, and photo-electrolysis) or biomass-derived compounds (e.g. thermochemical and biological) [6, 85, 86].

1.4.2.1 Hydrogen Production from Water

Water is the most sustainable and abundant resource for hydrogen production, and it can be split into hydrogen and oxygen to produce hydrogen gas if enough energy is provided [87, 88]. In the electrolysis process, an electrical current is passed between two electrodes to break water into hydrogen and oxygen. The alkaline electrolyser is the most common technology to convert electrical energy to chemical energy and form hydrogen. Proton exchange membrane (PEM) and solid oxide electrolysis cells (SOES) technologies are still under research and development [69]. In an alkaline cell in **Figure 1.21**, direct current is passed through and the water which is decomposed into hydrogen and OH^-. The OH^- travels to the anode where O_2 is formed. The hydrogen is left in the alkaline solution and then separated from the water in a gas-liquid separation unit [66].

Anode: $4OH^- \rightarrow 2H_2O + O_2 + 2e^-$ **Equation 1.12**

Cathode: $2H_2O + 2e^- \rightarrow H_2 + 2OH^-$ **Equation 1.13**

Overall process: $H_2O \rightarrow H_2 + \frac{1}{2}O_2$ **Equation 1.14**

$\Delta H^{\circ}_{298K} = -288\ kJ\ mol^{-1}$

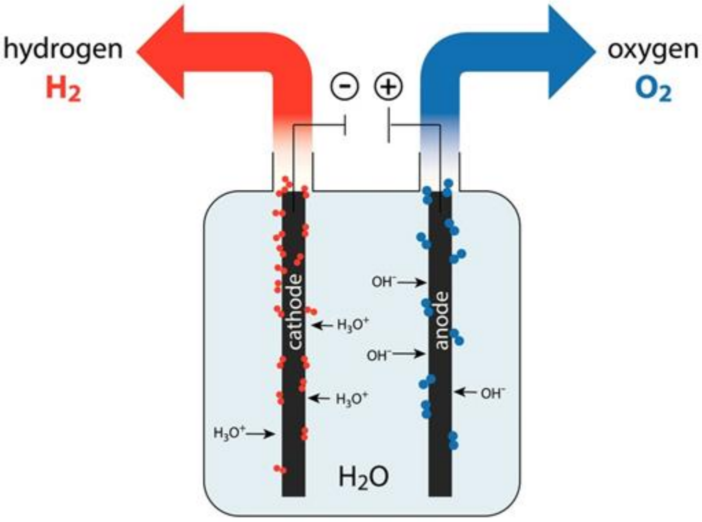

Figure 1.21 Schematic illustration of alkaline water electrolysis (Adapted from Ref.[66]).

Green hydrogen is produced when power is supplied from renewable sources, i.e., wind or solar PV. However, thermal energy (thermolysis) can also be applied to split water using heat as energy source, photonic energy (photoelectrolysis), and biophotolysis using microorganisms; these processes are summarized in **Table 1.6**.

Table 1.6 Summary of hydrogen production technologies from water [86, 89].

Technology	Energy source	Operation conditions	Maturity
Electrolysis	Electricity	Up to 30 bars 50–900 °C (depending upon the method used)	Commercial
Thermolysis	Heat	Temperature of >2500 °C (<1000 °C for thermochemical cycles)	R & D
Photoelectrolysis	Solar	Ambient conditions	R & D
Biophotolysis	Microorganism metabolism	Ambient conditions	R & D

1.4.2.2 Hydrogen Production from Biomass

Biomass is a renewable resource of fuels and chemical feedstocks derived from agricultural and marine residues, and forest and animal by-products [90, 91]. Hydrogen production from biomass is economically viable with current technologies. It has been stated that biomass will cover by up to 25% of the energy demand by 2050 [92]. Unlike fossil fuels, hydrogen green production processes reduce CO_2 emissions, leading to an apparent neutral carbon emission scenario. There are two essential processes to produce hydrogen from biomass, namely, biological, and thermochemical. The thermochemical process is usually much faster than the biological process and offers a higher hydrogen yield.

Table 1.7 summarises the main technologies for both processes, which will be subsequently developed, along with the kind of biomass used, the operational conditions, and their technological maturity.

Table 1.7 Summary of hydrogen production technologies from biomass [90].

Technology	Principle	Energy source	Operation conditions	Maturity
Pyrolysis	Thermochemical	Dried biomass	300–1000 °C in the absence of oxygen	Commercial
Gasification	Thermochemical	Dried biomass	800–900 °C	Commercial
Steam reforming	Thermochemical	Biomass-derived liquids	800–1000 °C	Commercial
Hydrothermal liquefaction	Thermochemical	Wet biomass	250–370 °C 4–22 MPa	R & D
Dark fermentative	Biological	Carbohydrate-rich substrates	Anoxic conditions	R & D
Photofermentative	Biological	Small organic molecules	Anaerobic conditions	R & D

1.4.3 The Hydrogen Economy from a Global Perspective

The concept of hydrogen economy is using hydrogen to decarbonise domestic and industrial sectors in order to limit global warming. The vision of the hydrogen economy is based on two perspectives: First, hydrogen can be produced from local energy sources in an affordable and environmentally friendly manner. And second, its technologies could gain market share in competition with alternatives [93].

Hydrogen production can be decarbonized through different renewable technologies, which have different CO_2 emissions and technology readiness levels (TRL). Low-carbon hydrogen can be produced through electrolysis, splitting biomass using steam methane reforming, and gasification technologies. Importantly, hydrogen production from biomass, also known as bio-hydrogen, is the only hydrogen production route that can generate net-negative CO_2 emissions when coupled with CCS [94-96]. **Table 1.8** give an outline of the CO_2 emission intensities of different hydrogen production routes estimated from life cycle analyses of hydrogen supply chains.

Table 1.8 CO_2 emission intensity of hydrogen production routes [94].

Technology	TRL[*]	Emissions ($kgCO_2/kgH_2$)	
		Low	High
Fossil methane with SMR	9	10.09	17.21
Fossil methane with SMR and CCS	7-8	2.97	9.16
Coal gasification	9	14.72	30.9
Coal gasification with CCS	6-7	2.11	10.35
Electrolysis (with wind and solar)	9	0.47	2.5
Biomass gasification	5-6	0.31	8.63
Biomass gasification and CCS	3-5	-17.5	-11.66
Bio-methane with SMR	9	1.2	8.6
Bio-methane with SMR and CCS	7-8	-11.6	-8.84

[*] TRL: Technology Readiness Level. TRLs are based on a scale from 1 to 9, with 9 being the most mature technology.

According to the IEA study to the 2019 G20 summit in Japan, there is unprecedented momentum for hydrogen, with a common belief worldwide that the time is right to tap into hydrogen's potential to play a key role in a clean, secure, and affordable energy future. According to Dr. Fatih Birol, Executive Director of IEA: *"Hydrogen is today enjoying unprecedented momentum. The world should not miss this unique chance to make hydrogen an important part of our clean and secure energy future"* [9].

Grey and Blue hydrogen are currently cheaper to produce. However, it is expected that the cost of Green hydrogen will catch up by 2030. The target cost for Green hydrogen is 1 $/Kg to be competitive with Blue hydrogen [97]. For that reason, Blue hydrogen is considered by many countries, particularly Europe, as a bridge between the current situation and the ultimate goal of renewable energy-based Green hydrogen [98]. By 2030, the European Commission estimates that €13-15 bn could be invested in electrolysers across the EU, in addition to €50-150 bn for a dedicated wind and solar capacity of 50 -75 GW [99]. Japan has established a 30 year plan for gradual shift to hydrogen/ammonia use as energy source and is putting extensive efforts to develop technologies for hydrogen/ammonia use in gas turbines, marine engines, fuel cells, and industrial furnaces [100]. Saudi Arabia has announced the world's largest Green hydrogen project in NEOM (Saudi new city), a partnership with Air Products and ACWA Power to build a $5 Billion green ammonia production facility aiming to convert it to hydrogen fuel at the end-user destination. This will Supply 650 tons per day of carbon-free hydrogen for transportation globally and save the world 3 MT per year of CO_2. The project is set to start operation by 2025 with Air Products as the sole off-taker/exporter of green ammonia [101, 102].

There are several challenges facing the hydrogen economy, including high production cost, low efficiency, high water consumption, difficulty to handle and transport, and finally, the threat it poses to fossil fuels demand [103]. For Green hydrogen, large-scale projects require huge areas of flat, sunny, and windy spaces near the sea. Few regions worldwide meet all these requirements. Hydrogen production by electrolysis consumes at least 9 tons of water per ton of hydrogen. Brine discharge from desalination will be returned to the sea, which is an environmental concern [104]. Electrolysis cost is expected to drop significantly (up to 50% in some estimates) in the future due to technology advancement, production scale-up, and government regulatory support leading it to eventually being comparable to fossil-based hydrogen [105]. In conclusion, technology advances, cost decrease, and strong government support are pushing toward making the hydrogen economy a reality.

The SWOT analysis (strengths, weaknesses, opportunities and threats) for the hydrogen economy is listed as follows in **Figure 1.22**.

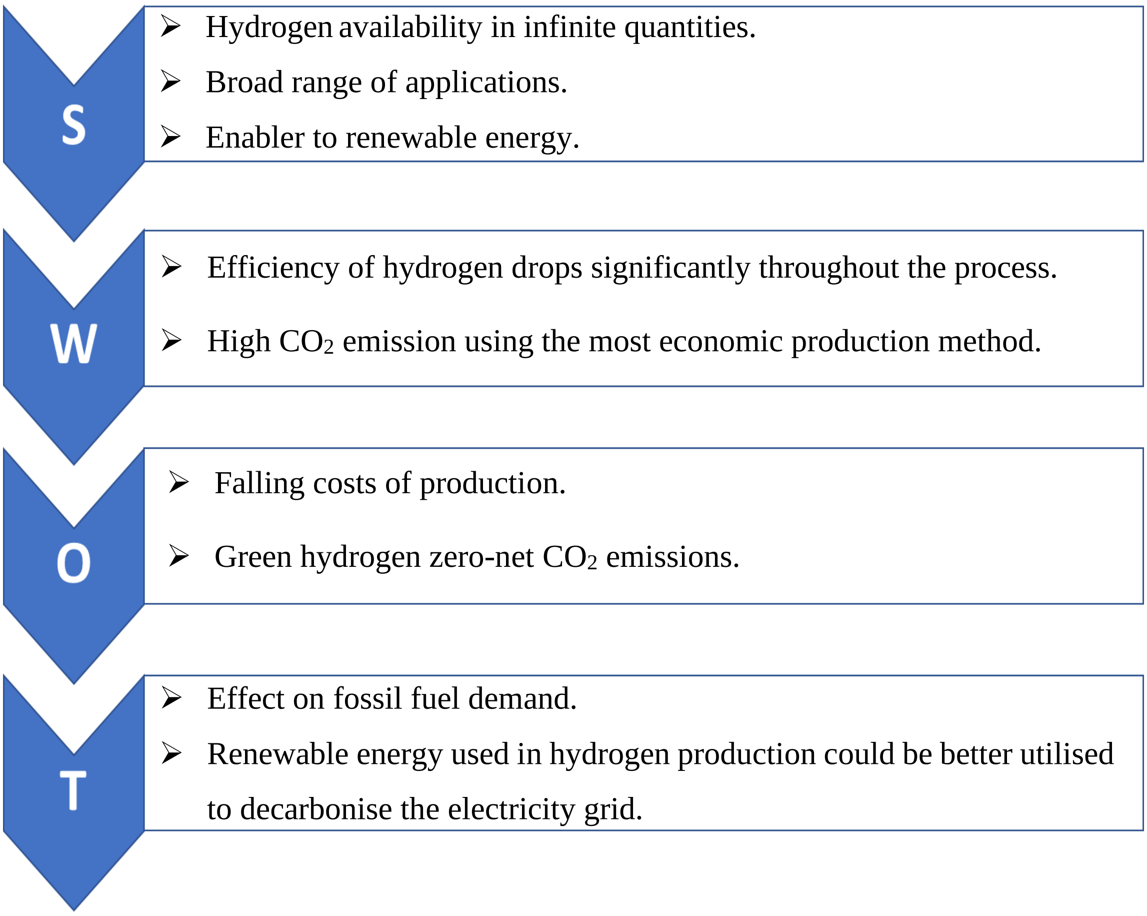

S
- Hydrogen availability in infinite quantities.
- Broad range of applications.
- Enabler to renewable energy.

W
- Efficiency of hydrogen drops significantly throughout the process.
- High CO_2 emission using the most economic production method.

O
- Falling costs of production.
- Green hydrogen zero-net CO_2 emissions.

T
- Effect on fossil fuel demand.
- Renewable energy used in hydrogen production could be better utilised to decarbonise the electricity grid.

Figure 1.22 SWOT analysis of the hydrogen economy. (Adapted from Ref.[106, 107]).

1.5 Microwave Energy

1.5.1 Background

The production of thermal energy by the burning of wood and fossil fuels unavoidably generates greenhouse gases such as CO_2, responsible in part for global warming. One of the promising solutions to sustain life and preserving the environment is to rely on the energy from electromagnetic waves. Over the past decades, microwave radiation has been used as a heat source in various technological and scientific fields, such as: food processing, drying processes, waste water purification, activated carbon regeneration; sintering of metals and ceramics, pyrolysis processes and many other chemical and physical uses [108, 109]. The advantages of microwave heating compared to conventional processing methods include energy-saving rapid heating rates and short processing times, deep penetration of the microwave energy, instantaneous and precise electronic control, clean heating processes, and no generation of secondary waste. Microwave technologies have become an attractive candidate in several fields of chemistry including organic, inorganic, catalysis, and synthesis. It has been also claimed that microwave could become very efficient in producing innovations in oil processing applications [108, 110, 111].

Microwave radiation is part of the electromagnetic spectrum situated between the radio and infrared frequencies with a frequency that ranges from approximately 300 MHz to 300 GHz, which corresponds to wavelength ranging from 1m down to 1mm (**Figure 1.23**). Due to legislation, the commercially available magnetrons for chemical processing operate at one of the following frequencies: 915 MHz, 2.45 GHz and 5.85 GHz, in order to avoid any interference with broadcast and communications bands [108, 112, 113]. The heating behaviour of any reacting materials under microwave radiation is mainly influenced by their dielectric properties.

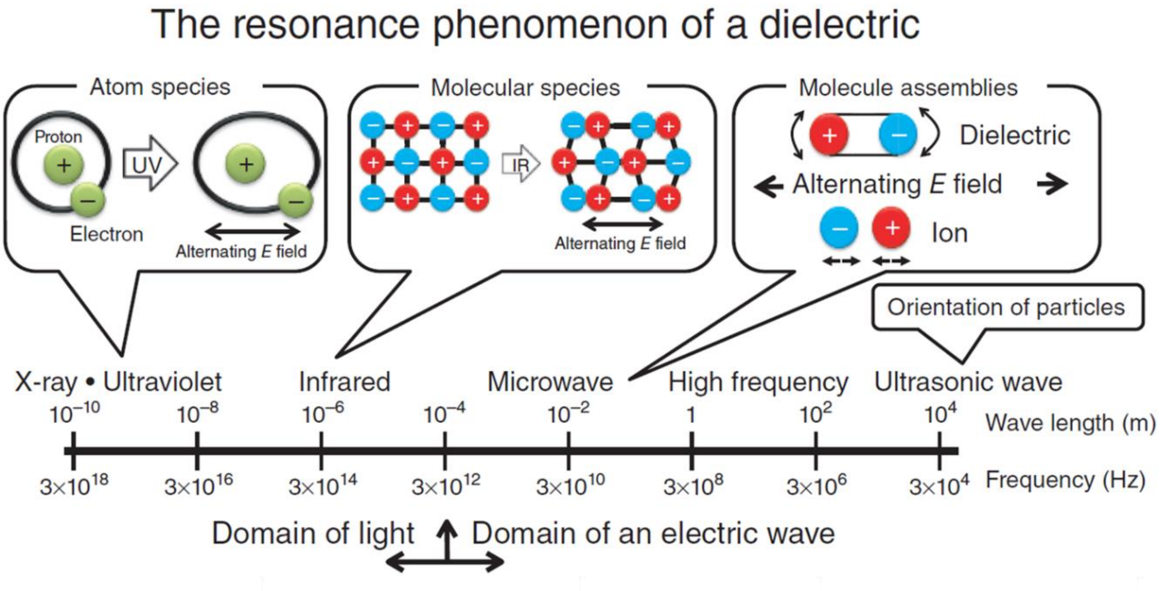

Figure 1.23 Regions of the electromagnetic spectrum with the resonance phenomenon of a dielectric. (Reproduced from Ref.[108])

1.5.2 Interaction of Microwaves with Matter

In general, the interaction of microwave irradiation with matter is characterized by three different processes: absorption, transmission, and reflection (**Figure 1.24**). Whilst high dielectric materials, like polar organic solvents, lead to strong absorption of microwaves and consequently to a rapid heating of the medium, non-polar (microwave transparent) materials show only small interactions with microwaves (transmission). Microwaves pass through such materials. This makes them ideally suitable as construction materials for reactors. If microwave radiation is reflected by the material surface, there is almost no introduction of energy into the system [108, 114-116].

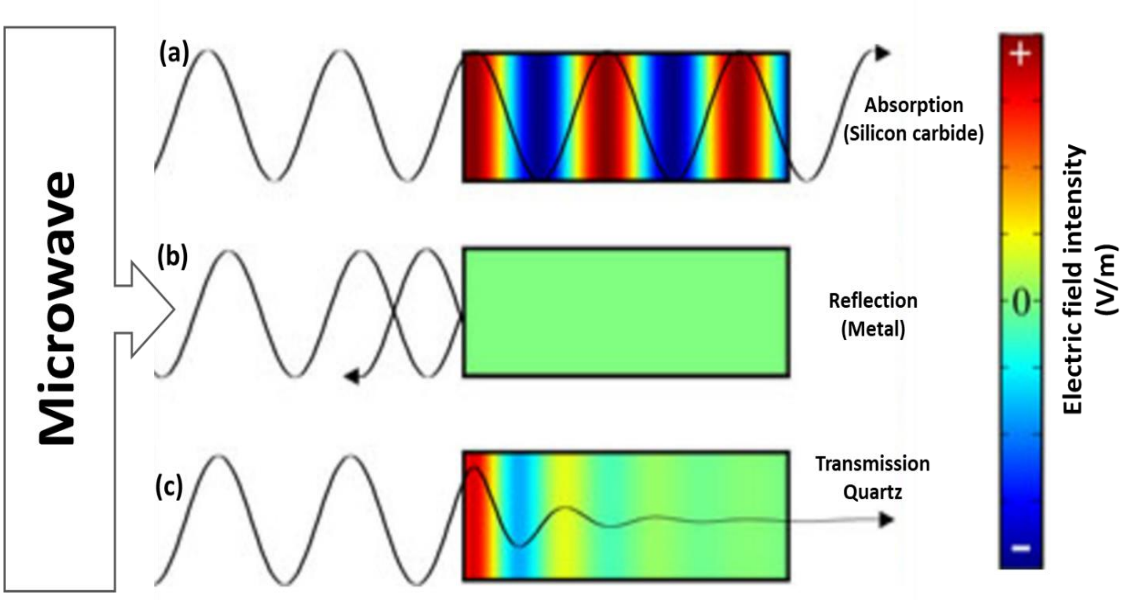

Figure 1.24 A schematic representation of the interaction of different materials with microwaves: (a) absorbing materials (e.g. silicon carbide), (b)electrical conductors (e.g. metals), and (c) insulation materials (e.g. Teflon, glass, quartz). (Adapted from Ref.[112]).

The conventional method of heating a reaction mixture (particularly with low thermal conductivity such as hydrocarbons) is comparatively slow and energy inefficient, since first the heat energy is transferred from the outside of the container to the bulk of the material. In contrast, microwave irradiation results in energy efficient internal heating by direct coupling of microwave energy with dipoles and/or ions that are present *within* the reaction mixture. Microwaves pass through the (almost) microwave-transparent vessel wall and heat the reaction mixture by direct interaction with the molecules or catalyst particles. This important and fundamental difference with conventional heating arises from the fact that microwave irradiation results in inverted temperature gradients as compared to a conventionally heated system (**Figure 1.25**) [111, 117].

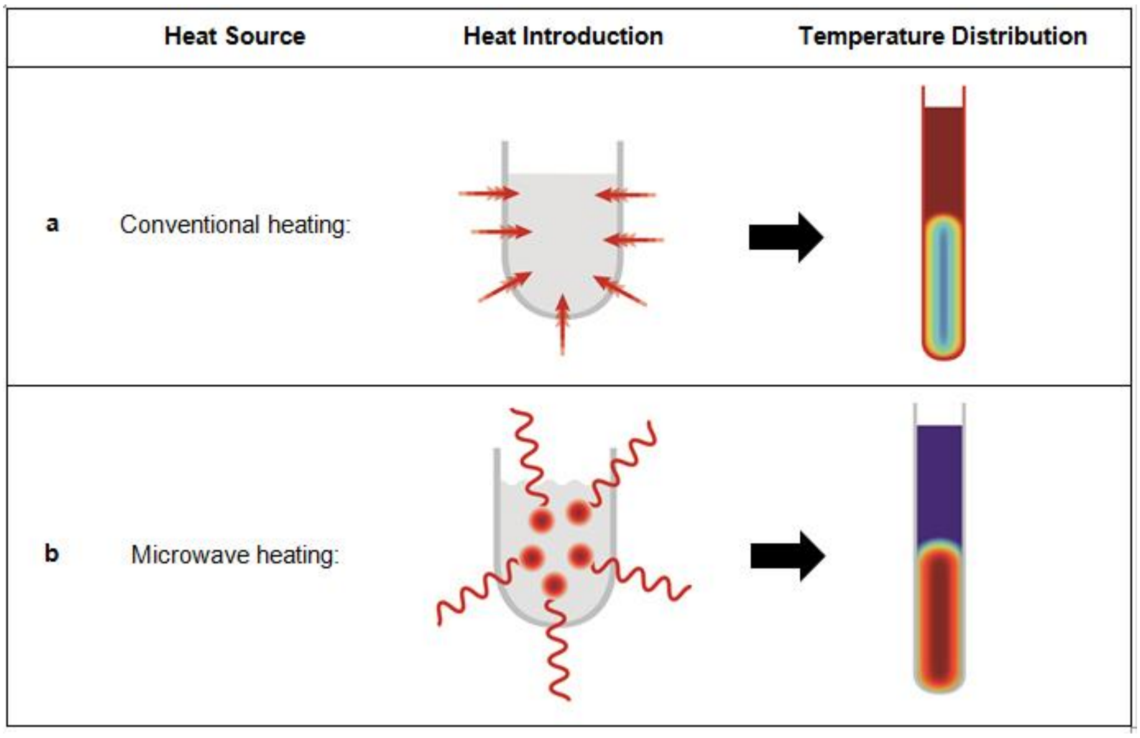

Figure 1.25 Schematic representation of heat introduction and temperature distribution: (a) conventional heating and (b) microwave heating. (wiki.anton-paar.com).

For example, water is a polar molecule with a partial positive charge at one end and negative at the other, and the electromagnetic waves create energy in the water molecules. By definition, the waves have electrical and magnetic fields that change direction rapidly, for the domestic microwave oven (2.45 GHz), the direction of the fields change 2,450,000,000 times per second. The water molecules will try to align with the radiation's electric field, the changing field rocks the water molecules back and forth rapidly and molecular friction from this generates heat as the motion disrupts the hydrogen bonds between neighbouring water molecules (**Figure 1.26**) [108, 110].

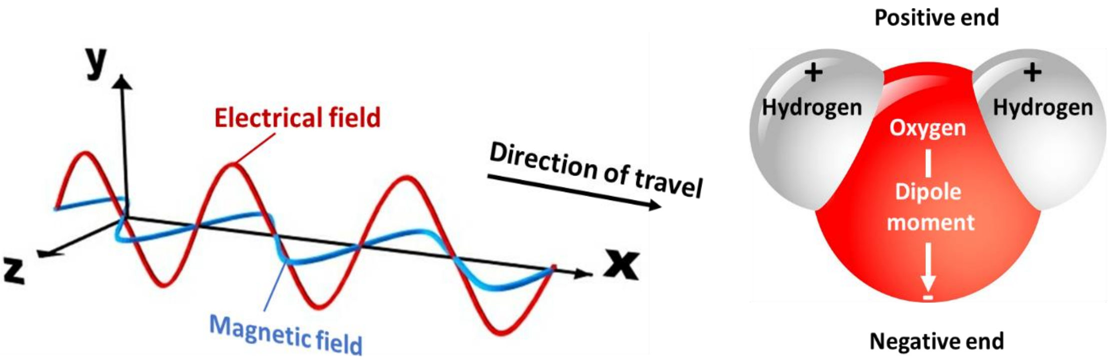

Figure 1.26 Electromagnetic wave (left) and the structure of water molecules (right). (Adapted from Ref. [110])

By definition, the dielectric constant or permittivity of a material is a measure of the extent to which the electric charge distribution in the material can be distorted or polarized by the application of an electric field. The electric susceptibility and permittivity are non-dimensional real quantities. The complex dielectric constant or dielectric permittivity (ε^*) is given in **Equation 1.15** which consists of a real part (ε') and an imaginary part (ε''). The real part of the relative permittivity (ε') (i.e. dielectric constant) measures the ability of a molecule (or assembly of molecules) to be polarised by an electric field, and the imaginary part (ε'') (i.e. dielectric loss) represents the ability of a medium to convert dielectric energy into molecular rotation, and hence heat [119, 120];

$$\varepsilon^* = \varepsilon' + \varepsilon'' \qquad \textbf{Equation 1.15}$$

The loss tangent (tan δ) defined as the ratio of the imaginary part of the permittivity to the real part and is commonly used to measure the interaction of a dielectric with the microwaves and describe the ability of a material to convert electromagnetic energy into heat energy. The loss tangent depends on the dielectric properties of the material and is defined by **Equation 1.16** [119, 120];

$$\tan\delta = \frac{\varepsilon''}{\varepsilon'}$$ **Equation 1.16**

The value of (tan δ) of a system or mixture depends on several factors: the frequency of the electromagnetic waves, the temperature and the physical state and composition of the mixture. A material that has tan δ = 0 is completely transparent to microwave irradiation, and the incident irradiation passes through with its path unchanged, and materials with tan δ approaching 1 are very strong microwave absorbers. For instance, ethanol (tan δ = 0.941) is an exceptional absorbers of microwave irradiation at 2.45 GHz (**Table 1.9**) [111, 118].

Table 1.9 Dielectric constant (ε'), dielectric loss (ε''), and loss tangent (tan δ) for selected solvents at a frequency of 2.45 GHz [113].

Solvent	Dielectric constant (ε')	Dielectric loss (ε'')	Loss tangent (tan δ)
Water	80.4	9.89	0.123
Ethanol	24.3	22.9	0.941
Acetone	20.7	1.11	0.054
Toluene	2.4	0.096	0.04
Hexane	1.9	0.038	0.02
Acetonitrile	37.5	2.32	0.062

Other important term in microwave interaction with materials is the relaxation time (τ), which is define as the time required after the removal of an externally applied electric field for the polarization of a dielectric to fall to 1/e of its initial value [119, 120];

$$\tau = \frac{1}{2\pi f_c}$$ **Equation 1.17**

Where f_c is the critical frequency at which the dielectric loss is a maximum.

The penetration depth and the skin depth are important parameters in microwave heating of metals and metal particles. The penetration depth (D_p) is defined as the distance from the surface of material to the level at which microwaves pervade into the material and the power level reduced to 1/e (~ 37%). This depends on the applied frequency and the electronic nature of the heated material [112];

$$D_p = \frac{\lambda}{2\sqrt{2\pi}} [\varepsilon' \left(\sqrt{1 + \left(\frac{\varepsilon''}{\varepsilon'} \right)^2} - 1 \right)]^{-1/2}$$ **Equation 1.18**

Where, λ is the wavelength of the radiation, ε' and ε'' are as defined earlier.

In metals, microwave propagation is usually described in terms of skin depth (δ). It can be defined as the depth at which the electric field decreases to 1/*e* of the value at the surface. It is related to frequency (*f*), permeability (μ), and conductivity (σ), by the relation [121];

$$\delta = \frac{1}{\sqrt{\pi . f . \mu . \sigma}}$$ **Equation 1.19**

The behaviour of a bulk metal powder and particles under microwave radiation are different depending on the skin depth. In metal powders, due to eddy currents and plasma effects, very rapid heating and localised hot spots takes place without any discharge. However, in bulk metals an instantly recognised electric discharge will occur when interacting with microwaves [122, 123].

1.5.3 Non-Thermal Effect of Microwaves

Microwave heating can have two kinds of effects: thermal and non-thermal [124]. The thermal effect is caused by the temperature difference produced by microwave dielectric heating. Non-thermal effects refer to circumstances where the outcome of a synthesis performed under microwave conditions was different from when a conventionally heated counterpart was carried out at the same apparent temperature, that is, microwaves participate in the reaction [125]. However, the existence of non-thermal microwave effects is a controversial topic. It is generally agreed upon by most scientists in the field that in the majority of cases, the experimentally observed effects in microwave chemistry are the result of purely thermal phenomena, without non-thermal microwave effects [126]. In addition, Gutmann et al. [127] considered that the phenomenon that the experimental results under microwave conditions are different from those under conventional heating at the same apparent temperature is related to the wrong temperature measurement or poor control of experimental conditions rather than the real non- thermal effect.

Microwave fields on the outside of any objects are enhanced a bit. As the object polarises, charges gather at the surfaces and the increased charge density leads to a higher field strength at that point. This effect is most pronounced in metals, and if the electrical field is increased at the metal surface enough, it can cause enhanced local heating and even ionisation. This is the reason that we see sparks if we put a metal fork in our microwave ovens at home.

Many of the interesting effects observed in microwave heating of particulates are down to highly localised heating. In metal particulates these can be dramatic. However, that it's often difficult to determine precisely the extent to which such phenomena are present and influencing reactions.

1.5.4 The Size-Induced Metal-Insulator Transition (SIMIT)

The conductivity of metallic materials can be affected by several factors or variables such as temperature, pressure, chemical composition. Small changes in these variables can be transfer the conducting metals into semi-conductors or even insulators [128].

Porch, Slocombe and Edwards have presented detailed principles for the microwave absorption and thus the effective heating of powders of small conducting particles for a range of particle sizes and conductivity [129]. From this one can begin to develop a scheme for the optimisation of the heating processes of small catalytic (nominally) metallic particles. **Figure 1.27** shows the total electromagnetic absorption as a function of both conductivity and mean particle radius for specified conditions and an operating frequency of 2.45GHz.

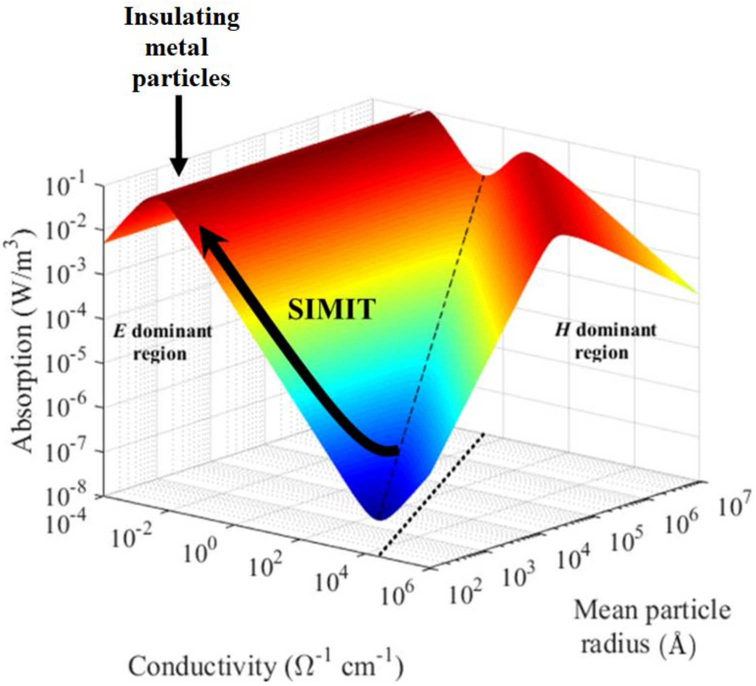

Figure 1.27 Total electromagnetic absorption in non-magnetic particles as a function of conductivity and mean particle radius. Optimal electric absorption and optimal magnetic absorption are marked in red. (Reproduced from Ref.[129]).

From this, one can see that small, highly conducting particles do not heat effectively when placed in a microwave electric field (the configuration in our experimental set-up) because of the screening of the incident field from within the particle. This arises from the sea of itinerant conduction electrons within the particle, generating eddy currents, and hence highly effective screening of the incident radiation. Therefore, there exists a region of low electromagnetic absorption (shown in blue) where sub-micron sized, highly conducting particles absorb- and hence heat- poorly.

In contrast, one can clearly see regions of dominant electric and magnetic field absorption, marked in red in **Figure 1.27**, which will lead to extremely efficient heating. This enhancement of absorption (and thus heating) within sub-micron particles can clearly be triggered by the SIMIT. For particles of a critical size, having traversed the SIMIT, the lack of conduction (low conductivity) within the particle, absorption is predominantly due to electric dipole absorption (driven by the electric field).

Moreover, magnetically ‘lossy’ samples - the casein for Fe particles in this study - one will also expect an additional enhancement of magnetic absorption (and thus heating) within such sub-micron particles.

Whatever the exact, magnetic, and electric components (still needing further study), the maximum microwave absorption can be assured by simple selection of the mean particle radius. It was our contention that such effects would be maximised as Fe catalyst particles traversed the SIMIT. The following study aimed to probe experimental conditions (particularly the Fe catalyst particle size) where we expect optimal electric and optimal magnetic absorption, marked in red in **Figure 1.27**, for the selective, and highly efficient heating of catalyst particles. The aim was then to see if such properties were evident in the actual catalytic dehydrogenation of LCO.

1.5.5 Microwave-Initiated Heterogeneous Catalytic Reactions

Microwave radiation plays an important role as a heat source for various chemical reactions, and it has applications in different chemical fields including organic chemistry biochemistry, polymer chemistry, analytical chemistry, photo chemistry, and the inorganic chemistry of materials [108, 130, 131].

Microwave-initiated effects for homogeneous catalysis has been investigated for over three decades with a few processes coming to commercial stages, particularly in the pharmaceutical industry. Of late, microwave irradiation for heterogeneous gas phase catalytic reactions have garnered increased attention due to the so-called "thermal-effect", which is clearly evident in the enhancement of the reaction rate and products yield and selectivity over the conventional thermal process [108, 132]. The reported thermal effects of microwave irradiation are due to three phenomena: hot-spot formation, selective heating, and overheating.

Microwave thermal effects are enhanced through hot-spot generation, which results of the non-uniform distribution of electromagnetic field on the catalyst surface, where the temperature is considerably higher than the average temperature and hence reactions occur at a much higher rate. In the microwave dielectric heating of the gas phase decomposition of H_2S catalysed by metal sulphides on a γ-Al_2O_3 support, Zhang *et al*. reported the formation of hot-spots which have been observed between 90-1000 µm and up to 200 °C higher than the bulk temperature of the catalytic bed [133]. Importantly, several research studies have recently reported to observe the formation and control of "hot spots" on catalysts by using a high-speed camera (**Figure 1.28**). Different factors may influence the hot-spots, such as the particle size, metal loading or the field intensity [112, 132]. However, this well-accepted mechanism has been recently questioned, because the formation of hot-spots on a catalyst surface can be deleterious to microwave catalytic reactions [130, 134].

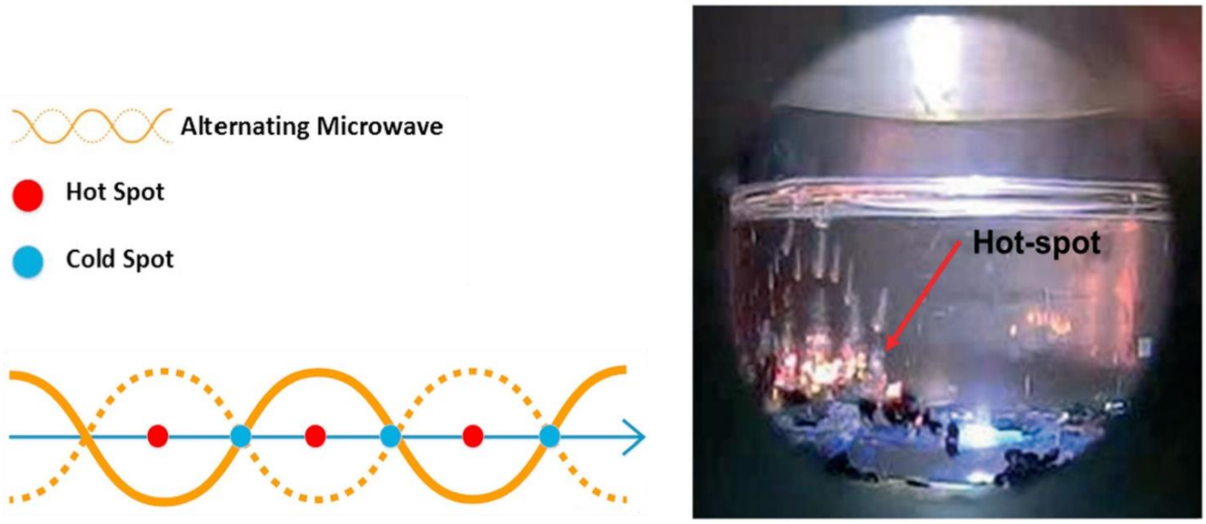

Figure 1.28 High-speed camera photograph of the hot-spots occurring on the activated carbon in toluene solvent under the microwaves' E-field irradiation. (Adapted from Ref. [108, 130, 135, 136]).

Selective heating of a catalyst material occurs in heterogeneous systems when they are subjected to microwave irradiation. In gas/solid systems the selective heating of a catalyst particle can occur while the bulk surrounding medium remains at lower temperature. A change in temperature can cause the migration of product from the catalytic surface to the bulk gas phase. This form of selective heating was proposed by Roussy *et al*. [137], and could result in enhanced selectivity towards desired products. Another way microwaves can create temperature differences and through heating a certain part of the individual catalyst particles more than the rest. It is known that microwave active metals (Fe, Pt, Mo, Pd) can be heated up by microwave irradiation very rapidly to high temperatures, while the low loss support materials, such as alumina, are heated to lower temperatures. This selective heating of metallic particles and catalytic sites can cause increased reaction rates [132, 138].

1.6 Thesis Objectives

My DPhil research work centres on the utilization of hydrogen as a fuel source through the microwave-initiated catalytic deep-dehydrogenation of fossil hydrocarbons – sometimes known as "H_2 – Stripping". Importantly, this process creates solid carbon as a by-product of the process instead of evolved CO_2 and therefore does not contribute to climate change. The approach also has the potential to synthesise other high-value hydrocarbons as by-products.

In this work, I demonstrate the direct application of this process to one of the most widely – available natural fossil hydrocarbons – Saudi Arabian Light Crude Oil (LCO). Particular attractive features of LCO are that it has a high proportion of light hydrocarbon fractions (and hence an intrinsically higher hydrogen content) a low density and flows freely at room temperature and generally has a low wax content.

This study initially describes the strong influence of the composition of several model hydrocarbon compounds over the hydrogen productivity followed by an in-depth study of the microwave-initiated dehydrogenation of LCO for hydrogen production. The last part of this work also describes an unprecedented approach for the direct conversion of LCO to syngas (H_2+CO) through microwave-initiated catalysis.

All of these investigations form the basis of a detailed interpretation of the underlying mechanisms (and optimisation) of this microwave-initiated deep-dehydrogenation "or stripping" of hydrocarbons.

A proposed reaction system configuration for microwave-initiated deep-dehydrogenation of LCO is given in **Figure 1.29**.

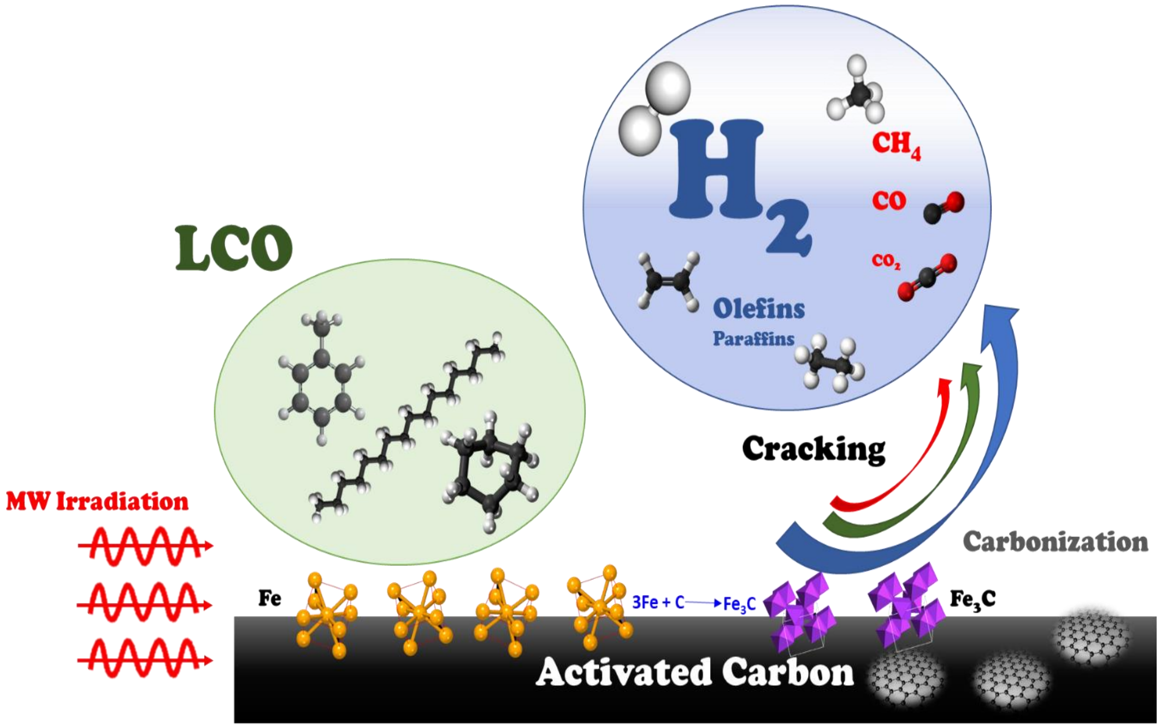

Figure 1.29 A schematic of a proposed reaction system configuration for microwave-initiated deep-dehydrogenation of LCO considering both the formation of gaseous and solid compounds and the transformation of Fe catalyst to Fe_3C.

References

[1] British Petroleum (bp), Statistical Review of World Energy, (2020).

[2] A. Demirbas, Bio-Hydrogen: for Future Engine Fuel Demands, Springer, Dordrecht; London, (2009).

[3] International Energy Agency (IEA), World Energy Balances: Overview, (2020).

[4] N. Zhou, J.W. Zhou, L.L. Dai, F.Q. Guo, Y.P. Wang, H. Li, W.Y. Deng, H.W. Lei, P. Chen, Y.H. Liu, R.O.E. Ruan, Syngas production from biomass pyrolysis in a continuous microwave assisted pyrolysis system, Bioresource Technology, 314 (2020).

[5] S. Gonzalez-Cortes, D.R. Slocombe, T. Xiao, A. Aldawsari, B. Yao, V.L. Kuznetsov, E. Liberti, A.I. Kirkland, M.S. Alkinani, H.A. Al-Megren, J.M. Thomas, P.P. Edwards, Wax: A Benign Hydrogen-Storage Material that Rapidly Releases H_2-Rich Gases Through Microwave-Assisted Catalytic Decomposition, Scientific Reports, 6 (2016).

[6] C. Kalamaras, A. Efstathiou, Hydrogen Production Technologies: Current State and Future Developments, Conference Papers in Energy, 3 (2013) 1-9.

[7] Shell Hydrogen Study - Energy of The Future? Sustainable Mobility through Fuel Cells and H_2, (2017).

[8] National Research Council and National Academy of Engineering, The Hydrogen Economy: Opportunities, Costs, Barriers, and R&D Needs, The National Academies Press, Washington, DC, (2004).

[9] International Energy Agency (IEA), The future of Hydrogen - Seizing Today's Opportunities, (2019).

[10] M. Kayfeci, A. Keçebaş, M. Bayat, Chapter 3 - Hydrogen production, Solar Hydrogen Production, Academic Press (2019), 45-83.

[11] F. Joos, R. Spahni, Rates of Change in Natural and Anthropogenic Radiative Forcing Over the Past 20,000 years, Proceedings of the National Academy of Sciences, 105 (2008) 1425 - 1430.

[12] R. keeling, Global Monitoring Laboratory, (2021) http://gml.noaa.gov.

[13] International Energy Agency (IEA), Global Energy Review - CO_2 emissions, (2021).

[14] United States Environmental Protection Agency (EPA), Overview of Greenhouse Gases, (2019).

[15] The Intergovernmental Panel on Climate Change (IPCC), Climate Change - Synthesis Report, (2007).

[16] L. Jackson and L. Jerome, Learning About Climate Change, Goodside. www.joingoodside.com

[17] The Intergovernmental Panel on Climate Change (IPCC), Mitigation of Climate Change, (2014).

[18] A. Tuladhar, K. Iatridis, D. Dimov, Chapter 6 - History and Evolution of the Circular Economy and Circular Economy Business Models, Circular Economy and Sustainability, Elsevier (2022), 87-106.

[19] J.L. Cardoso, The Circular Economy: Historical Grounds, The Diverse Worlds of Sustainability, (2018).

[20] House of Commons Environmental Audit Committee, Growing A Circular Economy: Ending the Throwaway Society, (2014).

[21] The Economist - Intelligence Unit, Boosting Circularity Across Saudi Arabia, (2021).

[22] R.P. Lee, F. Keller, B. Meyer, A Concept to Support the Transformation from A Linear to Circular Carbon Economy: Net Zero Emissions, Resource Efficiency and Conservation Through A Coupling Of The Energy, Chemical And Waste Management Sectors, Clean Energy, 1 (2017) 102-113.

[23] R.G. Grim, Z. Huang, M.T. Guarnieri, J.R. Ferrell, L. Tao, J.A. Schaidle, Transforming the Carbon Economy: Challenges and Opportunities in The Convergence Of Low-Cost Electricity And Reductive CO_2 utilization, Energy & Environmental Science, 13 (2020) 472-494.

[24] Saudi Aramco, Managing Our Footprint-Circular Carbon Economy. www.aramco.com

[25] A. Alkhowaiter, Y. Mufti, An Alternative Energy Transition Pathway Enabled by the Oil and Gas Industry, The Oxford Institute for Energy Studies, (2020).

[26] Circular Carbon Economy National Program, (2021), www.cce.org.sa

[27] Z. Jiang, T. Xiao, V.L. Kuznetsov, P.P. Edwards, Turning Carbon Dioxide into Fuel, Philosophical Transactions of the Royal Society A: Mathematical, Physical and Engineering Sciences, 368 (2010) 3343-3364.

[28] R. Robinson, The Origins of Petroleum, Nature, 212 (1966), 1291-1295.

[29] H. Devold, Oil and Gas Production Handbook - An Introduction to Oil and Gas Production, Transport, Refining and Petrochemical Industry, (2013).

[30] R. Selley, S. Sonnenberg, Elements of Petroleum Geology, 3rd Ed. (2015).

[31] M. Fingas, Introduction to Oil Chemistry and Properties, Handbook of Oil Spill Science and Technology (2014), 51-77.

[32] J.G. Speight, Handbook of Petroleum Refining, (2017).

[33] J.G. Speight, The Chemistry and Technology of Petroleum 4th Ed. (2006).

[34] M.A. Fahim, T.A. Alsahhaf, A. Elkilani, Chapter 2 - Refinery Feedstocks and Products, in: M.A. Fahim, T.A. Alsahhaf, A. Elkilani (Eds.) Fundamentals of Petroleum Refining, Elsevier, Amsterdam, (2010), 11-31.

[35] R. Sadeghbeigi, Chapter 3 - FCC Feed Characterization, in: R. Sadeghbeigi (Ed.) Fluid Catalytic Cracking Handbook (Third Edition), Butterworth-Heinemann, Oxford, (2012), 51-86.

[36] C. Yang, C.E. Brown, B. Hollebone, Z. Yang, P. Lambert, B. Fieldhouse, M. Landriault, Z. Wang, Chapter 4 - Chemical Fingerprints of Crude Oils and Petroleum Products, in: M. Fingas (Ed.) Oil Spill Science and Technology (2nd Edition), Gulf Professional Publishing, Boston, (2017), 209-304.

[37] K. Kolmetz, Kolmetz Handbook of Process Equipment Design -Crude Oil Properties, 2016.

[38] M. Chinenyeze, U. Ekene, Physical and Chemical Properties of Crude Oils and Their Geologic Significances, International Journal of Science and Research (IJSR), 6 (2017).

[39] C. Barker, Chapter 2 - Origin, Composition and Properties of Petroleum, in: E. Donaldson, G. Chilingarian, T. Yen (Eds.) Developments in Petroleum Science, Elsevier (1985), 17, 11-45.

[40] R.C. Selley, S.A. Sonnenberg, Chapter 2 - The Physical and Chemical Properties of Petroleum, in: R.C. Selley, S.A. Sonnenberg (Eds.) Elements of Petroleum Geology (3rd Edition), Academic Press, Boston, 2015, pp. 13-39.

[41] J. Rullkotter, J. Farrington, What Was Released? Assessing the Physical Properties and Chemical Composition of Petroleum and Products of Burned Oil, Oceanography, 34 (2021).

[42] S. Treese, D. Jones, P. Pujado, Handbook of Petroleum Processing-Introduction to Crude Oil and Petroleum Processing, 2015.

[43] W. Al-Dahhan, S. Mahmood, Classification of Crude Oils and its Fractions on the Basis of Paraffinic, Naphthenic and Aromatics Al-Nahrain Journal of Science, 22 (2019) 35-42.

[44] G. Yasin, M. Bhanger T. Ansari, S. Naqvi, M. Ashraf, K. Ahmad, F. Talpur, Quality and Chemistry of Crude Oils, Journal of Petroleum Technology and Alternative Fuels, 4 (2013) 53-63.

[45] Heavy Sour Crude Oil: A Challenge for Refiners. Commodity Trading Today, www.commodity-trading-today.com.

[46] N. Hyne, Nontechnical Guide to Petroleum Geology, Exploration, Drilling, and Production, Penn Well Corporation, 3rd Ed. (2012).

[47] M. Raymond, W. Leffler, Oil and Gas Production in Nontechnical Language, Penn Well Corporation, (2006).

[48] U.R. Chaudhuri, Fundamentals of Petroleum and Petrochemical Engineering, 1st Ed., CRC Press, (2011).

[49] US Energy Information Administration (EIA), Different Quality Characteristics of Crude Oils, (2012), www.eia.gov.

[50] Energy Insights By McKinsey, Crude Grades, www.mckinseyenergyinsights.com

[51] US Energy Information Administration (EIA), Oil and Petroleum Products Explained-Refining Crude Oil, www.eia.gov

[52] How Crude Oil is Separated into Fractions, Enerpac Blog, (2018), www.enerpac.com.

[53] S. Aldrees, Solid Acid Zeolite Catalysts for Benzene/Ethylene Alkylation Reactions, MSc thesis, Oxford University, UK, (2011).

[54] US Environmental Protection Agency (EPA), Chapter 5: Petroleum Industry, 5.1 Petroleum Refining. AP 42, 5th Ed. 1 (2015), www.epa.gov.

[55] B.H. Diya'uddeen, W.M. Daud, A.R. Abdul Aziz, Treatment Technologies for Petroleum Refinery Effluents: A Review, Process Safety and Environmental Protection, 89 (2011) 95-105.

[56] J. Adolf, C. Balzer, J. Louis, U. Schabla, M. Fischedick, K. Arnold, A. Pastowski, D. Schüwer, Shell Hydrogen Study Energy of the Future? Sustainable Mobility through Fuel Cells and H_2, (2017).

[57] A.V. da Rosa, J.C. Ordóñez, Chapter 10 - Hydrogen Production, in: A.V. da Rosa, J.C. Ordóñez (Eds.) Fundamentals of Renewable Energy Processes (Fourth Edition), Academic Press, Oxford, (2022), 419-470.

[58] Hydrogen Production and Uses, World Nuclear Association, (2021), www.world-nuclear.org.

[59] I. Dincer, Green Methods for Hydrogen Production, International Journal of Hydrogen Energy, 37 (2012) 1954-1971.

[60] M. Steinberg, Fossil Fuel Decarbonization Technology for Mitigating Global Warming, International Journal of Hydrogen Energy, 24 (1999) 771-777.

[61] J.A. Turner, Sustainable Hydrogen Production, Science, 305 (2004) 972-974.

[62] E.L. Miller, S.T. Thompson, K. Randolph, Z. Hulvey, N. Rustagi, S. Satyapal, Hydrogen and Fuel Cell Technologies Perspectives, US Department of Energy, MRS Bulletin, 45 (2020) 57-64.

[63] International Energy Agency (IEA), Global Hydrogen Review, Technology report (2021), www.iea.org.

[64] Hydrogen Scaling Up, Hydrogen Council, (2017), www.hydrogencouncil.com.

[65] M. Balat, Potential Importance of Hydrogen as A Future Solution to Environmental and Transportation Problems, International Journal of Hydrogen Energy, 33 (2008) 4013-4029.

[66] P. Nikolaidis, A. Poullikkas, A Comparative Overview of Hydrogen Production Processes, Renewable and Sustainable Energy Reviews, 67 (2017) 597-611.

[67] I. Staffell, D. Scamman, A. Velazquez Abad, P. Balcombe, P.E. Dodds, P. Ekins, N. Shah, K.R. Ward, The Role of Hydrogen and Fuel Cells in The Global Energy System, Energy & Environmental Science, 12 (2019) 463-491.

[68] B.E. Lebrouhi, J.J. Djoupo, B. Lamrani, K. Benabdelaziz, T. Kousksou, Global Hydrogen Development - A Technological and Geopolitical Overview, International Journal of Hydrogen Energy, 47 (2022) 7016-7048.

[69] J.D. Holladay, J. Hu, D.L. King, Y. Wang, An Overview of Hydrogen Production Technologies, Catalysis Today, 139 (2009) 244-260.

[70] R. Kothari, D. Buddhi, R.L. Sawhney, Comparison of Environmental and Economic Aspects of Various Hydrogen Production Methods, Renewable and Sustainable Energy Reviews, 12 (2008) 553-563.

[71] F. Mueller-Langer, E. Tzimas, M. Kaltschmitt, S. Peteves, Techno-Economic Assessment of Hydrogen Production Processes for The Hydrogen Economy for The Short and Medium Term, International Journal of Hydrogen Energy, 32 (2007) 3797-3810.

[72] D.C.C. Barranon, Methanol and Hydrogen Production: Energy and Cost Analysis, Lulea University of Technology, Lulea, Sweden, (2006).

[73] P. Dodds, W. McDowall, A Review of Hydrogen Production Technologies for Energy System Models, UCL Energy Institute, University College London, (2012).

[74] M. Steinberg, H.C. Cheng, Modern and Prospective Technologies for Hydrogen Production from Fossil Fuels, International Journal of Hydrogen Energy, 14 (1989) 797-820.

[75] C. Alvarez-Galvan, M. Melian, L. Ruiz-Matas, J.L. Eslava, R.M. Navarro, M. Ahmadi, B. Roldan Cuenya, J.L.G. Fierro, Partial Oxidation of Methane to Syngas Over Nickel-Based Catalysts: Influence of Support Type, Addition of Rhodium, and Preparation Method, Frontiers in Chemistry, 7 (2019) 1-16.

[76] L. Li, N.H. Md Dostagir, A. Shrotri, A. Fukuoka, H. Kobayashi, Partial Oxidation of Methane to Syngas via Formate Intermediate Found for a Ruthenium–Rhenium Bimetallic Catalyst, ACS Catalysis, 11 (2021) 3782-3789.

[77] P. Vernon, M. Green, A. Cheetham, A. Ashcroft, Partial Oxidation of Methane to Synthesis Gas, Catalysis Letters, 6 (1990) 181-186.

[78] A. Ashcroft, A. Cheetham, M. Green, P. Vernon, Partial Oxidation of Methane to Synthesis Gas Using Carbon Dioxide, Nature, 352 (1991) 225-226.

[79] M. Zahedi nezhad, S. Rowshanzamir, M.H. Eikani, Autothermal Reforming of Methane to Synthesis Gas: Modeling and Simulation, International Journal of Hydrogen Energy, 34 (2009) 1292-1300.

[80] G. Nahar, V. Dupont, Recent Advances in Hydrogen Production Via Autothermal Reforming Process (ATR): A Review of Patents and Research Articles, Recent Patents on Chemical Engineering, 6 (2013) 8-42.

[81] S.A. Ghoneim, R.A. El-Salamony, S.A. El-Temtamy, Review on Innovative Catalytic Reforming of Natural Gas to Syngas, World Journal of Engineering and Technology, 4 (2016) 116-139.

[82] N. Muradov, Emission-Free Fuel Reformers for Mobile and Portable Fuel Cell Applications, Journal of Power Sources, 118 (2003) 320-324.

[83] S. Schneider, S. Bajohr, F. Graf, T. Kolb, State of the Art of Hydrogen Production via Pyrolysis of Natural Gas, ChemBioEng Reviews, 7 (2020) 150-158.

[84] International Energy Agency (IEA), World Energy Outlook 2019, www.iea.org.

[85] P.J. Megía, A.J. Vizcaíno, J.A. Calles, A. Carrero, Hydrogen Production Technologies: From Fossil Fuels toward Renewable Sources. A Mini Review, Energy & Fuels, 35 (2021) 16403-16415.

[86] M. Wang, G. Wang, Z. Sun, Y. Zhang, D. Xu, Review of Renewable Energy-Based Hydrogen Production Processes for Sustainable Energy Innovation, Global Energy Interconnection, 2 (2019) 436-443.

[87] F. Safari, I. Dincer, A Review and Comparative Evaluation of Thermochemical Water Splitting Cycles for Hydrogen Production, Energy Conversion and Management, 205, (2020) ,112182.

[88] A. Bolt, I. Dincer, M. Agelin-Chaab, A Review of Unique Aluminum–Water Based Hydrogen Production Options, Energy & Fuels, 35 (2021) 1024-1040.

[89] I. Dincer, C. Zamfirescu, Sustainable Hydrogen Production Options and The Role of IAHE, International Journal of Hydrogen Energy, 37 (2012) 16266-16286.

[90] H.C. Ong, W.-H. Chen, A. Farooq, Y.Y. Gan, K.T. Lee, V. Ashokkumar, Catalytic Thermochemical Conversion of Biomass for Biofuel Production: A Comprehensive Review, Renewable and Sustainable Energy Reviews, 113 (2019) 109266.

[91] T. Lepage, M. Kammoun, Q. Schmetz, A. Richel, Biomass-To-Hydrogen: A Review of Main Routes Production, Processes Evaluation and Techno-Economical Assessment, Biomass and Bioenergy, 144 (2021) 105920.

[92] S.E. Hosseini, M.A. Wahid, Hydrogen Production from Renewable and Sustainable Energy Resources: Promising Green Energy Carrier for Clean Development, Renewable and Sustainable Energy Reviews, 57 (2016) 850-866.

[93] Committee on Alternatives and Strategies for Future Hydrogen Production and Use, The Hydrogen Economy: Opportunities, Costs, Barriers, and R&D Needs, The National Academies Press, (2004).

[94] L. Rosa, M. Mazzotti, Potential for Hydrogen Production from Sustainable Biomass with Carbon Capture And Storage, Renewable and Sustainable Energy Reviews, 157 (2022) 112123.

[95] B. Parkinson, P. Balcombe, J.F. Speirs, A.D. Hawkes, K. Hellgardt, Levelized Cost of CO_2 Mitigation from Hydrogen Production Routes, Energy & Environmental Science, 12 (2019) 19-40.

[96] C. Antonini, K. Treyer, A. Streb, M. van der Spek, C. Bauer, M. Mazzotti, Hydrogen Production from Natural Gas and Biomethane with Carbon Capture and Storage – A Techno-Environmental Analysis, Sustainable Energy & Fuels, 4 (2020) 2967-2986.

[97] L. Collins, Green Hydrogen will be Cost-Competitive with Grey H_2 By 2030 - without a carbon price, Recharge, (2021), www.rechargenews.com

[98] J. Parnell, Europe's Green Hydrogen Revolution Is Turning Blue, GTM, (2020) www.greentechmedia.com.

[99] European Commission, A Hydrogen Strategy for A Climate-Neutral Europe, (2020), www.ec.europa.eu.

[100] International Energy Agency (IEA), Japan 2021, Energy Policy Review (2021), www.iea.org.

[101] Air Products, ACWA Power and NEOM Sign Agreement for $5 Billion Production Facility in NEOM Powered by Renewable Energy for Production and Export of Green Hydrogen to Global Markets, (2020) www.airproducts.com.

[102] Air Products, ACWA Power and NEOM sign agreement for $5 billion production facility in neom powered by renewable energy for production and export of green hydrogen to global markets, (2020), www.acwapower.com.

[103] F. Eljack, M.-K. Kazi, Prospects and Challenges of Green Hydrogen Economy via Multi-Sector Global Symbiosis in Qatar, Frontiers in Sustainability, 1 (2021).

[104] R.R. Beswick, A.M. Oliveira, Y. Yan, Does the Green Hydrogen Economy Have a Water Problem?, ACS Energy Letters, 6 (2021) 3167-3169.

[105] H. Evans, Green hydrogen Costs Need to Fall Over 50% to be Viable: S&P Global Ratings, Energy transition, S&P Glabal, (2020), www.spglobal.com.

[106] H. Çora, E. Mikail, 21st Century Hydrogen Energy Economics, SWOT Review and Selected Examples of Global Patterns, (2020).

[107] J. Ren, S. Gao, H. Liang, S. Tan, L. Dong, Chapter 1 - The Role of Hydrogen Energy: Strengths, Weaknesses, Opportunities, and Threats, in: A. Scipioni, A. Manzardo, J. Ren (Eds.) Hydrogen Economy, Academic Press, (2017), 1-33.

[108] S. Horikoshi, N. Serpone, Microwaves in Catalysis: Methodology and Applications, Wiley-VCH, Weinheim, Germany, (2016).

[109] N. Makul, P. Rattanadecho, D.K. Agrawal, Applications of Microwave Energy in Cement and Concrete – A Review, Renewable and Sustainable Energy Reviews, 37 (2014) 715-733.

[110] M. Taylor, B. Atri, S. Minhas, Developments in Microwave Chemistry, Evalueserve, (2005).

[111] T. Laird, Microwave Heating as a Tool for Sustainable Chemistry, Org. Process Res. & Dev., 15 (2011) 478-478.

[112] V. Palma, D. Barba, M. Cortese, M. Martino, S. Renda, E. Meloni, Microwaves and Heterogeneous Catalysis: A Review on Selected Catalytic Processes, Catalysts, 10 (2020) 246.

[113] G. Stefanidis, A. Muñoz, G. Sturm, A. Stankiewicz, A Helicopter View of Microwave Application to Chemical Processes: Reactions, Separations, And Equipment Concepts, Reviews in Chemical Engineering, 30 (2014) 233-259.

[114] S. Mutyala, C. Fairbridge, J. Paré, J. Bélanger, S. Ng, R. Hawkins, Microwave Applications to Oil Sands and Petroleum: A Review, Fuel Processing Technology, 91 (2010) 127-135.

[115] L.M. Kustov, I.M. Sinev, Microwave Activation of Catalysts and Catalytic Processes, Russian Journal of Physical Chemistry A, 84 (2010) 1676-1694.

[116] D. Bogdal, A. Prociak, Microwave-Enhanced Polymer Chemistry and Technology, Blackwell, (2007).

[117] A. Grewal, K. Kumar, S. Redhu, S. Bhardwaj, Microwave Assisted Synthesis: A Green Chemistry Approach, International Research Journal of Pharmaceutical and Applied Sciences, 3 (2013) 278-285.

[118] B. Hayes, Microwave Synthesis: Chemistry at the Speed of Light, CEM Pub., (2002).

[119] C.P. Smyth, Microwave Absorption and Molecular Structure in Liquids. Dielectric Relaxation Times and Shapes of Rigid Molecules, Proceedings of the National Academy of Sciences, 42 (1956) 234-239.

[120] A. Ward, Dielectric Materials for Advanced Applications, NRC, (2016).

[121] R. Newnham, S. Jang, M. Xu, F. Jones, Fundamental Interaction Mechanisms Between Microwave and Matter, Ceramic Transactions, 21 (1991) 50-67.

[122] V. Saxena, U. Chandra, Microwave Synthesis: A Physical Concept., InTech, (2011).

[123] A. Aldawsari, Dielectric Measurements and Catalytic Cracking of Heavy Oils Using Advanced Microwave Technologies, Ph.D. thesis, University of Oxford, (2017).

[124] J. Asomaning, S. Haupt, M. Chae, D. C. Bressler, Recent developments in microwave-assisted thermal conversion of biomass for fuels and chemicals, Renewable and Sustainable Energy Reviews, 92 (2018) 642-657.

[125] C. Kappe, Controlled Microwave Heating in Modern Organic Synthesis, Angew Chem Int Ed Engl, 43 (2004) 6250-6284.

[126] C. Kappe, Unraveling the Mysteries of Microwave Chemistry Using Silicon Carbide Reactor Technology, Accounts of Chemical Research, 46 (2013) 1579-1587.

[127] B. Gutmann, A. Schwan, B. Reichart, C. Gspan, F. Hofer, and C. Kappe, Activation and Deactivation of a Chemical Transformation by an Electromagnetic Field: Evidence for Specific Microwave Effects in the Formation of Grignard Reagents. Angew. Chem. Int. Ed., 50 (2011) 7636-7640.

[128] P. Edwards, R. Johnston, C.N.R. Rao, On the Size-Induced Metal-Insulator Transition in Clusters and Small Particles, in: P. Braunstein, L. A. Oro, P. R. Raithby (Eds.), Metal Clusters in Chemistry, Wiley-VCH, (2008), 1454-1481.

[129] A. Porch, D. Slocombe, P.P. Edwards, Microwave Absorption in Powders of Small Conducting Particles For Heating Applications, Physical Chemistry Chemical Physics, 15 (2013), 2757-2763.

[130] S. Horikoshi, N. Serpone, Role of Microwaves in Heterogeneous Catalytic Systems, Catalysis Science & Technology, 4 (2014) 1197-1210.

[131] S. Horikoshi, N. Serpone, Microwaves in Nanoparticle Synthesis: Fundamentals and Applications, Wiley, (2013).

[132] P.D. Muley, Y. Wang, J. Hu, D. Shekhawat, Microwave-Assisted Heterogeneous Catalysis, in Catalysis, RSC Publishing, (2021), 1-37.

[133] X. Zhang, D. O. Hayward, D. Michael P. Mingos, Apparent Equilibrium Shifts and Hot-Spot Formation for Catalytic Reactions Induced By Microwave Dielectric Heating, Chemical Communications, (1999) 975-976.

[134] W. Xu, J. Zhou, Z. Su, Y. Ou, Z. You, Microwave Catalytic Effect: A New Exact Reason for Microwave-Driven Heterogeneous Gas-Phase Catalytic Reactions, Catalysis Science & Technology, 6 (2016) 698-702.

[135] S. Horikoshi, A. Osawa, S. Sakamoto, N. Serpone, Control of Microwave-generated Hot Spots. Part v. Mechanisms of Hot-Spot Generation and Aggregation of Catalyst in a Microwave-assisted Reaction in Toluene Catalyzed by Pd-loaded AC Particulates, Applied Catalysis A: General, 460–461 (2013) 52–60.

[136] C. Mgbemena, D. Li, M. Lin, P. Liddel, K. Katnam, V. Thakur, H. Nezhad, Accelerated Microwave Curing of Fibre-Reinforced Thermoset Polymer Composites for Structural Applications: A Review of Scientific Challenges, Composites Part A: Applied Science and Manufacturing, 115 (2018) 88-103.

[137] G. Roussy, J.M. Thiebaut, M. Souiri, E. Marchal, A. Kiennemann, G. Maire, Controlled Oxidation of Methane Doped Catalysts Irradiated by Microwaves, Catalysis Today, 21 (1994) 349-355.

[138] T. Durka, Microwave Effects in Heterogeneous Catalysis: Application to Gas-Solid Reactions For Hydrogen Production, Chemical Engineering, Ph.D. thesis, Warsaw University of Technology, (2013).

Chapter2

Experimental Methods

The purpose of this chapter is to summarise the experimental set-up, catalysts synthesis methods and analytical techniques applied in this work, and the set of characterisation techniques used in this thesis including: X-ray powder diffraction (XRD), nuclear magnetic resonance (NMR) spectroscopy, scanning electron microscopy (SEM), transition electron microscopy (TEM), Thermogravimetric analysis (TGA), N_2 physisorption for BET surface area, gas chromatography (GC), and gas chromatography-mass spectrometry (GC/MS).

2.1 Experimental Set-up and Catalyst Evaluation

2.1.1 Microwave-Initiated Catalytic System

The experimental setup consisted of a microwave generation system, a custom-built microwave cavity and a control system. Typically, 0.5 g of the feedstock was mixed (unless specified differently) with a 0.5 g of supported metal catalyst (1:1 wt.%) and loaded in a quartz (silica) tubular fixed-bed reactor with 9 mm inner and 10 mm outer diameters. The sample was plugged above and below by 1 cm of quartz wool, and the tube was placed axially in the microwave cavity in a vertical position and located at the centre to ensure uniform microwave irradiation. The temperature was monitored using an infrared pyrometer (Raytek M13) which was positioned horizontally facing a hole in the side of the microwave cavity pointing at the catalyst bed. The system was then purged with dry argon at a flow rate of 20 ml.min^{-1} for 10 min before the microwaves were turned on.

The experiment was carried out at a frequency of 2.45 GHz, with different input powers. After 10 minutes of reaction, the microwave radiation was switched off and the temperature monitoring switched off once the sample reached 50 °C. The time of the experiment (reaction) was chosen to be 10 min because by that time all the gaseous evolution was stopped. The generated gases were passed through an ice bath to trap out any condensable or unreacted liquid, and then into a water-filled, inverted 500 ml graduated cylinder to collect gaseous products which were analysed quantitively by gas chromatography (GC) using a Perkin-Elmer, Clarus 580 GC. The liquid products and/or the unreacted feedstocks are collected using a cold trap and analysed by Gas Chromatograph Mass Spectrometer (GC-MS) using a SHIMADZU, GCMS-QP2010 SE (**Figure 2.1**). When the reaction was used in continuous operation mode, a syringe pump (Cole-Parmer, 74900 series) was used to pump fresh liquid feedstock into the fixed quartz tube reactor at a flow rate of 0.05 $ml.min^{-1}$.

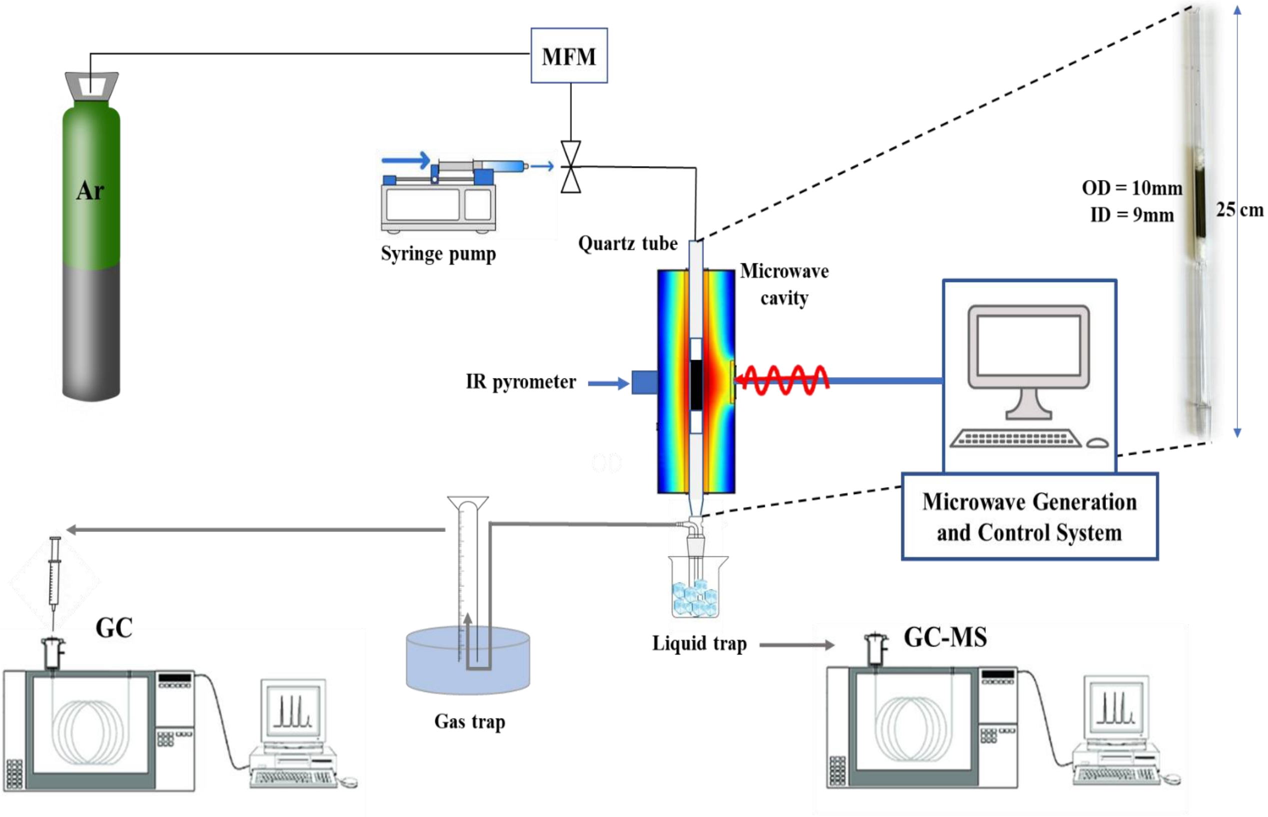

Figure 2.1 Schematic experimental apparatus for microwave system.

The microwave heating system chain consisted of a power generator, microwave head, microwave circulator, dummy load, microwave power meters, tuneable waveguide sections, and applicator (**Figure 2.2**). The system was designed and supplied by the French company (Sairem AIIRIS MWR) and was computer-controlled using the Labview software. The applicator was fabricated in the Inorganic Chemistry Laboratory (ICL) and designed in a single-mode cavity built up of aluminium. The TM010 mode used in this work is created as only a uniform electric field is presented in the centre of the cylindrical cavity. A quartz tube is used as the reactor because quartz is highly transparent to the induced microwave irradiation and can reduce the exclusion of samples from the microwave field.

The sample temperature is measured using an infrared (IR) pyrometer, which is the most popular temperature measurement technique used in the microwave system. The conventional thermocouples can interfere between the electromagnetic field and the metallic probe, which can potentially lead to interference in sparking [1, 2], and would give an unreliable temperature because of direct heating of the thermocouple. However, it must be noted that the pyrometer only measured the surface temperature of the catalyst bed, which is not necessarily indicative of the bulk temperature, due to regions of intense localised heat, leading to the generation of 'hotspots', as discussed in **Section 1.5.3** which can occur and reduce the legitimacy of a surface temperature reading. The temperature (T) versus time (t) of the reaction profile was recorded during the microwave experiment via the Labview software. **Table 2.1** summarises the main parts of the microwave system and their functions [3, 4].

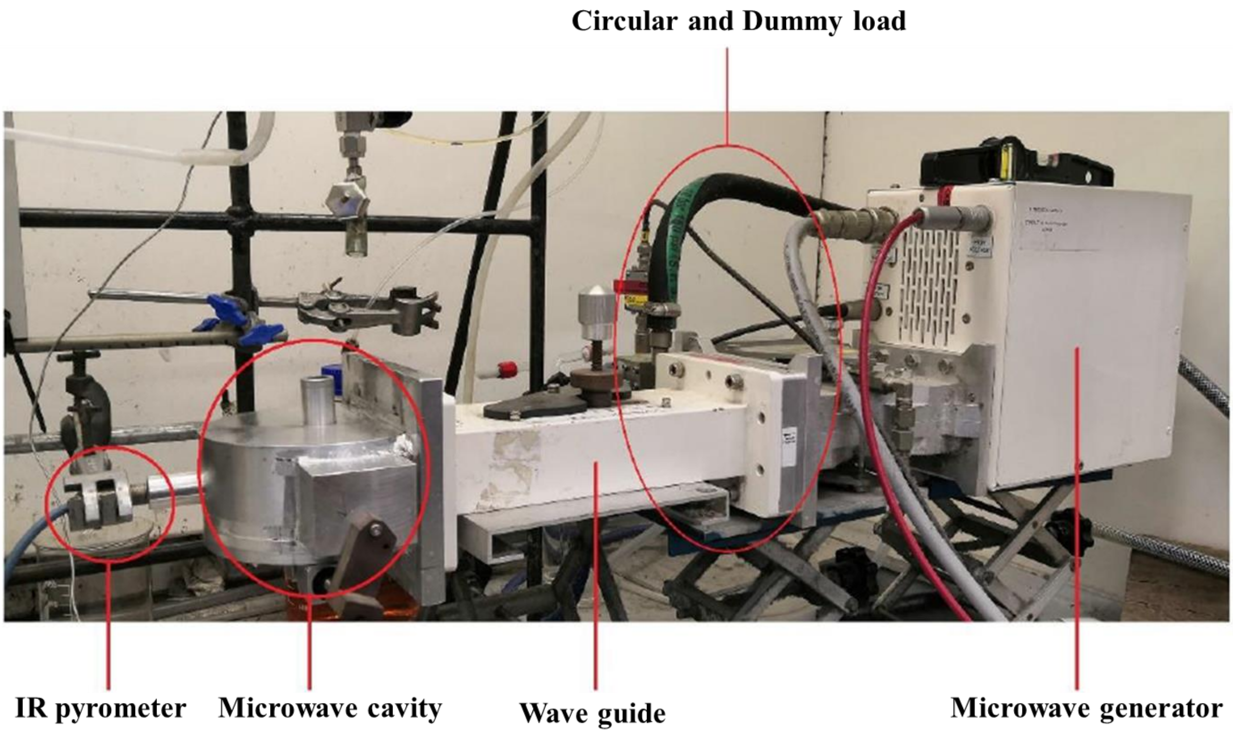

Figure 2.2 Microwave system configuration (Reproduced from Ref. [3]).

Table 2.1 Microwave system main parts and functions [3, 4].

Microwave system part	Function
Microwave generator	Equipped with a magnetron (microwave source) and operated at a frequency of 2.45 GHz (±0.025 GHz).
Circular and Dummy load	Protects the power generator from the damage by the reflected power which hasn't been absorbed by either the samples or the system.
Waveguide	Guides the microwave radiation to the cavity.
Microwave cavity	Where the sample is exposed to the microwave electric field and the actual chemical reaction takes place.
IR pyrometer	Measures the sample temperature.

2.1.2 Conventional (Thermal) Catalytic System

For comparison purposes, conventional thermal experiments were also carried out in an electric tubular furnace (Nabertherm B400/410). The sample system was the same as described in the previous section. In this case, a sample pre-loaded with hydrocarbons was loaded into a pre-heated tube furnace. Dry argon gas was used to purge the reactor tube; however, with this set-up, the whole system could not be purged as the reactor tube could only be connected to the rest of the set-up after being inserted into the tube furnace. The reactor tube was then placed into a tube furnace, which was already at a temperature of 800 °C. The argon gas was switched off once the reactor tube and cold trap were connected and the products were collected in the same way as described in **Section 2.1.1**. (**Figure 2.3**).

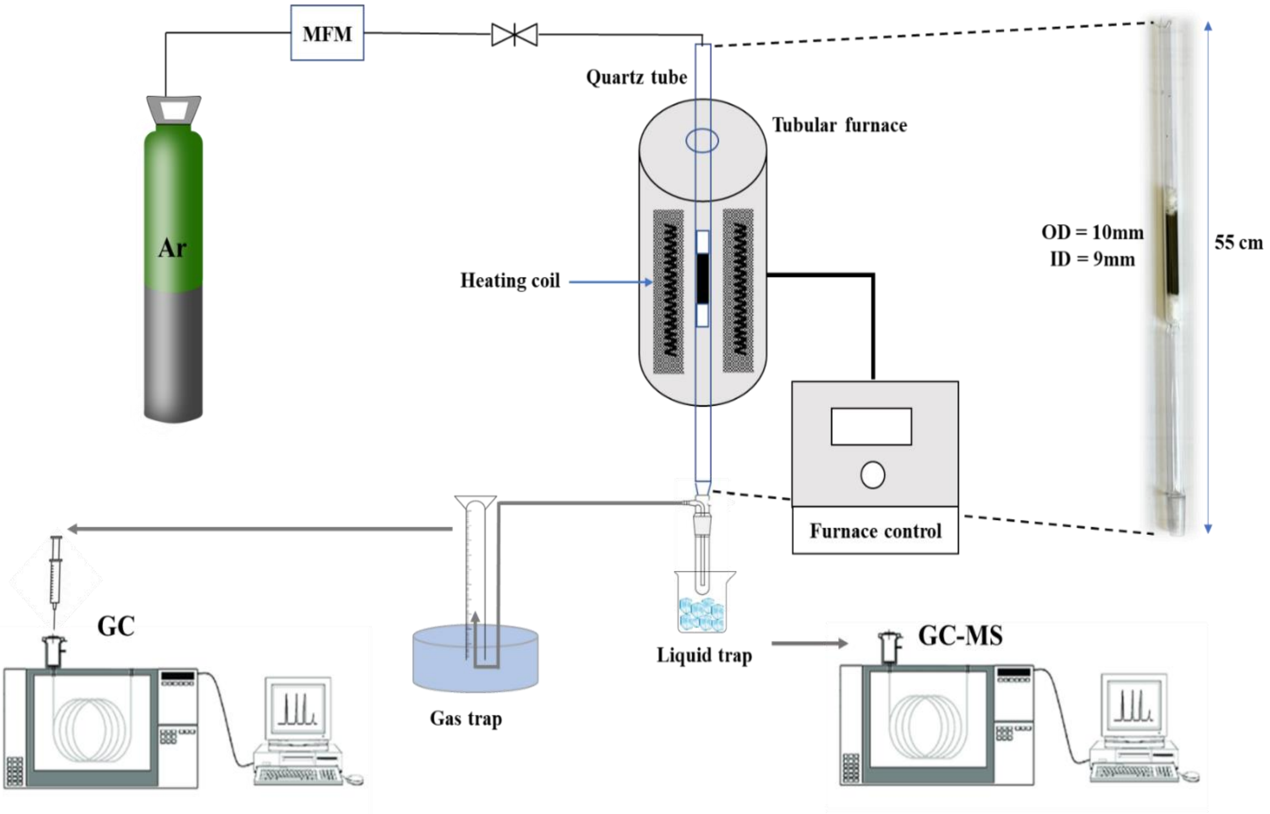

Figure 2.3 Schematic experimental apparatus for the conventional thermal system.

2.1.3 CO_2 Solubility Test in Water

The CO_2 gas is quite soluble in water in which more than 99% exists as the dissolved gas and less than 1 % as carbonic acid H_2CO_3 [5]. As described earlier in this chapter, the generated gases from the microwave and thermal reactions passed through a water-filled inverted 500 ml graduated cylinder to collect gaseous products. So, it was necessary to conduct a test of the solubility of CO_2 gas in the water in order to ensure the accuracy of the GC analysis for the CO_2 gas.

A laboratory test was conducted by injecting 100 ml of CO_2 gas in the same water-filled inverted 500 ml graduated cylinder. After 10 minutes, there was no change observed in the CO_2 volume (100 ml), and this was indicating that there was no solubility of CO_2 in water in the 10 minutes time.

2.2 Catalysts Preparation

The catalysts were synthesised using the so-called wet impregnation method. Metal nitrate, for example, $Fe(NO_3)_3.9H_2O$ (Iron (III) nitrate nonahydrate, 99 %, Sigma-Aldrich) was used as an iron precursor. Support materials used for the catalyst preparation were AC (activated carbon, Sigma-Aldrich) and Al_2O_3 (aluminium oxide, γ-phase, Alfa Aesar). The powders of support were mixed with an aqueous solution of metal nitrate, the concentration of which was calculated to produce a desired content of metal on the support. The mixture was then stirred at 150°C on a magnetic hot plate in a fume hood under refluxing for 3h. The suspended solid was filtered off and then moved into the drying oven, for drying overnight. The targeted metal catalysts were then obtained by a careful reduction process in a horizontal tube furnace in flowing 10% H_2/Ar gaseous mixtures at 750 °C for 8 h with a heating rate of 5 °C/min.

2.3 Product Analysis

According to the International Union of Pure and Applied Chemistry (IUPAC), “chromatography is defined as a physical separation method in which the components to be separated are distributed between two phases, one of which is stationary (stationary phase) while the other (the mobile phase), is moving in a defined direction” [6, 7]. Gas Chromatography (GC) and Gas chromatography-mass spectrometry (GC/MS) are both widely used techniques for quality and purity control in the manufacture of many products in the chemical, pharmaceutical, and food industries. This section will cover some fundamentals and describe how these techniques work.

2.3.1 Gas Chromatography (GC)

A Gas chromatograph (GC) is a commonly used analytical instrument, in many research and industrial laboratories, for separating and identifying chemical substances based primarily on their volatilities. As shown in **Figure 2.4**, the GC consists of a flow controller to control the carrier gases’ flow rate, an injection port in which the sample is injected, a column where separations occur, an oven as a thermostat for the column, and a detector which is connected to a data processor to record and display the chromatogram. Commonly used carrier gases are inert, and include nitrogen (N_2), helium (He) or hydrogen (H_2) are preferred and commonly used and are introduced at a constant flow rate to the injection port. The sample is injected into the injection port and is instantaneously vaporized and transported by the mobile gas phase (i.e., the carrier gas) through the column. The column itself contains a liquid stationary phase which is held in the oven and is heated during the analysis to elute the less volatile components. The main reason why different compounds can be separated in GC is the interaction of the compound with the stationary phase. The stronger the interaction, the longer the compound remains attached to the stationary phase and so it takes more time to go through the column (longer retention time). The outlet of the column is inserted into the detector which responds to the chemical components eluting from the column to produce a signal. The signal is recorded by the acquisition software on a computer to produce a chromatogram [8, 9].

There are many detectors which can be used in gas chromatography. The most common are the flame ionization detector (FID) and the thermal conductivity detector (TCD). Both are sensitive to a wide range of components, and both work over a wide range of concentrations. Their characteristics are outlined in **Table 2.2** [10].

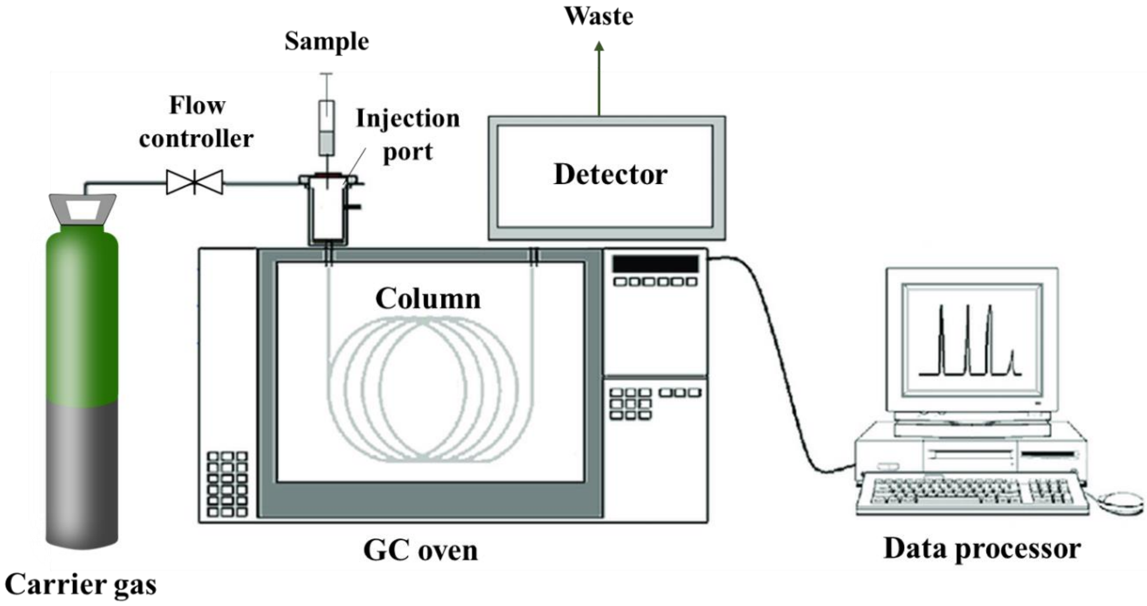

Figure 2.4 Schematic representation of typical gas chromatography (Adapted from Ref. [7]).

Table 2.2 Comparison of characteristics of general-purpose GC detectors [10].

Detector	Principle	Detectable compound
Flame ionization detector (FID)	Burns compounds in H_2/O_2 flame at 2000˚C and measures ion created	Organic compounds
Thermal conductivity detector (TCD)	Measures difference in thermal conductivity of gases	All compounds except for carrier gas

In this thesis, a Perkin-Elmer, Clarus 580 GC was used (**Figure 2.5**) which is equipped with both FID (to detect hydrocarbons such as methane, propane, propylene … etc), and TCD which can detect H_2, CO, CO_2, and air. A 50 m long column is used and is located in a coiled form in the GC oven which is heated at a rate of 25 °C/min from 80 °C to 200 °C. Helium is used as a carrier gas for TCD with a flow rate of 40 ml/min and a temperature of 200 °C. For FID, H_2 and air are used with flow rates of 45 ml/min and 450 ml/min, respectively, and at 250 °C operating temperature.

Figure 2.5 Perkin-Elmer, Clarus 580 GC, Inorganic Chemistry Laboratory (ICL), University of Oxford.

2.3.2 Gas Chromatography/Mass Spectrometry (GC/MS)

Mass spectrometry (MS) is an analytical technique that can be coupled to a GC and used instead of the GC detector. GC can separate many volatile and semi-volatile compounds with great resolution, but not always selectively identify them whereas MS can selectively identify many compounds but not always separate them. By combining the two techniques, the advantages become obvious. Therefore, GC/MS is widely used for qualitative and quantitative determination of volatile and semi-volatile organic compounds in a variety of fields [11].

Figure 2.6 shows the MS component of a GC/MS system including a sample inlet into a vacuum-sealed chamber that houses an ionisation source, a mass analyser, and a mass detector. In the MS system, the sample inlet is maintained at a high temperature (up to 400 °C), to ensure that the sample remains in the gas phase. Next, the sample is introduced directly to the ionizer chamber. Once ionized, the gaseous eluted compounds, are separated in a vacuum based on their mass to charge ratio (m/z). The detector measures the intensity of each ion, these intensities are recorded to produce the mass spectrum. A sample's mass spectrum is then shown, classified, and likened to a library of known mass spectra by a computer data system.[10, 12].

In this thesis, the liquid products were analysed by a gas chromatograph/mass spectrometer (SHIMADZU GC/MS-QP 2010 SE) (**Figure 2.7**) equipped with a capillary column (SHIM-5MS) 30 m in length and 0.25 mm in diameter. The ion source temperature is 200 °C, the interface temperature is 250 °C and the detector voltage is 0.7kV. Helium is used as carrier gas, and dichloromethane (≥ 99.8%, Sigma-Aldrich) as a solvent.

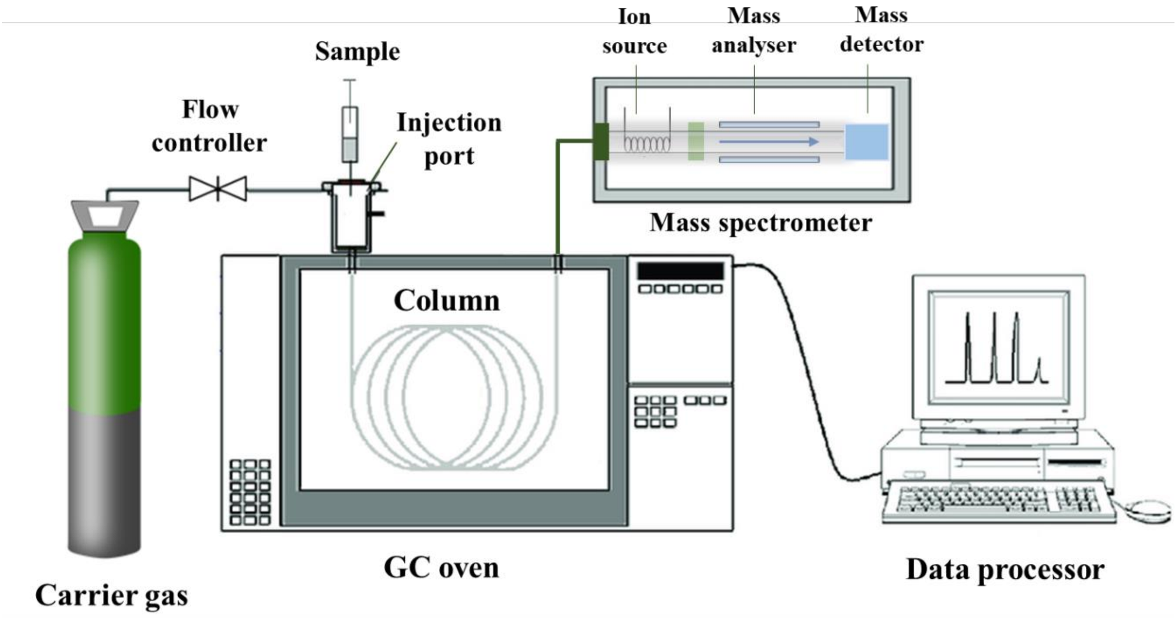

Figure 2.6 Schematic representation of a typical gas chromatography/mass spectrometer. (Adapted from Ref.[7, 12]).

Figure 2.7 Shimadzu GC/MS-QP 2010 SE, Inorganic Chemistry Laboratory (ICL), University of Oxford.

2.4 Techniques used for the Characterisation of Catalysts

Catalyst characterisation plays an important role in heterogeneous catalysis including synthesis, development and optimisation. Also, during fouling or catalytic performance-related investigations. This section briefly describes the concepts and main principles of the techniques used in this thesis for catalyst characterisation.

2.4.1 X-ray Diffraction (XRD)

Powder X-ray diffraction (XRD) is a standard tool which is the most frequently applied technique in solid-state chemistry used to provide information about bulk structures, phases, and sizes of particles [13, 14].

X-rays interact with electrons in atoms. When an X-ray beam collides with electron clouds of the atom in a crystal, it is diffracted into many specific directions. If the wavelength of these scattered x-rays did not change, this phenomenon is known as elastic scattering. The X-rays elastically scattered from the atoms in a solid interfere. If the atoms exist in a periodic array (i.e., a crystal) there is constructive interference in a few special directions resulting in a diffractogram consisting of several peaks separated by a very low background scattering. The peak positions are as determined by Bragg's Law [14];

$$n\lambda = 2dsin\theta \qquad \textbf{Equation 2.1}$$

Where the variable (n) is a diffraction order, (λ) is the wavelength of the incident X-rays, (d) is the spacing between layers of atoms, and (θ) is the Bragg angle between the incident rays and the surface of the crystal. The *d*-spacings are determined by the periodicity of the system (**Figure 2.8**). The intensities of the peaks are determined by the arrangement of atoms. If the solid is amorphous (i.e., not crystalline) then there will not be peaks in the diffraction pattern.

The crystallite size can be estimated using the Scherrer equation (**Equation 2.2**) by XRD radiation by measuring the full width at half maximum of peaks (FWHM) at any 2θ in the pattern [13];

$$\tau = \frac{K\,\lambda}{\beta \cos\theta} \qquad \textbf{Equation 2.2}$$

Where (τ) is the mean size of the ordered (crystalline) domains, (K) is a dimensionless shape factor, with a value close to unity, (λ) is the wavelength of the incident X-rays, and (β) is the width at half the maximum intensity.

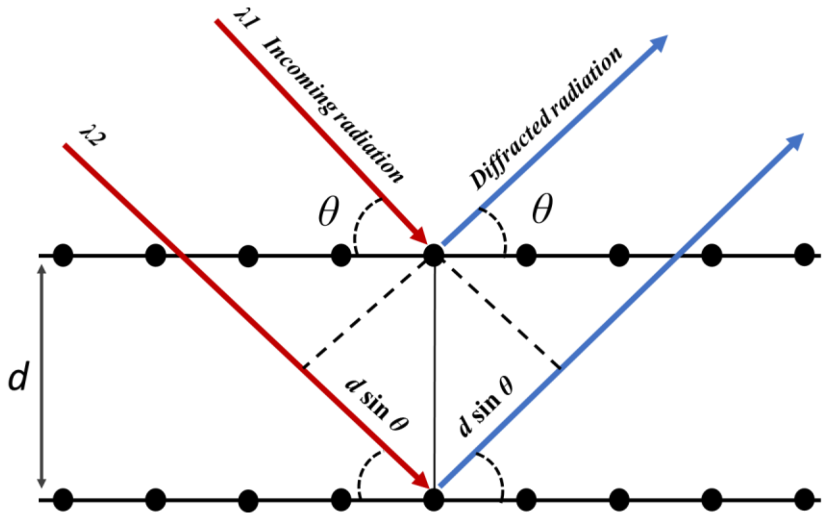

Figure 2.8 Illustration of Bragg's diffraction. (Adapted from Ref.[10]).

In this thesis, powder XRD patterns were collected using a BRUKER D8 ADVANCE Eco diffractometer (**Figure 2.9**) using a Cu Kα X-ray source (40 kV, 25 mA), and the scan diffraction angle (2θ) is from 5° to 90°. The crystallite sizes were estimated from the powder diffraction data by the Scherrer equation using X'Pert HighScore software [16].

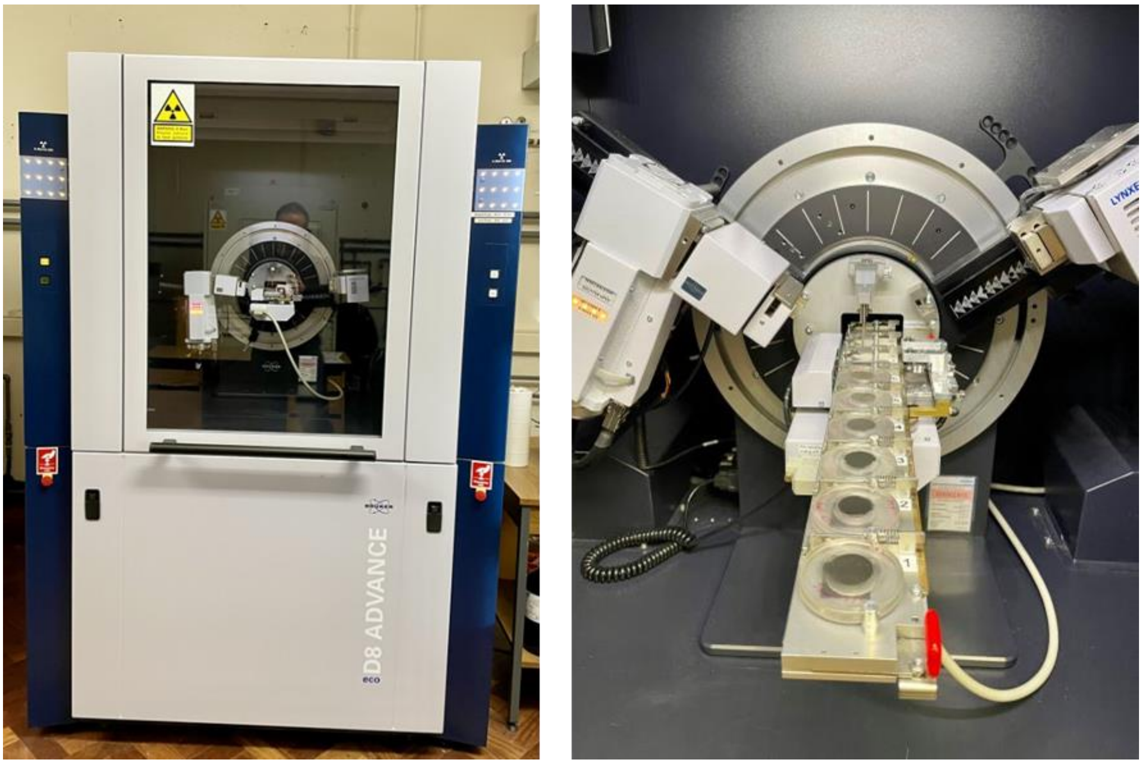

Figure 2.9 BRUKER D8 ADVANCE diffractometer, Inorganic Chemistry Laboratory (ICL), University of Oxford.

2.4.2 Thermogravimetric Analysis (TGA)

Thermogravimetric analysis (TGA) is a powerful technique to determine composition, purity, and thermal stability of materials. The technique is one in which the mass of a sample is measured as a function of temperature or time, at which physical changes occur when a sample is heated or cooled in a controlled atmosphere. The mechanisms of weight change in TGA differ according to whether it is gain or loss [17, 18]. **Table 2.3** shows examples of some chemical and physical phenomena can occur during the TGA analysis.

Table 2.3 Examples of some chemical and physical phenomena can occur during the TGA analysis [18].

Weight loss	Weight Gain
• Thermal decomposition in an inert atmosphere with the formation of gaseous products • Evaporation of volatiles, loss of water • Reduction reaction when the sample interacted with a reducing atmosphere (hydrogen, ammonia, etc). • Desorption	• Oxidation of metals in air or oxygen • Absorption or Adsorption.

Moreover, a differential scanning calorimetry (DSC) analyser measures the energy change (absorption or release) of a sample during heating or cooling, and this enables one to define the phase transitions or chemical transformations and their temperatures and whether the reaction is exothermic or endothermic. So, the use of DSC simultaneously with thermogravimentric analysis can offer more useful information than either the DSC or TGA technique does alone. Additionally, the atmosphere used in the TGA analysis plays an important role and depends on the type of information required (oxidation, reduction … etc) [3, 18].

Thermogravimetric analysis for this work was carried out using a TA Instruments, SDT Q-600 and was employed for TGA-DSC measurement (**Figure 2.10**). A specific amount of the sample was heated from room temperature to 1000 °C with a heating rate of 10 °C/min under appropriate atmosphere or carrier gas at 100 ml/min. The resulting data were recorded using TA Instrument Explorer.

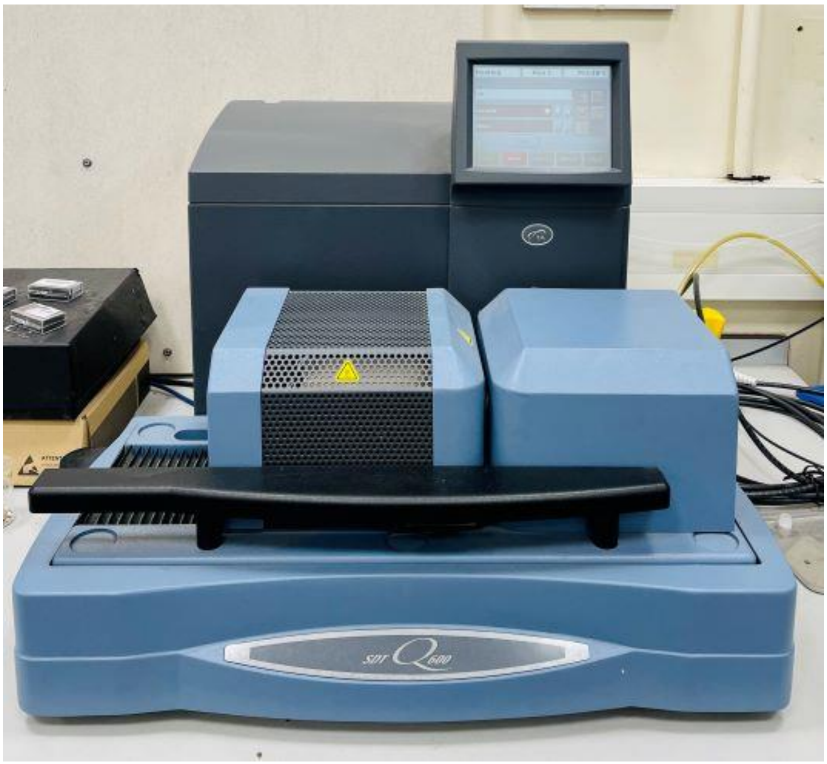

Figure 2.10 Thermogravimetric Analyser (TA) Instrument, SDT Q-600, Inorganic Chemistry Laboratory (ICL), University of Oxford.

2.4.3 N_2 Physisorption for BET Surface Area

The surface area is one of the most important quantities for characterizing porous materials and plays an important factor determining catalytic activity and catalysts applications. Typically, the surface area is determined from nitrogen adsorption isotherms using BET analysis. The BET theory was an extension of the Langmuir theory and was developed by Stephen Brunauer, Paul Emmett, and Edward Teller in 1938 [19, 20]. Langmuir theory relates to monolayer adsorption of gas molecules while in BET theory adsorption is multi-layered with the following hypotheses: (a) gas molecules are physically adsorbed on a solid in layers infinitely; (b) there is no interaction between each different adsorption layer; and (c) the Langmuir theory can be applied to each layer (**Figure 2.11**) [10, 19].

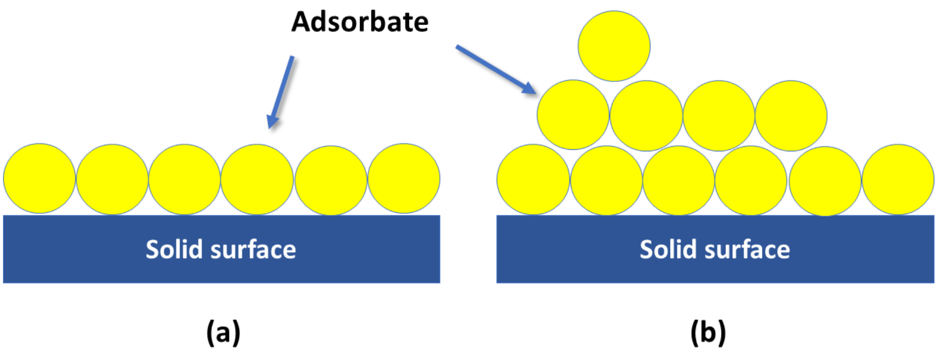

Figure 2.11 Schematic of the adsorption of gas molecules onto the surface of a sample showing (a) the monolayer adsorption model assumed by the Langmuir theory and (b) the multilayer adsorption model assumed by the BET theory. (Adapted from Ref. [19]).

BET surface area (m^2/g) is the multi-point measurement through gas adsorption analysis, where an inert gas such as nitrogen is constantly flowed over a solid sample. the surface is cooled using liquid N_2 to obtain measurable amounts of adsorption due to the weak interaction between gaseous and solid phase (Van der Waals forces) [19]. This measured amount of adsorption in monomolecular layer, and the rate of adsorption, can be used to calculate the specific surface area of a solid sample and its porous geometry. The data collected is displayed in the form of a BET isotherm, which plots the amount of gas adsorbed as a function of the relative pressure (p/p_o) where p is the N_2 partial saturation pressure and p_o is the saturation pressure at 77 K. The six IUPAC standard adsorption isotherms are shown in **Figure 2.12**, they differ because the systems demonstrate different gas/solid interactions.

The BET equation describes the relationship between the number of gas molecules adsorbed (X) at given relative pressure (p/p_o) [19]:

$$\frac{1}{X\left[\left(\frac{p_0}{p}\right)-1\right]} = \frac{1}{X_m C} + \frac{C-1}{X_m C}\left(\frac{p}{p_0}\right) \qquad \textbf{Equation 2.3}$$

Where C is a second parameter related to the heat of adsorption.

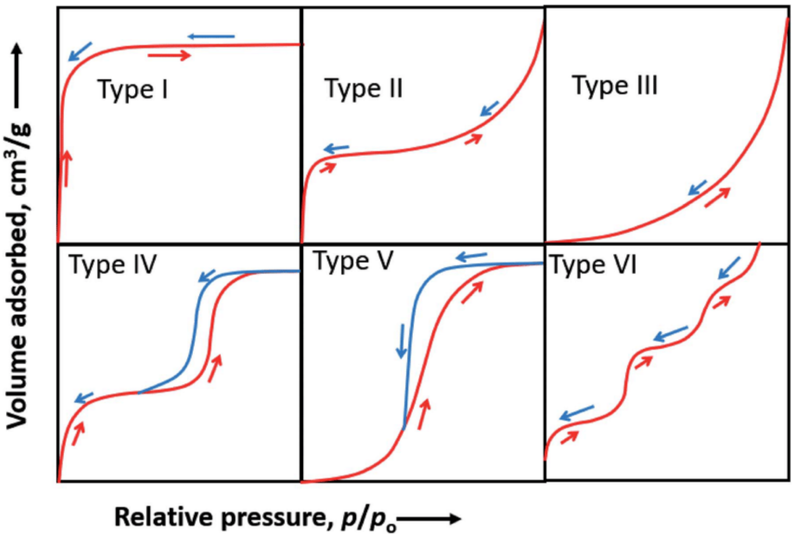

Figure 2.12 Different types of adsorption isotherms as classified by IUPAC. (Reproduced from Ref.[21]).

In this thesis, textural properties such as surface area, pore volume and pore size measurements studies were carried out by using physisorption technique. The adsorption-desorption isotherm for nitrogen was measured at 77K. The data collected is displayed in the form of a BET isotherm, which plots the amount of gas adsorbed as a function of the relative pressure. The isotherm was measured using a Micromeritics 3flex surface characterisation system which is located in Atatürk University, Erzurum, Turkey (**Figure 2.13**).

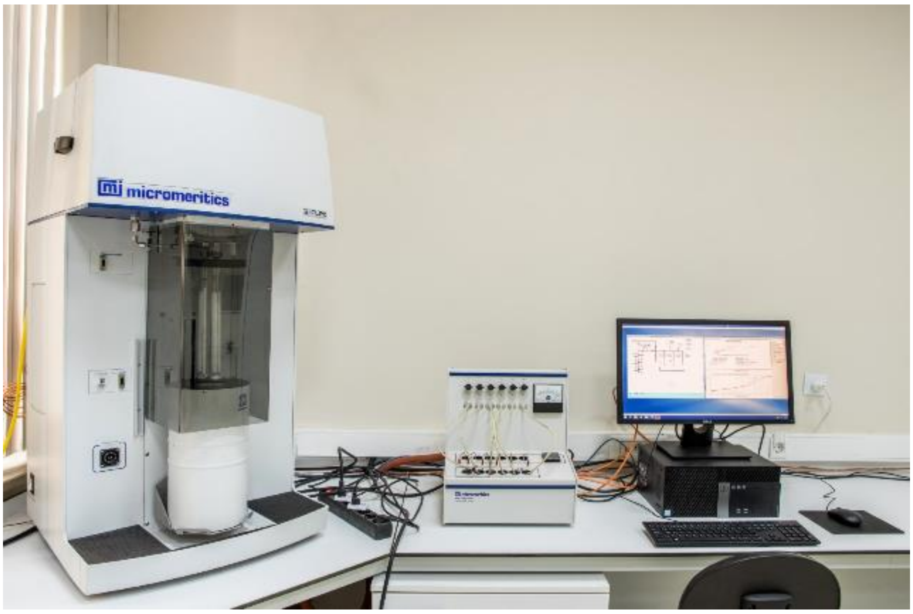

Figure 2.13 Micromeritics 3flex surface characterisation system.

2.4.4 Microwave Cavity Perturbation Measurements

The cavity perturbation techniques with the designed cavity resonator are commonly used in the measurement of dielectric parameters (relative permittivity and permeability) at microwave frequencies [30]. The method in principle consists of measuring the change in resonant frequency and Q factor of a microwave cavity resonator when it is suitably loaded with a small amount of the sample [31].

As described earlier in Chapter 1, The relative permittivity (ε') (or dielectric constant) indicates the ability to polarise a material imposed to an electrical field. The imaginary permittivity (ε'') (or dielectric loss) represents the ability of a medium to convert dielectric energy into heat.

Thus, the dielectric property of the sample can be calculated from the difference in the resonant frequency (Δf) and the change of bandwidth ΔBW (**Figure 2.14**) by **Equation 2.4** and **Equation 2.5** [3];

$$\frac{\Delta f}{f_0} = (\varepsilon' - 1)AV_s \qquad \textbf{Equation 2.4}$$

$$\frac{\Delta BW}{f_0} = 2\varepsilon'' AV_s \qquad \textbf{Equation 2.5}$$

where A is a constant determined by the size and geometry of the cavity and Vs is the effective volume of the sample in the cavity. Here in this thesis, all measurements carried out in an aluminium cavity, and the value of A is calculated to be 7.554×10^{-3} and Vs is about 0.13 cm^3.

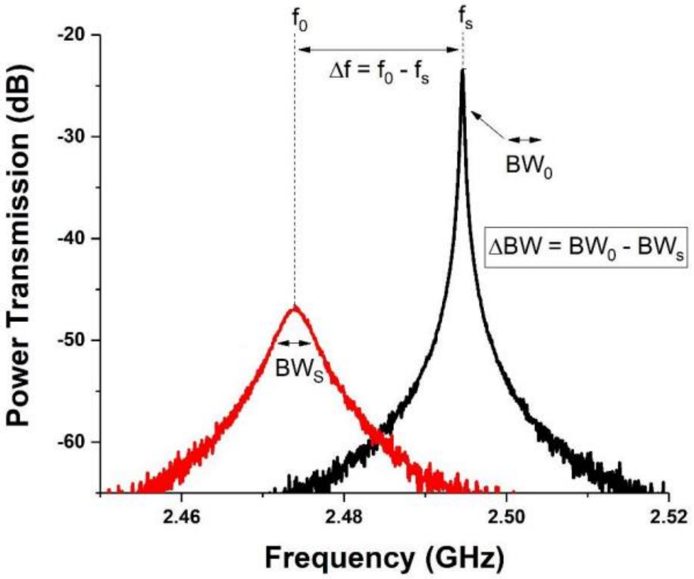

Figure 2.14 Example of microwave cavity perturbation measurement. Where (Δf) is the difference in the resonant frequency, and ΔBW is the change of bandwidth, between the sample and empty reference. (Reproduced from Ref.[3]).

The perturbation cavity system used in this thesis is illustrated in **Figure 2.15**. A quartz tube (inner diameter 2mm, outer diameter 4mm) is used as a sample container and placed in the centre of the cavity, at the maximum of a standing wave.

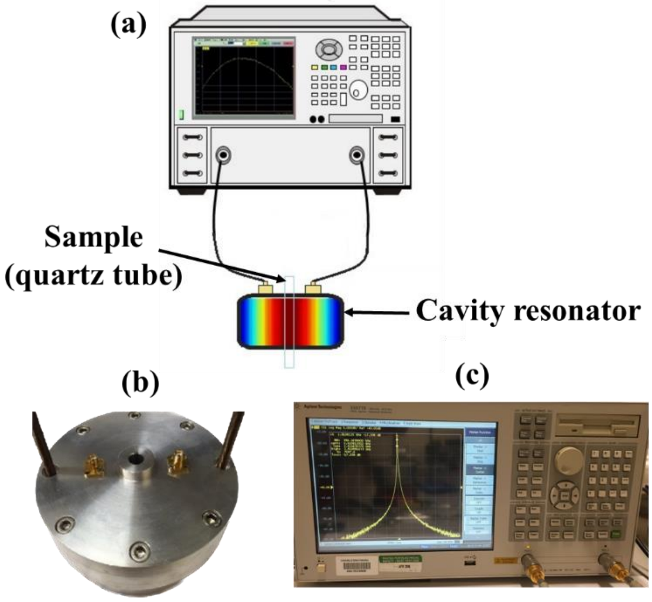

Figure 2.15 Schematic of dielectric measurement system. (a) Network analyser, (b) Aluminium host cavity showing the central hole where samples are introduced along the axis of the electric field, (c) Front panel and input keys of the VNA 8753E. (Reproduced from Ref [4]).

2.4.5 Scanning Electron Microscopy and Energy-dispersive X-ray Spectroscopy (SEM-EDS)

Scanning electron microscopy (SEM) is a mature, well-established technique applied widely in many scientific fields for imaging the microstructure and morphology of the materials. **Figure 2.16** shows the typical layout of the SEM components which comprise the electron gun, electromagnetic lenses, a vacuum chamber, sample stage, and a selection of detectors to collect the signals emitted from the sample. A beam of electrons is generated from a tungsten filament lamp placed at the top of the column with typically 1-30 keV accelerating voltage. The electron beam follows a vertical path through the microscope, which is held within a vacuum. The beam travels through electromagnetic fields and lenses, which focus the beam down toward the sample. The beam of electrons interacts with the sample to produce signals that give information about the sample's composition and surface topography.

Two types of electrons are mainly detected in SEM: Backscattered electrons (BSE) and Secondary electrons (SE). BSE are reflected back after elastic interaction between the primary electrons and the sample, while SE are a result of the collision (inelastic) between the primary electrons and the loosely bonded outer electrons (**Figure 2.17**). Both are used to produce an image and carry different types of information; the SE play the primary role of detecting the morphology and topography of the sample while the BSE show contrast in the composition of the elements of the sample [10, 22].

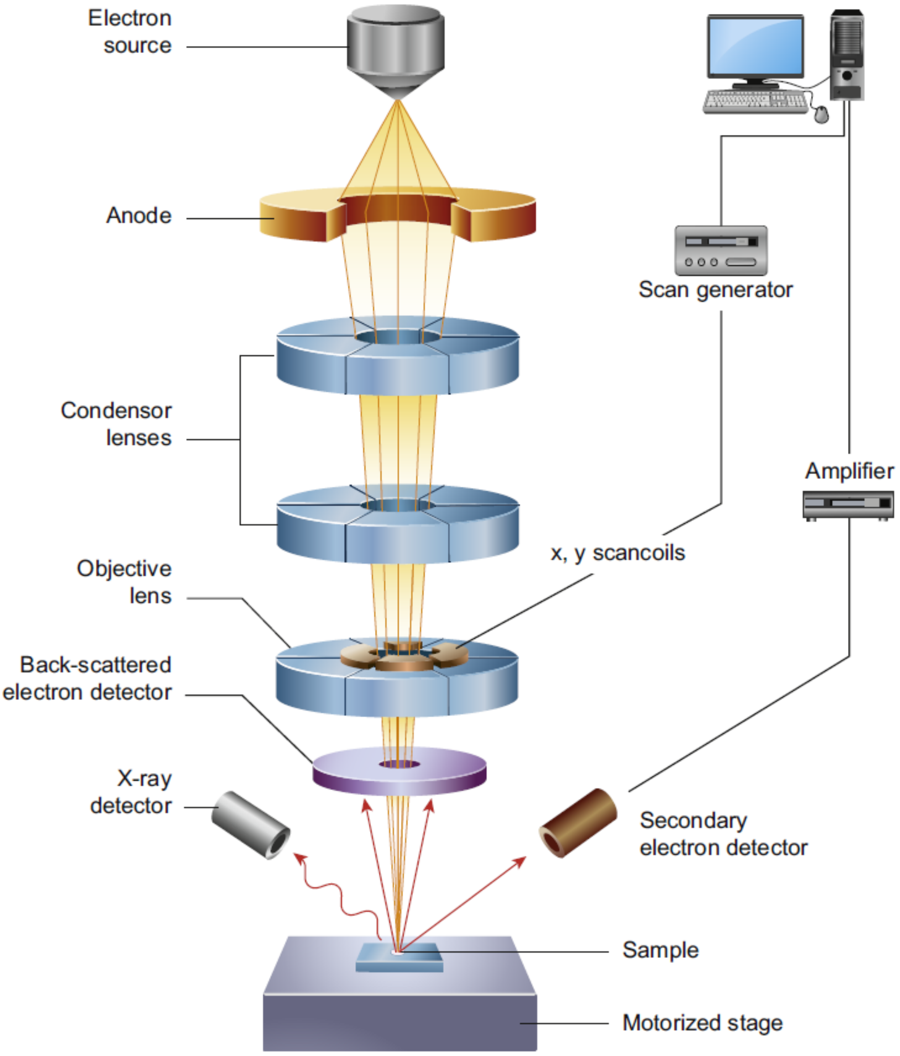

Figure 2.16 Schematic diagram of the SEM microscope. (Reproduced from Ref.[22])

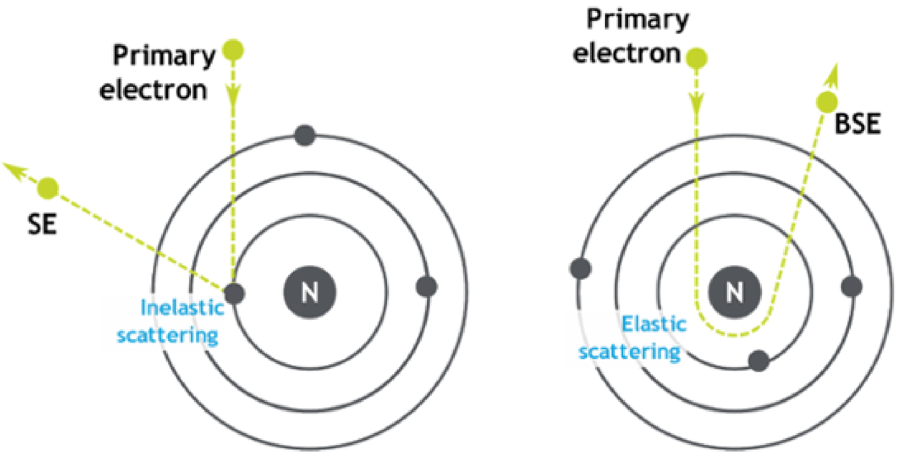

Figure 2.17 Secondary electrons (left) and backscattered electrons (right). (Reproduced from Ref. [23]).

Energy Dispersive X-Ray (EDS) analysis is an analytical technique used to provide a quantitative analysis of the chemical composition with the aid of proper X-ray detectors. When the collision occurs between the sample and the primary electrons in the SEM, the atoms of the sample were ionised due to the exciting and ejecting of the electrons in the inner shells of the atoms. The energy released from these transitions which is in the form of X-ray are detected by the EDS system. [23, 24]. The X-ray spectrum is characteristic of each element, and the relative intensities in the spectrum enable quantitative analysis.

In this thesis, images were taken using the Inlens detector of the Zeiss Sigma 300 Scanning Electron Microscope which is located in Atatürk University, Erzurum, Turkey (**Figure 2.18**). The samples were poured onto carbon tape and coated with a mini sputter for 300 seconds. Images were taken at 5 KV at different magnifications. The surface elemental analysis is carried out with the equipped Energy-dispersive X-ray spectroscopy analysis which was performed from a wide-angle general surface at 15 KV.

Figure 2.18 Zeiss Sigma 300 Scanning Electron Microscope.

2.4.6 Transmission Electron Microscopy (TEM)

TEM is a powerful tool for material science which offers invaluable information about the internal structure of the sample, such as crystal structure, and morphology, while SEM provides information about the sample's surface and its composition. Instruments for both techniques are equipped with similar key parts and used electrons to obtain images of samples [25, 26], but there are important differences. **Figure 2.19** shows the main components of a TEM microscope, which consist of the electron gun, electrostatic lenses to focus the electrons before and after the sample, a transmitted electron detection system (image producing system), and image recording system. Typically, an electron source is generated electrons through 80-300 kV acceleration voltage which is higher than the voltage used in SEM (1-30 kV) in order to give sufficient energy can pass through up 1µm of sample. The electrons travel through a vacuum and are focused onto the sample using the condenser lenses. The electrons then collide with the sample and parts of it are transmitted depending upon the thickness and electron transparency of the specimen. The transmitted electrons are focused by the objective lens into an image on a fluorescent screen, which converts the electrons into visible light signal for viewing and recording via a detector such as a (CCD) camera [21, 27, 28].

In this thesis, images were obtained using a Hitachi HT-7700 which is located in Atatürk University, Erzurum, Turkey (**Figure 2.20**). Powdered samples were placed in Eppendorf tubes with distilled water. The amount of solid sample in the suspension should be between 0.1% and 1%. The solid sample in the suspension is kept in an ultrasonic water bath until it is completely homogeneously dispersed. Care should be taken to avoid any visible lumps. About 3-5 µl of the resulting suspension was dripped onto the carbon-coated grid using a micropipette. The sample on the carbon-coated grid then dried completely. The dried sample was then mounted on the sample holder of the Hitachi HT-7700 instrument. This instrument used a Lanthanum hexaboride (LaB6) electron gun, operating under accelerating voltage in the range of 40-120 kV. As the device can switch from search mode (viewing the on-screen camera) to high-quality, full-size picture capture mode (main camera mode) with the push of a button, it enables quick image capture of the selected area.

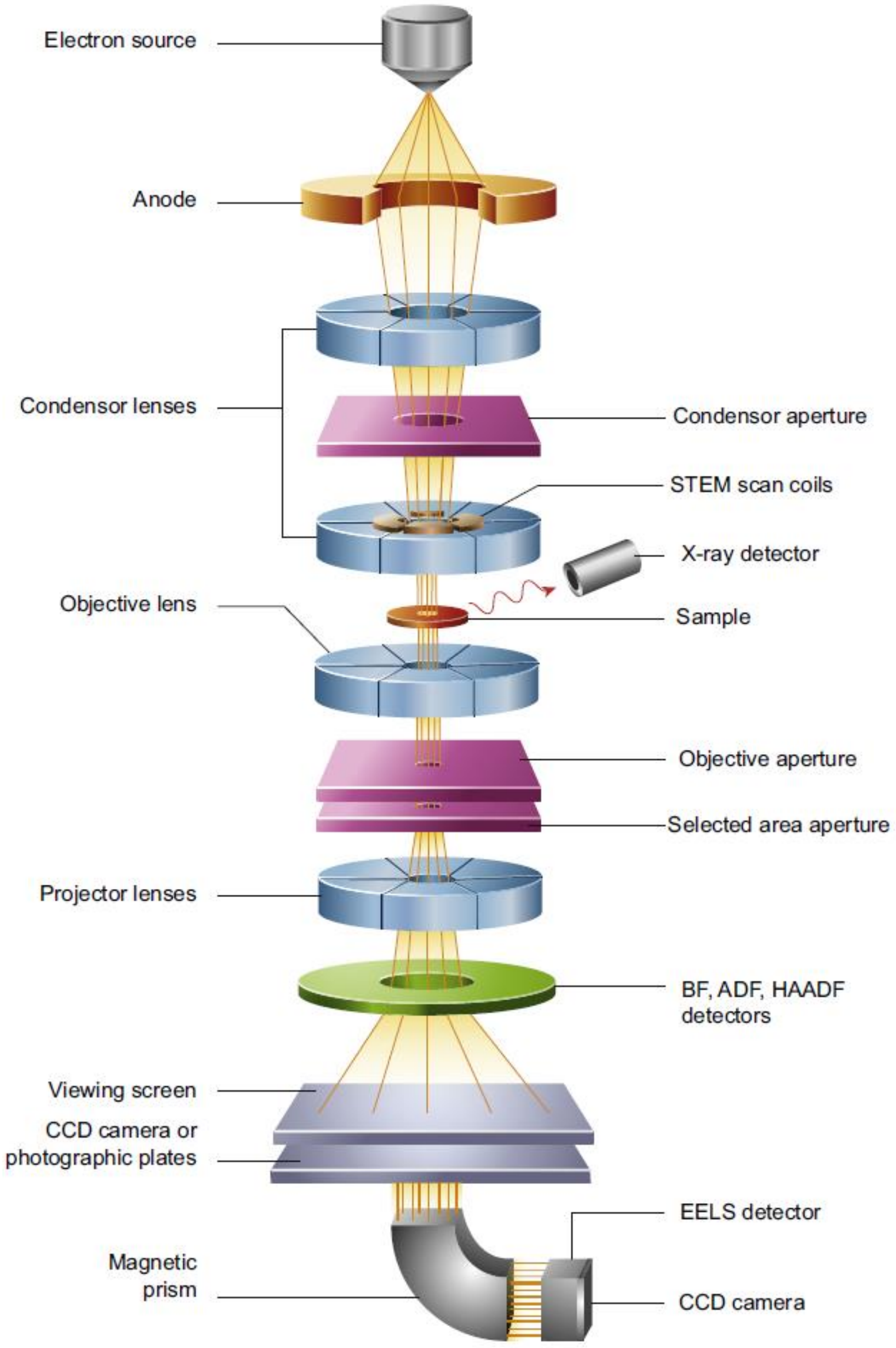

Figure 2.19 Schematic diagram of the of a TEM microscope. (BF) bright-field, (ADF) annular dark-field, (HAADF) high angle annular dark field, (EELS) electron energy loss spectroscopy, and (CCD) charged coupled devices. (Reproduced from Ref. [22]).

Figure 2.20 Hitachi HT-7700 transmission electron microscope.

2.5 Light Crude Oil Characterisation

The light crude oil (LCO) which was used in the catalytic reactions was characterised using several analytical techniques.

2.5.1 Fourier Transform Infrared Spectrometer (FTIR)

Fourier transform infrared spectroscopy (FTIR) is a technique which is used to detect different functional groups by analysis of molecular vibrations of gases, liquids, and solids. Each functional group has its own discrete vibrational energy, and this can be used to identify a molecule through the presence of various functional groups. The FTIR spectrum is recorded between 4000 and 400 cm^{-1}, and used mathematical process (Fourier transform) to translate the raw data (interferogram) into the actual spectrum. The technique is widely used in organic synthesis, petrochemical engineering, polymer science, pharmaceutical industry and food analysis [32, 33].

The normal instrumental FTIR consists of three main components: source, an interferometer, a sample compartment, detector, and computer (**Figure 2.21**). When the source emits infrared energy, the beam passes through an aperture which controls the amount of energy presented to the sample, then to the detector. The beam enters the interferometer and split to two beams of light to make precise measurements. The resulting interferogram signal exits the interferometer and enters the sample compartment. This is where specific frequencies of energy which are uniquely characteristic of the sample are absorbed. The beam passes into the detector for final measurement and the measured signal is digitised and sent to the computer where the Fourier transform takes place [32, 34].

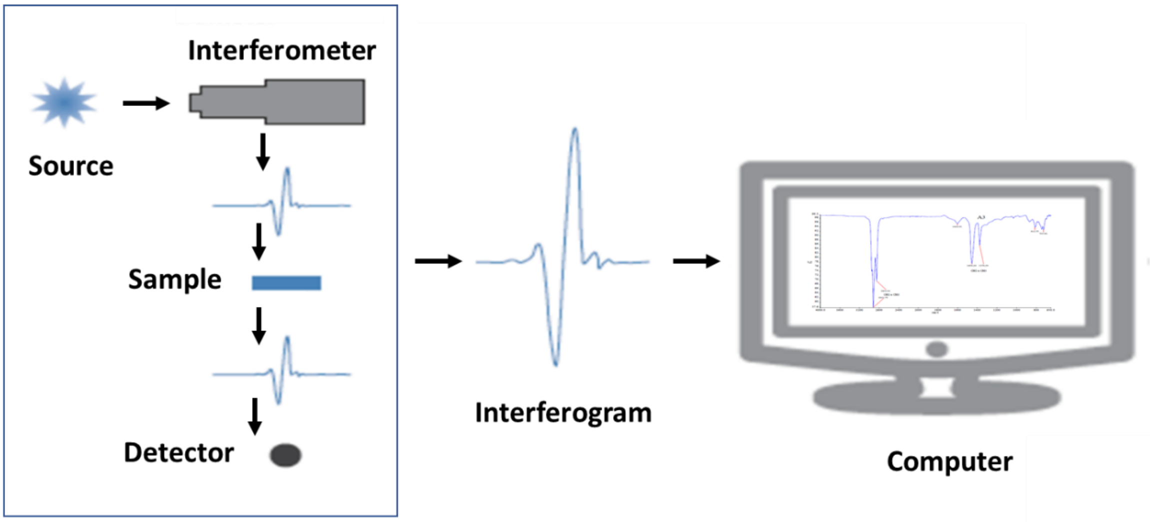

Figure 2.21 The main components of Fourier transform infrared spectroscopy (FTIR). (Adapted from Ref.[33]).

The light crude oil fractions are measured by SHIMADZU IRAffinity-1S spectrophotometer, which is located in the chemistry department, University of Oxford. The IR spectra used in this thesis were recorded between 400 and 4000 cm^{-1} (**Figure 2.22**).

Figure 2.22 SHIMADZU IRAffinity-1S spectrophotometer, Chemistry Research Laboratory (CRL), University of Oxford.

2.5.2 Nuclear Magnetic Resonance (NMR) Spectroscopy

Nuclear magnetic resonance (NMR) is arguably the most versatile of the spectroscopic techniques yielding quantitative and structural information. NMR experiments can embrace the widest range of materials: liquids and solids, organic and inorganic molecules, and a wide range of sample conditions (temperature, pressure, concentration …, etc) can all be studied [34].

The basic principle of NMR spectroscopy is based on the magnetic properties of atomic nuclei, which have spin and are electrically charged. When the sample is placed under the action of an external magnetic field (B_0), an energy transfer through a radiofrequency (RF) transmitter from the base energy (E_1) to a higher energy level (E_2), The energy transfer takes place at a wavelength that corresponds to radio frequencies and when the spin returns to its base level (relaxation), energy is emitted at the same frequency. The absorption of energy is then detected in an RF receiver and recorded as a spectral line, the so-called "resonance signal" [36] (**Figure 2.23**).

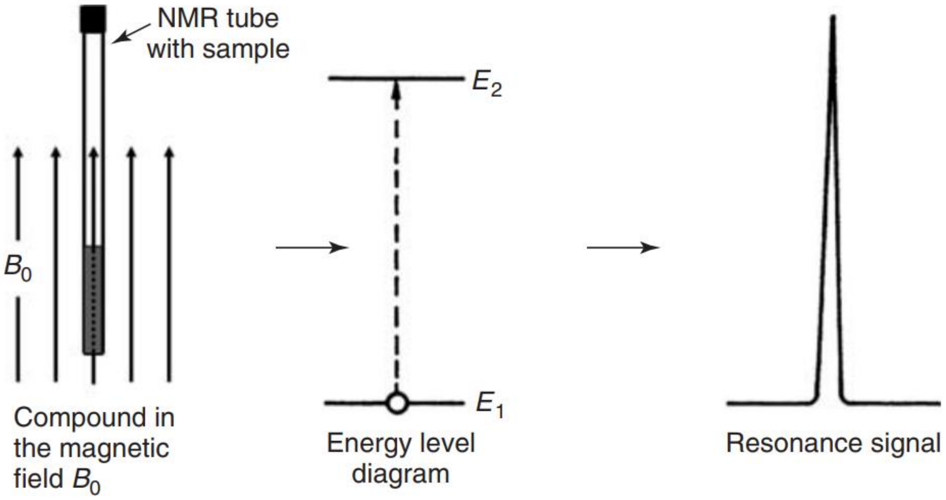

Figure 2.23 Formation of an NMR signal. (Reproduced from Ref.[36]).

In NMR spectroscopy, the chemical shift is the precise resonant frequency of an atomic nucleus in a magnetic field with reference to a standard compound. This field is affected by electron shielding which is in turn dependent on the chemical environment. Tetramethylsilane [TMS;$(CH_3)_4Si$] is a common standard used to determine the chemical shift of the commonly measured ^{1}H resonance in compounds: δTMS = 0 ppm by definition. Information about the composition of atomic groups within organic molecules can be derived from the chemical shift of the ^{1}H resonant frequencies. **Figure 2.24** shows the ^{1}H chemical shift range for organic compounds [37, 38]. The position of signals indicates the type of hydrogen that molecule contains (i.e. it is characteristic of functional groups), the number of signals gives information about the different types of hydrogen, and the intensity of signals show the relative amounts (quantity) of each kind of hydrogen in the molecule.

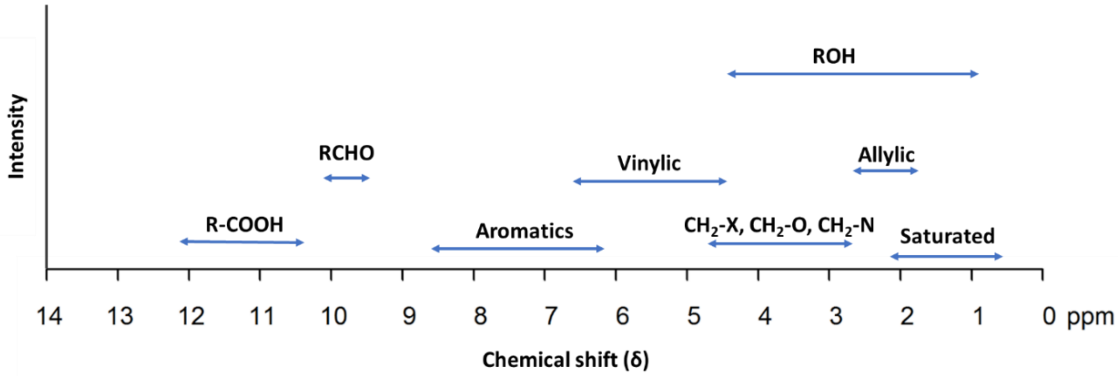

Figure 2.24 ^{1}H chemical shift ranges for organic compounds. (Adapted from Ref.[37]).

Several factors also influencing peak split in NMR spectrum, including spin-spin coupling, relaxation time, and signal intensity. Spin-spin coupling (also called *J*-coupling) is a magnetic interaction between individual nuclear spins transmitted by the bonding electrons through which the nuclear spins are indirectly connected. It can provide information about the connectivity of chemical bonds and structure. Relaxation time can provide information on molecular dynamics.

All the NMR spectra reported in this thesis have been recorded using a Bruker AVANCE III HD (600 MHz) spectrometer, which is located in the chemistry department, University of Oxford (**Figure 2.25**) equipped with a 9.4 T superconducting magnet and a triple-resonance indirect detection probe. All the spectra were acquired and processed using the standard Bruker software Topspin 2.0. The solvents used was $CDCl_3$ and their deuterium signal was used for the locking, shimming and internal referencing procedures.

Figure 2.25 Bruker AVANCE III HD (600 MHz) NMR spectrometer, Chemistry Research Laboratory (CRL), University of Oxford.

References

[1] E. Pert, Y. Carmel, A. Birnboim, T. Olorunyolemi, D. Gershon, J. Calame, I. Lloyd, O. Wilson, Temperature Measurements During Microwave Processing: The Significance of Thermocouple Effects, Journal of the American Ceramic Society, 84 (2004) 1981-1986.

[2] T. Durka, Microwave Effects in Heterogeneous Catalysis: Application to Gas-Solid Reactions for Hydrogen Production, Ph.D. thesis, Warsaw University of Technology, 2013.

[3] X. Jie, Microwave-Initiated Catalytic Dehydrogenation of Fossil Fuels for the Facile Production and Safe Storage of Hydrogen, D.Phil thesis, University of Oxford, 2020.

[4] A. Aldawsari, Dielectric Measurements and Catalytic Cracking of Heavy Oils using Advanced Microwave Technologies, D.Phil thesis, University of Oxford, 2017.

[5] W. Knoche, Chemical Reactions of CO_2 in Water, in: C. Bauer, G. Gros, H. Bartels (Eds.) Biophysics and Physiology of Carbon Dioxide, Springer Berlin Heidelberg, Berlin, Heidelberg, (1980), 3-11.

[6] Recommendations on Nomenclature for Chromatography, Pure and Applied Chemistry, 37 (1974) 445-462.

[7] P. Vasconcellos, G. Da Rocha, E. Caramão, M. Machado, L. Krause, Chromatographic Techniques for Organic Analytes, 2015, 267-309.

[8] E. Stashenko, J. Martínez, Gas Chromatography-Mass Spectrometry, in: X. Guo (Ed.) Advances in Gas Chromatography (2014).

[9] Basics & Fundamentals Gas Chromatography, Shimadzu, (2020), www.shimadzu.eu.com.

[10] S. Aldrees, Solid Acid Zeolite Catalysts for Benzene/ Ethylene Alkylation Reactions, MSc thesis, Oxford University, UK, (2011).

[11] J. Sneddon, S. Masuram, J.C. Richert, Gas Chromatography-Mass Spectrometry-Basic Principles, Instrumentation and Selected Applications for Detection of Organic Compounds, Analytical Letters, 40 (2007) 1003-1012.

[12] Gas Chromatography Mass Spectrometry (GCMS), Shimadzu, (2020), www.shimadzu.eu.com.

[13] J. Hargreaves, Powder X-Ray Diffraction and Heterogeneous Catalysis, Crystallography Reviews, 11 (2005) 21-34.

[14] A. Bunaciu, E. Udriştioiu, H. Aboul-Enein, X-Ray Diffraction: Instrumentation and Applications, Critical Reviews in Analytical Chemistry, 45 (2015) 289-299.

[15] C. Stan, C. Beavers, M. Kunz, N. Tamura, X-Ray Diffraction under Extreme Conditions at the Advanced Light Source, Quantum Beam Science, 2 (2018) 4.

[16] BRUKER D8 ADVANCE Diffractometer, Inorganic chemistry laboratory (ICL), University of Oxford, 2022.

[17] R. Parameshwaran, A. Sarı, N. Jalaiah, R. Karunakaran, Chapter 13 - Applications of Thermal Analysis to the Study of Phase-Change Materials, in: S. Vyazovkin, N. Koga, C. Schick (Eds.) Handbook of Thermal Analysis and Calorimetry, Elsevier Science, (2018), 519-572.

[18] P. Gabbott, Principles and Applications of Thermal Analysis, Blackwell Pub., (2008).

[19] P. Raja, A. Barron, BET Surface Area Analysis of Nanoparticles, Physical Methods in Chemistry and Nano Science, LiberTexts, (2021).

[20] S. Brunauer, P.H. Emmett, E. Teller, Adsorption of Gases in Multimolecular Layers, Journal of the American Chemical Society, 60 (1938) 309-319.

[21] K.V. Kumar, S. Gadipelli, B. Wood, K.A. Ramisetty, A.A. Stewart, C.A. Howard, D.J.L. Brett, F. Rodriguez-Reinoso, Characterization of the Adsorption Site Energies and Heterogeneous Surfaces of Porous Materials, Journal of Materials Chemistry A, 7 (2019) 10104-10137.

[22] B.J. Inkson, 2 - Scanning Electron Microscopy (Sem) and Transmission Electron Microscopy (Tem) for Materials Characterization, in: G. Hübschen, I. Altpeter, R. Tschuncky, H.-G. Herrmann (Eds.) Materials Characterization Using Nondestructive Evaluation (NDE) Methods, Woodhead Pub. (2016), 17-43.

[23] How to Mix Backscattered and Secondary Electron Images, Thermo Fisher, (2018).

[24] M. Mutalib, M. Rahman, M. Othman, A. Ismail, J. Jaafar, Scanning Electron Microscopy (SEM) and Energy-Dispersive X-Ray (EDX) Spectroscopy, Membrane Characterization, Elsevier, (2017), 161-179.

[25] J.E. Welton, SEM Petrology Atlas, 4 (1984).

[26] P.S. Kumar, K.G. Pavithra, M. Naushad, Chapter 4 - Characterization Techniques for Nanomaterials, in: S. Thomas, E.H.M. Sakho, N. Kalarikkal, S.O. Oluwafemi, J. Wu (Eds.) Nanomaterials for Solar Cell Applications, Elsevier, (2019), 97-124.

[27] F. Krumeich, Introduction into Transmission and Scanning Transmission Electron Microscopy, Laboratoty of Inorganic Chemistry, ETH Zurich, (2022).

[28] M. Kannan, Transmission Electron Microscope -Principle, Components and Applications Illumination System (Electron gun and condenser lenses), Electron gun, (2018), 93-101.

[29] A. Vyas, V. Rana, D. Gadani, A. Prajapati, Cavity Perturbation Technique for Complex Permittivity Measurement of Dielectric Materials at X-Band Microwave Frequency, International Conference on Recent Advances in Microwave Theory and Applications, (2008), 836-838.

[30] S. Sen, P.K. Saha, B.R. Nag, New Cavity Perturbation Technique for Microwave Measurement of Dielectric Constant, Review of Scientific Instruments, 50 (1979) 1594-1597.

[31] D. Pavia, G. Lampman, G. Kriz, J. Vyvyan, Introduction to Spectroscopy, 5th ed., (2013).

[32] S. Khan, S. Khan, L. Khan, A. Farooq, K. Akhtar, A. Asiri, Fourier Transform Infrared Spectroscopy: Fundamentals and Application in Functional Groups and Nanomaterials Characterization, in: S. Sharma, D. Verma, L. Khan, S. Kumar (Eds.) Handbook of Materials Characterization, Springer, (2018), 317-344.

[33] Introduction to Fourier Transform Infrared Spectrometry, Thermo Nicolet, (2001).

[34] T. Polenova, R. Gupta, A. Goldbourt, Magic Angle Spinning NMR Spectroscopy: A Versatile Technique for Structural and Dynamic Analysis of Solid-Phase Systems, Analytical Chemistry, 87 (2015) 5458-5469.

[35] H. Gunther, NMR Spectroscopy Basic Principles, Concepts, and Applications in Chemistry, 3rd Ed., Wiley, (2013).

[36] H. Biava, Chemical Shifts in ^{1}H NMR Spectroscopy, Organic Chemistry II, LibreTexts, (2021).

[37] B. Diehl, Chapter 1 - Principles in NMR Spectroscopy, in: U. Holzgrabe, I. Wawer, B. Diehl (Eds.) NMR Spectroscopy in Pharmaceutical Analysis, Elsevier, (2008), 1-41.

Chapter3

The Production of Hydrogen through the Microwave-Initiated Catalytic Dehydrogenation of Model Hydrocarbon Compounds without Significant CO_2 Emissions

The composition of crude oil varies depending on its source; however, it is principally composed of three families of hydrocarbons (paraffins, naphthenes, and aromatics) [1-4]. In this chapter, hexadecane, cyclohexane, and BTX (benzene, toluene, and xylene) were selected to simulate the role of paraffins (alkanes), naphthenes, and aromatics present in crude oil. These hydrocarbons were investigated as model compounds for microwave-initiated dehydrogenation to gain insight into the effect on the evolved hydrogen for each component separately, then mixed in proportions close to their real proportions in the light crude oil (LCO) to create, in essence, a “synthetic crude oil”. The synthetic mixture was used to check the interactions between components and to compare the results with LCO to investigate if there are other components (or impurities) that reduce the hydrogen yield.

3.1 Introduction

Currently, the steam reforming of methane (SRM), which is the main constituent of natural gas, is the most frequently applied process and cheapest source of industrial hydrogen and comprises nearly 50% of global hydrogen production [5-8]. Unfortunately, there is a very considerable amount of CO_2 produced. Consequently, this chapter uses SRM as the benchmark technology for hydrogen production. In the process of steam reforming in a hydrogen plant, the methane is heated between 700-1000 °C and reacted with steam under 3-25 bar in the presence of nickel (Ni) catalysts [9-13]. Although the technology is well-established and offers high hydrogen yields, still there are downsides and limitations including the release of significant levels of greenhouse gases into the atmosphere, harsh reaction conditions, catalyst deactivation, and excessive energy input [6, 14, 15]. In this regard, catalysts play a critical role at the heart of these processes, and the development of less expensive catalysts with high stability and selectivity is crucial.

Noble metal catalysts such as Ru, Rh, Pd, Ir, and Pt are used due to their remarkable catalytic performance and higher resistance to carbon deposition as a consequence of the difficulties of dissolving carbon in them to produce metal carbide [6, 16, 17]. Jones *et al*. [18] proposed the SRM activity order as Ru > Rh > Ir > Pt, indicating that Pt catalysts as the least active. However, designing a system to usher in a new hydrogen economy by focusing on noble metals would be counterproductive as they are too expensive for commercial operation. For this, the earth-abundant base-metal catalysts such as Fe, Co, Ni, and Cu have attracted attention due to their low cost and ease of extraction from their ores [6, 19-21]. However, iron compounds will be rapidly oxidized by O_2 while cobalt derivatives are unstable in steam [6]. Therefore, nickel-based catalysts have been widely used and studied in SRM for their high catalytic activity and relatively cheap cost, being supported on many metal oxides, such as Al_2O_3, MgO, CeO_2, or La_2O_3, and promoted with a second metal [6, 22, 23]. On the other hand, the serious deactivation of Ni catalysts due to the easy sintering when the catalyst melts just sufficiently close to pores, and the coke formation are the main challenges in SRM processes.

Another process that has attracted attention recently is the dry reforming of methane with CO_2 (DRM) [24], an innovative alternative method, based on a strongly endothermic reaction in the absence of steam, for the production of equimolar synthesis gas (H_2 + CO) that utilises two greenhouse gases; CO_2 and CH_4, thus lowering the carbon emissions of any industrial plant. The main drawback of this process is the significant production of coke, which leads to a reduced catalyst lifetime [23, 25, 26]. The tendency for carbon deposition may depend on the atomic ratio O/C and H/C in the feed gas. Lower H_2O/CH_4 and H_2/CO ratios correspond to a higher tendency toward coke formation [27].

Alternative techniques for hydrogen production using methane as a feedstock were developed including partial oxidation with O_2 (POM) [28, 29], autothermal reforming with H_2O and O_2 [30, 31], low-temperature SRM [32, 33], combined steam and dry reforming of methane (CSDRM) [34, 35], a chemical looping SRM process (CL-SRM) [8, 36], a sorption-enhanced SMR (SE-SRM) [37, 38], as well as a combined CL-SE-SRM process [39, 40]. Each process generates a syngas mixture with an alternating H_2:CO ratio due to different reaction conditions, such as temperature and pressure. Decomposition of methane offers another route to hydrogen production. Eliminating the water gas shift unit in SRM makes the process more sustainable with solid carbon being the main coproduct. This process has been reviewed extensively [41-47]. The biggest challenge facing the whole field is the stability and activity of the catalysts. Extensive research has been carried out to develop highly efficient and cheaper catalysts and eco-friendly technology (**Figure 3.1**).

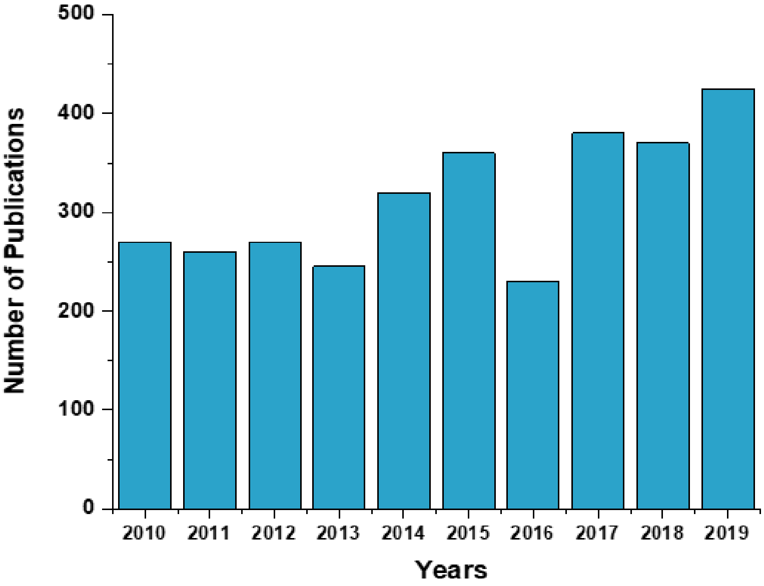

Figure 3.1 Publications on methane steam reforming in the past decade. (Adapted from Ref.[8])

Table 3.1 summarises the most investigated catalysts for hydrogen production under different conditions. Note that the catalyst metal loading is relatively low (below 15 wt. %) whilst Pt-promoted catalysts are particularly active at low reaction temperatures (i.e. 550 to 600 °C).

Table 3.1 Summary of catalysts and operating conditions used in hydrogen production.

Catalyst	**Metal loading (wt.%)**	**Promoter**	**Temperature (°C)**	**CH_4 conversion* (%)**	**H_2 selectivity** (%)**	**Reference**
Ni/Al_2O_3	5	CeO_2–ZrO_2	650	65	35	[48]
	7	Au	550	84	70	[49]
	12	Co	800	70	NA	[50]
	13	Ce	800	75	65	[51]
	15	Nb_2O_5	750	98	78	[52]
Mo/MgO	30	NA	800	75	59	[53, 54]
Ni/HZSM-5/ MCM-41	10	NA	620	66	78	[55, 56]
$Ni/SiO_2Al_2O_3$	10	NA	700	96	83	[57]
	10	NA	900	98	75	[58]
Co-Fe/Al	15Co,30Fe	NA	700	73	72	[59, 60]
$Fe/CeZrO_2$	15	NA	700	85	83	[59, 61]
$Fe\text{-}Co/CeZrO_2$	15Fe,5Co	NA	700	90	90	[61, 62]
$Fe\text{-}Mo/CeZrO_2$	15Fe,5Mo	NA	700	90	90	[61, 63]
Rh/Al_2O_3	1	NA	600	69	NA	[64]
$Rh/MgAl_2O_4$	5	NA	850	50	NA	[65]

*Conversion: describe how much of methane was consumed in the reaction.
**Selectivity: describe how much hydrogen was formed in relation to the undesired product(s).

In the last two decades, attempts have been made to reduce the consumption of energy and the reaction time in organic synthesis processes by using microwave techniques. Some of the earliest uses of microwaves in chemical literature reported by Giguere *et al.* about using commercial microwave ovens in organic synthesis, finding that the use of the microwave can reduce the required energy and the reaction time [66]. Since then, the use of microwave energy in many sectors has become a well-known technique. Moreover, this technique has been proposed as the technology of the future for a wide range of applications [67-70]. Microwaves are utilised in many applications such as; chemical synthesis [71-75], reforming of methane [76-80], microwave-assisted extraction [81-84], microwave-assisted catalysis [85-88], oil sands separation [89-91], water/oil emulsion separation [92-94], removal of naphthenic acids [95, 96], hydrodesulphurisation and hydrodenitrogenation [97-102], demetallisation [103-105], heavy oil cracking [106-109], food drying and processing [110-112], and several pyrolysis studies have been conducted using microwaves as a heating source, with a range of feedstocks, and were reviewed by Motasemi *et al.* [113]

Recently, there has been increasing interest in producing hydrogen from hydrocarbons initiated by microwave radiation. Gonzalez-Cortes *et al.* [114] have reported that 7 wt. % hydrogen is rapidly produced from paraffin wax $C_{26}H_{54}$ by microwave-assisted catalysis using ruthenium nanoparticles supported on activated carbon. Following this work, Jie *et al.* [115] discovered a means of rapidly liberating hydrogen by the microwave-initiated catalytic dehydrogenation of liquid alkanes using iron and nickel particles supported on silicon carbide. The selectivity of hydrogen produced from all evolved gases was 98% after 30 minutes of irradiation time. CO, CO_2, methane, ethane and other hydrocarbons were also produced as minor products. In addition, they obtained elemental carbon as the major by-product. Using microwave heating, Jie *et al.* [116] also showed that the catalytic dehydrogenation of hexadecane with the assistance of microwaves gave hydrogen with a selectivity of 94% after

30 minutes of irradiation time. They have used iron particles supported on silicon carbide as a catalyst. They also reported that CO, CO_2, methane, ethane, elemental carbon and other hydrocarbons were also produced as by-products. In other work, Jie *et al*. [117] developed a rapid method initiated by microwave to catalyse the conversion of various plastic wastes into hydrogen and high-value carbon using iron- aluminium oxide catalysts. The hydrogen concentration in the evolved gases reached of ~90 vol. %, and 55.6 mmol of hydrogen were obtained from each gram of plastic.

In recent research work, Jie *et al*. [118] investigated the catalytic activities of a range of carbon materials and reported that the activated carbons and graphene nanoplatelets were found to be highly effective for the microwave-initiated dehydrogenation of hexadecane towards hydrogen production.

The aim of this chapter is to set the scene for the subsequent study of the microwave-initiated dehydrogenation of crude oil by investigating the contribution of a single compound (or model compound) and combinations of these compounds for the production of hydrogen. Model compounds such as hexadecane, cyclohexane and benzene, toluene, and xylene (BTX) that represent paraffins (alkanes), naphthenes, and aromatics respectively in crude oil are comprehensively assessed. This study gives insight into the interaction of these compounds with the catalyst and their capability to undergo catalytic deep dehydrogenation reactions under microwave heating.

3.2 Experimental

3.2.1 Preparation of Fe/AC Catalyst

In this chapter, the catalyst used was based on iron metal (Fe) supported on activated carbon (AC). Iron is a cheap, readily available and a good absorber of microwave energy. The term activated carbon refers to carbonaceous materials with a high degree of porosity and a very large surface area of more than 3000 m^2/g [119]. It has been widely used as a catalyst support, energy storage material and a microwave absorber [120].

The catalyst was synthesised using the so-called wet impregnation method [114] as shown schematically in **Figure 3.2**. Iron nitrate, $Fe(NO_3)_3.9H_2O$ (Iron (III) nitrate nonahydrate, 99%, Sigma-Aldrich) was used as the iron precursor. A series of Fe catalysts supported on AC (activated carbon, powder, 95%, Sigma-Aldrich) was synthesised with Fe loading ranges between 0-50 wt. %. Firstly, a calculated amount of iron nitrate was dissolved in 100 ml of deionised water, next the support was added slowly to the aqueous solution of iron nitrate. The mixture was vigorously stirred at 150 °C for 4 hours under reflux. The mixture left for overnight to cool to room temperature. The pH of the mixture was adjusted between 9 and 10 unit by adding the required amount of $NaHCO_3$ (sodium bicarbonate, powder, 99.5%, Sigma-Aldrich). In this step the following reaction take place:

$$\mathrm{Fe(NO_3)_3.9H_2O + 3NaHCO_3 \rightarrow Fe(HCO_3)_3 + 3NaNO_3 + 9H_2O}$$ **Equation 3.1**

The possible way for the decomposition of the formed iron (III) hydrogen carbonate ($Fe(HCO_3)_3$) is in the following reaction:

$$\mathrm{2Fe(HCO_3)_3 \rightarrow Fe_2O_3 + 3H_2O + 6CO_2}$$ **Equation 3.2**

Subsequently, 50 g of $(CH_2OH)_2$ (ethylene glycol, 99%, Sigma-Aldrich) was added slowly to the mixture under stirring for a period of 10 minutes, next the mixture was stirred vigorously and heated at 150 °C for 4 hours under reflux. The solution left again for overnight to cool to room temperature. The purpose of adding the ethylene glycol is to react with the excess amount of sodium bicarbonate and produced monosodium glycolate, water, and CO_2 as the following reaction:

$$(CH_2OH)_2 + NaHCO_3 \rightarrow C_2H_5NaO_2 + H_2O + CO_2$$ **Equation 3.3**

The resultant solid was extensively washed with deionised water to remove any formed salts until the filtrate solution achieved neutral pH, then separated from the aqueous solution by filtration. The solid was finally dried in the oven at 90 °C overnight. The required metal-catalysts were obtained by a careful reduction of the above material in flowing 10 vol.% H_2/Ar gaseous mixtures at 750 °C for 8 h using a heating rate of 5 °C/min, as the following reaction:

$$Fe_2O_3 + 3H_2 \rightarrow 2Fe + 3H_2O$$ **Equation 3.4**

The catalysts were tested and characterised both before and after the microwave-initiated deep-dehydrogenation experiments using a purpose-built microwave cavity system (see chapter 2). Various characterisation techniques, also described in detail in chapter 2, were used to check the catalyst composition and to provide data on the catalyst activity.

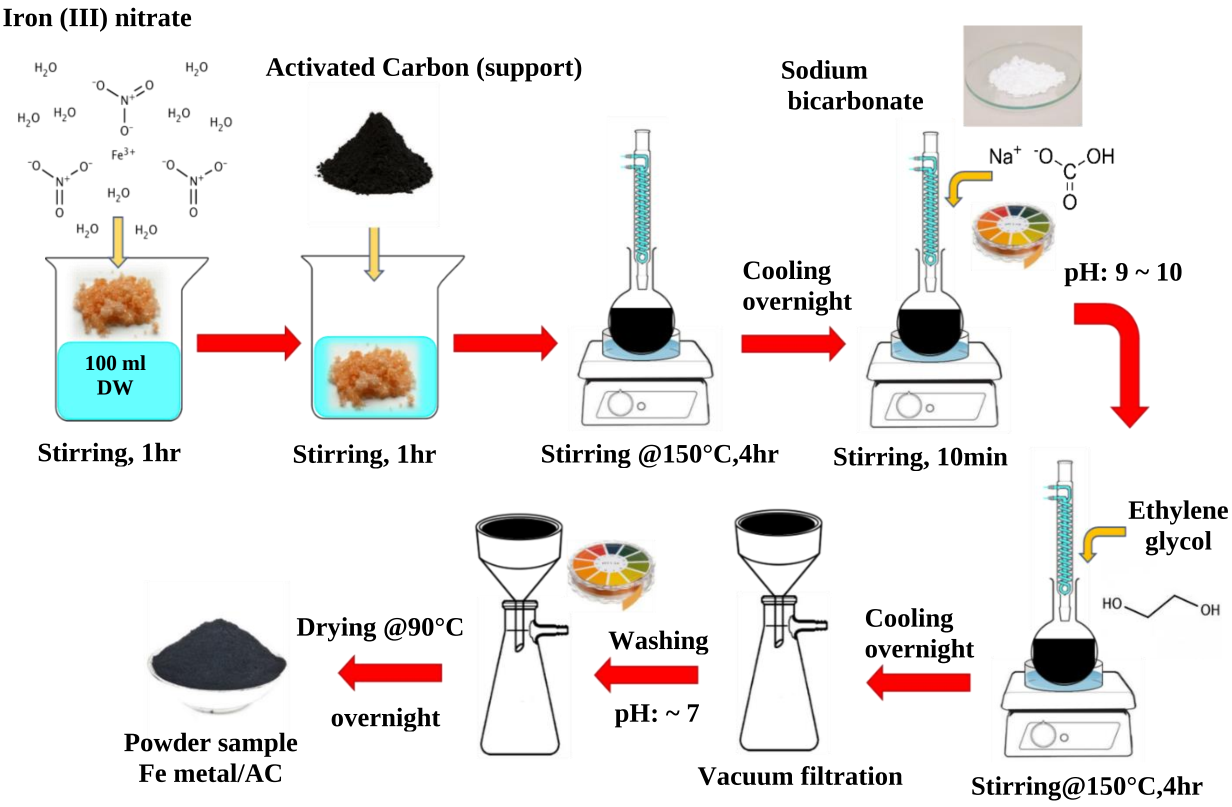

Figure 3.2 Schematic preparation of Fe/AC catalysts by an impregnation method. DW= deionised water.

3.2.2 Preparation of Iron Carbide (Fe_3C) Catalyst

The carbothermal reduction of a 30 wt.% Fe-impregnated activated carbon sample was conducted in a quartz (silica) tubular reactor placed in a furnace and heated under mixture of CO, H_2, and N_2 with concentrations of 60%, 30%, and 10% respectively. 5 grams of the sample was packed in a quartz boat in the middle of the quartz (silica) tubular reactor (4 cm inner and 4.5 cm outer diameter and 90 cm in length), which was heated by a tubular furnace (**Figure 3.3**). The experiment was performed at atmospheric pressure, and the temperature was increased at a rate of 5 °C/min to 320 °C and kept at 320 °C for 24 h. After that, the furnace was turned off and the samples were cooled to ambient temperature under the purging gas flow.

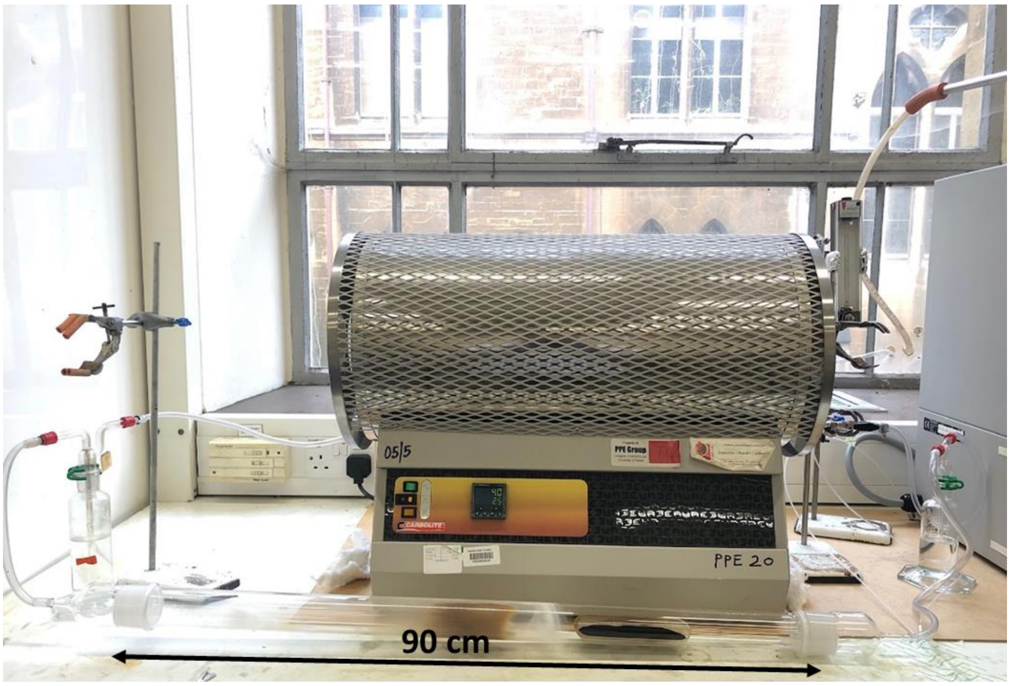

Figure 3.3 Experimental apparatus for carbothermal reduction experiment.

As stated earlier in this chapter, hexadecane (99%, Sigma-Aldrich), cyclohexane (99+% Sigma-Aldrich), and a mixture of 10 wt.% benzene (≥ 99%, Sigma-Aldrich), 60 wt.% toluene (99.8%, Sigma-Aldrich), and 30 wt.% *p*-xylene (99%, Sigma-Aldrich) (BTX), were selected and investigated for microwave-initiated deep dehydrogenation process.

3.2.3 Characterisation of Catalysts

Different characterisation techniques including XRD, TGA, SEM, and TEM were used for the prepared catalysts before and after microwave-initiated deep dehydrogenation experiments, in order to study the effect of different Fe loadings, the influence of number of experiments cycles on the metallic iron particles and the amount of carbon deposition on the spent catalyst surface.

3.3 Result and Discussions

3.3.1 Microwave-initiated Catalytic Deep-Dehydrogenation of Hydrocarbon Model Compounds

Hexadecane, as a hydrocarbon model compound, has been extensively studied in the Edwards group toward producing hydrogen via microwave-initiated catalytic dehydrogenation [115, 116, 118, 121, 122]. The following series of experiments were carried out in order to optimise the yield of H_2 via microwave-initiated catalytic deep dehydrogenation of model compounds using Fe catalysts under variable conditions.

Three experiments were conducted for the optimal system to ensure the reproducibility and the accuracy of the results. (Appendix A).

3.3.1.1 Effect of Different Fe Catalyst Loading

In this study, the decomposition of hexadecane was investigated in a fixed-bed reactor at 1000 W for 10 minutes microwave irradiation to explore the effect of the paraffinic feedstock on the H_2 yield under different (increasing) Fe loadings (0, 5, 10, 20, 30, 40, and 50 wt. %) on an AC support. In the fixed-bed system the hexadecane mixed with the catalyst in (1:1) weight ratio. The effect of the Fe content of the catalyst on hexadecane conversion, hydrogen yield, and hydrogen selectivity are presented in **Figure 3.4**.

Based on gas chromatography/mass spectrometry (GC/MS) analysis, the conversion of hexadecane; and the H_2 selectivity and yield were calculated by applying the following equations:

$$H_2\ \text{Yield}\ (\%) = \frac{\text{volume of } H_2 \text{ in gas products (experimental)}}{\text{calculated total volume of } H_2 \text{ in feedstock (theoretical)}}\ \text{X}\ 100 \qquad \textbf{Equation 3.5}$$

$$\text{Conversion}\ (\%) = \frac{\text{hydrocarbon (in)} - \text{hydrocarbon (out)}}{\text{hydrocarbon (in)}}\ \text{X}\ 100 \qquad \textbf{Equation 3.6}$$

$$H_2\ \text{Selectivity (vol.\%)} = \frac{\text{volume of } H_2 \text{ in gas products}}{\text{volume of gas products}}\ \text{X}\ 100 \qquad \textbf{Equation 3.7}$$

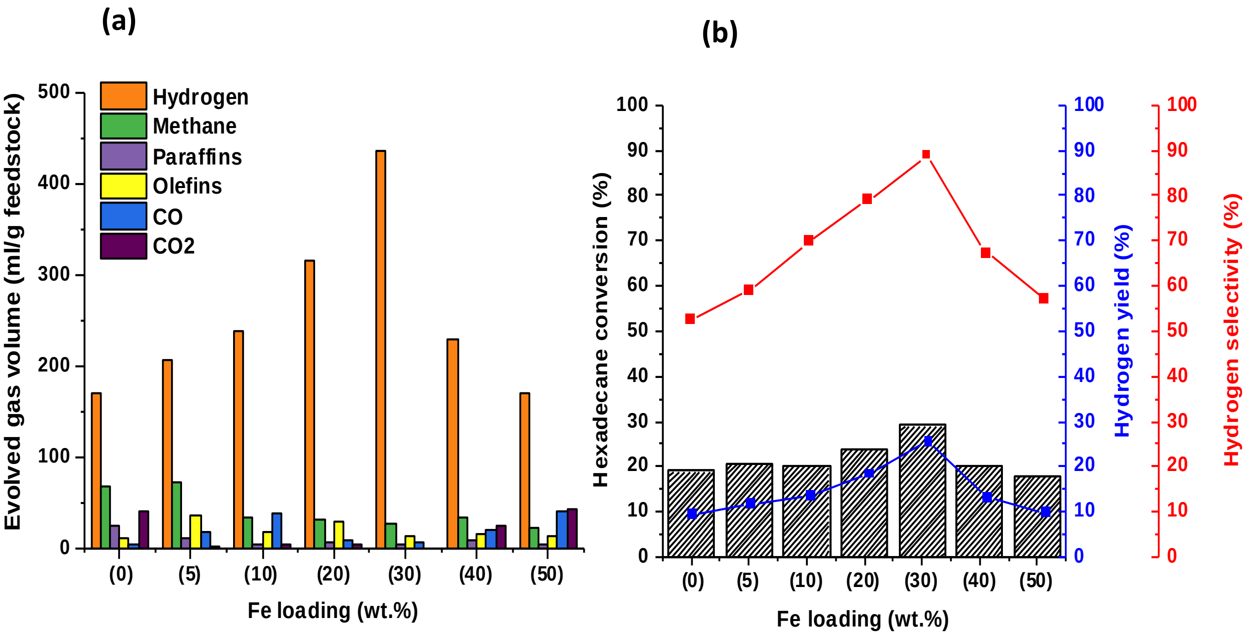

Figure 3.4 Microwave-initiated dehydrogenation of 0.5 g hexadecane mixed with 0.5 g of Fe/AC catalysts at different Fe loadings, (a) the total evolved gas volume, and (b) hexadecane conversion, hydrogen yield and selectivity at a microwave input power of 1000 W for 10 min.

It can be seen from **Figure 3.4b** that using the catalyst with an Fe loading of 30 wt. % at a microwave power of 1000 W for 10 minutes irradiation resulted in a conversion of hexadecane of about 30 % with a H_2 yield and selectivity of 26 and 89 vol. % respectively. This was the optimal system. The conversion decreased to 18.5 % when the loading of Fe increased to 40 and 50 wt. % with the H_2 yield and selectivity also reduced to 10 % and 58 % respectively (for the 50 wt. % Fe loading). Moreover, low levels of light hydrocarbons (methane, olefins and paraffins) and CO_x gases were observed as shown in **Table B1** (Appendix B). These reached their lowest value for the 30 wt.% Fe catalysts.

The higher Fe loading (i.e., 40 and 50 wt.%) showed a remarkable diminution in H_2 yield and selectivity, with increases in CO_x and light hydrocarbon gases. The excess of metal may lead to blockage of catalyst active sites (i.e., low Fe dispersion) and thus a decrease in the catalytic activity.

3.3.1.2 Effect of Variable Microwave Input Power at an Fe loading of 30 wt.% on AC

As seen from the experiments on the various loadings of Fe, the highest conversion of hexadecane was around 30 %, with the H_2 yield and selectivity around 26 % and 89 % respectively were obtained with the Fe loading of 30 wt.% on activated carbon at a microwave input power of 1000 W for 10 minutes irradiation. Therefore, in order to optimise the conversion of hexadecane and the yield and selectivity of the H_2, a series of experiments were carried out using an Fe loading 30 wt. % on AC at variable microwave input powers (500, 750, 1000, and 1250 W). (**Figure 3.5**).

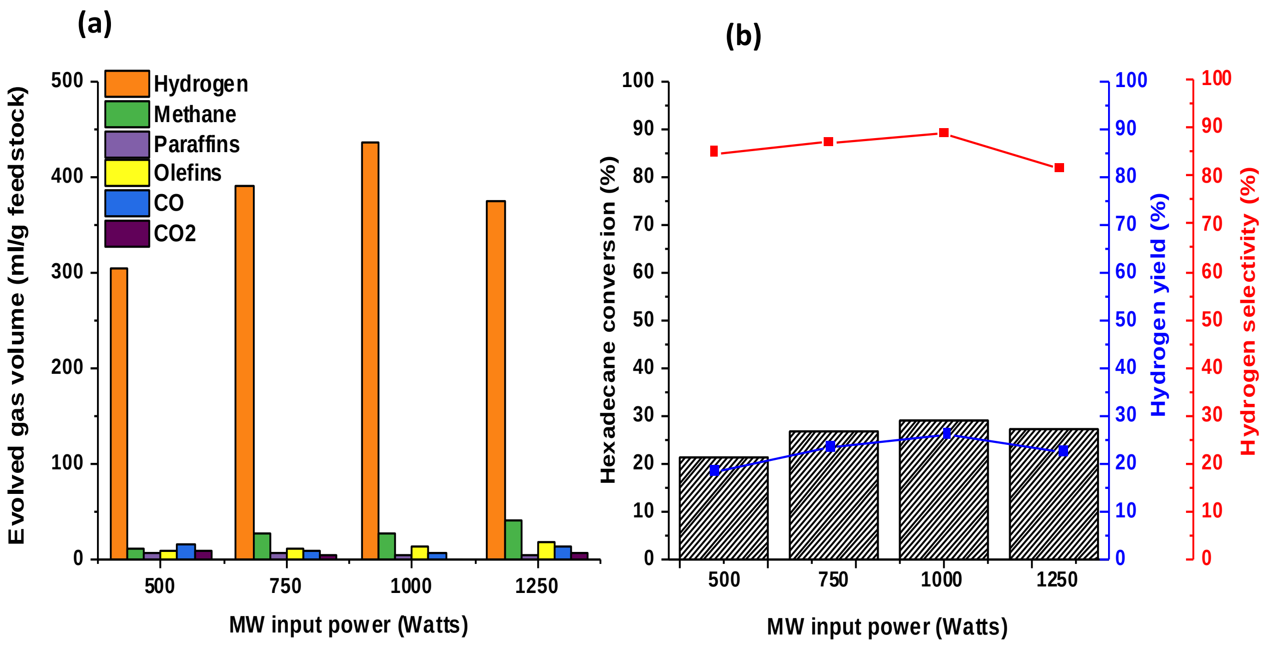

Figure 3.5 Microwave-initiated dehydrogenation of 0.5 g hexadecane mixed with 0.5 g of 30 wt.% Fe/AC catalyst at different microwave input power (a) the total evolved gas volume, and (b) hexadecane conversion, hydrogen yield and selectivity for 10 min.

It can be seen from the results shown in **Figure 3.5b** that the conversion of hexadecane at a microwave power of 500 W for 10 minutes irradiation reached to about 21 % with the H_2 yield and selectivity at about 18 % and 85 % respectively. At a higher microwave input power of 750 W for 10 minutes irradiation, the conversion of hexadecane rose up to 26.7 % with the H_2 yield and selectivity 23 % and 87 % respectively. While at 1000 W, the conversion was slightly increased from 26.7 % to about 30 % with the H_2 yield and selectivity around 26 % and 89 % respectively. But, at a higher microwave power of 1250 W for 10 minutes irradiation the activity of the catalyst was decreased with the conversion of hexadecane slightly decreased to 27.3 % with the H_2 yield and selectivity around 22 % and 82 % respectively.

The decrease in the conversion of hexadecane was accompanied by the decrease in yield and selectivity of H_2 at the higher microwave power than 1000 W and can be attributed to the rise in heating rate as it could increase the temperature of the catalyst layer in the reactor. The higher temperature could cause a formation of carbon on the surface and in the pores of the supported catalyst, blocking the catalyst active sites, which leads to decreasing in conversion of hexadecane with decreasing in the yield and selectivity of H_2.

Based on the results from the effect of Fe/AC catalysts at different Fe loadings and the effect of variable microwave input power, the best catalytic activity for deep dehydrogenation and the optimum conditions for higher percentage conversion of hexadecane with an accompanying high yield and selectivity of H_2 centred on using a Fe loading at 30 wt.% on AC at microwave power 1000 W for 10 minutes irradiation.

Moreover, small amounts of undesirable light hydrocarbons (methane, olefins and paraffins), CO and, interestingly, nearly zero CO_2 gases were observed as shown in **Table B2** (Appendix B).

It can be seen from the **Figure 3.5** and **Table B2** (Appendix B) that the amounts of each of methane, CO and CO_2 increase at the higher microwave input power (1250 W). This phenomenon may be attributed to H_2-involving secondary reactions such as carbon hydrogenation:

$$\mathrm{C} + 2\mathrm{H_2} \rightarrow \mathrm{CH_4}$$ **Equation 3.8**

And the reverse water-gas shift reaction:

$$\mathrm{CO_2} + \mathrm{H_2} \leftrightarrow \mathrm{CO} + \mathrm{H_2O}$$ **Equation 3.9**

3.3.1.3 Effect of Several Catalytic Cycles in an attempt to increase the production of hydrogen

As seen from the various loading of Fe and microwave power irradiation that the highest conversion of hexadecane was about 29 % with the H_2 yield and selectivity about 26 % and 89 % respectively, were obtained with the Fe loading 30 wt.% at microwave power 1000 W for 10 minutes irradiation. In order to investigate the catalytic activity and possible production of higher amounts of H_2 under the same conditions, several catalytic cycles were carried out with successive additions of fresh hexadecane to the test sample.

Figure 3.6 shows the result of several catalytic cycles through successive addition of fresh feedstock to the sample. Through successive cycles of the catalytic reaction from cycle 1 to cycle 5, the conversion of hexadecane gradually decreased from 29 % to 6 % with the gradually decreasing of H_2 yield from about 26 % to 3 % and selectivity from about 89 % to 51 %.

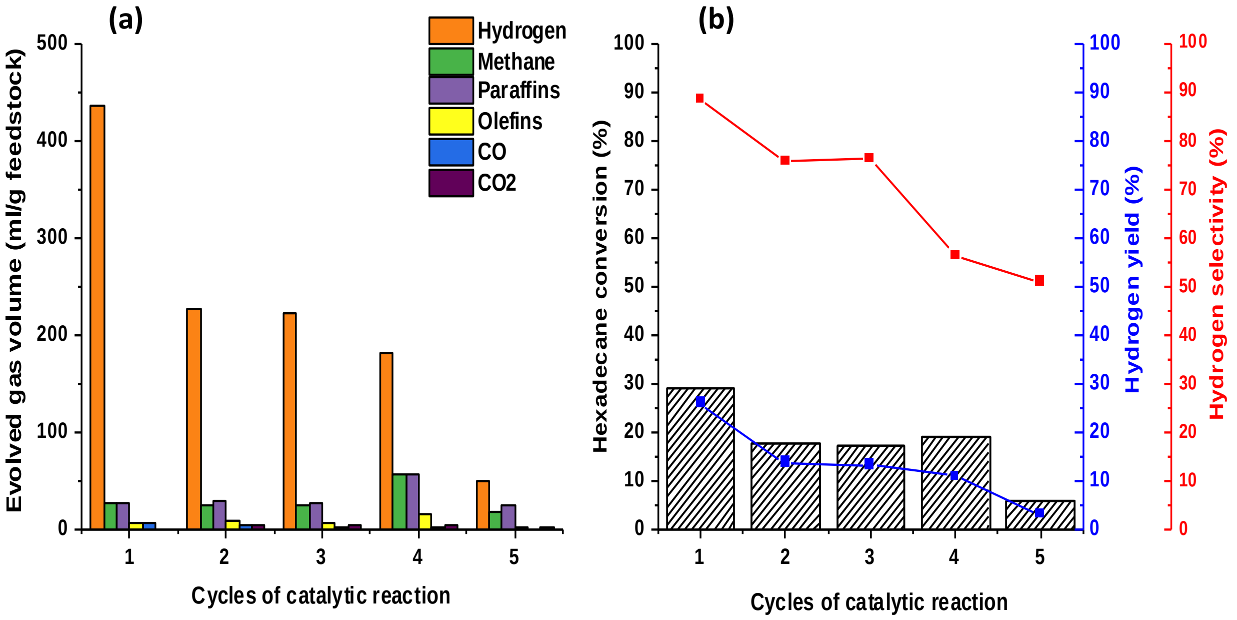

Figure 3.6 Microwave-initiated dehydrogenation of a recharging catalytic cycle for a 0.5 g hexadecane mixed with 0.5 g of 30 wt.% Fe/AC, (a) the total evolved gas volume, and (b) hexadecane conversion, hydrogen yield and selectivity at a microwave input power of 1000 W for 10 min.

It can also be seen that small amounts of CO_x were formed, and the methane and paraffin (light alkanes) concentrations also gradually increased as a consequence of the carbon deposition on the metal catalyst active sites as shown in **Table B3** (Appendix B). Importantly, although less H_2 was produced in the fifth cycle, nevertheless, the catalyst remained active through the second, third and fourth cycles, and this behaviour leads to speculation whether the iron carbides formed can act as active sites for this reaction. Importantly, Fe-free activated carbon is also able to produce H_2 under similar conditions; hence the residual carbon generated upon each cycle of reaction could also assist in the H_2 production reaction or even in the side reactions that produce light hydrocarbons. This will be discussed in the section on X-ray diffraction (XRD) analysis of the spent catalysts.

3.3.1.4 Study of the Activity of Iron Carbide (Fe_3C) Catalyst on Hydrogen Production

In order to study the activity of Fe_3C supported on AC catalyst on hydrogen production, following the observation in the section above, the Fe_3C catalyst was prepared independently (according to **Section 3.2.2**) and tested for microwave-initiated dehydrogenation of hexadecane at a microwave input power 1000 W for 10 minutes irradiation. **Figure 3.7** shows the comparison of the evolved gas composition and the catalytic activity of 30 wt. % Fe/AC and 30 wt. % Fe_3C /AC catalysts. The supported Fe_3C and Fe catalysts showed a fairly similar composition for the dehydrogenation products with a H_2 selectivity of nearly 90 % and relatively small amounts of methane, paraffins, olefins, CO and CO_2 produced as shown in **Table B4** (Appendix B).

The carbide catalyst gave a H_2 yield around 25 %, similar to that produced by the 30 wt. % Fe/AC. Importantly, a supported iron carbide catalyst is widely known to be the active catalytic species for Fischer–Tropsch synthesis and plays a crucial role in the subsequent C–C chain growth reactions [123, 124]. On the other hand, the deep dehydrogenation reaction entails the selective cleavage of C-H bonds to produce atomic carbon and hydrogen. These data encouraged further investigations of carbide-based catalysts in the dehydrogenation reaction.

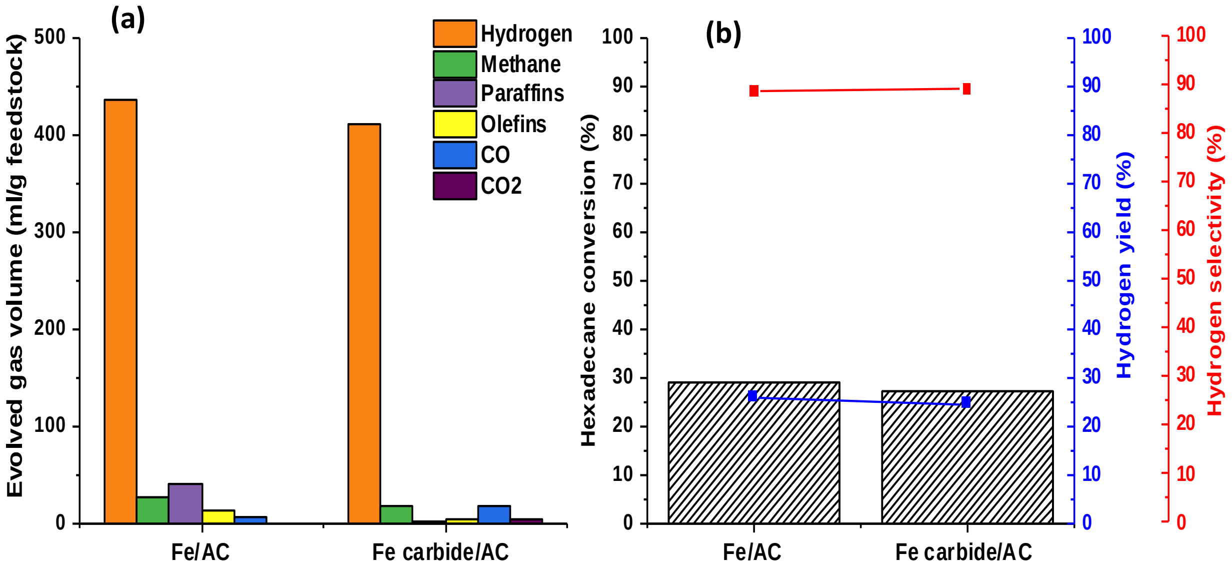

Figure 3.7 A comparison of microwave-initiated dehydrogenation for a 0.5 g hexadecane mixed with 0.5 g of both 30 wt.% Fe/AC and 30 wt.% iron carbide catalysts, (a) Evolved gas volume and (b) hexadecane conversion, hydrogen yield and selectivity at a microwave input power of 1000 W for 10 min.

3.3.1.5 Effect of Naphthenic and Aromatic compounds on Hydrogen Production

According to the above-described experimental results (**Figure 3.4** and **Figure 3.5**), the 30 wt.% Fe/AC catalyst at 1000 W input power gave the best results for microwave-initiated catalytic dehydrogenation reaction of hexadecane. Using these same conditions, cyclohexane and BTX (benzene, toluene, and xylene) as model compounds were individually tested to explore the effect of the naphthenic and aromatic feedstocks on the production of H_2 operating over the Fe catalyst. **Figure 3.8** shows a comparison of the evolved gas composition for these different feedstocks. There are decreases in both yield and selectivity for H_2 in the case of cyclohexane and BTX in comparison with hexadecane under the same conditions, as a consequence of the intrinsic molecular composition of the feedstocks and their chemical reactivity. This partially reflects the greater C-H bond strength in the cyclic compounds and in particular in the aromatics compared to the paraffins. Another factor is the stability of the carbonium ion on radical formed by the heterolytic (or homolytic) cleavage of the C-H bond. This influences the rate toward the cleavage of C-H bonds.

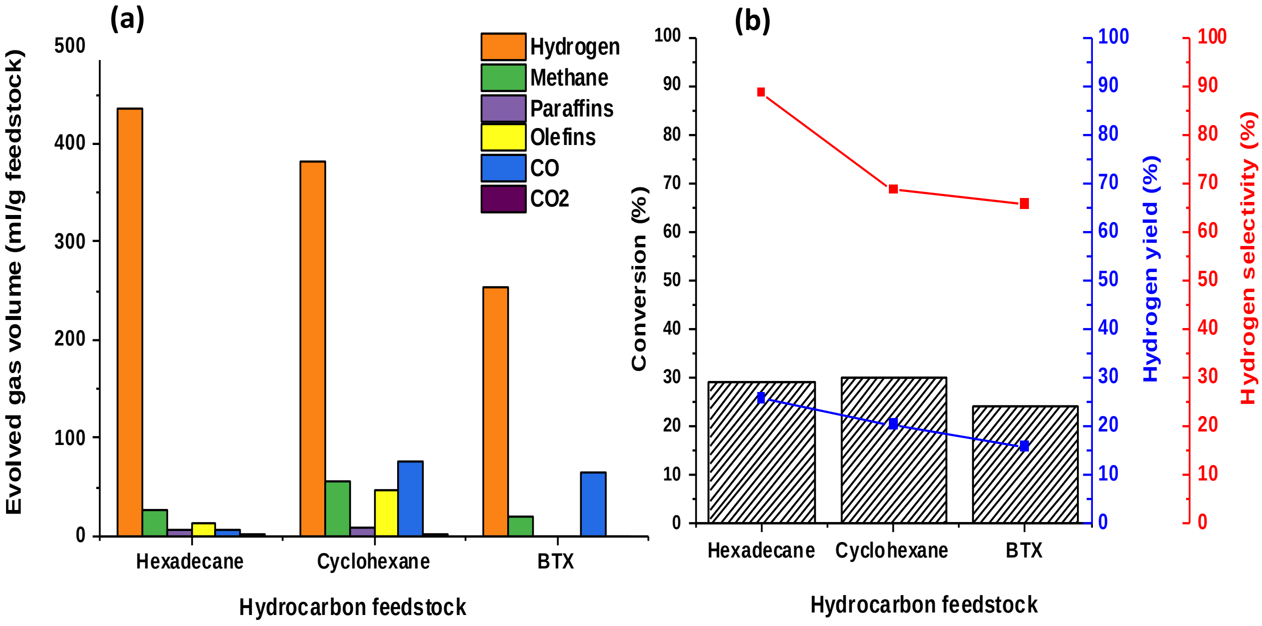

Figure 3.8 Microwave-initiated dehydrogenation of a 0.5 g hexadecane, 0.5 g cyclohexane, and 0.5 g BTX mixed independently with 0.5 g of 30 wt.% Fe/AC catalyst (a) Evolved gas volume and (b) Feedstock conversion, hydrogen yield and selectivity at a microwave input power of 1000 W for 10 min.

It can also be seen from **Figure 3.8a** that small amounts of methane, paraffins, olefins and CO were formed from those model compounds as shown in **Table B5** (Appendix B).

In fact, according to the stoichiometry of the reaction of hydrogen and carbon production, n-hexadecane can produce 17 H_2-mol/ $C_{16}H_{34}$-mol (**Equation 3.10**), followed by cyclohexane (6 H_2-mol/ C_6H_{12}-mol) (**Equation 3.11**), and to a lesser extent xylene (5 H_2-mol/ C_8H_{10}-mol) (**Equation 3.12**). Note that this trend follows the total volume of evolved gases (i.e., hexadecane > cyclohexane > BTX) in agreement with the concentration of H_2 (or the saturation degree of carbon). It is important to highlight that at similar molar composition hexadecane would produce nearly 2.8 times more H_2 than cyclohexane, but at similar weight composition (i.e., 50 wt. %) this ratio would be smaller, in agreement with the data given **Table B5** (Appendix B), owing to the different molecular weights of these molecules.

The enthalpies of the three model compounds were calculated as follows,

$C_{16}\,H_{34} + 48\,Fe\ \rightarrow 16\,Fe_3C + 17H_2$

$\Delta H^{\circ}_{298K} = +\ 783.97$ kJ mol^{-1*} **Equation 3.10**

$C_6\,H_{12} + 18\,Fe\ \rightarrow 6\,Fe_3C + 6H_2$

$\Delta H^{\circ}_{298K} = +\ 282$ kJ mol^{-1*} **Equation 3.11**

$C_6H_6 +\ C_7H_8 +\ o - C_8H_{10} +\ p - C_8H_{10} +\ m - C_8H_{10} + 111Fe\ \rightarrow 37F_3C + 22H_2$

$\Delta H^{\circ}_{298K} = +\ 790.2$ kJ mol^{-1*} **Equation 3.12**

*Details of the enthalpy calculations is shown in Appendix D

In addition, paraffins have linear chains of carbon atoms, but only weak van der Waals forces hold the molecules together, and the aromaticity in BTX increases the stability of molecule because of low hydrogen to carbon ratio and high resonance energy of the delocalised π electrons (note that the H:C ratio in an alkane is >2). For the aromatic compounds, the structural formulas contain a large number of double bonds [125]. According to the literature, the C-H bond dissociation for benzene is ca. 477 kJ/mol whilst lineal hydrocarbons show C-H bond dissociation about 404-440 kJ/mol, which are significantly lower than that for benzene. Therefore, the relatively high C-H bond energies dissociation can also contribute to the lower generation of H_2 from feedstock with a high content of aromatics.

3.3.1.6 Effect of Mixtures of Model Hydrocarbon Compounds on Hydrogen Production using a 30 wt.% Fe/AC Catalyst

As described earlier in this chapter, crude oils are classified as: paraffin base, naphthene base, and aromatic base. Paraffinic crude oils are rich in straight-chain and branched paraffin hydrocarbons, whereas naphthenic crude oils contain mainly naphthenic and aromatic hydrocarbons. In order to study the effect of the chemical composition of crude oil on the ability to produce H_2 from hydrocarbon feedstocks, the chosen model hydrocarbon compounds (hexadecane, cyclohexane, and BTX) were the mixtures were as follows: (75 wt.% hexadecane + 25 wt.% cyclohexane), (55 wt.% hexadecane + 45 wt.% BTX), (70 wt.% BTX + 30 wt.% cyclohexane), and lastly (46 wt.% hexadecane+17 wt.% cyclohexane+37 wt.% BTX) as a "synthetic" crude oil to mimic light crude oil (LCO) used in this thesis which will be analysed extensively in chapter 4.

Figure 3.9 shows the evolved gas volume and the catalytic activity of various hydrocarbon feedstocks. It is noted that the paraffinic base mixture can evolve more hydrogen than naphthene/aromatic base mixture, and the presence of cyclic compounds may inhibit H_2 production. This finding is entirely consistent with the lower intrinsic content of hydrogen in cyclic compounds and, additionally, most likely their low chemical reactivity, particularly for BTX molecules, due to the high stability of aromatic compounds [126]. **Table B6** (Appendix B) shows the evolved gases composition of the different mixtures with 30 wt.% Fe/AC catalyst.

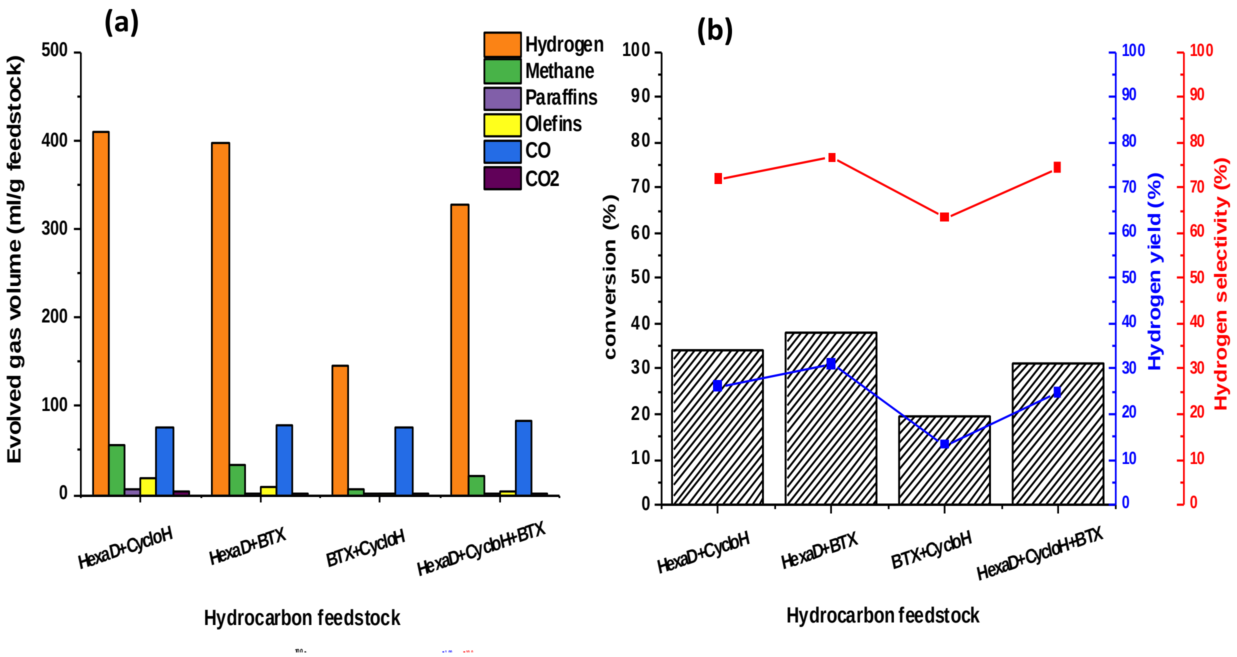

Figure 3.9 Microwave-initiated dehydrogenation of 0.5 g of different feedstock mixture mixed with 0.5 g of 30 wt.% Fe/AC catalyst (a) Evolved gas volume and (b) Feedstock conversion, hydrogen yield and selectivity at a microwave input power of 1000 W for 10 min.

Gas chromatography - mass spectrometer (GC-MS) (**Figure 3.10)** confirmed that all liquid collected after the microwave-initiated dehydrogenation reactions was unreacted hydrocarbon. Thus, the hydrocarbons feedstocks conversions, hydrogen selectivity and yields evaluated in this study are calculated by applying Equations **3.5, 3.6, and 3.7**.

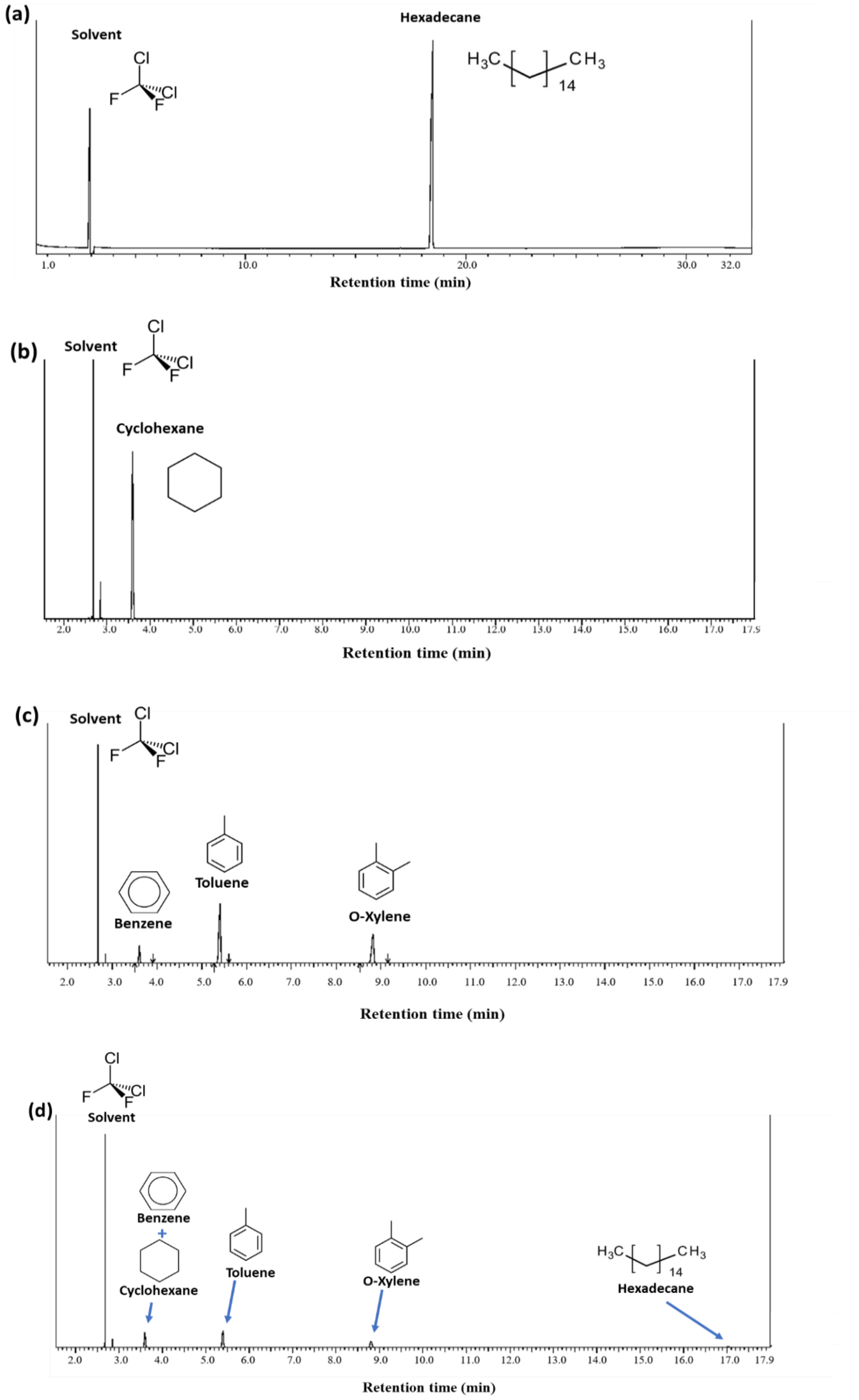

Figure 3.10 Typical gas chromatography-mass spectrometry (GC/MS) chromatograms for unconverted liquid after microwave-initiated dehydrogenation of (a) hexadecane, (b) cyclohexane, (c) BTX, and (d) hydrocarbons mixture.

3.3.2 Characterisation of Fresh and Spent Fe/AC Catalysts

In order to explore the change in the catalyst structure and understanding the entire process, the catalyst samples were analysed by X-ray diffraction (XRD), scanning electron microscopy (SEM), transmission electron microscopy (TEM), and temperature programmed oxidation (TPO), both before and after microwave experiments.

3.3.2.1 X-ray Diffraction of fresh and spent Fe/AC Catalysts with Different Fe loading

The XRD patterns for the Fe/AC catalysts before microwave-initiated catalytic dehydrogenation of hexadecane are displayed in **Figure 3.11a**. Two broad peaks for activated carbon are observed, an intense peak centred at ~ 25° and a less prominent peak at ~ 13° on the 2θ scale. These weak peaks suggest the presence of typical amorphous carbon, with a negligible content of ordered crystalline phase. Furthermore, several researchers have reported that activated carbon (AC) is an amorphous material [127-129]. In the range of the broad peak of AC, there are two peaks (i.e., at 27.7° and 29°) which are clearly observed on the fresh AC pattern (0) and attributed to the impurities in the AC. To confirm this, a certain amount of AC was heated in a muffle furnace at 600 °C , the remaining material was analysed by XRD (**Figure 3.11c**), which represent nearly 4.46 wt. % according to TGA analysis, and this percentage of impurities content is in agreement with the typical ash content (4.7 wt. %) provided from Sigma-Aldrich [130] . It is not clear what these residues are, but they could potentially contribute as oxygen sources for the formation of carbon monoxide.

The diffraction peaks for Fe metal at 46.42°, 67.6° and 85.6° were also detected, the peak intensity of metallic iron increased as expected when the Fe loading increased from 5 to 50 wt. %. Importantly, the partial formation of iron carbide (Fe_3C) was also confirmed in the fresh samples with peaks at 45.57° and 53°, and this was due to high temperature (750 °C) used in the reduction process during the catalyst preparation. Importantly, no diffraction peaks attributable to iron oxide were observed in the fresh Fe/AC catalyst series indicating the successful reduction of the catalyst.

The XRD pattern for the spent catalysts (**Figure 3.11b**) showed iron carbide as the main crystalline phase with also the presence of iron metal, which becomes evident with stronger peaks at high Fe loading (i.e., 50 wt.%). Interestingly, the catalysts with high Fe loadings (≥20 wt. %) show a very strong XRD peak at 25.79° in 2θ scale associated to partially ordered graphite structure likely due to the large content of Fe and high local temperatures generated by microwaves. To confirm this, a sample of pure graphite (powder, Sigma-Aldrich) was analysed by XRD, and its peak was detected at 25.82° in 2θ (**Figure 3.11c**). (All measurements used Cu K_α radiation).

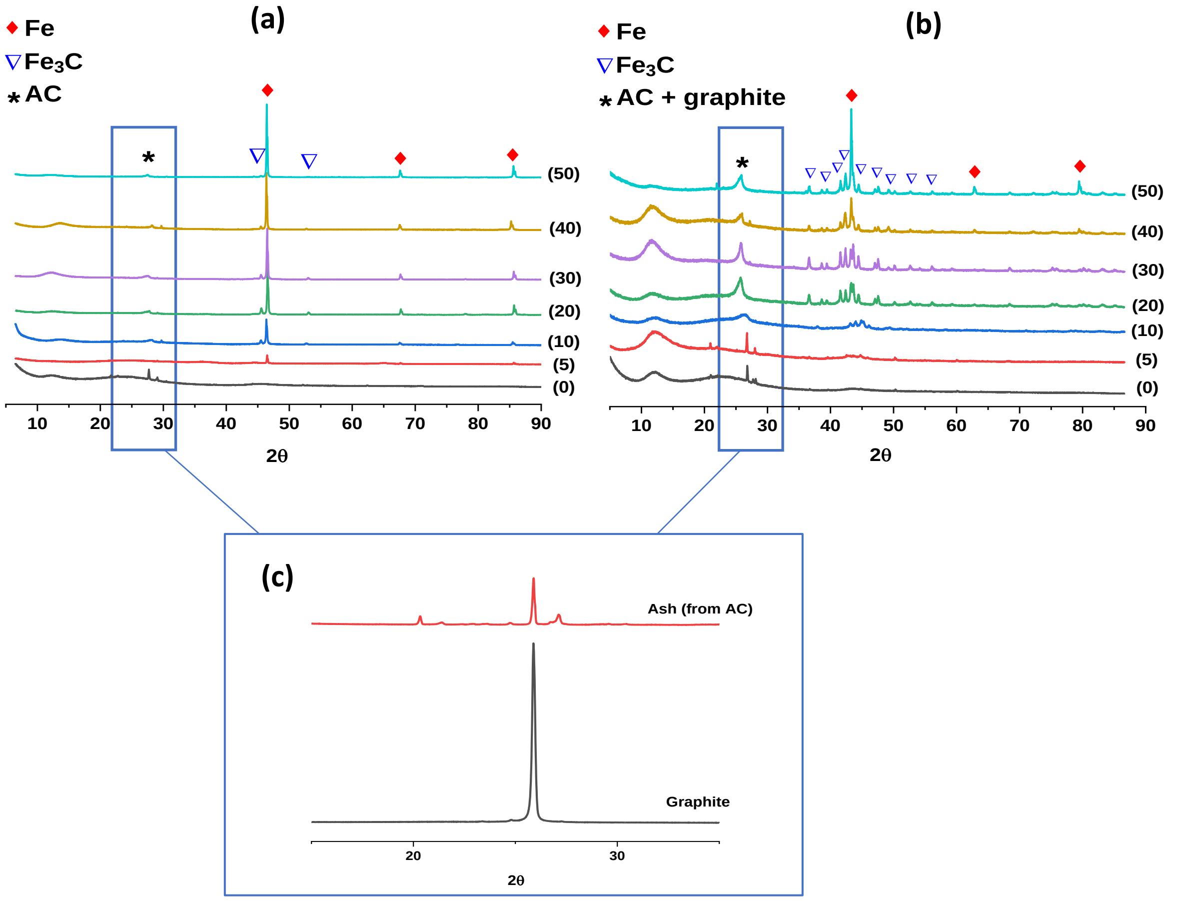

Figure 3.11 X-ray diffraction patterns of Fe/AC catalysts with different Fe loading (a) before, (b) after the microwave-initiated catalytic dehydrogenation of hexadecane, and (c) X-ray diffraction patterns of ash and graphite. Numbers in parentheses correspond to the Fe loading, in wt.

3.3.2.2 Scanning electron microscopy (SEM) of fresh and spent Fe/AC catalysts with different Fe loading

Scanning electron microscopy (SEM) of Fe/AC catalysts with different Fe loading was used to obtain high-resolution imaging and analysis of sub-micron features in the powder materials. **Figure 3.12** below illustrates the surface morphology of the samples before (fresh) and after (spent) the microwave experiments. The SEM images for the fresh samples shows that there is no clear sign of crystallinity for the typical amorphous carbon but there is clear evidence of an increase in iron crystallite size with increases in loading. There was no clear difference between samples before and after the microwave irradiation in terms of carbon deposited on the Fe-rich regions, except for the obvious changes on the surface that can be seen in image (S10) of the formation of some carbon filaments as the initial phase of the formation of carbon nanotubes. The absence of clear evidence of carbon filaments in the catalysts with large Fe content is probably to the incorporation of carbon into the Fe structure to produce iron carbide (Fe_3C) and also the formation of graphite as determined by XRD analysis.

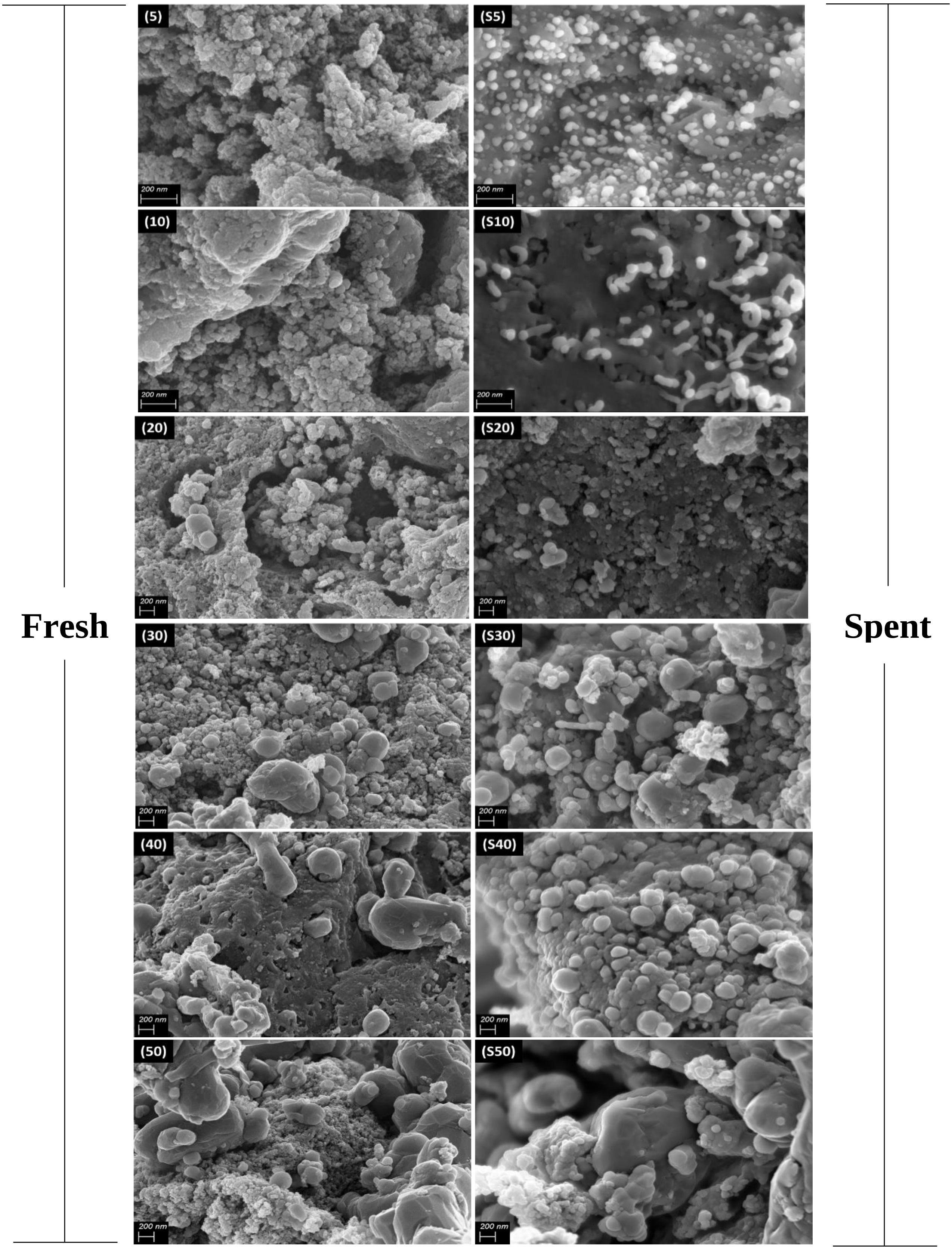

Figure 3.12 The scanning electron microscopy (SEM) images of Fe/AC catalysts with different Fe loading before and after the microwave-initiated catalytic dehydrogenation of hexadecane. Numbers in parentheses correspond to the Fe loading, in wt.%.

3.3.2.3 Pre- and Post- reaction Analysis of Fresh and Spent 30 wt.% Fe/AC Catalysts through Several Catalytic Cycles

The XRD pattern in **Figure 3.13a** show clearly that the amount of crystalline metallic iron decreased after the microwave reaction and the formation of iron carbides and graphite through several catalytic cycles can be clearly observed. The spent catalyst obtained after the second cycle showed the total transformation of iron into iron carbide. However, hydrogen was still the major product in the subsequent cycles (**Figure 3.6**), implicating that iron carbide is also catalytically active for the deep dehydrogenation of hexadecane. In order to identify the type of carbon formed in the spent sample after 5 cycles of the catalytic deep dehydrogenation, different type of carbons have been analysed by Temperature-programmed oxidation (TPO) (**Figure 3.13b**) including: activated carbon, multi-wall carbon nanotubes (MWCNTs), graphite, and carbon nanofiber. The TPO analysis showed the overlap between AC and MWCNTs peaks around 620 °C, and supported the proposal of the formation of MWCNTs on the Fe/AC spent catalyst with the peak around 570 °C. The peak observed at lower temperature, and the shift in temperature indicated the low-purity (content) or low crystallinity of MWCNTs. Moreover, a secondary peak at ca. 160 °C was also observed and this was ascribed to the unreacted hydrocarbon present in the spent sample. SEM and TEM images for cycle 5 spent sample in **Figure 3.13c,d** confirm clearly the formation of a substantial amount of filamentous carbon that encapsulate both iron and iron carbide nanoparticles. The generation of iron carbide suggested that the supported iron particles react with the hydrocarbon during the catalytic reactions under microwave initiation.

A schematic representation of the main results obtained in this chapter is given in **Figure 3.14**, which clearly illustrates the tremendous impact that the composition of the feedstock has over the hydrogen yield and also the evolution of the resulting nano-carbon material with the number of cycles to produce initially Fe_3C and graphite and then carbon nanotubes. It also highlights the evolution of the gas composition with the number of cycles and, remarkably, how the Fe/AC catalyst is still able to produce hydrogen after several operation cycles through the presence of Fe_3C even when there is no elemental Fe remaining.

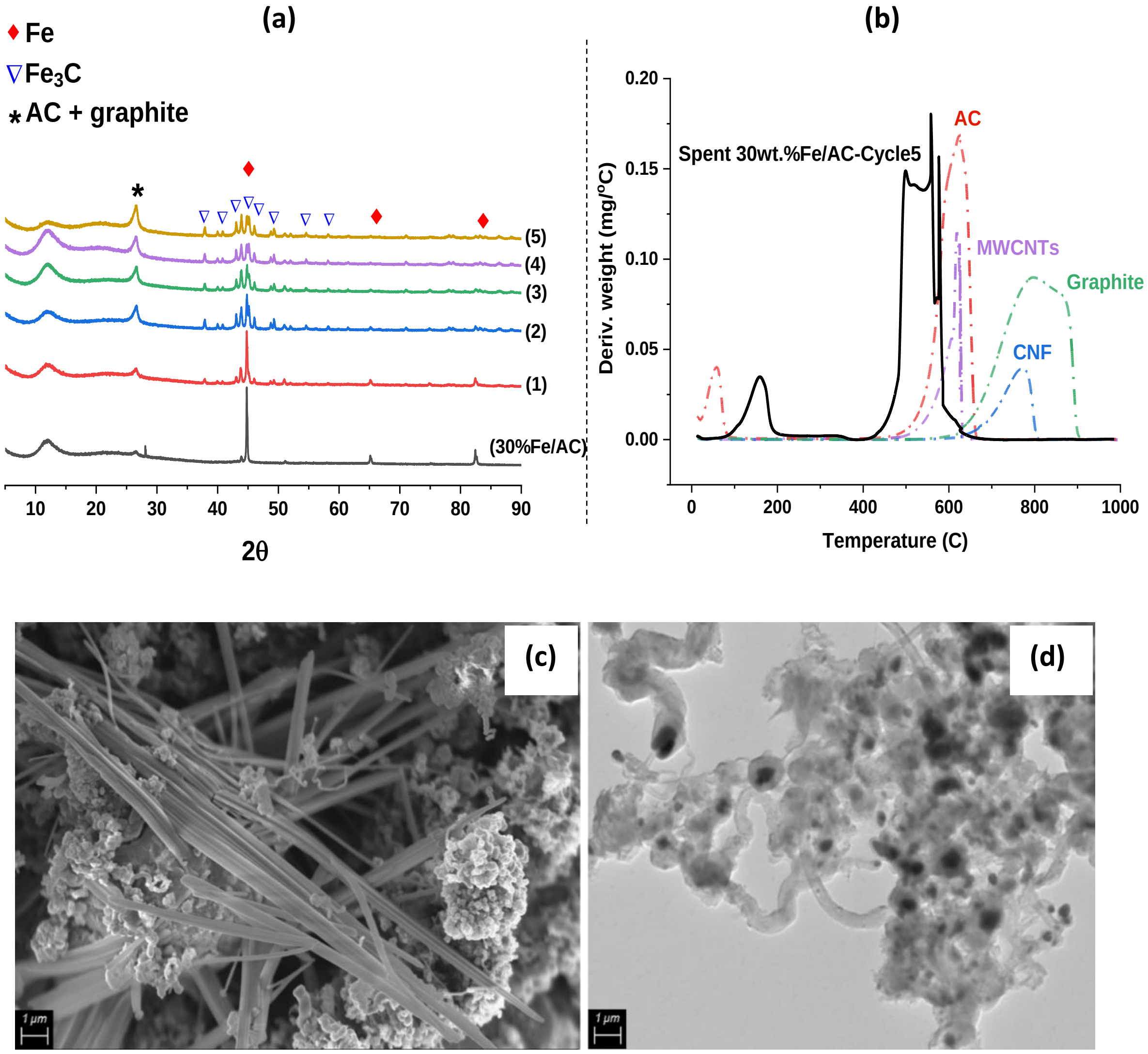

Figure 3.13 Representative of a recharging catalytic cycle for a 0.5 g hexadecane mixed with 0.5 g of 30 wt.% Fe/AC experiments. (a) X-ray diffraction patterns of 30% Fe/AC (fresh sample) and spent catalysts after microwave-initiated dehydrogenation of hexadecane for several catalytic cycles. (b) derivative plots of TPO of representative spent cycle5 sample compared with different carbon samples: activated carbon, multi-wall carbon nanotubes, graphite, and carbon nanofiber. (c) SEM image for spent cycle 5 sample. (d) TEM image for spent cycle5 sample.

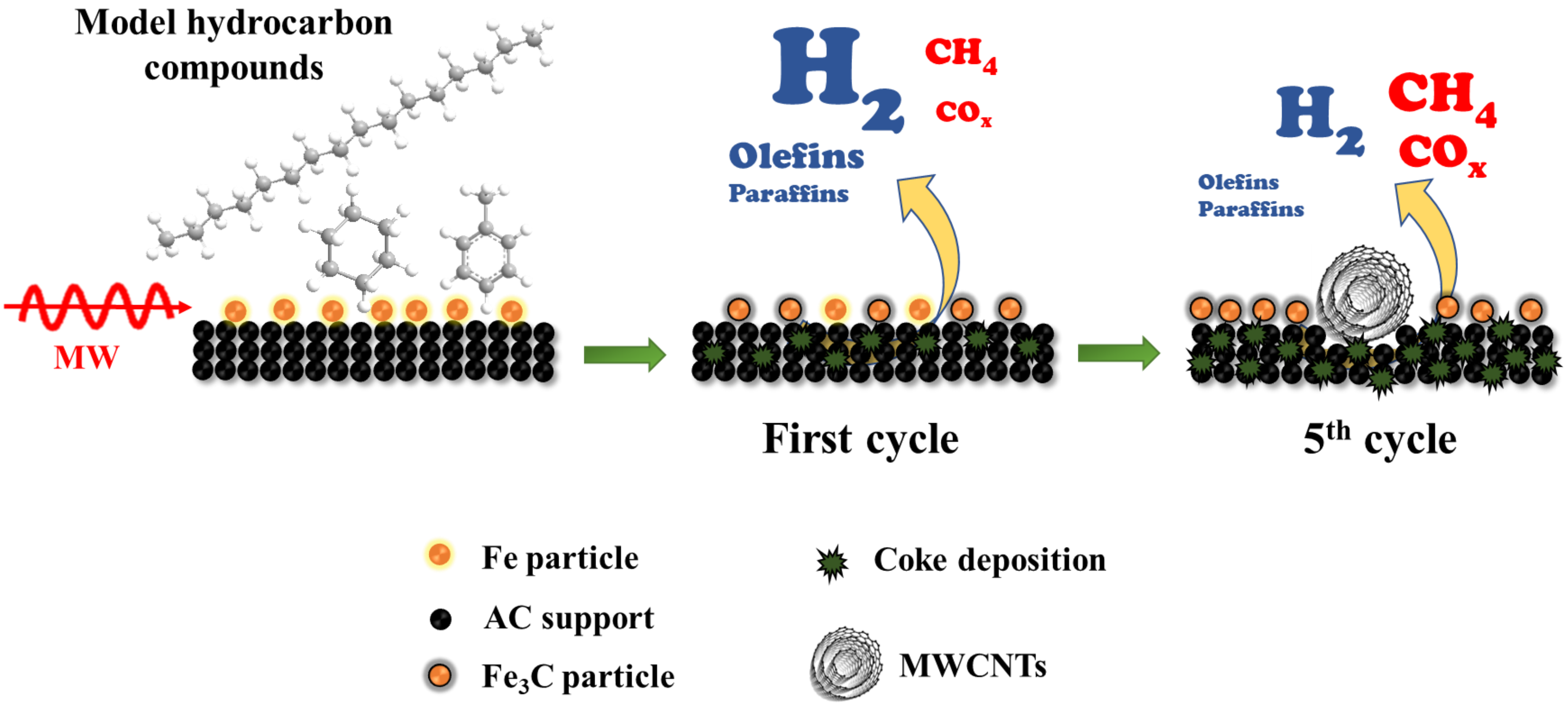

Figure 3.14 A representative diagram of hydrogen production, carbon deposition and transformation through microwave-initiated liquid hydrocarbons dehydrogenation over Fe/AC catalysts.

3.4 Conclusions*

These catalytic activity studies showed the feasibility of direct hydrogen production from different hydrocarbon feedstocks through microwave-initiated catalytic deep dehydrogenation using iron catalysts supported on activated carbon. Importantly, it also highlights this approach as a facile route to the ready production of significant amounts of carbon multiwalled nanotubes.

The Fe/AC catalyst with a loading of 30 wt. % of iron and 1000 W input power were the most effective combination/conditions to produce high yield and selectivity for hydrogen from hexadecane (~ 90 %). Hydrogen was the dominant gas product and there was very little CO_2 emission. The spent catalysts clearly showed the formation of iron carbide by XRD, and the results also show that this can act as active sites for this reaction. The carbide catalyst (Fe_3C) also showed high activity for the dehydrogenation reaction with high hydrogen selectivity with relatively low amounts of undesirable products. These data encouraged further investigations of carbide-based catalysts.

The Fe/AC catalysts can also effectively catalyse the dehydrogenation of hexadecane under microwave irradiation for several cycles. The eventual deactivation of the catalysts was attributed to carbon deposition. Moreover, it has been found that MWCNTs can be produced in the later cycles and cause deactivation of the catalysts.

The data showed that the paraffinic feedstock (i.e., hexadecane) was relatively better for producing hydrogen among other hydrocarbons, and the presence of cyclic hydrocarbons, particularly aromatics, may inhibit the hydrogen production.

*This chapter is prepared for publication at the 5th International Conference on Science & Technology Applications in Climate Change (STACLIM 2022), which will be held virtually on 29-30 November 2022, Institute of Climate Change, Malaysia. STACLIM 2022 (ukm.my)

References

[1] R. Robinson, The Origins of Petroleum, Nature, 212 (1966) 1291-1295.

[2] C.C. Walters, The Origin of Petroleum, in: C.S. Hsu, P.R. Robinson (Eds.) Practical Advances in Petroleum Processing, Springer, (2006), 79-101.

[3] H. Devold, Oil and Gas Production Handbook - An Introduction to Oil and Gas Production, (2007).

[4] C. Walters, Origin of Petroleum, (2017), 359-379.

[5] A. Basile, S. Liguori, A. Iulianelli, 2 - Membrane Reactors for Methane Steam Reforming (MSR), in: A. Basile, L. Di Paola, F.l. Hai, V. Piemonte (Eds.) Membrane Reactors for Energy Applications and Basic Chemical Production, Woodhead Pub. (2015), 31-59.

[6] L. Chen, Z. Qi, S. Zhang, J. Su, G.A. Somorjai, Catalytic Hydrogen Production from Methane: A Review on Recent Progress and Prospect, Catalysts, 10 (2020) 858.

[7] G. Collodi, F. Wheeler, Hydrogen Production via Steam Reforming with CO_2 Capture, Chemical engineering Transactions, 19 (2010) 37-42.

[8] H. Zhang, Z. Sun, Y.H. Hu, Steam Reforming of Methane: Current States of Catalyst Design and Process Upgrading, Renewable and Sustainable Energy Reviews, 149 (2021) 111330.

[9] T. Younus, A. Anwer, Z. Asim, M.S. Surahio, Production of Hydrogen by Steam Methane Reformation Process, 3rd International Conference on Advances on Clean Energy Research, 51 (2018) 03003.

[10] M. Younas, S. Shafique, A. Hafeez, F. Javed, F. Rehman, An Overview of Hydrogen Production: Current Status, Potential, and Challenges, Fuel, 316 (2022) 123317.

[11] R. Carapellucci, L. Giordano, Steam, Dry and Autothermal Methane Reforming for Hydrogen Production: A Thermodynamic Equilibrium Analysis, Journal of Power Sources, 469 (2020) 228391.

[12] M. Steinberg, H.C. Cheng, Modern and Prospective Technologies for Hydrogen Production from Fossil Fuels, International Journal of Hydrogen Energy, 14 (1989) 797-820.

[13] F. Ausfelder, A. Bazzanella, Chapter2: Hydrogen in the Chemical Industry, in: D. Stolten, B. Emonts (Eds.), Hydrogen Science and Engineering: Materials, Processes, System and Technology, Wiley, (2016).

[14] L. García, Hydrogen Production by Steam Reforming of Natural Gas and other Nonrenewable Feedstocks, in: V. Subramani, A. Basile, T. Veziroglu (Eds.), Compendium of Hydrogen Energy, (2015), 83-107.

[15] M. Hermesmann, T.E. Müller, Green, Turquoise, Blue, or Grey? Environmentally Friendly Hydrogen Production in Transforming Energy Systems, Progress in Energy and Combustion Science, 90 (2022) 100996.

[16] L. Zhou, J.M.P. Martirez, J. Finzel, C. Zhang, D.F. Swearer, S. Tian, H. Robatjazi, M. Lou, L. Dong, L. Henderson, P. Christopher, E.A. Carter, P. Nordlander, N.J. Halas, Light-Driven Methane Dry Reforming with Single Atomic Site Antenna-Reactor Plasmonic Photocatalysts, Nature Energy, 5 (2020) 61-70.

[17] Y. Tang, Y. Wei, Z. Wang, S. Zhang, Y. Li, L. Nguyen, Y. Li, Y. Zhou, W. Shen, F.F. Tao, P. Hu, Synergy of Single-Atom Ni1 and Ru1 Sites on CeO_2 for Dry Reforming of CH_4, Journal of the American Chemical Society, 141 (2019) 7283-7293.

[18] G. Jones, J.G. Jakobsen, S.S. Shim, J. Kleis, M.P. Andersson, J. Rossmeisl, F. Abild-Pedersen, T. Bligaard, S. Helveg, B. Hinnemann, J.R. Rostrup-Nielsen, I. Chorkendorff, J. Sehested, J.K. Nørskov, First Principles Calculations and Experimental Insight into Methane Steam Reforming Over Transition Metal Catalysts, Journal of Catalysis, 259 (2008) 147-160.

[19] S.A. Theofanidis, V.V. Galvita, H. Poelman, G.B. Marin, Enhanced Carbon-Resistant Dry Reforming Fe-Ni Catalyst: Role of Fe, ACS Catalysis, 5 (2015) 3028-3039.

[20] S. Abelló, E. Bolshak, D. Montané, Ni–Fe Catalysts Derived from Hydrotalcite-Like Precursors for Hydrogen Production By Ethanol Steam Reforming, Applied Catalysis A: General, 450 (2013) 261-274.

[21] L. Profeti, E. Ticianelli, E. Assaf, Co/Al_2O_3 Catalysts Promoted with Noble Metals for Production of Hydrogen By Methane Steam Reforming, Fuel, 87 (2008) 2076-2081.

[22] E. Meloni, M. Martino, V. Palma, A Short Review on Ni Based Catalysts and Related Engineering Issues for Methane Steam Reforming, Catalysts, 10 (2020) 352.

[23] H. Wu, V. La Parola, G. Pantaleo, F. Puleo, A.M. Venezia, L.F. Liotta, Ni-Based Catalysts for Low Temperature Methane Steam Reforming: Recent Results on Ni-Au and Comparison with Other Bi-Metallic Systems, Catalysts, 3 (2013) 563-583.

[24] C. Tanios, M. Labaki, Chapter 5 - Catalytic Reforming: A Sustainable Technology for Hydrogen Production, in: M. Jeguirim (Ed.) Recent Advances in Renewable Energy Technologies, Academic Press, (2022), 199-247.

[25] D. Pakhare, J. Spivey, A review of dry (CO_2) reforming of methane over noble metal catalysts, Chemical Society Reviews, 43 (2014) 7813-7837.

[26] J.-M. Lavoie, Review on Dry Reforming of Methane, A Potentially More Environmentally-Friendly Approach To The Increasing Natural Gas Exploitation, Frontiers in Chemistry, 2 (2014).

[27] J.H. Edwards, A.M. Maitra, The Chemistry of Methane Reforming with Carbon Dioxide and Its Current and Potential Applications, Fuel Processing Technology, 42 (1995) 269-289.

[28] B. Christian Enger, R. Lødeng, A. Holmen, A Review of Catalytic Partial Oxidation of Methane to Synthesis Gas with Emphasis on Reaction Mechanisms over Transition Metal Catalysts, Applied Catalysis A: General, 346 (2008) 1-27.

[29] V.R. Choudhary, K.C. Mondal, T.V. Choudhary, Partial Oxidation of Methane to Syngas with or Without Simultaneous Steam or CO_2 Reforming Over A High-Temperature Stable-$NiCoMgCeO_x$ Supported On Zirconia–Hafnia Catalyst, Applied Catalysis A: General, 306 (2006) 45-50.

[30] S. Rice, D. Mann, Autothermal Reforming of Natural Gas to Synthesis Gas, Sandia Report, (2007).

[31] J. Gao, Z. Hou, X. Liu, Y. Zeng, M. Luo, X. Zheng, Methane Autothermal Reforming with CO_2 and O_2 To Synthesis Gas at the Boundary Between Ni and ZrO_2, International Journal of Hydrogen Energy, 34 (2009) 3734-3742.

[32] S.D. Angeli, L. Turchetti, G. Monteleone, A.A. Lemonidou, Catalyst Development for Steam Reforming of Methane and Model Biogas at Low Temperature, Applied Catalysis B: Environmental, 181 (2016) 34-46.

[33] M.A. Nieva, M.M. Villaverde, A. Monzón, T.F. Garetto, A.J. Marchi, Steam-Methane Reforming at Low Temperature on Nickel-Based Catalysts, Chemical Engineering Journal, 235 (2014) 158-166.

[34] K. Jabbour, Tuning Combined Steam and Dry Reforming of Methane For “Metgas” Production: A Thermodynamic Approach and State-Of-The-Art Catalysts, Journal of Energy Chemistry, 48 (2020) 54-91.

[35] Y. Lim, C.-J. Lee, Y.S. Jeong, I.H. Song, C.J. Lee, C. Han, Optimal Design and Decision for Combined Steam Reforming Process with Dry Methane Reforming to Reuse CO_2 as a Raw Material, Industrial & Engineering Chemistry Research, 51 (2012) 4982-4989.

[36] K. Zhao, F. He, Z. Huang, G. Wei, A. Zheng, H. Li, Z. Zhao, Perovskite-Type Oxides $LaFe_{1-x}Co_xO_3$ for Chemical Looping Steam Methane Reforming to Syngas and Hydrogen Co-Production, Applied Energy, 168 (2016) 193-203.

[37] L. Barelli, G. Bidini, F. Gallorini, S. Servili, Hydrogen Production Through Sorption-Enhanced Steam Methane Reforming and Membrane Technology: A Review, Energy, 33 (2008) 554-570.

[38] N. Chanburanasiri, A.M. Ribeiro, A.E. Rodrigues, A. Arpornwichanop, N. Laosiripojana, P. Praserthdam, S. Assabumrungrat, Hydrogen Production via Sorption Enhanced Steam Methane Reforming Process Using Ni/CaO Multifunctional Catalyst, Industrial & Engineering Chemistry Research, 50 (2011) 13662-13671.

[39] T. Papalas, A.N. Antzaras, A.A. Lemonidou, Intensified Steam Methane Reforming Coupled with Ca-Ni Looping in A Dual Fluidized Bed Reactor System: A Conceptual Design, Chemical Engineering Journal, 382 (2020) 122993.

[40] J.R. Fernández, J.C. Abanades, R. Murillo, G. Grasa, Conceptual Design of A Hydrogen Production Process From Natural Gas With CO_2 Capture Using A Ca–Cu Chemical Loop, International Journal of Greenhouse Gas Control, 6 (2012) 126-141.

[41] J. Zhang, X. Li, H. Chen, M. Qi, G. Zhang, H. Hu, X. Ma, Hydrogen Production by Catalytic Methane Decomposition: Carbon Materials as Catalysts or Catalyst Supports, International Journal of Hydrogen Energy, 42 (2017) 19755-19775.

[42] A. Amin, W. Epling, E. Croiset, Reaction and Deactivation Rates of Methane Catalytic Cracking over Nickel, Industrial & Engineering Chemistry Research, 50 (2011) 12460-12470.

[43] Y. Li, D. Li, G. Wang, Methane Decomposition to COx-free Hydrogen and Nano-carbon Material on Group 8–10 Base Metal Catalysts: A review, Catalysis Today, 162 (2011) 1-48.

[44] J.X. Qian, T.W. Chen, L.R. Enakonda, D.B. Liu, G. Mignani, J.-M. Basset, L. Zhou, Methane Decomposition to Produce CO_x-Free Hydrogen and Nano-Carbon Over Metal Catalysts: A Review, International Journal of Hydrogen Energy, 45 (2020) 7981-8001.

[45] A.L. Dipu, Methane Decomposition into CO_x-free Hydrogen over a Ni-based Catalyst: An Overview, International Journal of Energy Research, 45 (2021) 9858-9877.

[46] H. Abbas, W. Daud, Hydrogen Production by Methane Decomposition: A Review, International Journal of Hydrogen Energy, 35 (2010) 1160-1190.

[47] Z. Fan, W. Weng, J. Zhou, D. Gu, W. Xiao, Catalytic Decomposition of Methane to Produce Hydrogen: A review, Journal of Energy Chemistry, 58 (2021) 415-430.

[48] A.J. de Abreu, A.F. Lucrédio, E.M. Assaf, Ni Catalyst on Mixed Support of CeO_2–ZrO_2 and Al_2O_3: Effect of Composition of CeO_2–ZrO_2 Solid Solution on the Methane Steam Reforming Reaction, Fuel Processing Technology, 102 (2012) 140-145.

[49] M. Dan, M. Mihet, A.R. Biris, P. Marginean, V. Almasan, G. Borodi, F. Watanabe, A.S. Biris, M.D. Lazar, Supported Nickel Catalysts for Low Temperature Methane Steam Reforming: Comparison Between Metal Additives and Support Modification, Reaction Kinetics, Mechanisms and Catalysis, 105 (2012) 173-193.

[50] X. You, X. Wang, Y. Ma, J. Liu, W. Liu, X. Xu, H. Peng, C. Li, W. Zhou, P. Yuan, X. Chen, Ni–Co/Al_2O_3 Bimetallic Catalysts for CH_4 Steam Reforming: Elucidating the Role of Co for Improving Coke Resistance, ChemCatChem, 6 (2014) 3377-3386.

[51] X. Yang, J. Da, H. Yu, H. Wang, Characterization and Performance Evaluation of Ni-based Catalysts with Ce Promoter for Methane and Hydrocarbons Steam Reforming Process, Fuel, 179 (2016) 353-361.

[52] J. Gonçalves, M. Souza, Effect of Doping Niobia over Ni/Al_2O_3 Catalysts for Methane Steam Reforming, Catalysis Letters, 148 (2018) 1478-1489.

[53] S. Miura, Y. Umemura, Y. Shiratori, T. Kitaoka, In Situ Synthesis of Ni/MgO Catalysts on Inorganic Paper-Like Matrix for Methane Steam Reforming, Chemical Engineering Journal, 229 (2013) 515-521.

[54] A.E. Awadallah, M.A. Deyab, H.A. Ahmed, Mo/MgO as an Efficient Catalyst for Methane Decomposition into CO_x-free Hydrogen and Multi-Walled Carbon Nanotubes, Journal of Environmental Chemical Engineering, 9 (2021) 106023.

[55] X. Guo, Y. Sun, Y. Yu, X. Zhu, C.-j. Liu, Carbon Formation and Steam Reforming of Methane on Silica Supported Nickel Catalysts, Catalysis Communications, 19 (2012) 61-65.

[56] L. Alalga, A. Benamar, M. Trari, Hydrogen Production via Methane Decomposition over Nickel Supported on Synthesized ZSM-5/MCM-41 Zeolite Composite Material, International Journal of Hydrogen Energy, 46 (2021) 28501-28512.

[57] B. Bej, N.C. Pradhan, S. Neogi, Production of Hydrogen by Steam Reforming of Methane Over Alumina Supported Nano-NiO/SiO_2 Catalyst, Catalysis Today, 207 (2013) 28-35.

[58] S. Ali, M.J. Al-Marri, A.G. Abdelmoneim, A. Kumar, M.M. Khader, Catalytic Evaluation Of Nickel Nanoparticles In Methane Steam Reforming, International Journal of Hydrogen Energy, 41 (2016) 22876-22885.

[59] V.K. Jaiswar, S. Katheria, G. Deo, D. Kunzru, Effect of Pt Doping on Activity and Stability of Ni/$MgAl_2O_4$ Catalyst for Steam Reforming of Methane at Ambient and High Pressure Condition, International Journal of Hydrogen Energy, 42 (2017) 18968-18976.

[60] A.S. Al-Fatesh, A.H. Fakeeha, W.U. Khan, A.A. Ibrahim, S. He, K. Seshan, Production of Hydrogen by Catalytic Methane Decomposition over Alumina Supported Mono-, Bi- and Tri-metallic Catalysts, International Journal of Hydrogen Energy, 41 (2016) 22932-22940.

[61] V. Ramasubramanian, H. Ramsurn, G.L. Price, Hydrogen Production by Catalytic Decomposition of Methane Over Fe Based Bi-Metallic Catalysts Supported on CeO_2–ZrO_2, International Journal of Hydrogen Energy, 45 (2020) 12026-12036.

[62] J.L. Rogers, M.C. Mangarella, A.D. D'Amico, J.R. Gallagher, M.R. Dutzer, E. Stavitski, J.T. Miller, C. Sievers, Differences in the Nature of Active Sites for Methane Dry Reforming and Methane Steam Reforming over Nickel Aluminate Catalysts, ACS Catalysis, 6 (2016) 5873-5886.

[63] U. Amjad, G. Gonçalves Lenzi, N.R. Camargo Fernandes-Machado, S. Specchia, MgO and Nb_2O_5 Oxides Used as Supports for Ru-Based Catalysts for the Methane Steam Reforming Reaction, Catalysis Today, 257 (2015) 122-130.

[64] J. Yu, Z. Zhang, F. Dallmann, J. Zhang, D. Miao, H. Xu, A. Goldbach, R. Dittmeyer, Facile Synthesis of Highly Active Rh/Al_2O_3 Steam Reforming Catalysts with Preformed Support by Flame Spray Pyrolysis, Applied Catalysis B: Environmental, 198 (2016) 171-179.

[65] D. Mei, V. Glezakou, V. Lebarbier, L. Kovarik, H. Wan, K.O. Albrecht, M. Gerber, R. Rousseau, R.A. Dagle, Highly Active and Stable $MgAl_2O_4$-supported Rh and Ir Catalysts for Methane Steam Reforming: A Combined Experimental and Theoretical Study, Journal of Catalysis, 316 (2014) 11-23.

[66] R.J. Giguere, T.L. Bray, S.M. Duncan, G. Majetich, Application of Commercial Microwave Ovens to Organic Synthesis, Tetrahedron Letters, 27 (1986) 4945-4948.

[67] H. Will, P. Scholz, B. Ondruschka, Heterogeneous Gas-Phase Catalysis Under Microwave Irradiation—a New Multi-Mode Microwave Applicator, Topics in Catalysis, 29 (2004) 175-182.

[68] J.R.J. Pare, Survey of Recent Industrial Applications of Microwave Energy Applications, The Journal of Microwave Power and Electromagnetic Energy: A Publication of the International Microwave Power Institute, 42 (2008) 24-44.

[69] J. Belanger, J.R.J. Pare, O. Poon, C. Fairbridge, S. Ng, S. Mutyala, R. Hawkins, Remarks on Various Applications of Microwave Energy, The Journal of Microwave Power and Electromagnetic Energy: A Publication of the International Microwave Power Institute, 42 (2008) 24-44.

[70] S. Alexandru Marius, U. Rohde, About Some Applications of Microwave Energy, Journal of Electrical and Electronics Engineering, 2 (2009).

[71] C. Kappe, Controlled Microwave Heating in Modern Organic Synthesis, Angew Chem Int Ed Engl, 43 (2004) 6250-6284.

[72] M. Nüchter, B. Ondruschka, W. Bonrath, A. Gum, Microwave Assisted Synthesis – A Critical Technology Overview, Green Chemistry, 6 (2004) 128-141.

[73] Z.Q. Tian, S.P. Jiang, Y.M. Liang, P.K. Shen, Synthesis and Characterization of Platinum Catalysts on Multiwalled Carbon Nanotubes by Intermittent Microwave Irradiation for Fuel Cell Applications, The Journal of Physical Chemistry B, 110 (2006) 5343-5350.

[74] R. Varma, Microwave Technology—Chemical Synthesis Applications, In Kirk-Othmer Encyclopedia of Chemical Technology, (Ed.), (2003)

[75] A. Grewal, K. Kumar, S. Redhu, S. Bhardwaj, Microwave Assisted Synthesis: A Green Chemistry Approach, International Research Journal of Pharmaceutical and Applied Sciences, 3 (2013) 278-285.

[76] H. Nguyen, J. Sunarso, C. Li, G. Pham, C. Phan, S. Liu, Microwave-Assisted Catalytic Methane Reforming: A review, Applied Catalysis A: General, 599 (2020) 117620.

[77] X. Zhang, C.S.M. Lee, D.M.P. Mingos, D.O. Hayward, Carbon Dioxide Reforming of Methane with Pt Catalysts Using Microwave Dielectric Heating, Catalysis Letters, 88 (2003) 129-139.

[78] N.A.K. Aramouni, J.G. Touma, B.A. Tarboush, J. Zeaiter, M.N. Ahmad, Catalyst Design for Dry Reforming of Methane: Analysis Review, Renewable and Sustainable Energy Reviews, 82 (2018) 2570-2585.

[79] S. Hamzehlouia, S. Jaffer, J. Chaouki, Microwave Heating-Assisted Catalytic Dry Reforming of Methane to Syngas, Scientific Reports, 8 (2018) 8940.

[80] A. Domínguez, B. Fidalgo, Y. Fernandez Diez, J. Pis, J.A. Menéndez, Microwave-Assisted Catalytic Decomposition of Methane over Activated Carbon for CO_2-free Hydrogen Production, International Journal of Hydrogen Energy, 32 (2007) 4792-4799.

[81] C. Eskilsson, E. Björklund, Analytical-Scale Microwave-Assisted Extraction, Journal of Chromatography A, 902 (2000) 227-250.

[82] M. Lucchesi, F. Chemat, J. Smadja, Solvent-Free Microwave Extraction of Essential Oil from Aromatic Herbs: Comparison with Conventional Hydro-Distillation, J Chromatogr A, 1043 (2004) 323-327.

[83] V. Mandal, Y. Mohan, S. Hemalatha, Microwave Assisted Extraction-An Innovative and Promising Extraction Tool for Medicinal Plant Research, Pharmacognosy Reviews, 1 (2007) 7.

[84] V. Yusa, O. Pardo, A. Pastor, M. Guardia, Optimization of a Microwave-Assisted Extraction Large-Volume Injection and Gas Chromatography–Ion Trap Mass Spectrometry Procedure for The Determination of Polybrominated Diphenyl Ethers, Polybrominated Biphenyls and Polychlorinated Naphthalenes in Sediments, Analytica Chimica Acta, 557 (2006) 304-313.

[85] P. Salagre, Y. Cesteros, Editorial Catalysts: Special Issue on "Microwave-Assisted Catalysis", Catalysts, 10 (2020) 842.

[86] V. Sánchez, A. Dafinov, P. Salagre, J. Llorca, Y. Cesteros, Microwave-Assisted Furfural Production Using Hectorites and Fluorohectorites as Catalysts, Catalysts, 9 (2019) 706.

[87] A.G.R. Howe, R. Maunder, D.J. Morgan, J.K. Edwards, Rapid Microwave-Assisted Polyol Synthesis of TiO2-Supported Ruthenium Catalysts for Levulinic Acid Hydrogenation, Catalysts, 9 (2019) 748.

[88] I. Julian, C.M. Pedersen, K. Achkasov, J.L. Hueso, H.L. Hellstern, H. Silva, R. Mallada, Z.J. Davis, J. Santamaria, Overcoming Stability Problems in Microwave-Assisted Heterogeneous Catalytic Processes Affected by Catalyst Coking, Catalysts, 9 (2019) 867.

[89] R.G. Bosisio, J.L. Cambon, C. Chavarie, D. Klvana, Exprimental Result on the Hesting of Athabasca Tar Sand Samples with Microwave Power, Journal of Microwave Power, 12 (1977) 301-307.

[90] J. Robinson, E. Binner, A. Saeid, M. Al-Harahsheh, S. Kingman, Microwave Processing of Oil Sands and Contribution of Clay Minerals, Fuel, 135 (2014) 153-161.

[91] S. Mutyala, C. Fairbridge, J.R.J. Paré, J.M.R. Bélanger, S. Ng, R. Hawkins, Microwave Applications to Oil Sands and Petroleum: A review, Fuel Processing Technology, 91 (2010) 127-135.

[92] N. Wolf, Use of Microwave Radiation in Separating Emulsions and Dispersions of Hydrocarbons and Water, US Patent, (1986) US 4582629.

[93] N.H. Abdurahman, R.M. Yunus, N.H. Azhari, N. Said, Z. Hassan, The Potential of Microwave Heating in Separating Water-in-Oil (W/O) Emulsions, Energy Procedia, 138 (2017) 1023-1028.

[94] V. Rajaković, D. Skala, Separation of Water-in-Oil Emulsions by Freeze/Thaw Method and Microwave Radiation, Separation and Purification Technology, 49 (2006) 192-196.

[95] L. Kong, S. Zhao, Q. Zhang, P. Li, L. Zhuang, Removing Naphthenic Acids from Diesel Oil by Microwave Irradiation, Petroleum Science and Technology, 24 (2006) 157-166.

[96] M. Huang, S. Zhao, P. Li, D. Huisingh, Removal of Naphthenic Acid by Microwave, Journal of Cleaner Production, 14 (2006) 736-739.

[97] J. Wan, J. Kriz, Hydrodesulphurization of Hydrocracked Pitch, US Patent, (1985) US 4545879.

[98] A. Miadonye, S. Snow, D. Irwin, M. Khan, A. Britten, Desulfurization of Heavy Crude Oil by Microwave Irradiation, Computational Methods in Multiphase Flow, 63 (2009) 455-465.

[99] R. Khan, E. Al-Shafei, Microwave-Promoted Desulfurization of Crude Oil, PCT Patent, (2009), WO 2009/064501.

[100] N. Leadbeater, M. Khan, Microwave-Promoted Desulfurization of Heavy and Sulfur-Containing Crude Oil, Energy & Fuels, 22 (2008) 1836-1839.

[101] G. Elsamak, N. Öztaş, Y. Yürüm, Chemical Desulfurization of Turkish Cayirhan Lignite with HI Using Microwave and Thermal Energy, Fuel, 82 (2003) 531-537.

[102] M. Ceron, D. Guzman-Lucero, J. Palomeque, R. Martínez-Palou, Parallel Microwave-Assisted Synthesis of Ionic Liquids and Screening for Denitrogenation of Straight-Run Diesel Feed by Liquid-Liquid Extraction, Comb Chem High Throughput Screen, 15 (2012) 427-432.

[103] M. Chamorro, C. Romano, Simultaneous Demetallization and Desulphuration of Carbonaceous Materials via Microwaves, US Patent (2000) US 606873.

[104] H. Shang, J. Shi, J. Li, Y.X. Liu, W. Zhang, Reactor Design of Microwave Assisted Demetallization of Heavy Crude Oil, Chemical Engineering Transactions, 39 (2014) 511-516.

[105] S. Wang, J. Yang, X. Xu, J. Gao, Influence of the Microwave Method on Vanadium Removal in Crude Oil, Petroleum Science and Technology, 27 (2009) 368 - 378.

[106] H. Paul T. Fanson, Masaya Ibe, Steven L. Suib, Young Chan Son, Process Using Microwave Energy and A Catalyst to Crack Hydrocarbons, US Patent, (2006) US 2006/0251557.

[107] A. Porch, D. Slocombe, J. Beutler, P. Edwards, A. Aldawsari, T. Xiao, V. Kuznetsov, H. Almegren, S. Aldrees, N. Almuqati, Microwave Treatment in Oil Refining, Applied Petrochemical Research, 2 (2012).

[108] J. Taheri-Shakib, A. Shekarifard, H. Naderi, The Experimental Study of Effect of Microwave Heating Time on The Heavy Oil Properties: Prospects for Heavy Oil Upgrading, Journal of Analytical and Applied Pyrolysis, 128 (2017) 176-186.

[109] M. Adam, H. Anbari, A. Hart, J. Wood, J.P. Robinson, S.P. Rigby, In-situ Microwave-Assisted Catalytic Upgrading of Heavy Oil: Experimental Validation and Effect of Catalyst Pore Structure on Activity, Chemical Engineering Journal, 413 (2021) 127420.

[110] X. Yanyang, Z. Min, A.S. Mujumdar, Z. Le-qun, S. Jin-cai, Studies on Hot Air and Microwave Vacuum Drying of Wild Cabbage, Drying Technology, 22 (2004) 2201-2209.

[111] M. Venkatesh, G. Raghavan, An Overview of Microwave Processing and Dielectric Properties of Agri-food Materials, Biosystems Engineering, 88 (2004) 1-18.

[112] J. Wang, Y.S. Xi, Drying Characteristics and Drying Quality of Carrot Using A Two-Stage Microwave Process, Journal of Food Engineering, 68 (2005) 505-511.

[113] F. Motasemi, M.T. Afzal, A Review on The Microwave-Assisted Pyrolysis Technique, Renewable and Sustainable Energy Reviews, 28 (2013) 317-330.

[114] S. Gonzalez-Cortes, D.R. Slocombe, T. Xiao, A. Aldawsari, B. Yao, V.L. Kuznetsov, E. Liberti, A.I. Kirkland, M.S. Alkinani, H.A. Al-Megren, J.M. Thomas, P.P. Edwards, Wax: A Benign Hydrogen-Storage Material That Rapidly Releases H_2-Rich Gases Through Microwave-Assisted Catalytic Decomposition, Scientific Reports, 6 (2016) 35315.

[115] X. Jie, S. Gonzalez-Cortes, T. Xiao, J. Wang, B. Yao, D.R. Slocombe, H.A. Al-Megren, J.R. Dilworth, J.M. Thomas, P.P. Edwards, Rapid Production of High-Purity Hydrogen Fuel through Microwave-Promoted Deep Catalytic Dehydrogenation of Liquid Alkanes with Abundant Metals, Angewandte Chemie International Edition, 56 (2017) 10170-10173.

[116] X. Jie, T. Xiao, B. Yao, S. Gonzalez-Cortes, J. Wang, Y. Fang, N. Miller, H. AlMegren, J.R. Dilworth, P.P. Edwards, On the Performance Optimisation of Fe Catalysts in the Microwave - Assisted H_2 Production by The Dehydrogenation of Hexadecane, Catalysis Today, 317 (2018) 29-35.

[117] X. Jie, W. Li, D. Slocombe, Y. Gao, I. Banerjee, S. Gonzalez-Cortes, B. Yao, H. AlMegren, S. Alshihri, J. Dilworth, J. Thomas, T. Xiao, P. Edwards, Microwave-Initiated Catalytic Deconstruction of Plastic Waste into Hydrogen and High-Value Carbons, Nature Catalysis, 3 (2020), 902-912.

[118] X. Jie, J. Wang, S. Gonzalez-Cortes, B. Yao, W. Li, Y. Gao, J.R. Dilworth, T. Xiao, P.P. Edwards, Catalytic Activity of Various Carbons during the Microwave-Initiated Deep Dehydrogenation of Hexadecane, JACS Au, 1 (2021), 2021-2032.

[119] E.C. Dillon, J.H. Wilton, J.C. Barlow, W.A. Watson, Large Surface Area Activated Charcoal and the Inhibition of Aspirin Absorption, Annals of Emergency Medicine, 18 (1989), 547-552.

[120] X. Jie, S. Gonzalez-Cortes, T. Xiao, B. Yao, J. Wang, D.R. Slocombe, Y. Fang, N. Miller, H.A. Al-Megren, J.R. Dilworth, J.M. Thomas, P.P. Edwards, The Decarbonisation of Petroleum and Other Fossil Hydrocarbon Fuels for the Facile Production and Safe Storage of Hydrogen, Energy & Environmental Science, 12 (2019), 238-249.

[121] X. Jie, Microwave-initiated catalytic dehydrogenation of fossil fuels for the facile production and safe storage of hydrogen, Ph.D Thesis, University of Oxford, (2020).

[122] X. Jie, R. Chen, T. Biddle, D.R. Slocombe, J.R. Dilworth, T. Xiao, P.P. Edwards, Size-Dependent Microwave Heating and Catalytic Activity of Fine Iron Particles in the Deep Dehydrogenation of Hexadecane, Chemistry of Materials, 34 (2022) 4682-4693.

[123] C. Yang, H. Zhao, Y. Hou, D. Ma, Fe5C2 Nanoparticles: A Facile Bromide-Induced Synthesis and as an Active Phase for Fischer–Tropsch Synthesis, Journal of the American Chemical Society, 134 (2012) 15814-15821.

[124] B. Yao, T. Xiao, O.A. Makgae, X. Jie, S. Gonzalez-Cortes, S. Guan, A.I. Kirkland, J.R. Dilworth, H.A. Al-Megren, S.M. Alshihri, P.J. Dobson, G.P. Owen, J.M. Thomas, P.P. Edwards, Transforming Carbon Dioxide into Jet Fuel Using an Organic Combustion-Synthesized Fe-Mn-K Catalyst, Nature Communications, 11 (2020) 6395.

[125] W. Reusch, Virtual Textbook of Organic Chemistry, Michigan State University, (2014).

[126] R. Morrison, and R. Boyd, Organic Chemistry, Boston: Allyn and Bacon, (1983).

[127] A. Mohamed, M. Mohammadi, G.N. Darzi, Preparation of carbon Molecular Sieve from Lignocellulosic Biomass: A review, Renewable and Sustainable Energy Reviews, 14 (2010) 1591-1599.

[128] A. Ip, J. Barford, G. McKay, Production and Comparison of High Surface Area Bamboo Derived Active Carbons, Bioresource Technology, 99 (2008) 8909-8916.

[129] M. Jung, K. Ahn, Y. Lee, K.-P. Kim, J. Rhee, J. Tae Park, K. Paeng, Adsorption Characteristics of Phenol and Chlorophenols on Granular Activated Carbons (GAC), Microchemical Journal, 70 (2001) 123-131.

[130] Sigma-Aldrich, Activated Charcoal, https://www.sigmaaldrich.com/GB/en/product/sigald/242276

Chapter4

Influence of Metal Catalyst Particle Size and Loading on the Microwave-Initiated Deep-dehydrogenation of Light Crude Oil

The microwave-initiated, catalytic deep-dehydrogenation of fossil hydrocarbons produces predominantly H_2 and solid, elemental carbon, instead of CO_2 as a by-product; remarkably this production process, therefore, does not lead to CO_2 emissions and potential climate change. This chapter shows an application of this approach to the catalytic deep-dehydrogenation of Saudi Arabian light crude oil (LCO) to produce H_2 without significant CO_2 production through microwave-initiated catalysis on a range of different metals supported on activated carbon catalysts. Further optimisation could make the new process potentially competitive with current H_2 production technologies, typically involving the steam reforming of methane, a process which invariably involves the release of significant amounts of CO_2 into the atmosphere.

4.1 Introduction

Fossil hydrocarbons still remain one of the major sources of energy for humanity and will remain so for the foreseeable future [1, 2]. The need to transition ultimately to a non-fossil fuel future of course is universally recognised. However, until that time in the mid- to long-term future, the present challenge is to maximise current production volumes from oil refineries with a corresponding minimum amount of damage to our environment. In addition, given the inevitable depletion of extant oil wells, a key commercial driver is also now the development of so-called ‘unconventional methods’ for the efficient and environmentally-acceptable processing of fossil hydrocarbons and other products. Crude oil, a major product of fossil sources, is a viscous fluid, composed of thousands of naturally-occurring hydrocarbon compounds and non-hydrocarbons (comprising nitrogen, oxygen, and sulphur), as well as trace quantities of metallic constituents (e.g. iron, nickel, and vanadium) [3-5].

Nowadays, most of the growth of global oil production has been concentrated on ultra-light and light crude, because the lower quality of heavy crudes with a higher proportion of impurities will affect the costs of refining, cracking or reforming, and tertiary treatments in the refinery. It is well-known that light crude oil (LCO) commands a higher price than heavy crude oil on oil markets because it contains a higher fraction of light hydrocarbon fractions (gasoline and diesel fuel) with correspondingly low wax and sulphur contents and requires less thermal and catalytic treatment. Therefore, heavy crude oil will be less attractive to a refiner and will have to be sold at a discount compared with the higher quality crude [4, 6, 7].

The largest and growing source of greenhouse gas emissions arises from the aerial combustion of fossil fuels; this is now driving the development of new technologies to reduce the negative impact of these emissions on climate change. In early work, Muradov [8] proposed a thermocatalytic decomposition of crude oil and other hydrocarbon feedstocks to produce only hydrogen and carbon, with the pure carbon being converted to useful chemicals. Rissman *et al.* [9] evaluated technical and policy interventions, in order to decarbonize the global industry sector to achieve climate stabilization including the use of zero-carbon hydrogen.

Hydrogen production from the deep-dehydrogenation of fossil fuels with reduced CO_2 emission is a key innovation for mitigating the CO_2 greenhouse gas climate change problem [10-13]. Krummenacher *et al.*[14] addressed the partial oxidation of low sulphur diesel fuel over a Rh-coated monolith catalyst. It was shown that synthesis gas is the primary product at > 98% fuel conversion with several hours of stable operation. Muradov [15] presented the experimental results of CO_2-free production of hydrogen-rich gas via catalytic pyrolysis of gasoline fuel using carbon based catalyst, and discussed that it is technically feasible to develop a hydrocarbon fuel reformer for mobile/portable fuel cell applications without CO_2 emissions. Takenaka *et al.* [16] investigated the thermal decomposition of kerosene fuel for production of hydrogen without CO_x emissions, and reported that among all catalysts tested in the study, a Ni/TiO_2 catalyst was the most effective catalyst at 500-600 °C. In another work [17], Takenaka and his co-authors investigated the catalytic performance of Ni–based catalysts for the decomposition of kerosene fuel into CO-free hydrogen and carbon fibers, and showed that $Ni–Pd/SiO_2$ catalyst has a high activity and long life at 550-600 °C.

As previously mentioned in chapter 1, pyrolysis (or decomposition) is an alternative process conducted in an inert atmosphere able to convert hydrocarbon fuels into hydrogen and carbon without the presence of steam or oxygen. In important work, Muradov [18] examined the catalytic pyrolysis of gasoline and diesel using different metal-oxide and carbon-based catalysts. It was reported that there was a hydrogen selectivity of about 40-50 % for gasoline and on average 25 % for diesel at 750 °C. In another work, Muradov also determined that a wide range of hydrocarbon fuels, including methane, propane, gasoline and diesel fuel could be efficiently converted into gaseous products with hydrogen selectivity up to 80 %, and the balance being methane, using a pyrolysis process in an air/water-free environment at temperature < 900 °C [19]. Moreover, fuel cracking/reforming by a so-called plasma process is being rapidly developed in order to produce hydrogen and lighter hydrocarbons, and several studies have been conducted in this field using different hydrocarbons fuels. It includes plasma reforming of gasoline, using microwave plasma or generating plasma nonthermal arc discharge [20-22], plasma reforming of diesel [23-28], kerosene [29-31] , naphtha [32], engine oil [33], heavy oil, and coke [34].

Microwave technologies have become an attractive innovation in fields of chemistry covering the areas of organic, inorganic, catalytic chemistry, and synthesis. It has been also suggested that the use of microwaves could become very efficient in producing innovations in oil processing itself [35, 36]. The use of so-called microwave-initiated catalytic deep-dehydrogenation technology in the process of upgrading heavy oil is one of the new processes that is actively being considered. This is gaining increasing attention, since specifically tailored, microwave-receptive catalysts can speed up many chemical reactions with high efficiency and high selectivity [37-40]. In addition, the application of microwave heating in oil processing has become increasingly attractive due to the environmental concerns that arise with conventional (thermal) heating methods which inevitably lead to large emissions of CO_2.

The microwave-initiated catalytic deep-dehydrogenation of liquid hydrocarbons is therefore a potential competitor route for low- or indeed CO_2-free production of H_2. The Edwards group reported that H_2 can be rapidly produced by this method from hexadecane and various hydrocarbon sources using different supported metal catalysts (**Figure 4.1**) [11, 12, 41]. Indeed, they have even found that the microwave-initiated catalytic deep-dehydrogenation of even the naturally-occurring, crude oils, and the resulting hydrocarbon fossil fuels allows for the rapid production of large volumes of H_2 using inexpensive and abundant Fe catalysts [12, 13].

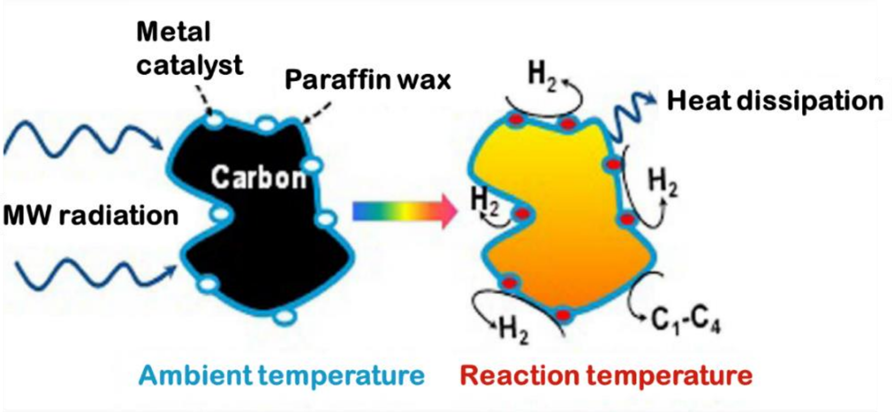

Figure 4.1 Pictorial representation of the hydrogen evolution reaction from the microwave-initiated catalytic decomposition of paraffin wax on carbon-supported metal catalyst. (Reproduced from Ref. [11]).

4.2 Experimental

4.2.1 Preparation of Catalysts

In this chapter, a range of metals were used to prepare a series of metallic and bimetallic catalysts for the deep-dehydrogenation of LCO to produce hydrogen. $Fe(NO_3)_3 \cdot 9H_2O$ (iron (III) nitrate nonahydrate, 98.0%, Sigma-Aldrich), $Ni(NO_3)_2 \cdot 6H_2O$ (nickel (II) nitrate hexahydrate, 98.0%, Alfa Aesar), $Co(NO_3)_2 \cdot 6H_2O$ (cobalt (II) nitrate hexahydrate, 98.0%, Sigma-Aldrich), were used as metal precursors. AC (activated carbon, Sigma-Aldrich) was used as a support material for the catalyst preparation (**Table 4.1**).

An wet impregnation method is used for all preparations, and it is similar to the procedure described in chapter 3. The preparation of bimetallic catalysts was conducted by mixing the supports with the aqueous solution of two metal nitrate precursors. All supported metallic and bimetallic catalysts were tested in the microwave-initiated deep-dehydrogenation system, and for comparison, some catalysts were tested in the thermal system.

Table 4.1 A list of metallic and bimetallic supported catalysts which have been prepared and tested in this chapter.

Catalyst	Metal content (wt. %)
Fe/AC	5, 10, 20, 30, 40, and 50 (Fe)
Ni/AC	5, 10, 20, 30, 40, and 50 (Ni)
Co/AC	5, 10, 20, 30, 40, and 50 (Co)
Fe-Ni/AC	5Ni25Fe, 10Ni20Fe, 15Ni15Fe, 20Ni10Fe, and 25Ni5Fe
Fe-Co/AC	5Co15Fe, 10Co10Fe, and 15Co5Fe

4.2.2 Characterisation of Catalysts

To check the catalyst composition and to provide data on the catalyst activity, the fresh and spent catalysts were carefully characterised by X-ray diffraction (XRD), thermogravimetric analysis (TGA), scanning electron microscopy (SEM), and transmission electron microscopy (TEM). The operating procedure and full details related to these techniques were given previously in chapter 2.

4.2.3 Light Crude Oil (LCO)

Saudi Aramco kindly provided the Saudi Arabian light crude oil (LCO). LCO was used in all catalytic experiments without any pre-treatment. The American Petroleum Institute (API) gravity was measured using the American Society for Testing and Materials (ASTM) method D-4052. The full specification analysis was listed in **Figure 4.2**. The main properties of the LCO were measured by ITS Testing Service (Intertek UK) Ltd. are summarised in **Table 4.2** and **Table 4.3**.

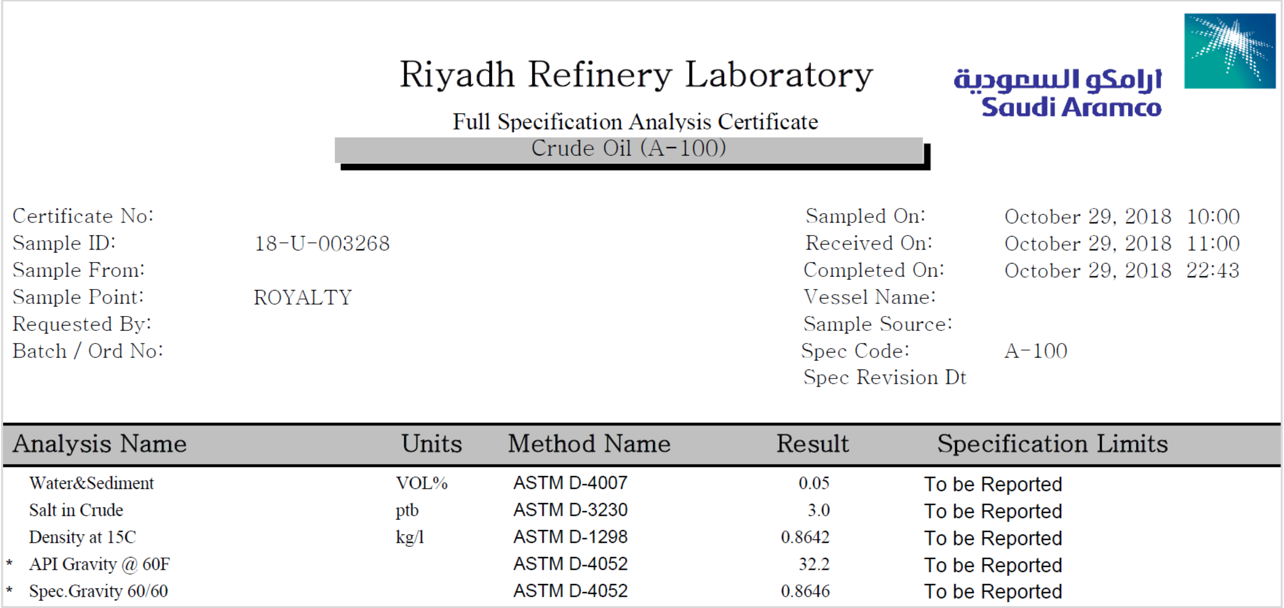

Riyadh Refinery Laboratory

ارامكو السعودية
Saudi Aramco

Full Specification Analysis Certificate
Crude Oil (A-100)

Certificate No:
Sample ID: 18-U-003268
Sample From:
Sample Point: ROYALTY
Requested By:
Batch / Ord No:

Sampled On: October 29, 2018 10:00
Received On: October 29, 2018 11:00
Completed On: October 29, 2018 22:43
Vessel Name:
Sample Source:
Spec Code: A-100
Spec Revision Dt

Analysis Name	Units	Method Name	Result	Specification Limits
Water&Sediment	VOL%	ASTM D-4007	0.05	To be Reported
Salt in Crude	ptb	ASTM D-3230	3.0	To be Reported
Density at 15C	kg/l	ASTM D-1298	0.8642	To be Reported
* API Gravity @ 60F		ASTM D-4052	32.2	To be Reported
* Spec.Gravity 60/60		ASTM D-4052	0.8646	To be Reported

Figure 4.2 Specification analysis certificate for Saudi light crude oil provided by Saudi Aramco.

Table 4.2 Saudi Arabian light crude oil LCO properties.

Components	Wt. %
Sulphur	1.96
Nitrogen	0.11
Carbon	85.1
Hydrogen	12.1

Table 4.3 Overall composition of LCO by multi-dimensional gas chromatography.

LCO content	Wt. %
Paraffin	45.74
Naphthene Content	16.58
Olefin Content	0.02
Aromatic Content	37.66

4.2.4 Characterisation of LCO

LCO was characterised using a number of standard analytical techniques including nuclear magnetic resonance (NMR) spectroscopy, Fourier transform infrared spectrometer (FTIR), and thermogravimetric analysis (TGA).

4.2.5 Microwave Initiated Deep-dehydrogenation Process

The microwave experimental set-up used in this investigation is similar to that previously reported in chapter 2 (**Figure 2.1**). Typically, 50 wt. % of LCO (0.5 g) was mixed with the catalyst (0.5 g) and loaded in a quartz (silica) tubular fixed-bed reactor with 9 mm inner and 10 mm outer diameters. The catalyst was purged with a dry argon gas at a flow rate of 20 ml.min^{-1} for 10 minutes before the microwave was turned on. The experiment was carried out at a frequency of 2.45 GHz, with different input powers (250-1250 W). After 10 minutes of reaction, the microwave radiation was switched off and the temperature monitoring switched off once the sample reached 50 °C. The collected gaseous products were analysed quantitively by gas chromatography (GC) using a Perkin-Elmer, Clarus 580 GC.

In this chapter, there was an inherent limitation in calculating the conversion of the LCO as described in the previous chapter (**Equation 3.6**) since the separation or distinguishing feature between the unreacted LCO and any other liquid hydrocarbons which may have been produced during the microwave experiment requires additional specialised equipment for analysis. Hence, the LCO conversion was calculated based on the hydrogen selectivity and yield by applying the following equation [42]

$$\text{Conversion (\%)} = \frac{\text{Yield}}{\text{Selectivity}} \text{ X } 100 \qquad \textbf{Equation 4.1}$$

Three experiments were conducted for the optimal system to ensure the reproducibility and the accuracy of the results. (Appendix A).

4.2.6 Conventional (Thermal) Catalytic Process

The thermal experiments for LCO deep-dehydrogenation were carried out in an electric furnace for direct comparison purposes with our microwave-initiated experiments. The experimental setup is shown in chapter 2 (**Figure 2.3**). A catalyst pre-loaded with 50 wt.% LCO was loaded into a pre-heated tube furnace. Dry argon gas was used to purge the reactor tube and the reactor tube was then placed into a tube furnace, which had already been preheated to different reaction temperatures (500, 800, and 1000 °C) to investigate the effect of the temperature factor on the gaseous products.

4.3 Results and Discussions

As concluded earlier in chapter 3, paraffinic feedstock was relatively better for producing hydrogen than other hydrocarbons. Therefore, the overall LCO compositions (paraffin-, naphthene- or aromatic-base) plays an important role in hydrogen production. For this purpose, different characterisation techniques were used, and the data are discussed below.

Moreover, the generation of H_2 from LCO via the microwave-initiated catalytic deep-dehydrogenation of metallic and bimetallic supported catalysts at different loading levels of metal catalyst is discussed. Then, the focus will be on the connection of this catalytic process with the so-called Size-Induced Metal-Insulator Transition (SIMIT) [43], with a particular emphasis on changes in the microwave absorption of metal catalyst particles with size across the SIMIT. Finally, the possible implications of the SIMIT characteristic of the solid catalysts and the catalysts performance are discussed.

4.3.1 LCO Characterisation

Crude oils are natural, complex mixtures containing thousands of different compounds (paraffins, naphthenes, olefins and aromatics) and are considered one of the most analytically complex samples [44, 45]. The quote below from Y. Zhang (ExxonMobil Research and Engineering) on 19th May 2021, about the possibility to characterise crude oils [46], clearly reflects the complexity of this task.

"Due to the super-complex nature of petroleum, there are limitations in every method. The most effective way is probably the divide-and-conquer strategy, i.e., chromatographic separation followed by characterisation techniques. The well-known and popular average structure strategy (use one or few representative structures to represent any petroleum fraction) based on NMR, MS etc. is obviously very limited because so many molecules. The high resolution MS can reveal up to a quarter million ion peaks easily, and probably the closest to understand the reality of petroleum species. However, we still don't know exactly how many

molecules in petroleum since each MS peak can represent many molecules and each formula has a "gazillion" of possible structures. So, we really don't know about exactly the structures unless there is a method to isolate individual molecule and characterize them, which is probably impossible. Most of the structures in papers or textbooks so far are still "cartoons" or schematics, i.e. they represent numerous structures".

So, the main goal of this section is to apply different analytical characterisation techniques for such a complicated sample and combine the data in an attempt to understand the effect of crude oil chemical composition on its behaviour during the catalytic reaction.

4.3.1.1 Nuclear Magnetic Resonance (NMR) Spectroscopy

^{1}H and ^{13}C NMR can be applied to obtain information on general functional groups (tertiary, secondary, and primary carbon atoms, aromatic cores) and the possible presence of olefins or water [47]. **Figure 4.3 (a, b, c, d)** shows the ^{1}H NMR spectra of an LCO sample in deuterated chloroform ($CDCl_3$) solvent using a Bruker AVANCE III HD spectrometer at resonance frequency 600 MHz. Field lock and shimming were performed using the deuterium signal of chloroform ($CDCl_3$) which shown at a chemical shift (δ) of 7.26 ppm.

It can be seen from the spectra that there are two main regions of peaks [48-50]:

- The region of aliphatic hydrocarbons at ranges between 0.5 to 3 ppm (**Figure 4.3a, b, c**). This range includes the protons of paraffinic and naphthenic (primary, secondary and tertiary hydrogens: -CH, $-CH_2$, and $-CH_3$) compounds, involving the protons of alkyl groups attached to aromatic rings. This can be divided into:

  a) δ= 0.8-0.94 ppm: H of $-CH_3$ (paraffinic H)

  b) δ= 1.1- 1.4 ppm: H of $-CH_2$ (naphthenic H)

  c) δ= 2.15- 2.5 ppm: -CH, $-CH_2$ and $-CH_3$ of paraffinic and naphthenic hydrocarbons. In addition to those H attached to aromatic rings.

- The region of aromatic hydrocarbons at chemical shift (δ) ranges between 6.8 to 7.5ppm (**Figure 4.3d)**. This range includes the protons of both mono and poly aromatic rings. The signals due to substituted groups in mono and poly aromatics appear in the (δ) ranges 2.15-2.40 ppm and 2.40-2.80 ppm which are due to CH_2 and CH_3 protons respectively.

It can be seen in the spectra that the intensity of mono and polyaromatic rings is very weak. This means that the content of aromatics in LCO is low compared with those paraffinic and naphthenic compounds. Also, the spectrum shows that there are no olefinic protons which should appear in the range δ= 4.5- 6 ppm, in agreement with the results obtained by ITS Testing Service (UK) Ltd.

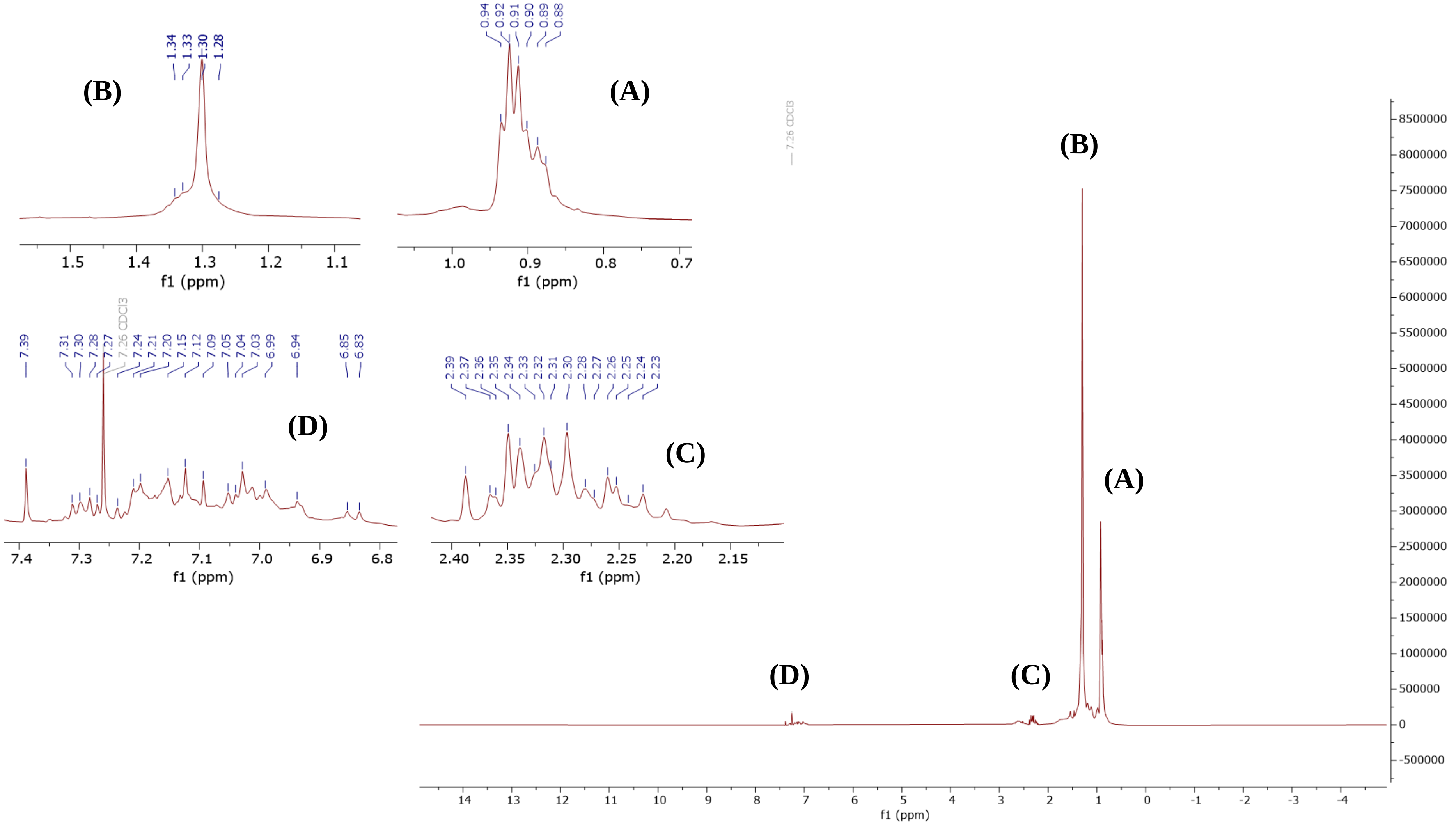

Figure 4.3 ^{1}H NMR spectra of light crude oil (LCO) sample at resonance frequency of 600 MHz.

Carbon-13 (^{13}C) is a natural stable isotope and present only 1.1% abundance. Due to low natural abundance, ^{13}C NMR spectrum does not show spin-spin splitting between adjacent carbons. However, the spectra of ^{13}C shows splitting of a carbon signal by directly bonded protons. Primary carbon - methyl groups ($-CH_3$) appear as quartets, secondary carbon- methylenes ($-CH_2$) as triplet, tertiary carbon- methines (-CH) as doublets, and quaternary carbon (-C) (carbon not attached to any protons) as singlets (**Figure 4.4**) [47, 50, 51].

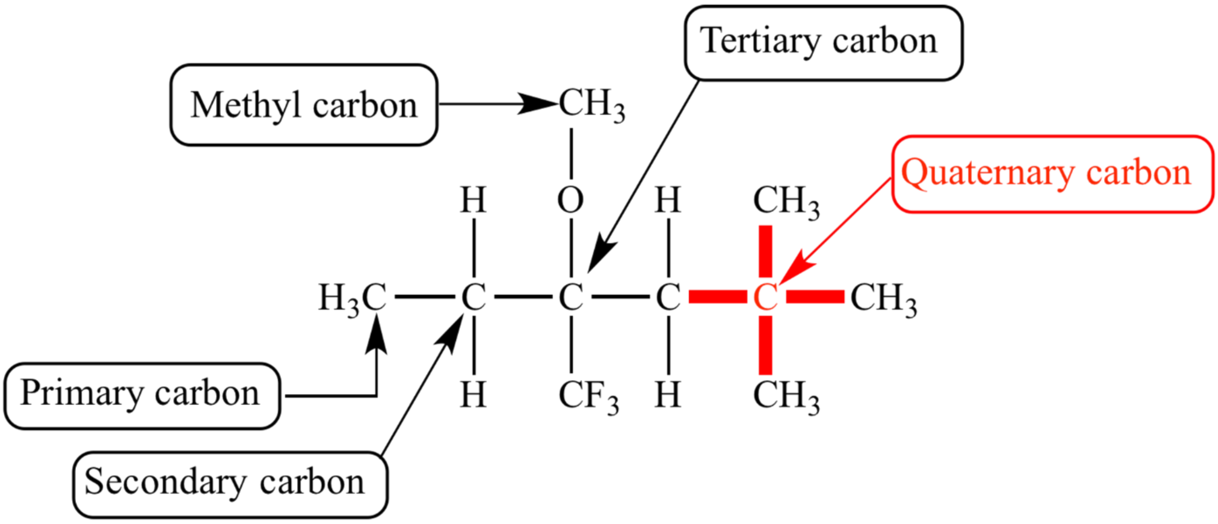

Figure 4.4 A schematic illustration of primary, secondary, tertiary, and quaternary carbon centres. (www.chem.ucla.edu)

Figure 4.5 shows ^{13}C NMR spectra of an LCO sample diluted in deuterated chloroform ($CDCl_3$) solvent using a Bruker AVANCE III HD spectrometer at resonance frequencies 600 MHz. Field lock and shimming were performed using deuterium signal of chloroform ($CDCl_3$) which shows a chemical shift at (δ) 77.17 ppm.

It can be seen from these spectra that there are two main regions of peaks:

- **Aliphatic hydrocarbons** at chemical shift (δ) range between 11.57 to 40 ppm (**Figure 4.5A,B**). This range includes paraffinic and naphthenic carbons. Types of carbons: -CH_3 (*pri*-Cs), -CH_2- (*sec*-Cs), CH (*tert*-Cs) and C (*qua*-Cs) respectively. In addition, there are carbons of alkyl groups attached to naphthenic and aromatic rings. Usually (*pri*-Cs) have a lower chemical shift than (*sec*-Cs) and (*sec*-Cs) have a lower chemical shift than CH (*tert*-Cs) and C (*qua*-Cs). It can be seen from the spectra that there are four main groups of peaks in this range:

  a) The first peak (split up into quartets, δ= 14.22, 14.28, 14.33, and 14.57 ppm) is related to *pri*-Cs of paraffinic (carbon-CH_3) and those attached to naphthenic and aromatic rings.

  b) The second peak (split up into triples 22.76, 22.82 and 22.84 ppm) is associated with *sec*-Cs of paraffinic and naphthenic (carbon-CH_2-) and those attached to low content of aromatic rings.

  c) The third peak (split up range 29.86-29.90 ppm) corresponds to *tert*-Cs of paraffinic and naphthenic (carbon CH) and those attached to naphthenic aromatic rings.

  d) The fourth peak (32.13 ppm) related to *qua*-Cs of paraffinic and naphthenic (carbon C) and those attached to naphthenic and aromatic rings (may exist). Quaternary carbons usually give sharper and weaker signals than another *pri*-Cs, *sec*-Cs and *tert*-Cs.

- **Aromatic hydrocarbons** appear at chemical shifts (δ) ranges between 122 to 132 ppm, and between 132 to 145ppm (**Figure 4.5C, D**). This range includes carbons of substituted and unsubstituted mono and polyaromatic rings. It can be seen that the intensity of mono and polyaromatic carbon rings is very weak. This means that the content of aromatics in the crude oil is very small compared with paraphinic and naphthenic compounds which agrees with ^{1}H NMR results.

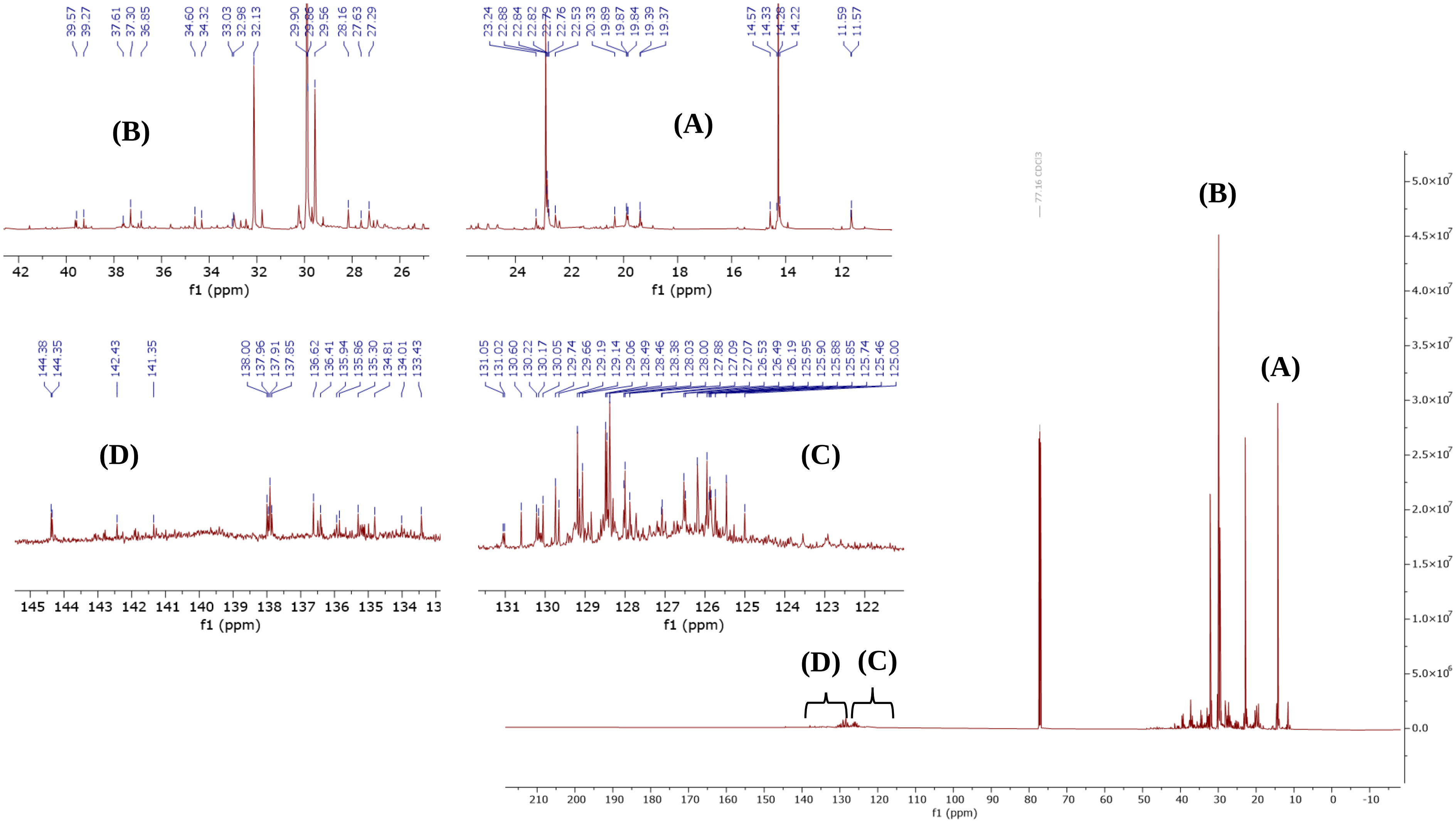

Figure 4.5 ^{13}C NMR spectra of light crude oil (LCO) sample at a resonance frequency of 600 MHz.

4.3.1.2 Fourier Transform Infrared Spectrometry (FTIR)

FTIR can identify the type of chemical bonds in a molecule by producing a fingerprint infrared absorption spectrum for organic samples arising from molecular vibrations. The spectrum produces a profile of the sample, a typical molecular fingerprint that can be used to screen and scan samples for many different components [52, 53]. In this study, FTIR is used to determine functional group types in the fractions of crude oils.

Generally, the IR spectrum can be divided into three wavenumber regions [53]: far-IR spectrum (< 400 cm^{-1}), mid-IR spectrum (400-4000 cm^{-1}) -which is the most widely used to provide information about the sample- , and near-IR spectrum (4000-13000 cm^{-1}).

Figure 4.6 showed the four regions of the mid-IR spectrum based on specific frequency of each functional groups in the analysed sample.

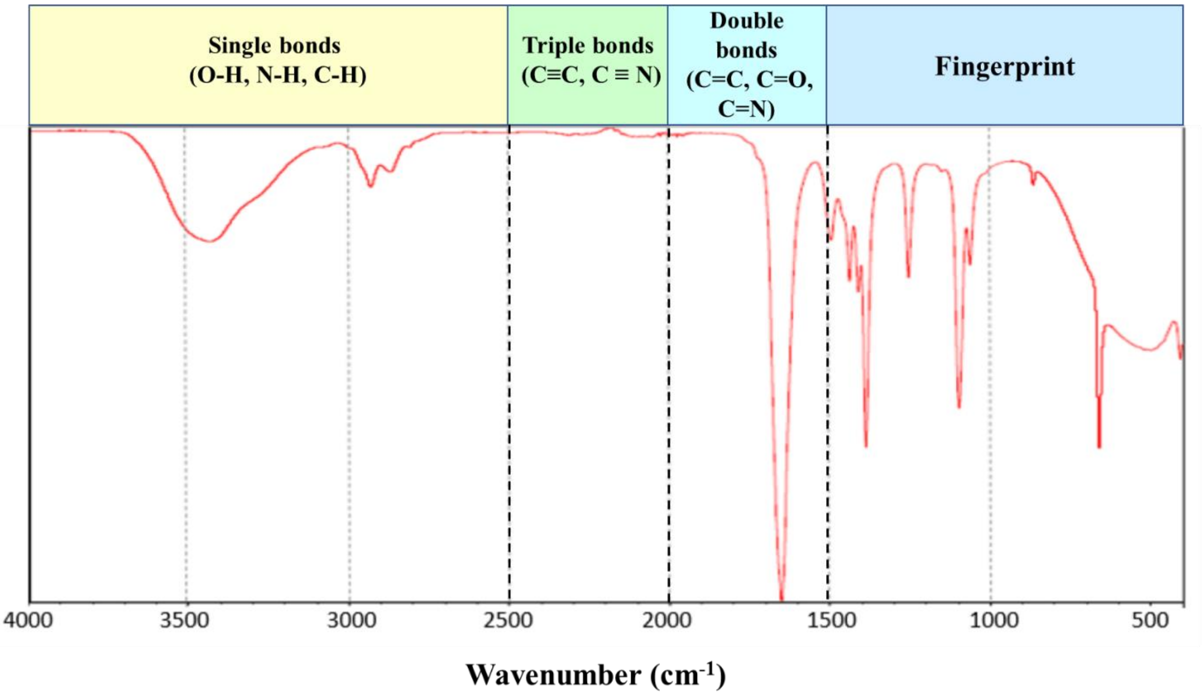

Figure 4.6 Schematic Mid-IR spectrum. (Adapted from Ref [53]).

Figure 4.7 depicts the FTIR spectrum of LCO fractions, this reveals strong absorption at 2924, 2853.7, 1456.7, and 1377 cm^{-1} because of methylene (CH_2) and methyl (CH_3) groups. In the spectral range typical for aromatic molecules at around 1600 and 810 cm^{-1}, there is no presence of any strong band and this confirms the low aromaticity in the LCO, which agrees with ^1H and ^{13}C NMR results [52]. Regarding the existence of oxygen in the LCO, the results show that the oxygen exists as carbonyl group: C=O in the spectra between 1695-1710 cm^{-1} (as in carboxylic acid, acid derivatives, ketone, and aldehyde) and hydroxyl group: -OH in the spectra between 3570-3200 cm^{-1} (as in alcohols, acids and phenolic compounds) [54, 55]. The prominent functional groups present in the oil are given in **Table 4.4**.

Table 4.4 Functional Group in the FTIR Spectra of the Crude Oil [53, 54].

Wavelength of absorption (cm^{-1})	**Mode of vibration**	**Functional group**
2852-2853	C–H stretching	– CH_2 and CH_3 of the saturate
2922-2923	C–H stretching	– CH_2 and CH_3 of the saturate
1460	C–H deformation	– CH_2 and CH_3 of the saturate
1376	C–H symmetric deformation	– CH_2 of the saturate
722	C–H bending	– C–H of substituted benzene
1640-1800	C=O stretching	– C=O of carbonyl/carboxylic group
3700-3100	O–H stretching	– OH of phenolic groups
1470-1590	C=C ring stretching	– C=C of aromatics

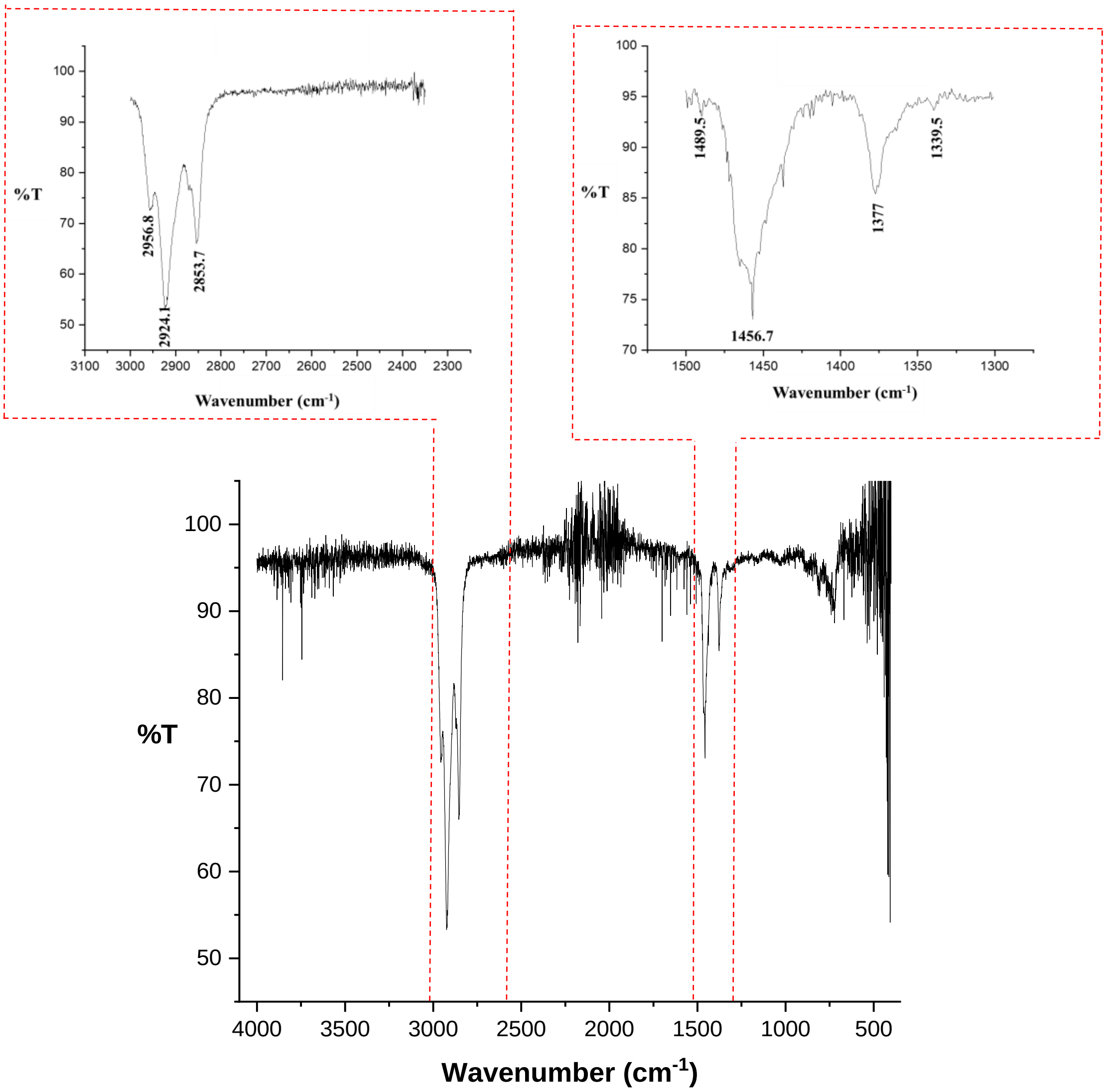

Figure 4.7 FTIR spectra of LCO fractions.

4.3.1.3 Thermogravimetric Analysis (TGA)

TGA is one of the techniques that involves a study of the thermo-oxidation and mass loss of crude oils over an extended temperature range. In this section, the change of weight for LCO is observed to occur in different stages depending on the temperature under a controlled heating rate of LCO sample. The weight variation of LCO sample is recorded as a function of temperature within a specific time interval.

The thermogravimetric analysis of the LCO sample was carried out in a flow of dry nitrogen (100 ml/min) with a heating rate 1.0 °C/min, over the temperature range 25 -1000 °C. The average weight of the LCO sample was 50.4 ± 0.1 mg at the start. The result of analysis is shown in **Figure 4.8**. It can be seen from the TGA curve of the LCO sample that the characteristic feature of this curve is the weight change at the beginning of the analysis and the sharp gradient in the temperature range between 25 °C to 450 °C due to evaporation of highly volatile components and then the higher boiling point hydrocarbons. The weight loss of the LCO sample was found to be 22% as the temperature rose to 150 °C, which is mainly due to the evaporation of moisture and/or volatile components in the LCO in the C_5-C_8 range.

As the temperature of the LCO sample is increased from 150 to 350 °C, the weight loss was 29.8% which may be due to evaporation of the higher-boiling-point hydrocarbons with the number of carbons less than 21 (C_9-C_{20}). Therefore, at temperature of 350 °C the total weight loss of the LCO sample was 51.8%. As the temperature of the LCO sample is further increased from 350 to 450 °C, the weight loss was 12% due to the evaporation of heaver organic components with less than 31 carbons (C_{21}-C_{30}). Accordingly, by a temperature of 450 °C the total weight loss of the LCO sample was 63.8%. On further increasing the temperature from 450 to 500 °C, the weight loss of the LCO sample is found to be negligible (~ 0.2%).

The change of weight in different stages of temperature from the beginning of the analysis up to 1000 °C, corresponds to 64.9% [56, 57]. Chemical reaction can also take place on increasing the temperature, producing heavier molecular fragments (fractions) and even residual carbonaceous material which account for the remaining weight of 35.1 wt. %.

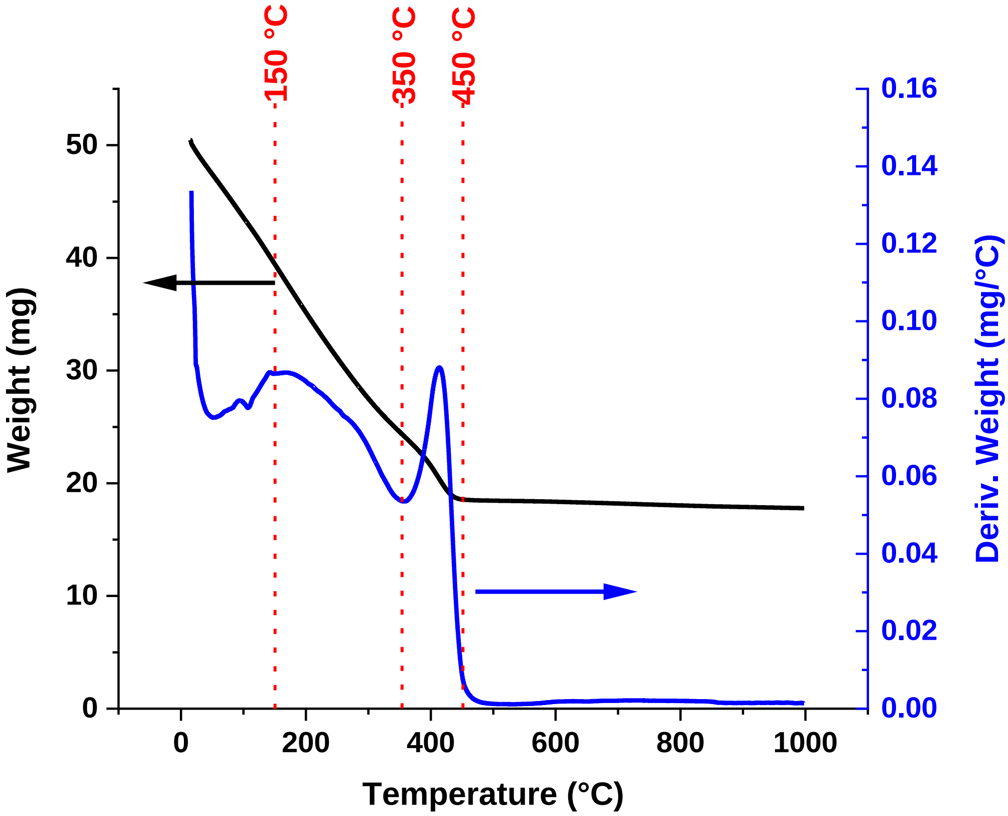

Figure 4.8 Thermogravimetric analysis of a LCO sample.

4.3.2 Microwave-initiated Catalytic Activity of Active-Carbon-Supported Fe Catalysts for the Deep-dehydrogenation of Light Crude Oil (LCO)

4.3.2.1 Effect of Different Fe Loadings on Fe/AC Catalysts

The feasibility to produce hydrogen through microwave-initiated deep-dehydrogenation of LCO was explored. Thus, a range of Fe-loaded catalyst compositions between 0 and 50 wt. % Fe on AC material were examined using LCO as a feedstock, whilst keeping all other experimental conditions constant (particularly the metal particle size). It was observed that large quantities of H_2-rich gases were rapidly released from the very onset of microwave initiation. The resulting catalytic performances are given in **Figure 4.9**.

As a general observation, AC as a support exhibits a high activity for the deep-dehydrogenation of LCO even without the presence of Fe metal, and generate a very little amount of CO. And with this support, the yield of H_2 produced steadily increased with higher Fe catalyst loading levels. The 30 wt. % Fe/AC catalyst exhibits the highest H_2 yield and selectivity at 24 and 62.5 % respectively with maximum LCO conversion around 40 %, whilst the 40 and 50 % Fe/AC formulation shows an unexpected diminution in H_2 yield, with increases in the production of CO_x gases and light hydrocarbons gases. This is because the excess of Fe metal may lead to blockage of the catalyst active sites. The decline in the activity patterns of the same composition of catalysts (40 % and 50 wt.% Fe/AC) was also observed earlier in chapter 3 during the process of dehydrogenation of model compounds. These data also shows that the AC support itself doesn’t make CO, but with Fe being present, the olefin and hydrogen have different formation mechanisms (e.g., water-gas shift reaction). A detailed composition analysis of products is given in **Table C1** (Appendix C).

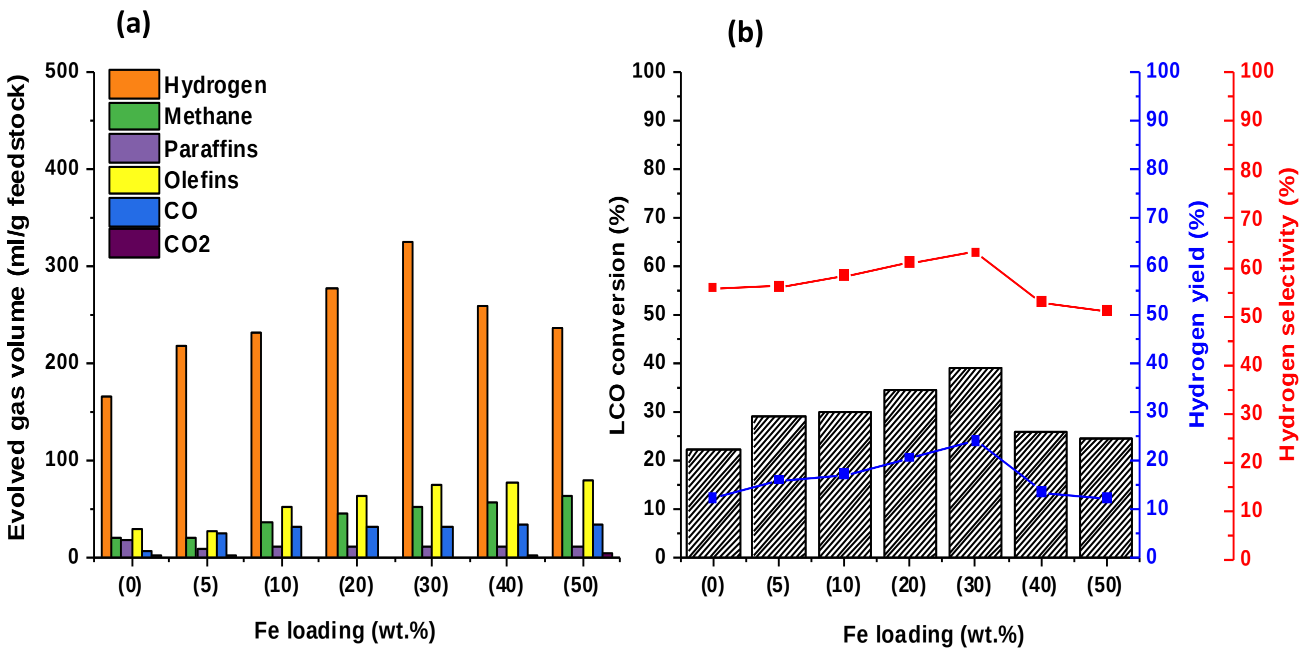

Figure 4.9 Microwave-initiated deep-dehydrogenation of a 0.5 g of LCO sample mixed with 0.5 g of Fe/AC catalyst at different Fe loadings, (a) the total evolved gas volume, and (b) LCO conversion, hydrogen yield and selectivity at a microwave input power of 1000 W for 10 min in all cases.

4.3.2.2 Effect of Variable Microwave Power at a fixed Fe loading, 30 wt.%, on AC

As seen from the various loadings of Fe that the highest conversion of LCO around 40 % with the hydrogen yield and selectivity at 24 %. and 62.5 % respectively were obtained with the Fe loading 30 wt.% on AC at microwave power 1000 W for 10 minutes irradiation. Therefore, in order to investigate the effect of varying the input microwave power and optimise the conversion of LCO, yield and selectivity of the hydrogen a series of experiments were also carried out using input microwave power from 250 to 1250 W using 30 wt.% Fe/AC catalyst with 50 wt.% LCO. **Figure 4.10a,b** shows that the H_2 was the dominant product with different power levels while a small amount of CO_2, methane and light hydrocarbons were obtained as minor products from the deep-dehydrogenation process. The amount of CO_2 in the produced gas is very small (less than 0.5 vol.%), hence the release of CO_2 in this process can be regarded as negligible.

The hydrogen yield increases significantly with increases in the input microwave power and the selectivity increases slightly. This appears to be a consequence of the higher reaction temperatures at the catalytic sites with increasing input microwave power (**Figure 4.10c**). This is understandable as the non-oxidative catalytic deep-dehydrogenation of hydrocarbons via C–H activation is a highly endothermic process that generally requires high temperatures to overcome unfavourable thermodynamics [58].

In contrast, the unexpected diminution in LCO conversion at the higher microwave input power (1250 W), directly led to a decrease in hydrogen yield (and selectivity). This is important and reflects the faster evaporation of LCO feedstock as compared to the rate of the chemical reaction upon exposing the sample to microwaves. In fact, under these situations the volatile hydrocarbons in the sample were indeed rapidly evaporating away and condensed at room temperature and were collected in a liquid trap as illustrated in chapter 2 (**Figure 2.1**). This obviously affects the catalyst/LCO contact time and therefore the catalytic deep-dehydrogenation reaction. A detailed composition analysis of products is given in **Table C2** (Appendix C).

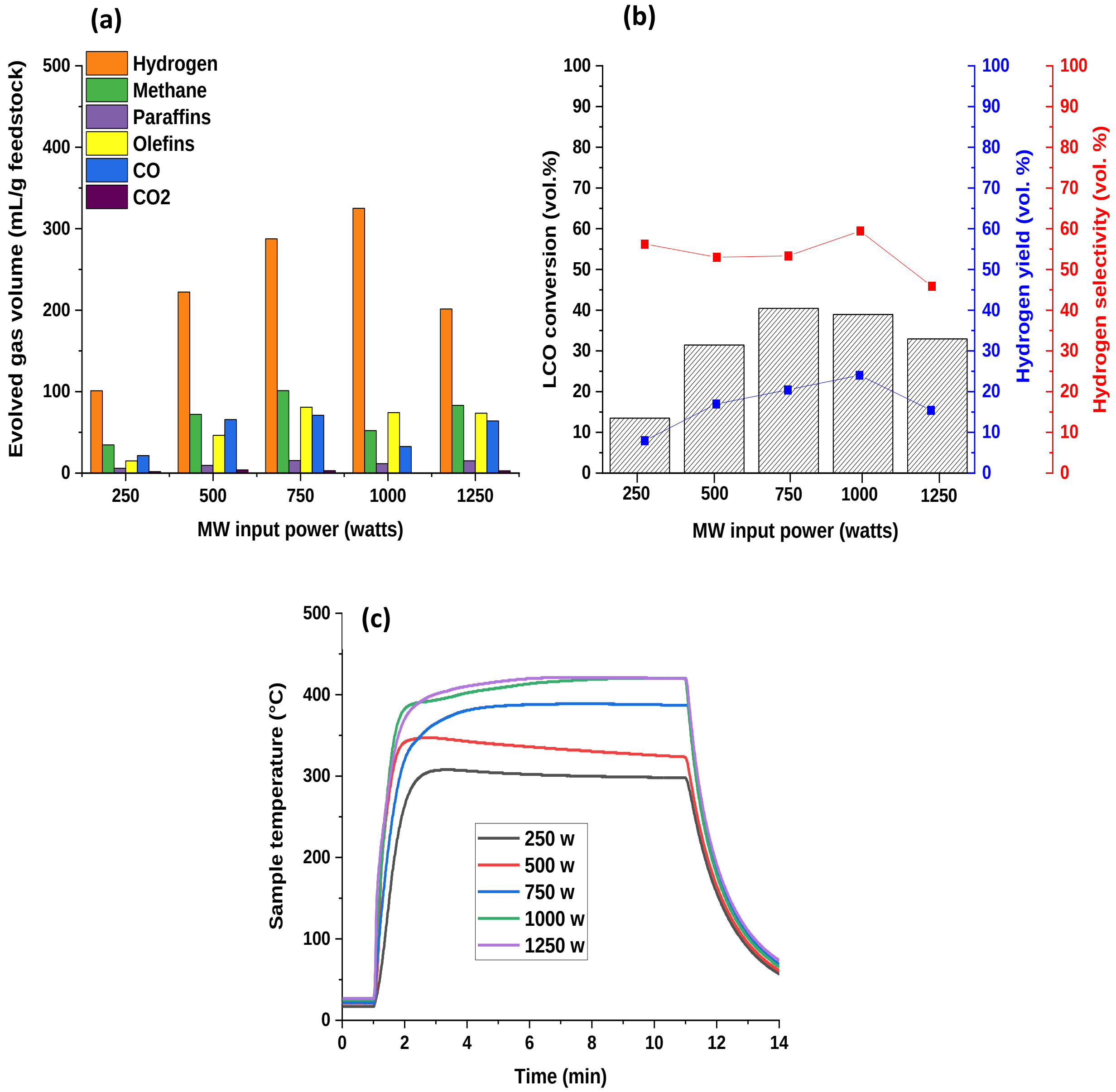

Figure 4.10 Microwave-initiated dehydrogenation of a 50 wt.% LCO mixed on a 30 wt.% Fe/AC catalyst at different microwave input powers (a) the total evolved gas volume, and (b) LCO conversion, hydrogen yield and selectivity for 10 min. (c) The dependence of the sample temperature profile with time. The decrease in bed temperature corresponds to the stage when the input microwave power is turned to zero.

4.3.2.3 Effect of Continuous Operation Conditions using Fe Loading 30 wt.% on AC

Since the sample with 30 wt. % Fe/AC and the microwave input power of 1000 W exhibited the highest H_2 yield and LCO conversion of the studied Fe/AC catalyst series, it is therefore feasible to assess its catalytic performance under continuous operation conditions.

Accordingly, the catalytic performance was investigated in a continuous operation of microwave-initiated deep-dehydrogenation of LCO mixed with 30 wt.% catalyst at microwave power input of 1000 W for 4 h irradiation time on stream. **Figure 4.11** shows the evolved gas volume of the continuous reaction on 30 wt.% Fe/AC catalyst, with feedstock (LCO) flow rate of 0.05 $ml.min^{-1}$ (or 3 $ml.(hr.g_{cat})^{-1}$ of liquid-hourly space velocity, [flow of oil/ weight of catalyst]. The level of H_2 production increased instantly and reached its peak after 10 min of reaction time. Thereafter, there was a dramatic decrease of evolved H_2 coincident with increasing amounts of light hydrocarbons, particularly olefins. A drastic diminution of evolved gases at 4 h (240 min) is almost certainly due to evolving (and inevitable) carbon deposition (hence the deactivation of the catalyst) on the operating catalyst; this corresponds to the maximum time (or catalyst lifetime) after this which there are no longer any evolved gases.

It is particularly noticeable that there is a significant increase of light olefins production and the corresponding diminution of the bed temperature with time-on-stream (**Figure 4.11a**). The changes in product distribution with time may reflect the ‘masking’ of Fe or Fe_3C sites by developing carbon deposition and thereafter the AC and Fe/Fe_3C may play a larger role in catalysis. Support for this proposal is the larger yield of olefins characteristic of AC alone acting as catalyst [59]. However, we cannot rule out the participation of Fe/Fe_3C catalysts in the generation of light olefins. Also worth mentioning is the possibility of catalyst poisoning with sulphur present in LCO and its effect on the iron (and other metals used in this study), and the effect that FeS or Fe_2S_3 may have on microwave chemistry. A detailed composition analysis of products is given in Table **C3** (Appendix C).

The dependence of the bed temperature and microwave absorbed power upon the reaction time (**Figure 4.11c**) needs to be further considered. It is striking that the catalyst bed temperature falls from 500 °C to 345 °C, and the absorbed power decreased to 90 W after 10 min of time-on-stream, and the temperature and absorbed power are then maintained until the microwave source is turned off. It can be shown that the heating rate of flowing LCO across the Fe/AC catalyst is directly determined by the imaginary permittivity (or dielectric loss) of the overall system (LCO + Fe/AC) and the field strength E (or input power) and inversely proportional to the density and the specific heat of LCO + Fe/AC according to the following equation [60];

$$\frac{\Delta T}{\Delta t} = \frac{2\pi f \varepsilon_0 \varepsilon'' |E|^2}{\rho C_p}$$

Equation 4.2

Where f is the frequency of the applied field, ε_0 and ε'' are the permittivity of free space and imaginary permittivity, respectively, $|E|$ is the strength of the microwave electric field, ρ is the density and C_p is the specific heat capacity of the heated material.

The high dielectric loss of Fe/AC and field strength might control the high heating rate at the beginning of the experiment whilst the abrupt diminution of the temperature after several seconds of reaction can be attributed to the relatively high heat capacity of LCO and heat absorption due to the ensuing endothermic chemical reaction.

It is worth mentioning that the present analysis does not consider the inevitable heat loss to the surroundings. One can conceive of the surroundings as the “Lattice (or host) bath” which is usually controlled by its characteristic thermal conductivity properties. The reduction in temperature is reflected in a strong diminution of H_2 levels and a clear increase of the olefin compositions in the evolved gases, suggesting that the formation of these gaseous products is not only affected by the possible coke-assisted catalyst deactivation but also, and most importantly, by the diminution of the dielectric loss of Fe/AC catalysts during time on stream, largely due to carbonisation of the catalyst itself.

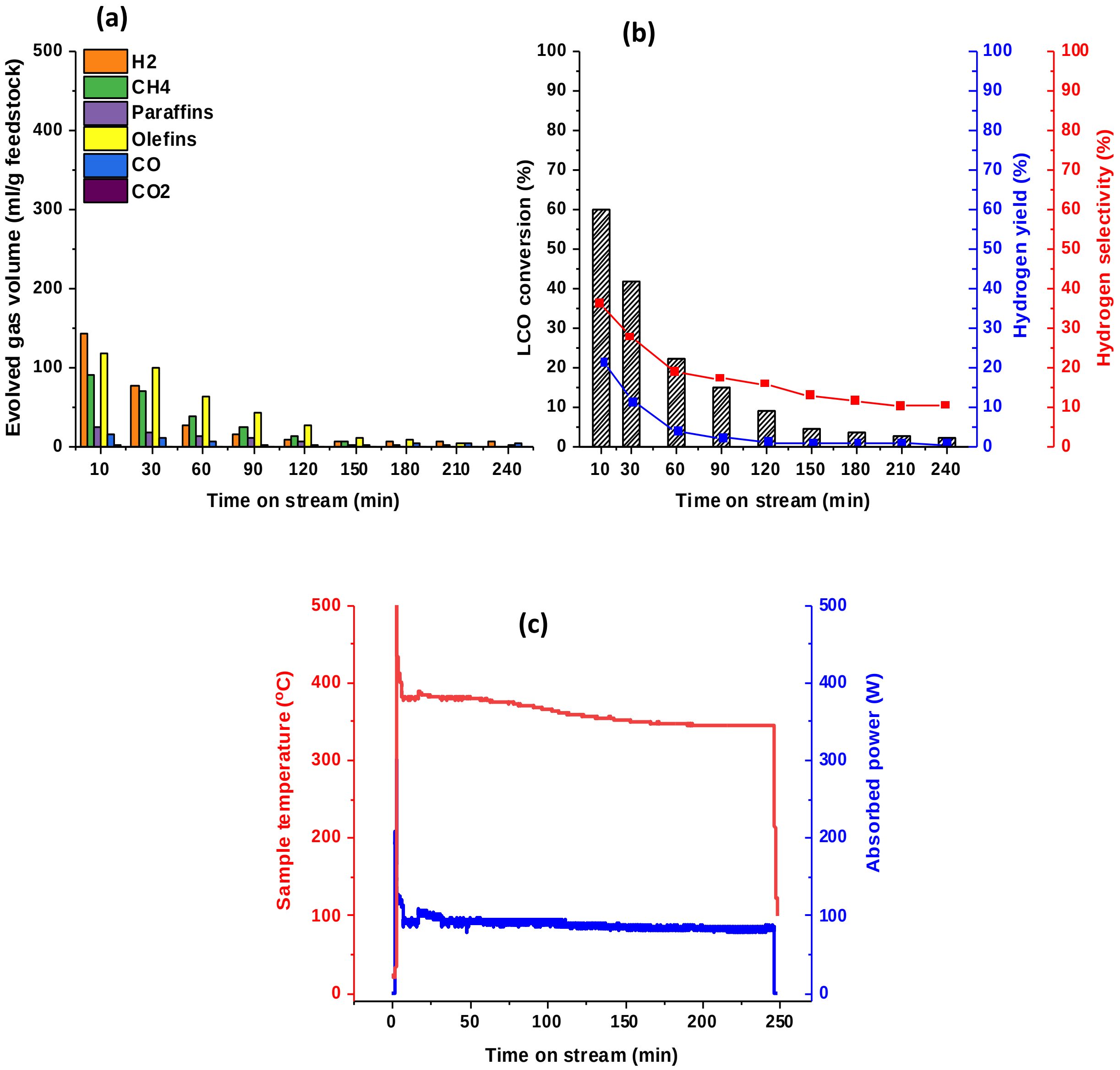

Figure 4.11 The continuous operation of microwave-initiated deep-dehydrogenation of LCO sample on 0.5 g of 30 wt.% Fe/AC catalyst. (a) the evolved gas volume of LCO for 'time-on-stream' evaluation, (b) LCO conversion, hydrogen yield, and selectivity for 'time-on-stream' evaluation, (b) LCO conversion, hydrogen yield, and selectivity for 'time-on-stream' evaluation (c) the sample (bed) temperature and corresponding microwave-absorbed power at microwave power input of 1000 W and for 4 h irradiation time.

4.3.3 A Comparison Between the Conventional (Thermal) and Microwave-initiated Deep-dehydrogenation Processes of Light Crude Oil (LCO)

The mechanism for incorporation of thermal energy with microwaves is fundamentally different from that of a conventional heating process. In a conventional heating process, thermal energy is initially transferred to the outer surface of the material, then gradually into the interior of the material itself through natural convection, conduction or radiation. Microwave heating uses the ability of some compounds to transform electromagnetic energy into thermal energy by means of the dielectric properties of the constituent molecules and solid materials [61, 62] and "volumetric heating" occurs when heat is generated across the whole volume. This improves the diffusion rate and minimises the reaction time [63]. Additionally, Antonio *et.al.* [64] presented measurements and theory which proved that the microwave heating can enhance the overall reaction rate by enhancing the diffusion of an active species compared with conventional heating. The thermal effect arises from the different characteristics of microwave dielectric heating and conventional heating which are summarised in **Table 4.5**.

Table 4.5 Characteristics of microwave and conventional heating [61].

Microwave heating	**Conventional heating**
Dielectric polarisation	Conduction/convection
Coupling at the molecular level	Superficial heating
Rapid	Slow
Volumetric	Superficial
Selective	Non-selective
Dependent on the properties of the material	Less dependent

Utilisation of microwaves provides more advantages than conventional heating including a rapid process heating (deep internal heating) (**Figure 4.12**), a reduced processing time as a result of the high heating rate, more uniform and homogeneous heating, and more energy efficiency [65, 66].

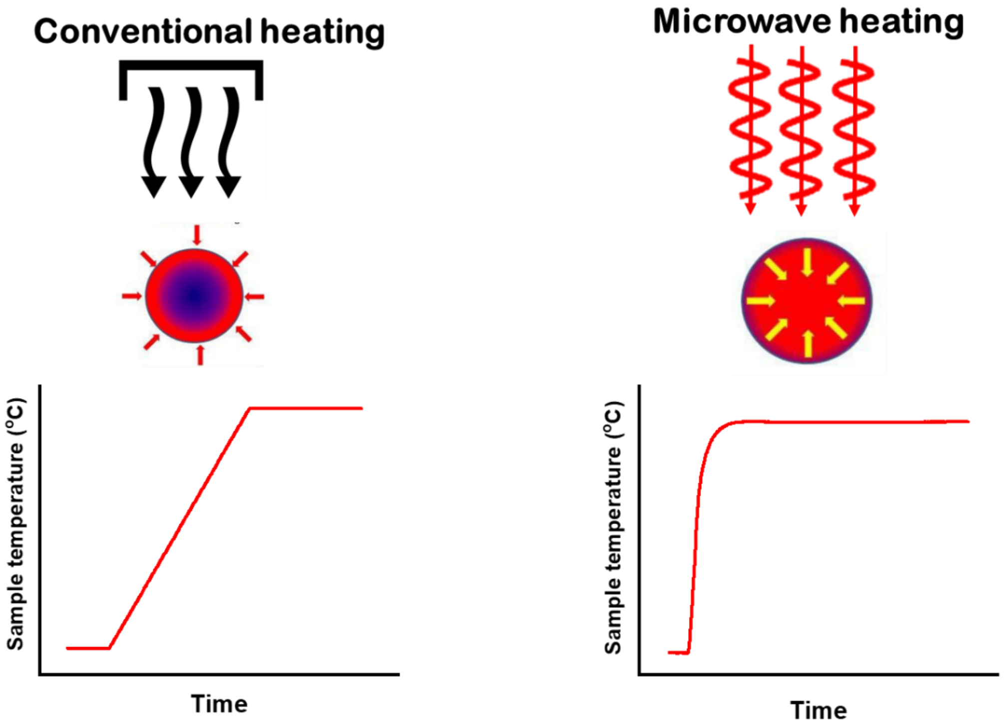

Figure 4.12 Schematic illustration of the difference between microwave and conventional (thermal) heating. (Adapted from Ref. [63]).

In order to confirm the benefit of the microwave heating over conventional heating in the deep-dehydrogenation of fossil hydrocarbons, conventional (thermal) experiments were carried out using an electric tubular furnace as described in detail in chapter 2. The results in **Figure 4.13** show clearly the significant decrease in gas production by the thermal process compared with microwave process. It is also observed that the amount of total evolved gases increased with increasing temperatures in the thermal-assisted process (**Figure 4.13a**), and the amount of hydrogen produced was highest at 1000 °C, but at such a high temperature this was accompanied by a remarkable increase in the evolution of light hydrocarbons and some undesired products (e.g. methane and CO_x), and this explains the drop in the hydrogen selectivity in **Figure 4.13b**. A clear trend was also observed in LCO conversion and hydrogen yield owing to the temperature increase.

Thus, the microwave experiment under the optimal conditions discussed above shows consistently higher hydrogen concentration than the corresponding thermal heating process, with nearly 2.5 times higher hydrogen yield and LCO conversion. This is confirmation that the rapid heating of the metal catalyst particles clearly increases the desirable product selectivity and yield likely as a consequence of the rapid diffusion of the molecules toward the active sites, high reaction rates and the concomitant diffusion away from the active site by molecular hydrogen. A detailed composition analysis of products is given in **Table C4** (Appendix C).

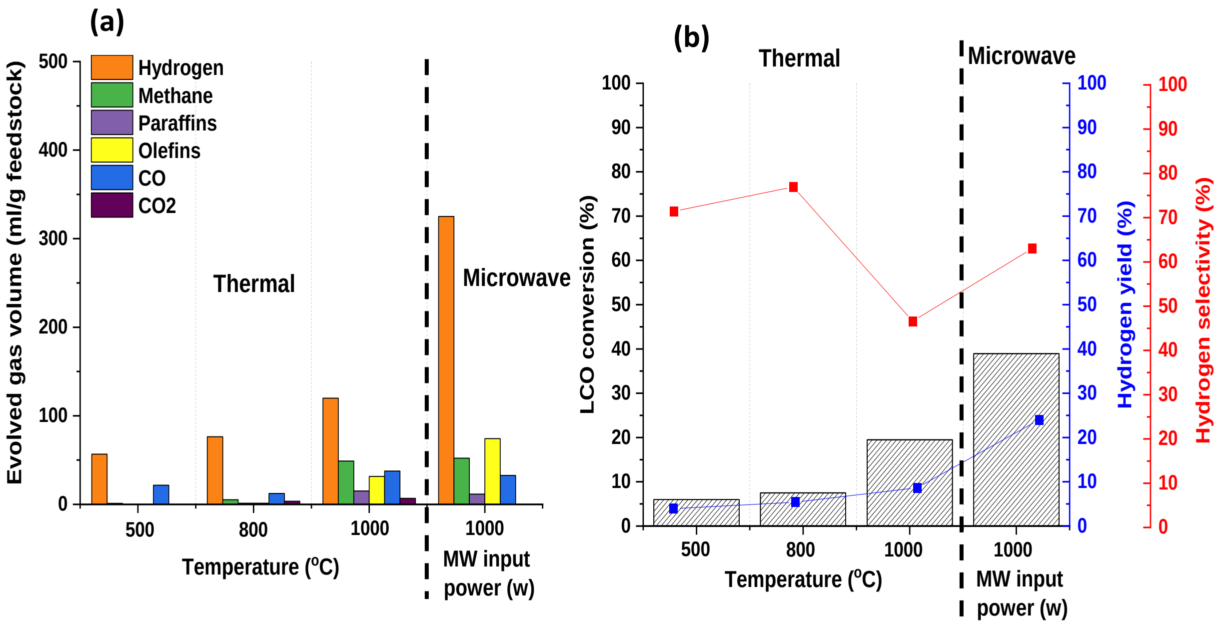

Figure 4.13 Comparison of microwave and conventional thermal process of 0.5 g of LCO sample mixed with 0.5 g of 30 wt.% Fe/AC. (a) the total evolved gas volume, (b) LCO conversion, hydrogen yield and selectivity for 10 min reaction time.

Turning to the important consideration of energy consumption in these processes, the electricity power consumption in both the microwave system and the electric furnace was calculated using the following equation;

$$E = P \times t \qquad \textbf{(Equation 4.3)}$$

Where, E is the energy in kilowatt-hours (kW.h), P is the power input in kilowatts (kW), and t is the reaction (irradiation) time in hours.

The experiment time was kept at 10 minutes, and the power input for electrical furnace and the microwave was 2 kW and 1 kW respectively. So, based on the **Equation 4.3** and by assuming the microwave magnetron efficiency is 100 %, the required energy for electrical furnace and the microwave was 0.33 and 0.167 kW.h respectively. We can therefore conclude that the microwave-initiated catalysis process is likely more efficient in saving energy than the electrical furnace in the lab scale.

Further studies and calculations need to be carried out in a such complex system with the combination of LCO and the catalyst will be required in order to calculate the complete energy balance and – particularly- how much energy is required to generate 1 mole of H_2.

4.3.4 Microwave-initiated Catalytic Activity of Different Transition Metals Catalysts Supported on Active-carbon for the Deep-dehydrogenation of Light Crude Oil (LCO)

Transition metals (such as cobalt, iron, and nickel) are widely used as catalysts in industrial processes due to their inherent chemical and physical properties like variable oxidation state and good conductivity of heat and electricity. They also have partially filled d-orbitals so they can easily give and take electrons depending on the nature of the reaction [67, 68]. Thus, a preliminary screening of different active metals has been done to identify trends in catalytic performance for hydrogen production using LCO. For this purpose, a variety of transition metals which were reported to be active for deep-dehydrogenation processes in earlier literature [69, 70] were investigated.

4.3.4.1 Effect of Ni/AC Catalysts at Different Ni loading

A range of Ni loading catalysts (5, 10, 20, 30, 40, 50 wt. %) were examined using LCO as feedstock and AC as a support material, whilst keeping constant all other experimental conditions (i.e. 1000 W input power and 10 minutes irradiation time using 50 wt.% LCO mixed with variable loadings of Ni/AC catalyst). The activity of the different Ni loading on the total evolved gas and LCO conversion, H_2 yield, and selectivity are presented in **Figure 4.14**. A clear trend was observed for H_2 concentration with an increase in Ni loadings, with a maximum value reached at around 275 ml/g LCO with 20 wt. % Ni loading (**Figure 4.14a)**. Moreover, the 20 wt. % Ni loading catalyst showed the highest LCO conversion of around 33 %, while the conversion level was fairly stable around 25 % for the other Ni loadings. The H_2 yield and selectivity also show a considerable increasing trend and reached their highest values around 22 % and 60 % respectively for the 20 wt.% Ni loading. The H_2 yield and selectivity then gradually decreased at the higher Ni loadings (30, 40, and 50 wt. %) to 10 and 39 % respectively, with increasing the formation of olefins and CO_X; and decreasing in the volume of methane (**Figure 4.14b)**. It can be seen from the distribution of the by-products (light hydrocarbons and CO_x gases) that their mechanisms are clearly different compared to the iron/iron carbide catalysts, where the main dehydrogenation mechanism was the same. A detailed composition analysis of products is given in **Table C5** (Appendix C).

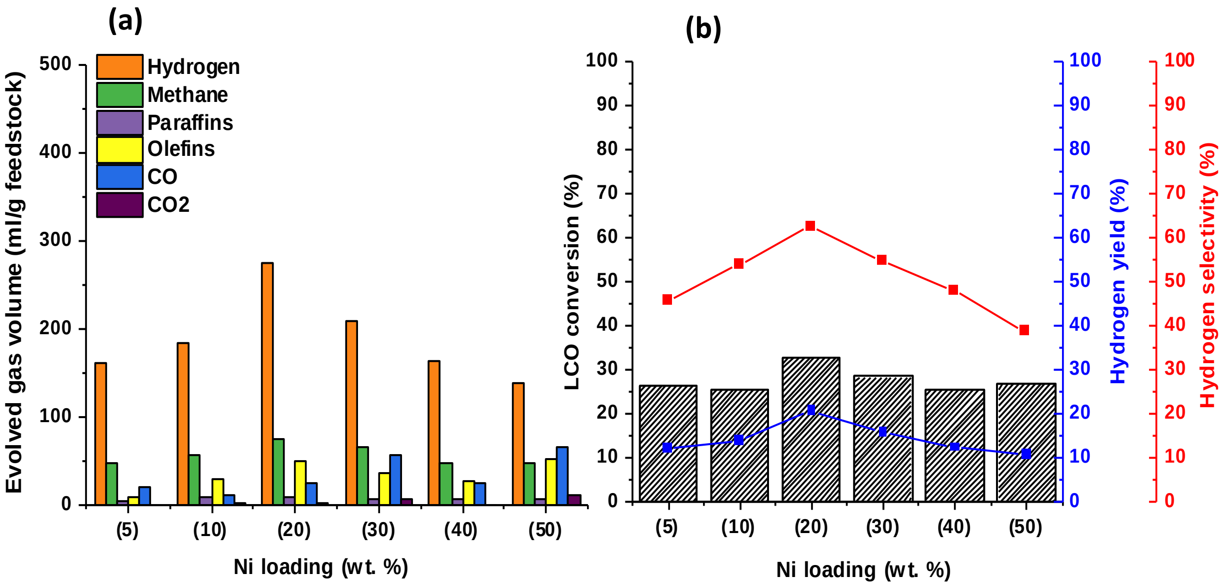

Figure 4.14 Microwave-initiated dehydrogenation of 0.5 g LCO mixed with 0.5 g of Ni/AC catalysts at different Ni loadings, (a) the total evolved gas volume, and (b) LCO conversion, hydrogen yield and selectivity at a microwave input power of 1000 W for 10 min.

4.3.4.2 Effect of Co/AC Catalysts at Different Co Loading

Under the same conditions as described with Ni catalysts, a series of experiments has been carried out in order to investigate the activity of different loadings (5, 10, 20, 30, 40, 50 wt. %) of cobalt supported on AC as shown in **Figure 4.15.** As a general observation, **Figure 4.15a** shows a fairly similar trend to that shown by Ni catalysts. There was a noticeable improvement in H_2 concentration compared with the Ni case: the 20 wt. % Co loading containing catalyst showed the highest hydrogen concentration at around 320 ml/g LCO, in line with LCO conversion at 37 % and H_2 yield and selectivity at 24 % and 65 % respectively. Moreover, low levels of light hydrocarbons (methane, olefins and paraffins) and CO_x gases were observed (**Figure 4.15b**). A detailed composition analysis of products is given in **Table C6** (Appendix C).

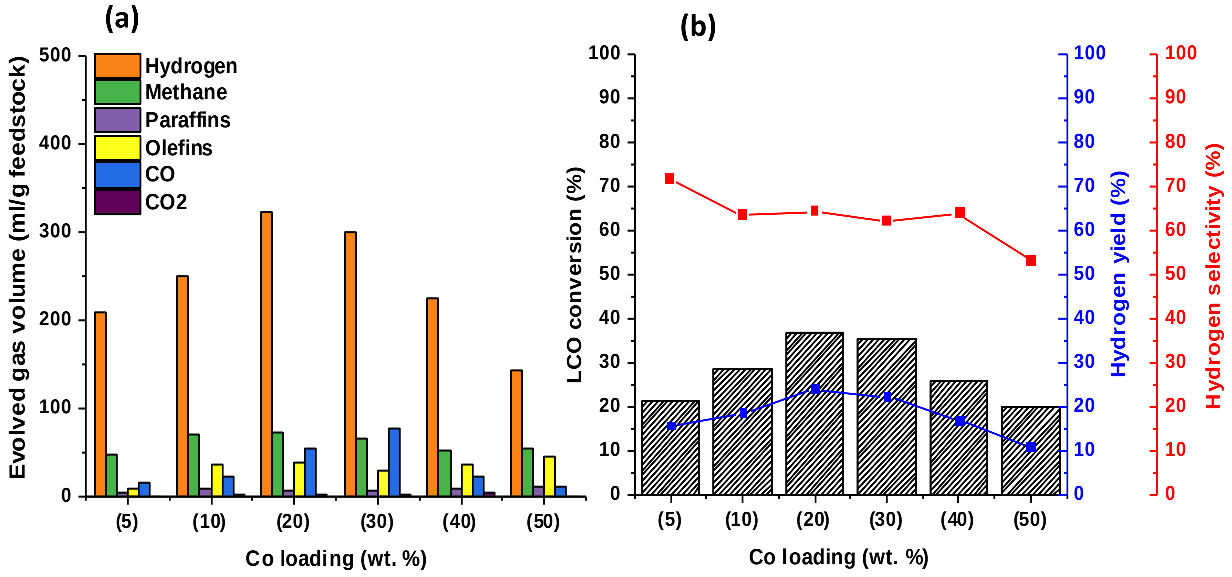

Figure 4.15 Microwave-initiated dehydrogenation of a 0.5 g LCO mixed with 0.5 g of Co/AC catalysts at different Co loadings, (a) the total evolved gas volume, and (b) LCO conversion, hydrogen yield and selectivity at a microwave input power of 1000 W for 10 min.

4.3.4.3 Effect of Bimetallic Ni-Fe supported Catalysts in AC at Different Loading

In summary, amongst the range of studied catalysts, the system comprising 30 wt. % Fe and 20 wt.% Ni and Co catalysts exhibited the highest H_2 yield and selectivity compared to the other catalysts of their own series at a microwave power input of 1000 W set at a period of 10 minutes of irradiation time. These data encourage us to further investigate the optimisation of bimetallic catalyst formulation in order maximise the hydrogen production. Thus, several bimetallic catalysts have been prepared (as described in **Section 4.2.1**) and tested under microwave initiation.

Figure 4.16 shows the catalytic activity data for Ni-Fe/AC bimetallic catalysts at different metal loadings. The selected total metal loading was 30 wt. % and several formulations were prepared by varying Ni and Fe loadings (i.e. 5Ni-25Fe, 10Ni-20Fe, 15Ni-15Fe, 20Ni-10Fe, and 25Ni-5Fe wt. %). There was no remarkable change in H_2 concentration, the composition varied between 200 and 300 ml/g LCO (**Figure 4.16a**), with stable concentration of light hydrocarbons and CO and nearly zero CO_2. **Figure 4.16b** shows small changes in LCO conversion and hydrogen yield with different metal loadings, i.e., conversion was between 30 and 37 %, whilst the hydrogen yield was around 20 %. Furthermore, there is a slight increase in hydrogen selectivity from 55 to ca. 67 %. A detailed composition analysis of products is given in **Table C7** (Appendix C).

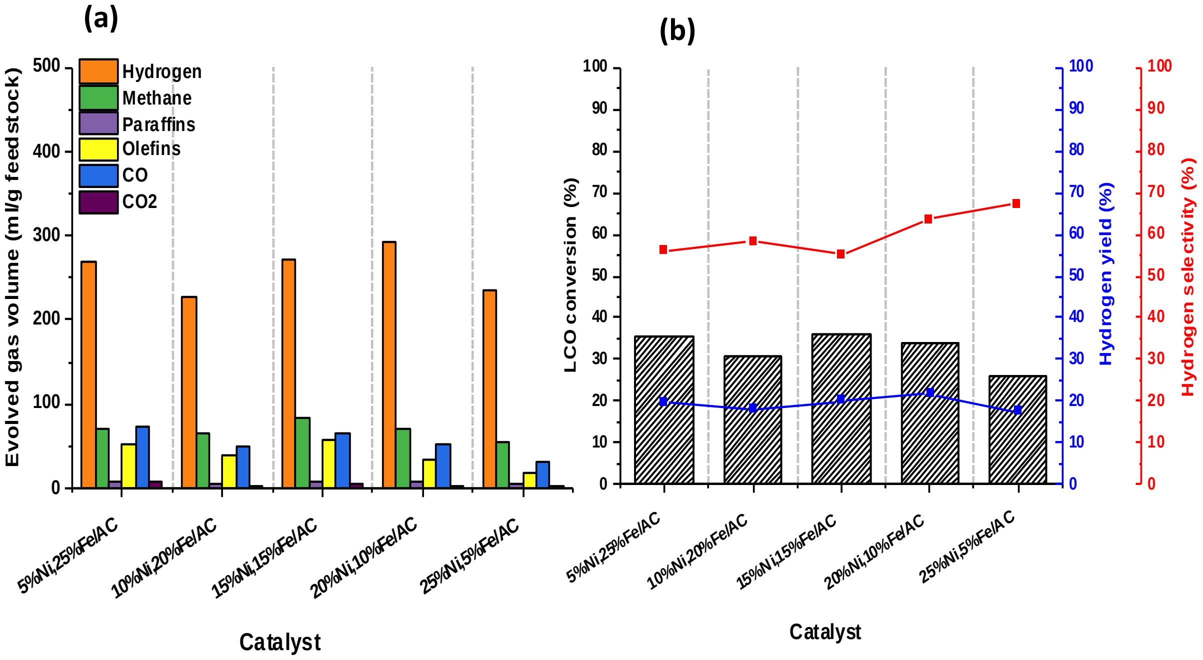

Figure 4.16 Microwave-initiated dehydrogenation of 0.5 g of LCO mixed with 0.5 g of bimetallic catalysts at different Ni and Fe loadings, (a) the total evolved gas volume, and (b) LCO conversion, hydrogen yield and selectivity at a microwave input power of 1000 W for 10 min.

4.3.4.4 Effect of Bimetallic Co-Fe Supported Catalysts on AC at Different Loading

Co-Fe bimetallic catalysts supported on AC were also investigated for H_2 production under microwave radiation (**Figure 4.17**). As previously observed in **Figure 4.15**, 20 wt.% content of Co was the optimal loading and the bimetallic catalysts used had the following compositions: (5Co-15Fe, 10Co-10Fe, and 15Co-5Fe wt.%). The H_2 concentration was fairly similar for all loadings and ranged between 250 and 300 ml/g LCO, associated with low level of CO and light hydrocarbon with no CO_2 emission. (**Figure 4.17a**).

A slight improvement in LCO conversion (39 %) and hydrogen yield (22 %) at total 20 wt. % metals loading (10Co + 10Fe) are depicted in **Figure 4.17b**, and this is consistent with the observation in **Figure 4.15** that 20 wt. % loading was the optimal catalytic system. The hydrogen selectivity was around 65 % and was diminished slightly at 10 wt. % Co,10 wt. %Fe/AC due to the increase of undesirable products (light hydrocarbons and CO). The relatively small effect of changing Fe and Ni or Co loadings on the catalyst performance of the bimetallic formulations might be associated with the comparable catalytic performances of the monometallic (Fe, Co and Ni) catalysts toward H_2 generation. A detailed composition analysis of products is given in **Table C8** (Appendix C).

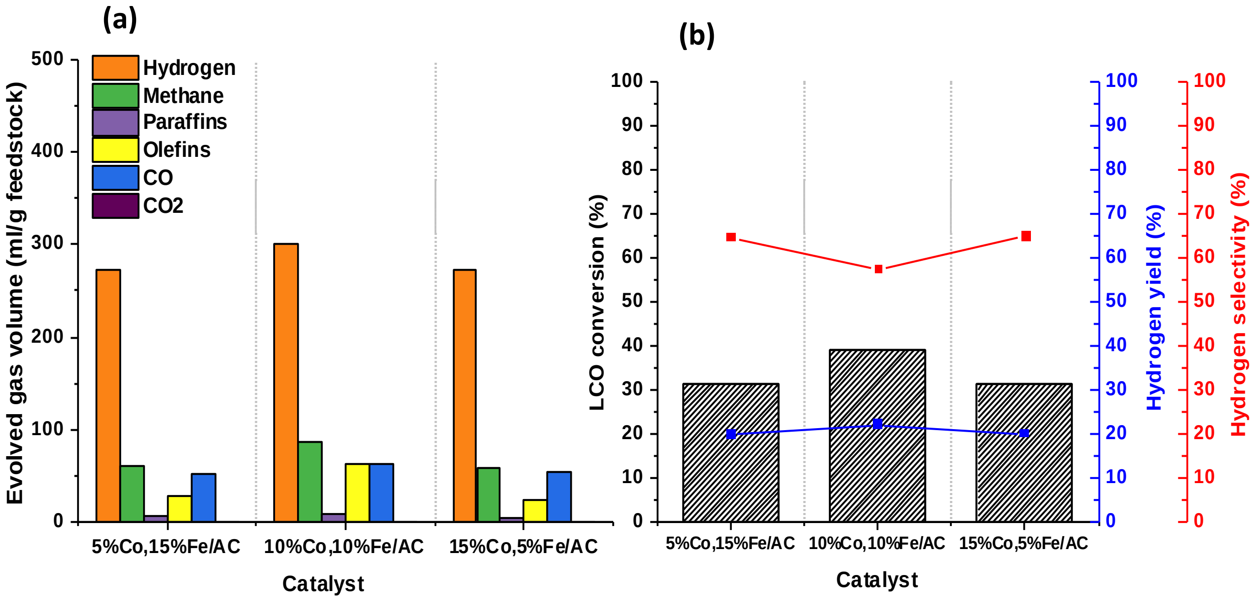

Figure 4.17 Microwave-initiated dehydrogenation of 50 wt.% LCO mixed with bimetallic catalysts at different Co and Fe loadings, (a) the total evolved gas volume, and (b) LCO conversion, hydrogen yield and selectivity at a microwave input power of 1000 W for 10 min.

4.3.5 The Size-Induced Metal-Insulator Transition (SIMIT): A Phenomenon for Optimising Heat Generation and Performance under Microwave-Initiation Catalysis

4.3.5.1 A Study of the of Temperature Dependence and Absorption Energy on Different Microwave Input Power on LCO

Microwave–initiated catalysis is a fascinating excellent example of an inherently complex system since the heating rate (or temperature) of the overall system involves the dielectric losses *both* of an individual heterogeneous catalyst particles and volume feedstock whose dielectric properties can suddenly change upon the reaction time.

For instance, the inevitable time-dependent deposition of elemental carbon and possible concomitant formation of Fe_3C will invariably affect the microwave absorption of a Fe/AC catalyst and hence the heating generated via interfacial polarization at the surface of the microwave-absorbing Fe/AC catalyst particles. Simultaneously, the large variety of organic molecules with different functional groups and imaginary permittivity (or dielectric loss) present in the LCO will generate heating via dipole polarization at the surface of Fe/AC catalyst particles. Moreover, LCO itself can contribute to the heating of the catalyst system as shown in the dependence of the sample temperature and adsorbed microwave power, as illustrated in **Figure 4.18** for LCO.

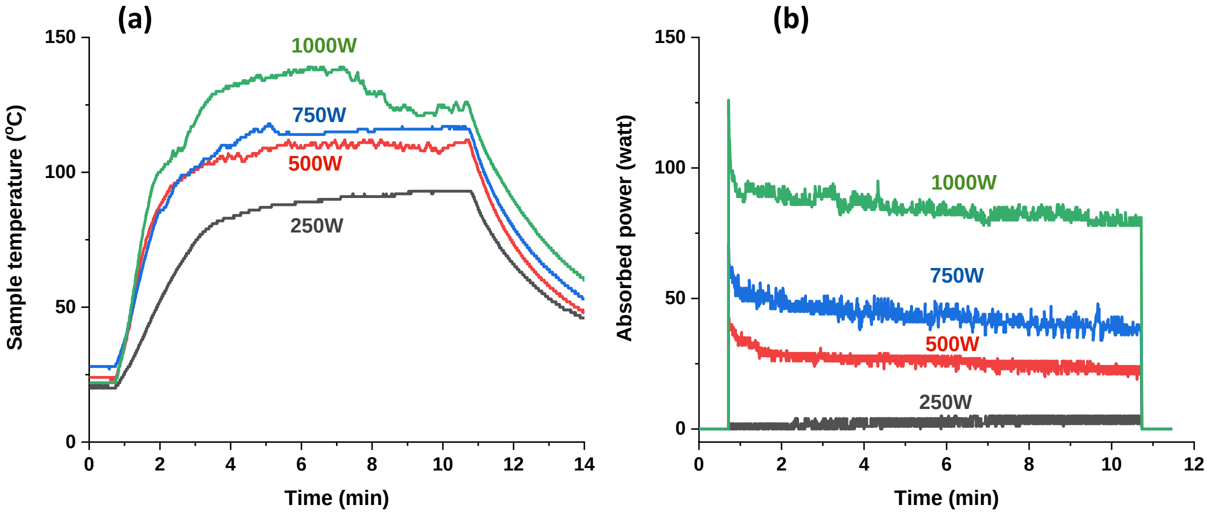

Figure 4.18 Dependence of (a) The sample temperature, and (b) Adsorbed microwave power, of LCO sample treated at different microwave input powers *without catalyst*.

Of course, this response to microwave radiation rapidly changes when the molecules are chemically adsorbed at the catalyst surface and catalytically dehydrogenated through a series of consecutive reactions with rapid desorption of product H_2 molecules and continuing time-dependent deposition of residual carbon.

4.3.5.2 Study of the Time Dependent Induced Temperature on LCO Sample with Various Loadings of Fe on AC with Time at a (constant) Microwave Input Power of 1000 W

Turning now to the behaviour of catalyst particles of different sizes under microwave irradiation, it is envisaged that a local increase in the electric field strength and a significant difference in heating rates between the catalyst particles and the LCO are taking place considering the temperature-time profiles given in **Figure 4.19** for the range of catalyst samples with different Fe loading levels.

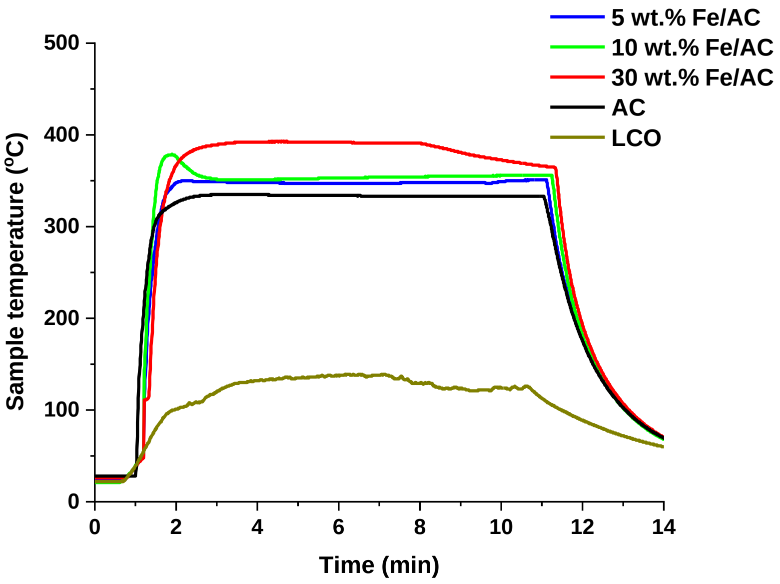

Figure 4.19 The dependence of the sample temperature with time of LCO, AC, as well as different wt.% loading of Fe/AC catalyst, at a microwave input power of 1000 W and 10 min irradiation time.

Interestingly, the 30 wt. % Fe/AC catalyst, reaches a temperature nearly 2.5 times higher than LCO alone over the same time period. It is also noticeable that the 5 and 10 wt. % Fe/AC catalysts show fairly similar temperature profiles, and their stable temperatures are only slightly lower than that for the 30 wt. % Fe/AC formulation. Obviously, these profiles are strongly affected by the changes in the density, heat capacity and dielectric loss. We further considered the dependence of the bed temperature and microwave absorbed power upon the reaction time (as shown in **Figure 4.11c**). It is striking that the catalyst bed temperature falls from 500 °C to 345 °C, and the absorbed power decreased to 90 W after 10 min of (continuous) time-on-stream, and the temperature and absorbed power are then maintained until the microwave source is turned off. This shows that the heating rate of flowing LCO across the Fe/AC catalyst is directly determined by the imaginary permittivity (or dielectric loss) of the overall system (LCO + Fe/AC) and the field strength E (or input power) and inversely proportional to the density and the specific heat of LCO + Fe/AC according to **Equation 4.2**. It is expected that the significant changes in the size of nanoparticles of Fe as a consequence of the different Fe loadings in the catalyst formulations also affect the temperature profiles.

The average crystallite size (τ) of the Fe nanoparticles with different Fe loadings was also determined for samples before and after microwave experiments through application of the Scherrer equation to the XRD data (**Equation 2.2**).

Table 4.6 shows the average crystallite size determined by X-ray powder diffraction analysis of Fe/AC samples using the X'Pert HighScore software. As expected, the crystallite size of the Fe nanoparticles increased at larger Fe loadings: 20 nm < 77 nm < 88 nm < 96 nm < 108 nm < 121 nm for 5, 10, 20, 30, 40, and 50 wt.% samples, respectively, which is indicative of lower Fe dispersion on the activated carbon. Also note that the H_2 yield steadily increased with Fe loading (and decreasing AC content) to achieve a maximum at 30 wt. % Fe and then decreased at higher Fe loading (i.e., 50 wt. %).

Table 4.6 Average crystallite size determined by X-ray powder diffraction analysis of Fe/AC catalysts before and after the microwave-initiated deep-dehydrogenation of LCO sample mixed with catalysts of different Fe loading on AC at 1000 W of input power. The error of the measurements is around ± 5 %*

Wt. %Fe/AC	Crystallite size [nm] (Before reaction)	Crystallite size [nm] (After reaction)
5	20	17
10	77	82
20	88	108
30	96	109
40	108	120
50	121	120

* The error calculation was estimated following the procedure described in Appendix A.

The increase in evolved H_2 amounts in the Fe/AC catalyst is attributed to enhanced catalytic performance of Fe/AC particles as the Fe content increases. It is possible that in this size regime that the so-called Size-Induced Metal-Insulator Transition (SIMIT) [71-73] might play a pivotal role in this critical catalytic behaviour.

The striking diminution of H_2 yield for high loading of Fe (50 wt.%) on AC is most likely associated with its poor microwave absorption due to high reflection of microwave energy due, potentially, to a larger crystallite size arising from the coalescence of Fe particles. Importantly, however, the average crystallite size of the spent samples after microwave initiation did not vary markedly relative to the sample before reaction (**Table 4.6**), excepting the significant diminution of the crystallite size of 5 wt.% Fe/AC catalyst due to the complete carburization of Fe into Fe_3C.

Apparently, the formation of iron carbide causes the segregation of Fe nanoparticles, thereby enhancing the catalyst stability.

To probe the size-dependence of the microwave absorption of different catalyst particle sizes, a number of catalyst samples were carefully heat-treated to induce controlled coagulation of the particles and hence increase their mean particle sizes. The dependence of crystallite size with annealing temperature is summarised in **Figure 4.20a,b**.

For example, a 10 wt.% Fe/AC catalyst was treated at various temperatures: 750, 850, 950, and 1050 °C to control the particle size. **Table 4.7** shows the average crystallite size of 10 wt.% Fe/AC catalysts under variable annealing temperatures. It is expected that the AC support does not take part in the coalescence of Fe nanoclusters since it is usually synthesised at high temperatures and has high thermal stability [74].

Turning to the effects of microwave irradiation on these various particles, and their subsequent microwave power absorption, it is important to note that the microwave heating and H_2 yield increased at lower crystallite size of Fe nanoparticles following the order: 121 nm (380 °C) < 137.8 nm (345 °C) < 148.1 nm (325 °C) < 150.9 nm (315 °C).

Table 4.7 Average crystallite size determined by X-ray powder diffraction analysis of 10 wt.% Fe/AC catalysts under variable annealing temperatures. The error of the measurements is around ± 5 %*.

Annealing temperature (°C)	Crystallite size [nm]
750	121
850	138
950	148
1050	151

* The error calculation was estimated following the procedure described in Appendix A.

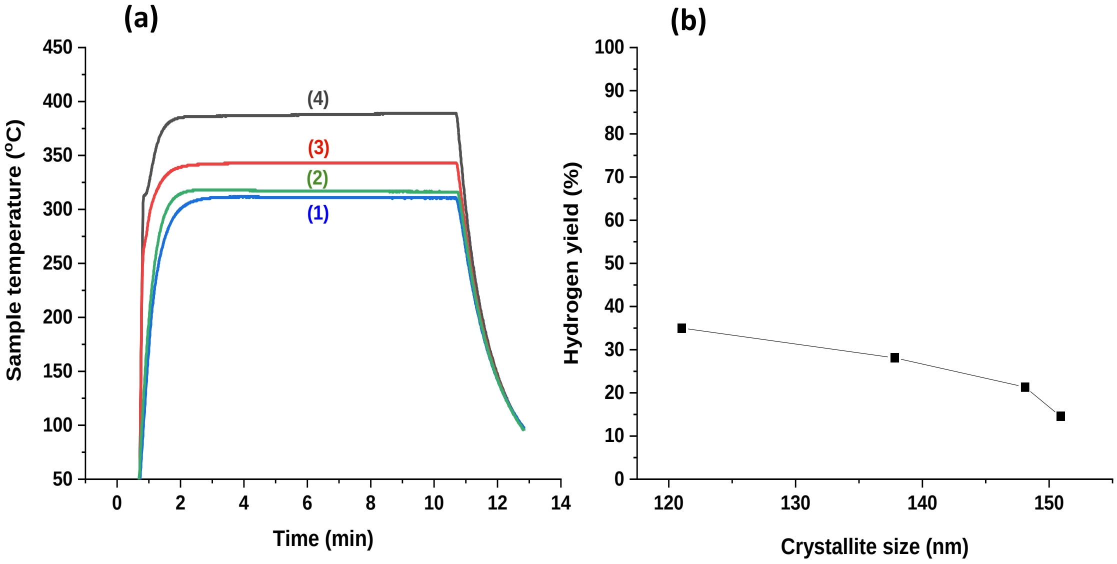

Figure 4.20 The dependence of the sample temperature with time of unsupported 10 wt.% Fe/AC, (a) Different pre-treatment temperatures: (1) 1050, (2) 950. (3) 850, and (4) 750 °C, (b) The dependence of the hydrogen yield with crystallite size, at microwave input power of 1000 W and 10 min irradiation time.

It is important to note that Scherrer's equation can only be applied for average sizes up to about 100–200 nm (depending on the instrument, sample, and signal-to-noise ratio), because diffraction-peak broadening decreases with increasing crystallite size and it becomes difficult to separate the peak broadening due to crystallite size from the broadening due to other factors. The average crystallite size can better and more efficiently be determined in conjunction with SEM and TEM techniques.

Turning to a consideration of the SIMIT, the successive fragmentation of metal particles can lead to fundamental changes in their electronic properties. A microscopic particle of bulk metal presents a continuous energy level, further fragmentation decreases the bandgap and metal particles in sub nanometric scale **(Figure 4.21**) [43]. Previous research studies in the literature have shown that the SIMIT effect also influences the fundamental dielectric properties of the metal particles [43, 71, 75, 76] and obviously their capability to generate the necessary heat via microwave absorption for any catalytic process. In fact, a recent study demonstrates that the relative permittivity and conductivity of the metal oxide-type supports followed by Pt metal size and Pt loading are very important parameters for efficient generation of microwave heating from Pt/metal oxide (Al_2O_3, $MgAl_2O_4$, TiO_2, $SrTiO_3$) composites [77].

Herein, we found strong experimental evidence that small Fe nanoparticles within the ca. 120-150 nm size range on a support of activated carbon contribution enhances not only the microwave heating but also - and most importantly - the generation of H_2 from LCO. This important finding indicates that the careful control of the nanosize of Fe particles is an excellent strategy to enhance not only the efficiency of microwave heating but also, with that, the catalyst performance toward H_2 generation (**Figure 4.20b**).

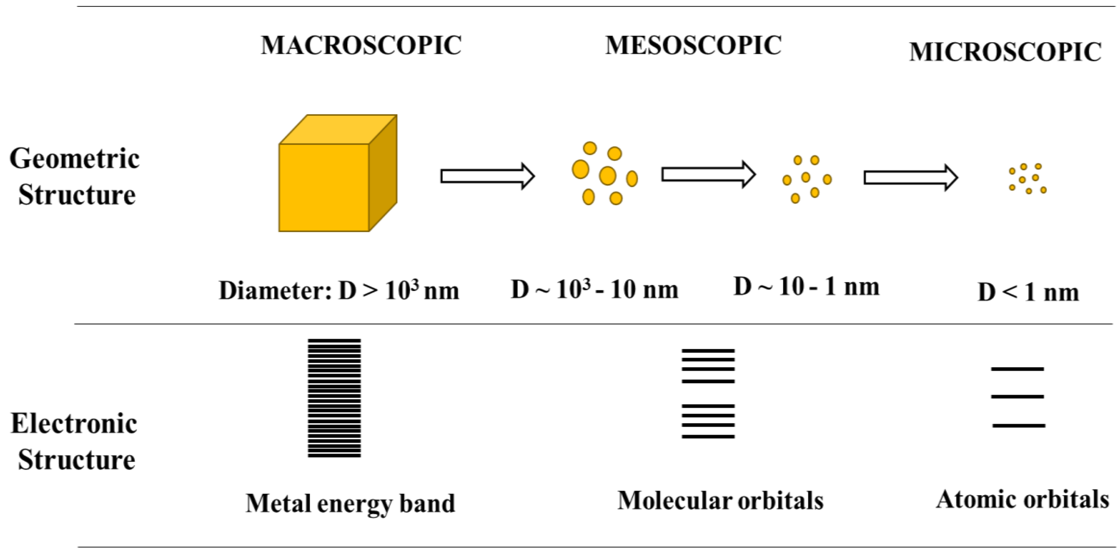

Figure 4.21 A representation of geometric and electronic structure of the successive fragmentation of a single grain of metal. (Adapted from Ref. [43, 72]).

4.3.6 Dielectric Properties of LCO and Prepared Catalytic Samples

This study was conducted in an attempt to understand the fundamental microwave absorption properties of the system as a prelude to their catalytic properties under microwave initiation.

4.3.6.1 Dielectric Properties of LCO

The change in the resonance peaks of the LCO and gasoline (for comparison) samples using the cavity perturbation technique are presented in **Figure 4.22**. It can be seen that the shift in frequency was higher for LCO than gasoline whilst the bandwidth was similar for both samples. This trend was confirmed with cavity perturbation measurements of the loss tangent (tan δ), resulting in values of 1.48×10^{-5} and 3.47×10^{-5} for gasoline and LCO respectively. The higher LCO loss tangent indicates its ability to convert microwave energy into heat, due to presence of polar molecules such as water, sulphur and nitrogen organic compounds. The low content of polar compounds in gasoline rationalises its low loss tangent [78].

These important data set the scene for any fossil-fuel-derived, intrinsic, contribution to the overall microwave absorption and therefore to the heating of the catalyst bed as discussed earlier in **Figure 4.18**, and of course the metal catalyst also makes an important contribution as previously reported.

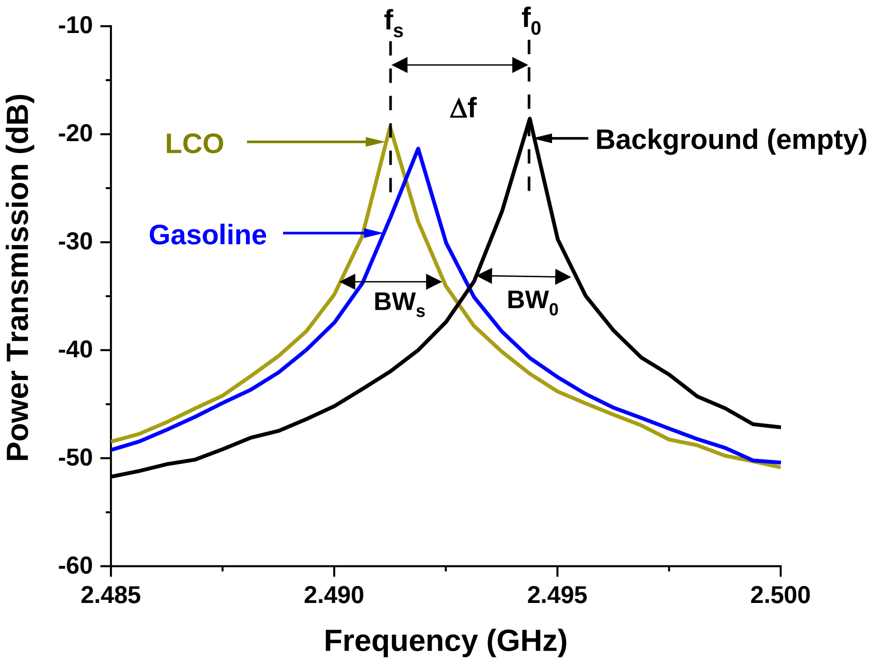

Figure 4.22 Microwave – absorption (cavity perturbation technique) resonant curves as a function of frequency for LCO and gasoline fuel.

4.3.6.2 Dielectric Properties of Unsupported Fe Particles having Different Sizes

The resonant curves for different Fe particle size are shown in **Figure 4.23a**. Noticeably, there is a strong shift in frequencies for Fe samples with particle size of 841 × 10^3, 210 × 10^3 and 35-45 nm, whilst the 60-80 and 25 nm Fe particles showed intermediate vales of resonant frequency, which is proportional to the real permittivity. On the other hand, the bandwidth for the samples with the smaller particle sizes (i.e., 25, 35-45 and 60-80 nm) was noticeably broader than the larger samples (i.e., 841 × 10^3, 210 × 10^3 nm) owing to their different imaginary permittivity values. In **Figure 4.23b**, Fe samples with nanoscale particle size

(<100 nm) show a plateau temperature in the ranging between 215 and 288 °C, noticeably higher than samples with larger particle size (which attain ~150 °C). A similar trend can be observed with the heating rate of the samples, indicating that the particle size affects both the heating rate and the plateau temperature of the sample and hence the catalytic activity **(Table 4.8)**.

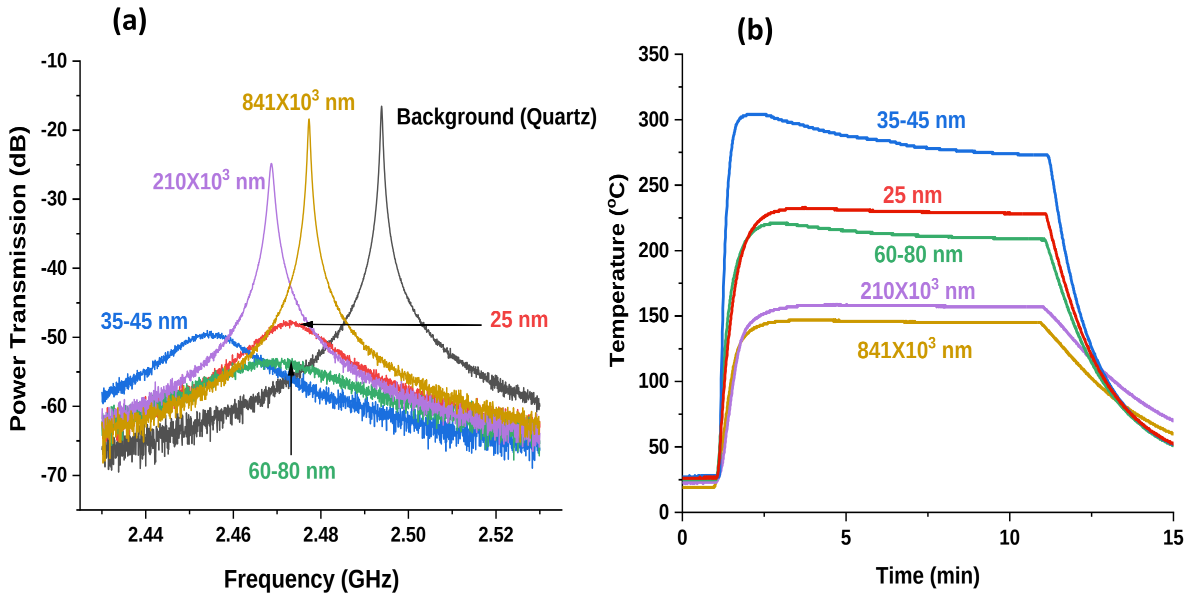

Figure 4.23 (a) Microwave – absorption (cavity perturbation technique) resonant curves as a function of frequency for the TM010 mode for different Fe particle sizes. (b)The dependence of the sample temperature with time of Fe/AC catalyst at different Fe particle sizes, at a microwave input power of 500 W and 10 min irradiation time.

Table 4.8 Dielectric properties of Fe samples with different particle sizes. The values given show an average of at least 3 measurements*

Fe Sample (nm)	Real permittivity (ε')	Imaginary permittivity (ε'') × 10^2	Loss tangent ($\tan \delta$) × 10^2	Sample temperature (°C)	Heating rate (°C/min)
25	NM**	NM	NM	231	276
35-45	NM	NM	NM	288	399
60-80	4.57	7.5	1.65	215	304
210 × 10^3	9.69	9.8	1.01	159	185
841 × 10^3	6.88	1.2	0.18	146	171

* The error calculation was estimated following the procedure described in Appendix A.
**NM: no measurement due to technical difficulties for lossy samples.

In fact, the Fe samples series in **Figure 4.24a** show a maximum bed temperature and heating rate at 288 °C and 399 °C/min respectively for the Fe particle size ranging between 35-45 nm with, importantly, the larger particle size showing a decrease in the sample temperature and heating rate. Obviously, the sample temperature and heating rate increased with rising loss tangent as given in **Figure 4.24b** due to the more effective conversion of microwave energy into heat.

This finding can be rationalised through a consideration of the SIMIT where the successive fragmentation, or division, of metal particles will ultimately inhibit the electronic conductivity within the metal particle and thereby decrease the bed temperature [74]. It is this transition from the metallic (bulk, macroscopic) through to the insulating (mesoscopic and microscopic) extremes within the catalyst particle that will ultimately enhance the microwave absorption of nominally metallic catalyst particles [43].

Interestingly, the skin depth of Fe particles is approximately 41.5 nm [79] in agreement with the maximum temperature of the studied Fe particle series, indicating that the absorbed electromagnetic energy is efficiently converted into heat. For Fe particles with sizes larger than the skin depth (> 40 nm) will absorb the microwave energy less efficiently and hence decreasing the bed temperature, as observed in this work.

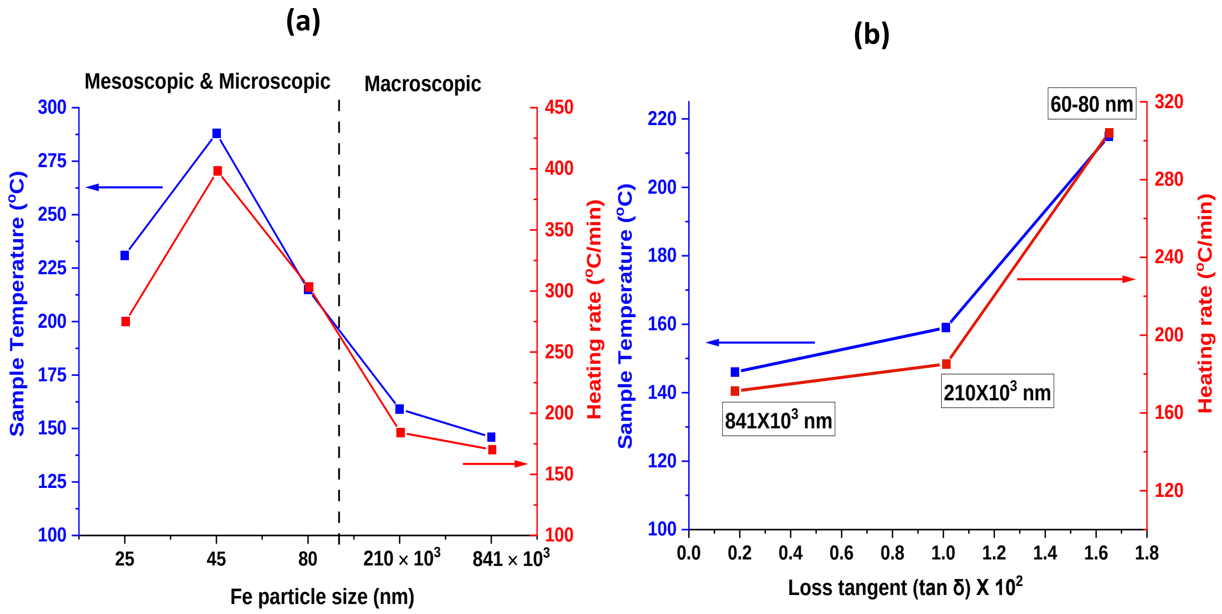

Figure 4.24 The dependence of the sample temperature and heating rate at different (a) Fe particle sizes. (b) loss tangent.

4.3.6.3 Dielectric Properties of Catalysts with Different Fe Loadings on AC support

The dependence of the resonant curves with Fe loadings for Fe/AC catalysts is highlighted in **Figure 4.25a**. Note the strong shift in the resonant frequencies relative to the empty tube frequency (i.e. unperturbed resonant frequency, f_0) for the samples with high loadings of Fe (i.e. 30, 40 and 50 wt. %) whilst low Fe loadings (i.e., 5, 10 and 20 wt. %) did not change markedly the resonant frequency. On the other hand, the bandwidth for the resonant traces of Fe/AC catalysts are clearly broader than that for the reference empty tube regardless of the Fe loading, a clear indication of their high imaginary permittivity values. This was obviously reflected in the T-t profile and the plateau temperature for Fe/AC catalyst at different Fe loadings as shown in **Figure 4.25b**.

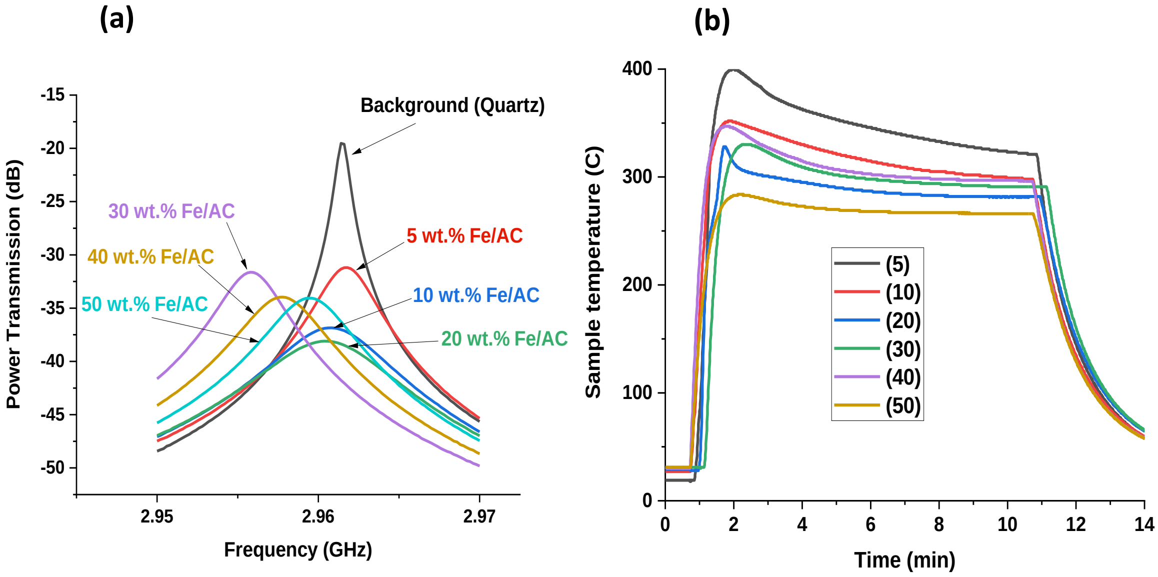

Figure 4.25 (a) Microwave – absorption (cavity perturbation technique) resonant curves as a function of frequency for the TM010 mode for different Fe loading on AC (0, 10, 20, 30, 40 and 50 wt.%). (b) the sample temperature with time of Fe/AC catalyst at different Fe loadings, the number in parentheses for each catalyst shows the metal content, in wt.%. at a microwave input power of 1000 W and 10 min irradiation time.

It is worth noting remarking that the dependency of the sample plateau temperature and heating rate with Fe loading (**Figure 4.26a**) is complex owing to the influence of activated carbon in the heat generation. However, when one considers the influence of Fe particle size, alone, instead of Fe loading, for the sample plateau temperature and heating rate a clear diminution of the sample temperature with the increase of Fe particle sizes is observed (**Figure 4.26b**). An apparent similar trend seems to follow the heating rate with the Fe particle size.

We believe that this experimental finding is a striking indication of the strong influence of Fe particle size in the heating mechanism of the Fe/AC catalyst despite the contribution of activated carbon in the heat generation. The detailed dielectric properties values of different Fe loading on the support AC are shown in **Table 4.9**.

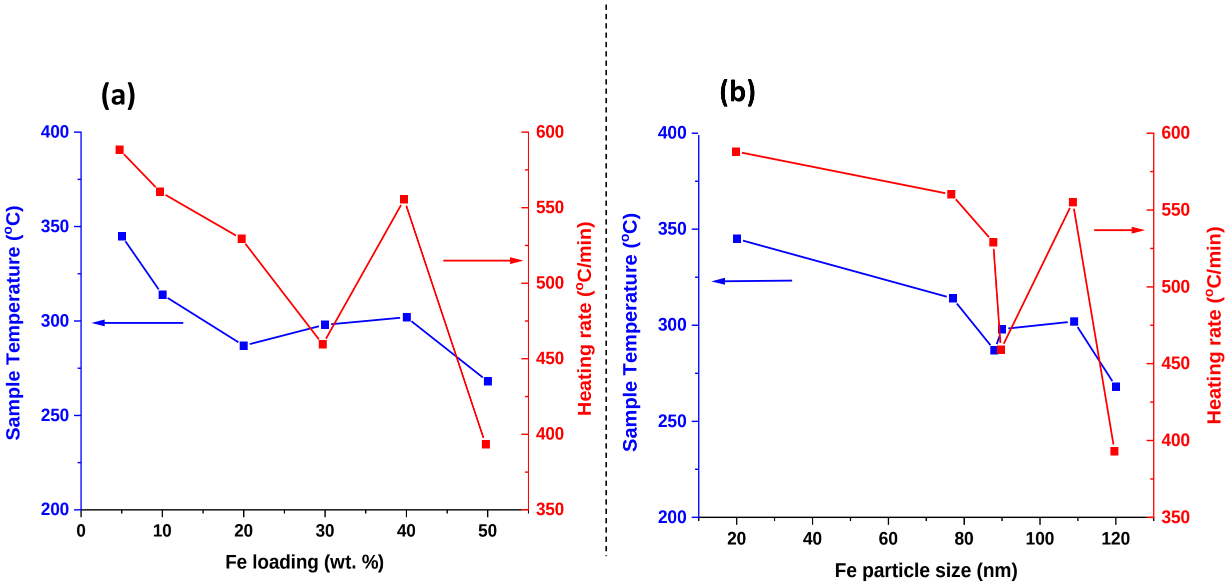

Figure 4.26 The dependence of the sample temperature and heating rate at different (a) Fe loading (wt.%) (b) Fe particle sizes (nm).

Table 4.9 Dielectric properties of different Fe loading on AC. The values given show an average of at least 3 measurements*.

Fe/AC (wt. %)	**Fe particle size (nm)**	**Dielectric constant (ε')**	**Dielectric loss (ε'') × 10^2**	**Loss tangent (tan δ) × 10^2**	**Sample Temperature (°C)**	**Heating rate (°C/min)**
5	20	8.78	2.36	0.27	345	588
10	77	10.04	4.03	0.40	314	560
20	88	9.31	5.12	0.55	287	529
30	90	15.79	3.53	0.22	298	459
40	109	13.56	2.98	0.21	302	555
50	120	11.87	3.03	0.25	268	393

* The error calculation was estimated following the procedure described in Appendix A.

4.3.7 Characterisation of Fresh and Spent Catalysts

4.3.7.1 X-ray Diffraction of fresh and spent Fe/AC Catalysts with Different Fe loading

Fresh catalysts with various Fe loadings on AC and spent samples after microwave-initiated dehydrogenation of LCO at 1000 W for 10 minutes irradiation were analysed by XRD as shown in **Figure 4.27**. No visible major changes were observed between these batches and what it has been shown in **Figure 3.11** in chapter 3 when the feedstock was Hexadecane.

The peaks for iron (Fe) metal at 45°, 66°, and 83° were detected. A very small fraction of iron carbide (Fe_3C) was also detected in the fresh samples according to the peaks at 44° and 52° in 2θ, however, the formation of Fe_3C was significantly enhanced in the spent samples owing to dissolution of carbon into the iron structure.

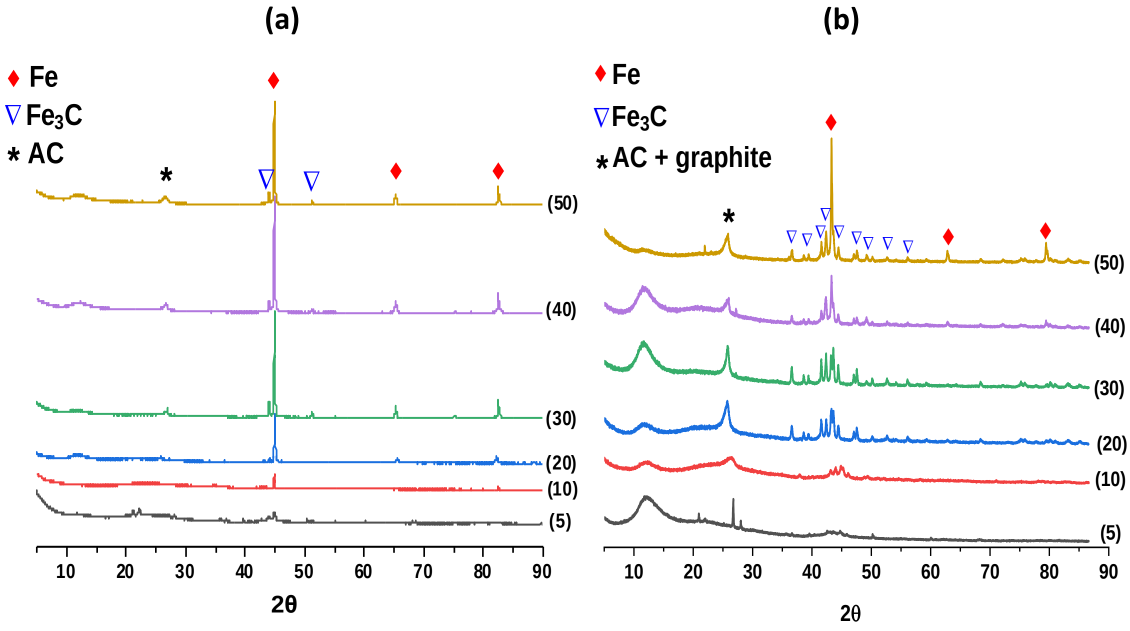

Figure 4.27 The characterization of the fresh and spent samples for microwave-initiated dehydrogenation of LCO. (a) X-ray diffraction patterns of fresh Fe/AC catalyst with different Fe loading (b) After microwave-initiated catalytic reaction. Numbers in parentheses correspond to the Fe loading in wt.%.

4.3.7.2 Scanning Electron Microscopy (SEM) of Fresh and Spent Fe/AC Catalysts with Different Fe Loading

Figure 4.28 shows the SEM images of Fe/AC catalysts both before and after microwave-initiated decomposition of LCO. In the fresh catalysts, particularly in the samples containing 5 wt. % Fe, lighter spots associated with Fe particles are clearly dispersed on large dark particles of AC. After the microwave-initiated catalytic reaction, some growth has occurred on the support surface and there was evidence of formation of other additional carbon phases, such as carbon filaments as shown clearly in the spent sample of 5 and 50 wt. % Fe/AC.

4.3.7.3 Transmission Electron Microscopy (TEM) of Fresh and Spent 30 wt.% Fe/AC Catalyst

A more detailed morphological characterization of the 30 wt.% Fe/AC catalyst was performed using Transmission Electron Microscopy (TEM). As shown in **Figure 4.29**, the iron and iron carbide particles (the dark spots) are well dispersed on the activated carbon surface. The TEM image for the spent sample displays amorphous activated carbon (the light surrounding) and some carbon filaments which are the initial phase of the formation of carbon nanotubes. It is noticeable that there is growth of the carbon fibres from iron nanoparticles and the presence of poorly crystallized carbon material.

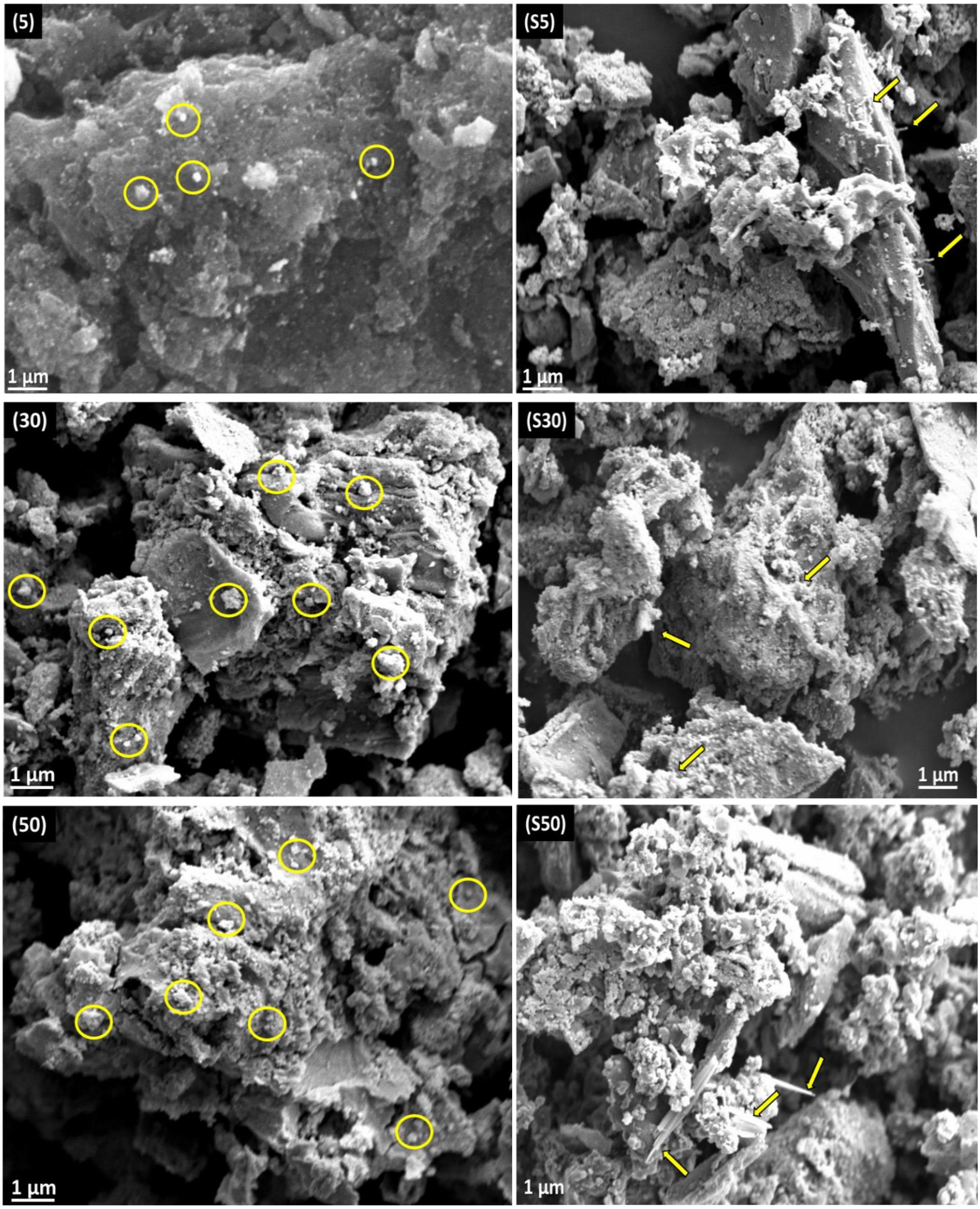

Figure 4.28 Scanning electron microscopy (SEM) of Fe/AC catalysts with various Fe loading, (5, 30, and 50) before and (S5, S30, and S50) after the microwave-initiated catalytic reaction. The number in parentheses shows the Fe loading in wt. %, whilst the circles of yellow colour highlight some of Fe particles, and the yellow arrow indicate carbon fibres.

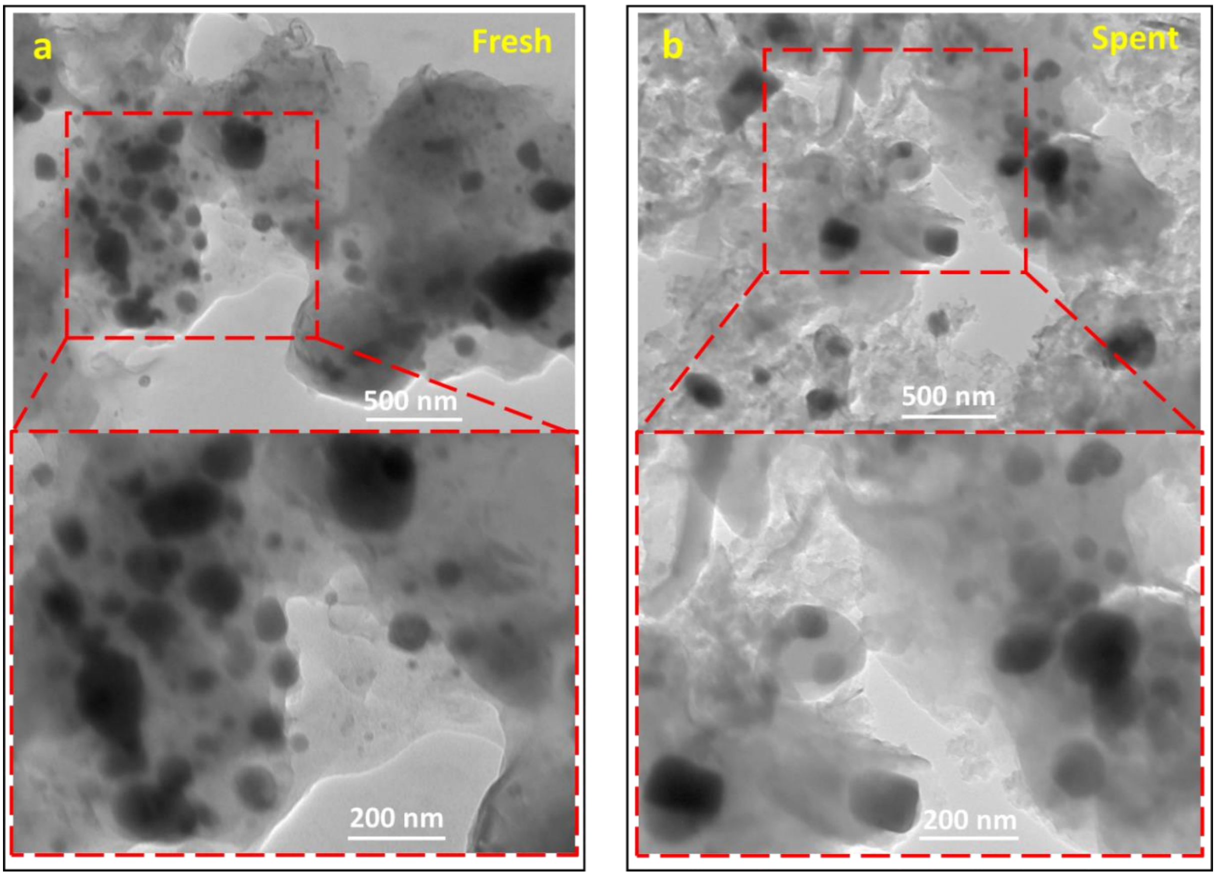

Figure 4.29 Transmission Electron Microscope (TEM) images of 30 wt.% Fe/AC catalyst before (a) and after (b) microwave-initiated decomposition of LCO. Bottom images correspond to amplification of fresh and spent samples.

4.3.7.4 Thermogravimetric Analysis (TGA) of Fresh and Spent 30 wt.% Fe/AC Catalyst

The temperature programmed oxidation (TPO) analysis of 30 wt.% Fe/AC before and after the deep- dehydrogenation of LCO over temperature ranges from 25 °C to 1000 °C are depicted in **Figure 4.30**. In the temperature range between 400 and 625 °C a maximum overall weight loss at 530 °C is observed for 30 wt.% Fe/AC. Within this range, two reactions likely occur simultaneously: the oxidation of the iron metal, which results in weight gain by formation of iron oxides, and the weight loss by the carbon combustion with evolved CO_2 gas. Note that based on the nominal catalyst composition (30 wt.% Fe) we should expect an overall weight loss of 70 wt. % for the fresh Fe/AC catalyst due to the combustion of carbon, however upon the treatment in the TGA in flowing air, Fe is oxidized to Fe_2O_3 and taking this into account, the total theoretical weight loss should be 62 wt. % instead.

The experimental weight loss of 47.2 % of the fresh catalyst suggests that nearly 35 wt.% Fe is indeed present in the catalyst since the XRD of the analysed TGA sample showed only Fe_2O_3 phase (**Figure 4.31**). The total weight loss of the fresh and spent catalysts were around 47% and 62% respectively, the difference in weight loss was about 15%, which corresponds to carbon deposition and likely unconverted long-chain hydrocarbons in the spent catalyst. On the other hand, the derivative weight showed one peak for the spent catalysts, which seem to indicate the presence of only one carbon phase, but oxidation of the iron carbide phase could also take place.

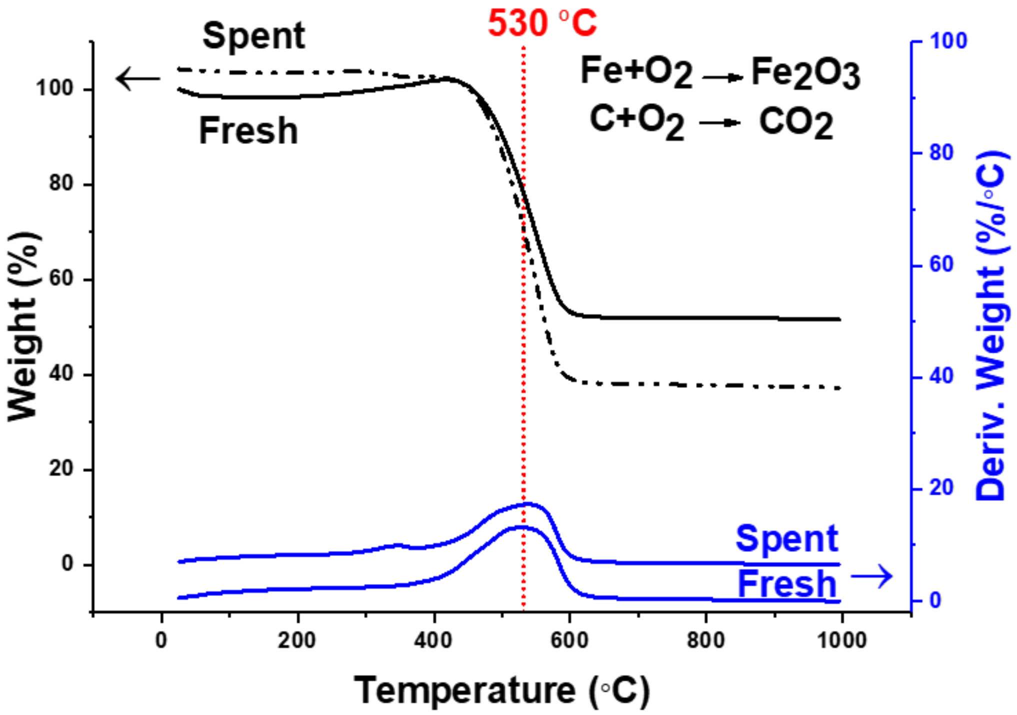

Figure 4.30 Temperature programmed oxidation (TPO) of 30 wt.% Fe/AC for both fresh and spent samples heated in air.

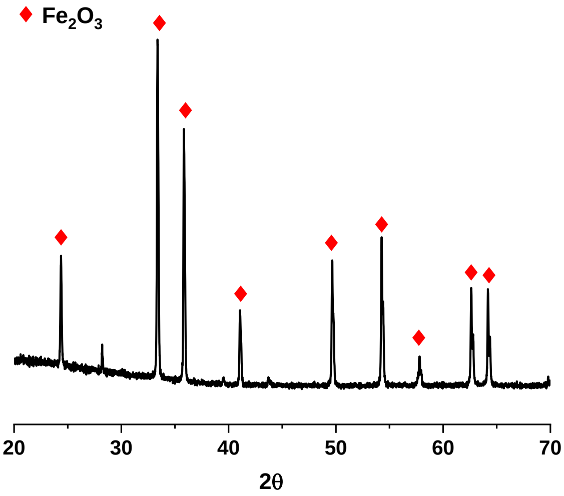

Figure 4.31 X-ray diffraction patterns of the analysed TGA 30 wt.% Fe/AC sample.

4.3.7.5 30 wt.% Fe/AC Catalyst Before and After 4 hr of Continuous Operation

As described earlier in this chapter, the continuous operation of microwave-initiated deep-dehydrogenation of LCO in 30 wt.% Fe/AC was studied at microwave input power of 1000 W and for 4 hours irradiation time. **Figure 4.32a** show the X-ray diffraction patterns of the spent sample of the catalyst. Interestingly, the presence of iron metal is observed and detected at 46°, 67° and 84.5° after 4 hours of operation time. And as expected and showed in the earlier spent Fe/AC catalysts, iron carbide (Fe_3C) appears as the main crystalline phase, with graphitic material indicated around $2\theta = 26°$ in a broad peak. The same sample was studied by temperature-programmed oxidation (TPO) (**Figure 4.32b)**. The resulted data was compared with different model carbons in order to investigate the carbon type in the spent sample of catalyst and whether some high-value carbons were formed in the shape of nanotube. The TPO analysis showed two peaks, one broad peak centred around 550°C which can be attributed to activated carbons and the deposited coke. The other sharp peak around 620°C is partially overlapped with a peak typical for MWCNTs, which is an indication of the formation of carbon nanotubes.

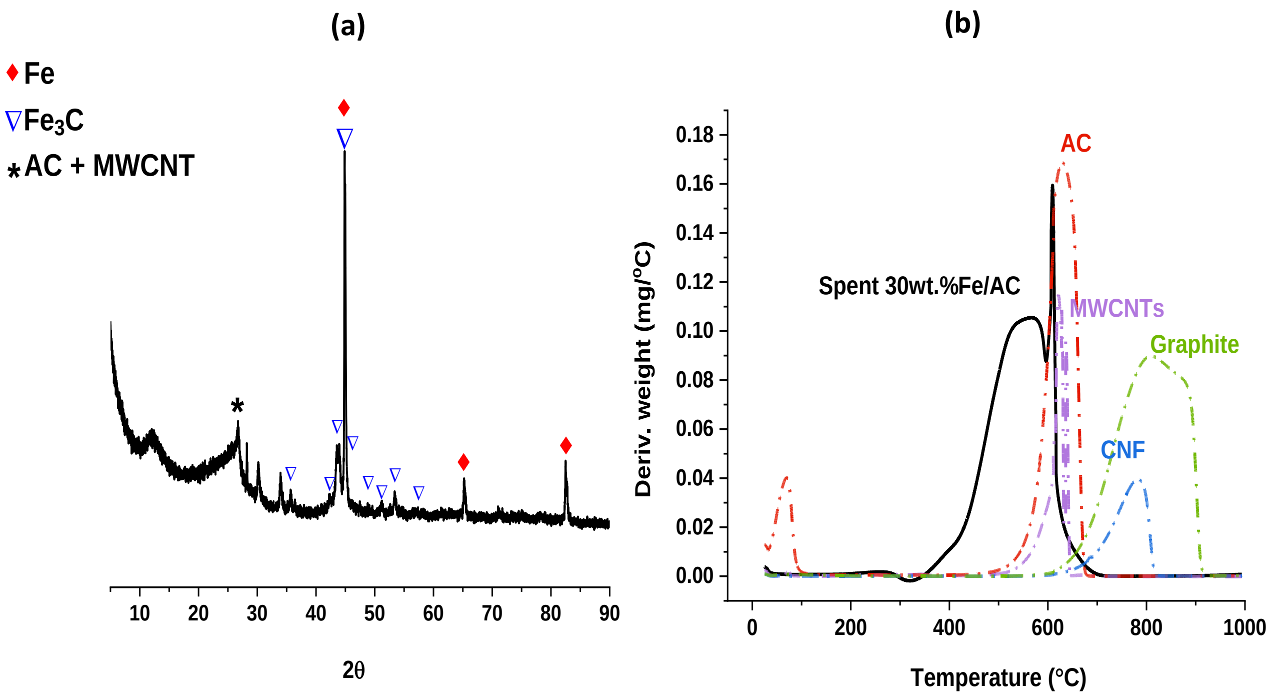

Figure 4.32 The characterization of the spent sample for the continuous operation of microwave-initiated deep-dehydrogenation of LCO in 30 wt.% Fe/AC. (a) X-ray diffraction pattern. (b) derivative plots of TPO of representative spent sample compared with different carbon samples: activated carbon, multi-wall carbon nanotubes, graphite, and carbon nanofiber.

Figure 4.33a,b shows the SEM images comparing the Fe/AC catalyst before and after the microwave experiment. The fresh catalyst in **Figure 4.33a** show lots of Fe sites, the small white clumps, on the AC support. In **Figure 4.33b**, some of these sites have been covered by carbon deposition on the catalysts' surface and a clear agglomeration can be observed in the spent samples. The TEM images in **Figure 4.33c** clearly shows the formation of MWCN and support the data in TPO analysis.

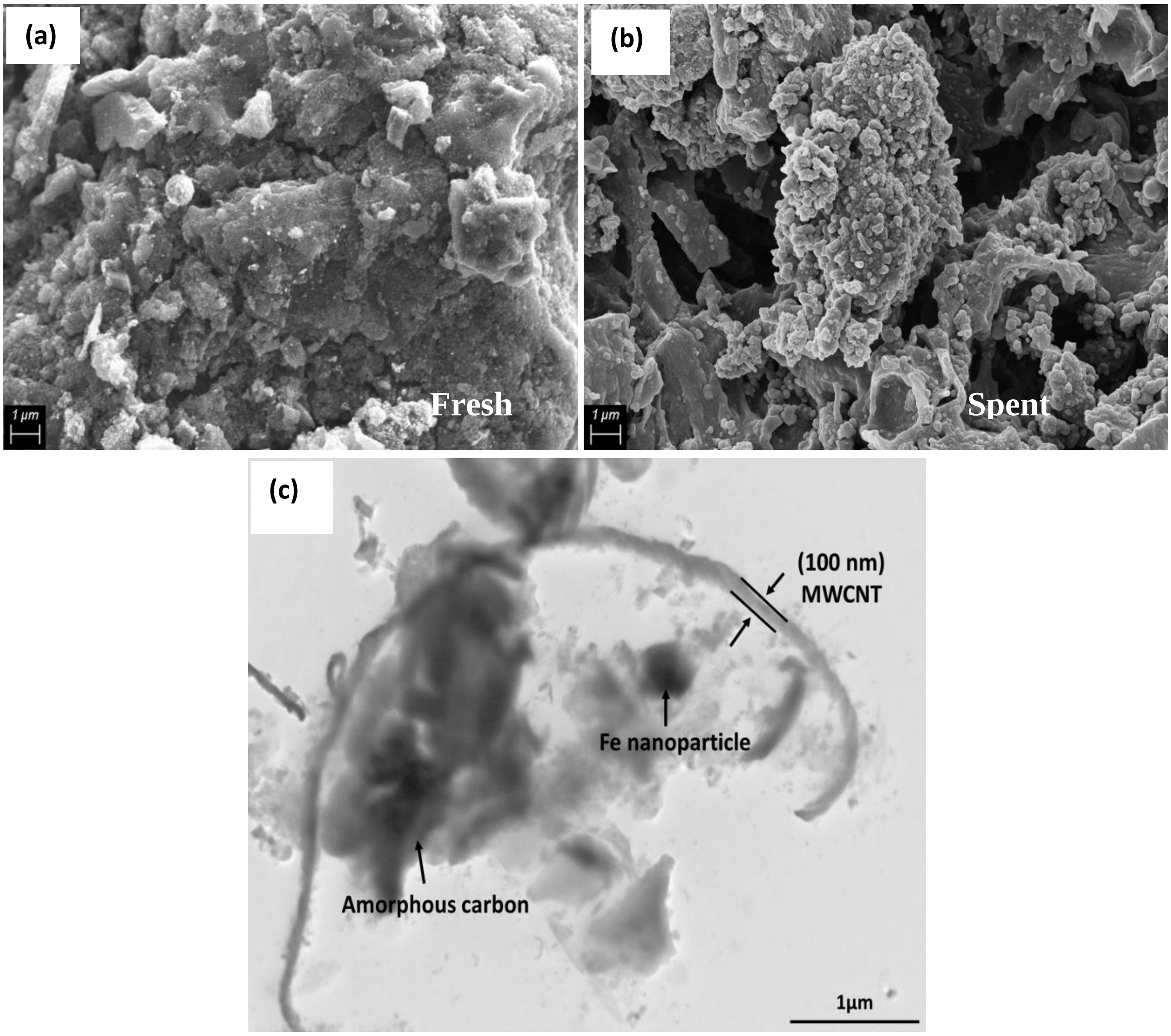

Figure 4.33 Characterisation of 30 wt.% Fe/AC catalyst (a) SEM image of fresh sample, (b) SEM image of the spent sample after 4 hours of continuous operation, and (c) TEM image of the spent sample after 4 hours of continuous operation.

4.3.7.6 Characterisation of Ni/AC and Co/AC Transition Metal Catalysts

Figure 4.34 shows the XRD patterns of both the fresh Ni/AC catalysts **(a)** and the spent samples **(b)** after 10 minutes of microwave-initiated dehydrogenation of LCO. Importantly, no visible major changes were observed. The peaks for nickel (Ni) metal at 44.8°, 52° and 76.5° were detected [80, 81]. Moreover, a very weak peak of activated carbon (AC) was also detected in both fresh and spent samples according to the peaks at 26.6°. There is no peak corresponding to the nickel carbide (NiC_3) formation, a clear indication of the low tendency of Ni to undergo carburisation reaction compared with iron.

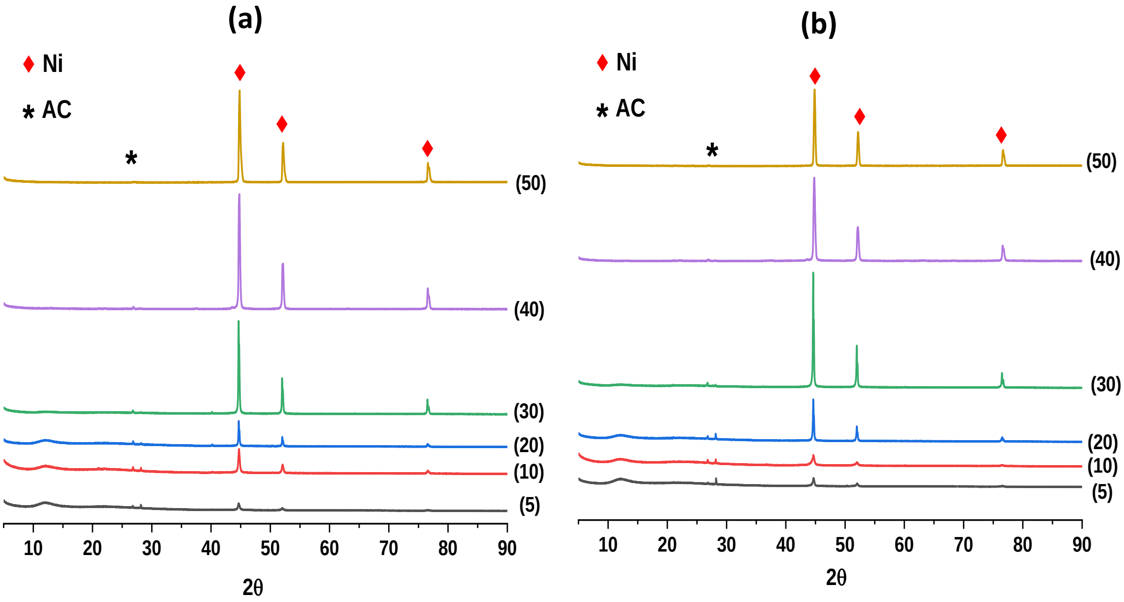

Figure 4.34 The characterization of the fresh and spent samples for microwave-initiated dehydrogenation of LCO. (a) X-ray diffraction patterns of fresh Ni/AC catalyst with different Ni loading (b) After microwave-initiated catalytic reaction. Numbers in parentheses correspond to the Ni loading in wt.%.

The constancy of the catalysts' structure suggests a high catalytic stability after the microwave heating and indicates the possible high activity for further cycles or even under continuous operation. Moreover, **Figure 4.35** shows the SEM images of 20 wt.% Ni/AC both before and after the microwave – initiated catalytic reaction. The fresh catalyst shows lighter spots of Ni particles clearly dispersed on the AC support (**Figure 4.35a)**. The spent sample

(**Figure 4.35b**) depicts some particle growth on the support surface. There was no evidence of formation of any other carbon phase (for example, carbon nanotube, carbon nanofibers, etc.) in contrast with Fe case.

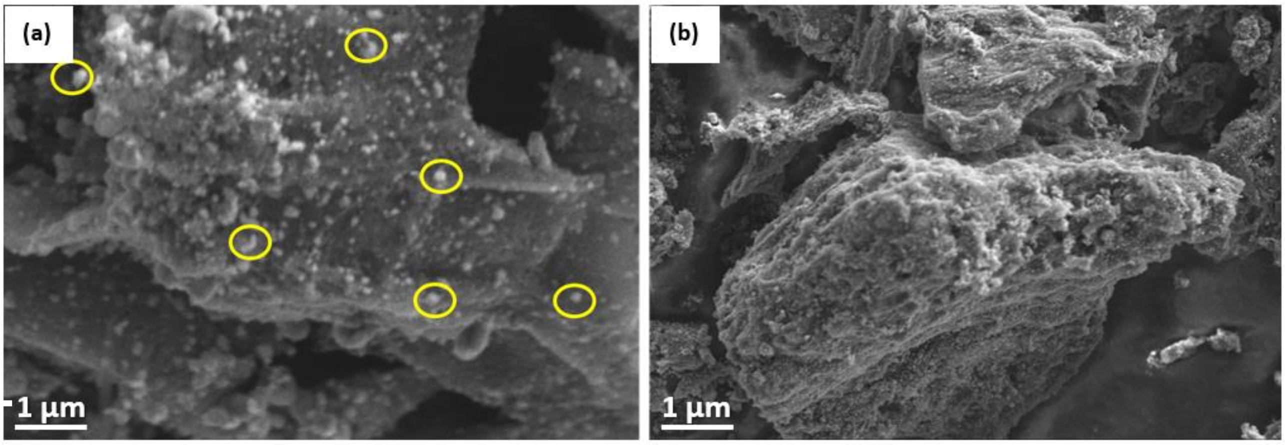

Figure 4.35 Scanning electron microscopy (SEM) of 20 wt.% Ni/AC catalysts, (a) before and (b) after the microwave-initiated catalytic reaction. the circles of yellow colour highlight some of the Ni particles.

Cobalt catalysts with variable Co content supported on AC were also investigated in this thesis. **Figure 4.36** shows the XRD patterns of both the fresh catalysts **(a)** and the spent samples **(b)** after 10 minutes of microwave-initiated decomposition of LCO. As previously seen in nickel catalyst, there were no significant changes in either fresh or spent Co/AC catalysts. In **Figure 4.36a**, three distinct peaks of cobalt metal are observed at 2θ = 44.4°, 51.7° and 76° respectively [82, 83]. A very weak peak of activated carbon (AC) was also detected in both fresh and spent samples according to the peaks at 26.6°. The formation of new phase was detected in spent samples at 2θ = 31.5°, 37°, 59.5° and 65.3° (**Figure 4.36b**). These are corresponding to an unidentified phase which appears to be face centred cubic.

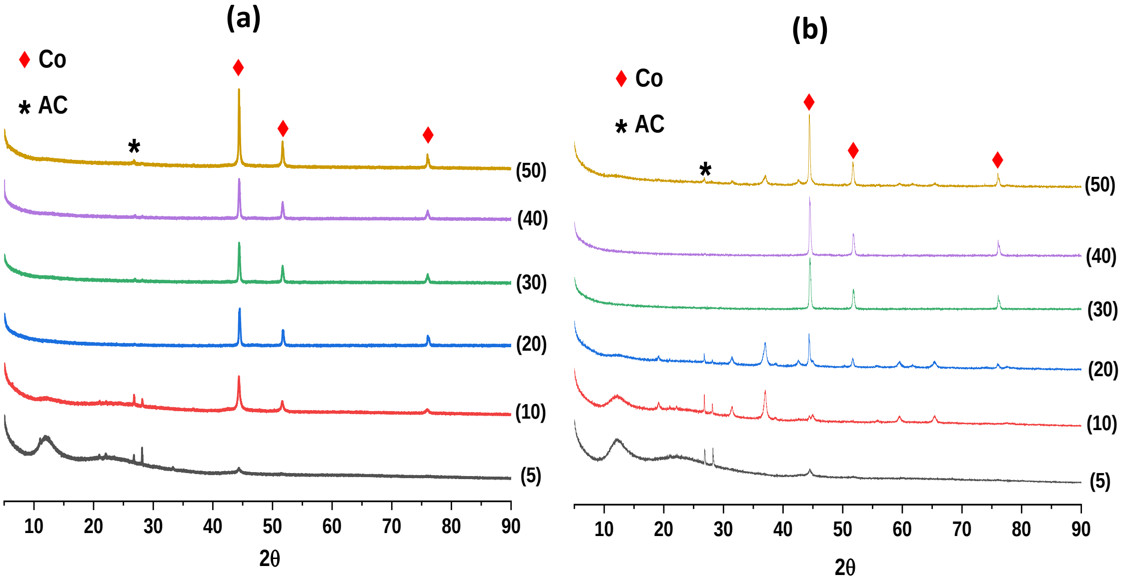

Figure 4.36 X-ray diffraction patterns of the fresh and spent samples for microwave-initiated dehydrogenation of LCO. (a)fresh Co/AC catalyst with different Co loading, (b) after microwave-initiated catalytic reaction. Numbers in parentheses correspond to the Co loading in wt.%.

Figure 4.37 shows the SEM images of 20 wt.% Co on AC before and after microwave-initiated decomposition of LCO. In the fresh sample, the Co particles was well dispersed on the support surface (**Figure 4.37a**), and there is no marked difference in the surface morphology of the fresh and spent samples.

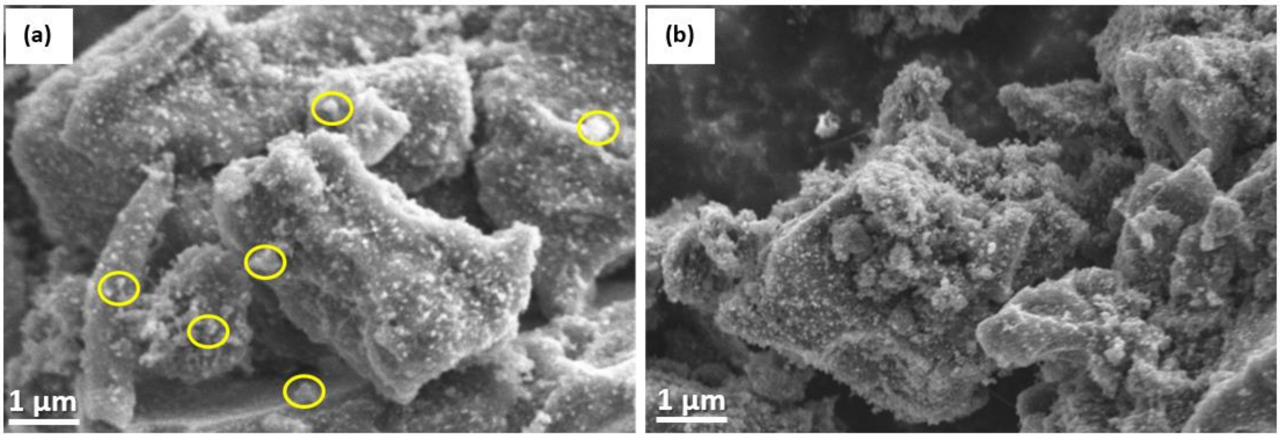

Figure 4.37 Scanning electron microscopy (SEM) of 20 wt.% Co/AC catalysts with various Fe loading, (a) before and (b) after the microwave-initiated catalytic reaction. the circles of yellow colour highlight some of the Co particles.

4.3.7.7 X-ray Diffraction of Bimetallic (Ni-Fe and Co-Fe) Catalyst

The bimetallic catalysts (i.e., Ni-Fe; Co-Fe) were also characterised before and after the catalytic reactions to gain understanding on the role of the presence of two metals on the catalyst performance. The synthesis of the bimetallic catalysts and their catalytic activity toward hydrogen production were described and investigated earlier in this chapter. **Figure 4.38** illustrates the XRD diffractograms of the Ni and Fe metals supported on AC with variable metals ratios and assessed in the microwave-initiated deep-dehydrogenation of LCO. The XRD patterns of the fresh samples (**Figure 4.38a)** shows the overlapping of Fe and Ni peaks at 2θ = 44.6°, and small iron peaks at 65° and 82° in the sample with a high Fe content (5 wt. % Ni, 25 wt. % Fe /AC). The other Ni peaks were also observed clearly at 2θ = 51.9° and 76.4° [81]. Furthermore, iron carbide (Fe_3C) was also observed in samples with higher Fe ratio (i.e., 20 and 25 wt. %) at 2θ = 44.9°. No iron carbide was observed in spent Ni-Fe/AC catalyst (**Figure 4.38b)**, and this importantly illustrates that adding Ni can possibly avoid the formation of iron carbide.

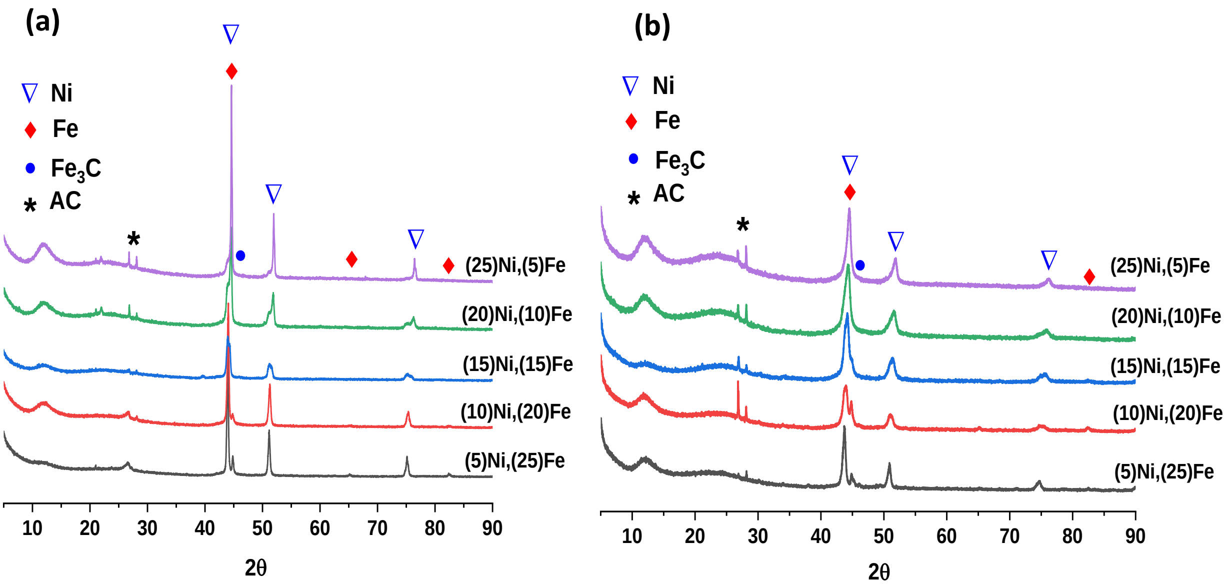

Figure 4.38 X-ray diffraction patterns of the fresh and spent bimetallic catalysts for microwave-initiated dehydrogenation of LCO. (a) fresh Ni-Fe/AC catalyst with different metals loading, (b) After microwave-initiated catalytic reaction. Numbers in parentheses correspond to the metals loading, in wt.%.

Figure 4.39 shows the XRD patterns of the Co and Fe metals supported on AC. There is no marked change in the fresh and spent sample. Fe and Co peaks overlapped at 2θ = 44.9° [84], and small Fe peaks were observed at 2θ = 65.4° and 85.5°. There is no sign of the formation of iron carbide phase, and this could due the low content of Fe in the catalyst. The fact that Fe_3C is not detected at high loadings of Co it is an indication of the possible Co-Fe interaction (or alloy formation) that hinders the formation of iron carbide.

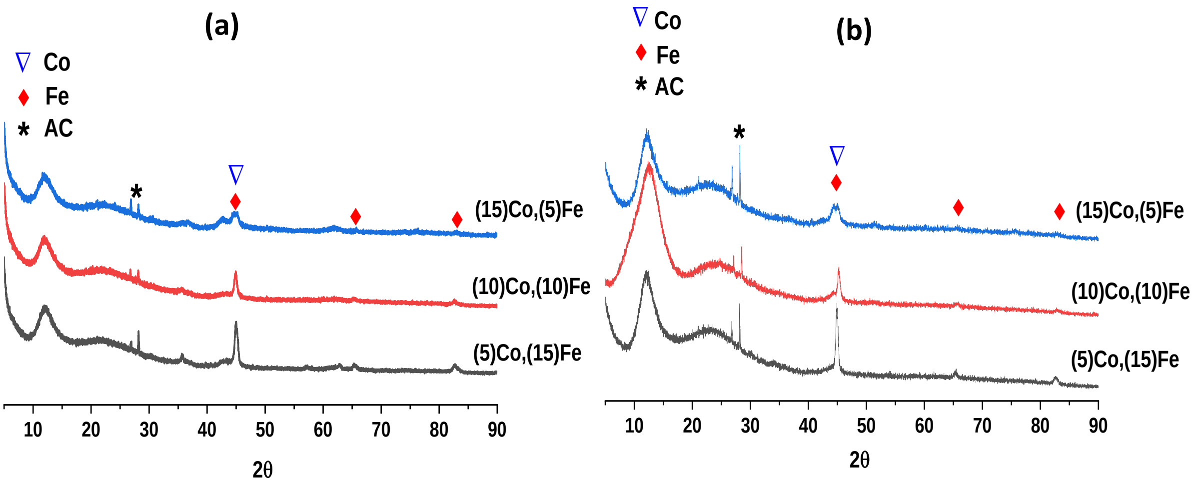

Figure 4.39 X-ray diffraction patterns of the fresh and spent bimetallic catalysts for microwave-initiated deep-dehydrogenation of LCO. (a) fresh Co, Fe/AC catalyst with different metals loading, (b) After microwave-initiated catalytic reaction. Numbers in parentheses correspond to the metals loading, in wt.%.

4.4 Conclusions*

The ^1H NMR, ^{13}C NMR, FT-IR spectroscopy and TGA analysis has been applied to determine the molecular profile of the light crude oil (LCO). The extended analysis of the results showed the presence of the following structural groups: paraffinic, naphthenic and aromatic compounds in agreement with the results given by ITS Testing Service (Intertek-UK) Ltd.

The catalytic activity study outlined in this chapter revealed the feasibility – and the limitations - of direct H_2 production from LCO. For example, through microwave-initiated catalytic deep-dehydrogenation using Fe catalysts supported on activated carbon (AC), it was found that the Fe/AC catalyst system with a loading of 30 wt.% of Fe was the most effective formulation to produce high levels of H_2. The dominant gas product was hydrogen with very small CO_2 formation. The evolution of gases followed a parallel reaction pathway in which H_2 is the principal gaseous product followed by light hydrocarbons and a smaller contribution of CO_x gases. This optimal composition of 30 wt.% Fe on activated carbon showed, by XRD, mainly metallic Fe, an excellent crystallite phase able to catalyse the deep-dehydrogenation of LCO to H_2 and graphitic fibre type carbon materials. However, this phase is severely carburised over the course of the reaction to produce a working catalytic system comprised of a combination of Fe and Fe_3C in the first cycle of operation of Fe/AC catalyst.

Furthermore, transition metal catalysts supported on activated carbon have also shown a relatively good hydrogen yield, and, importantly, the Fe-Co/AC bimetallic catalysts showed zero CO_2 emission. These data suggest that there should be further investigation of the bimetallic catalysts.

We have demonstrated that the Size-Induced Metal-Insulator Transition (SIMIT) strongly affects the performance of Fe/AC catalyst in the microwave-initiated deep-dehydrogenation of LCO for hydrogen production and the formation of MWCNTs material. Small size of Fe nanoparticles within ca. 35-45 nm range improves not only the microwave heating but also and most importantly the generation of H_2 through the conversion of LCO. The tuning of the nanosized Fe particles is an excellent strategy to enhance both the catalyst performance toward H_2 generation and most likely the properties of the residual carbon material.

The key is therefore to achieve the best 'tuning' of the utilised catalysts that can be initiated with a good microwave absorber. The balance between these two critical aspects can be manipulated to achieve the best catalytic performance in order to produce "Blue H_2" from LCO, as we have demonstrated in this work.

*This chapter is prepared for publication at the Proceedings of the National Academy of Sciences (PNAS), PNAS

References

[1] US Energy Information Administration (EIA), International Energy Outlook 2019 with projections to 2050, (2021). www.eia.gov.

[2] M. Adam, H. Anbari, A. Hart, J. Wood, J. Robinson, S. Rigby, In-Situ Microwave-Assisted Catalytic Upgrading of Heavy Oil: Experimental Validation and Effect of Catalyst Pore Structure on Activity, Chemical Engineering Journal, 413 (2021) 127420.

[3] J. Speight, The Chemistry and Technology of Petroleum, 4th ed., CRC Press, (2006).

[4] H. Devold, Oil and Gas Production Handbook: An Introduction to Oil and Gas Production, Transport, Refining And Petrochemical Industry, ABB, (2013).

[5] D. Jones, Introduction to Crude Oil and Petroleum Processing, in: S. Treese, P. Pujadó, D. Jones (Eds.) Handbook of Petroleum Processing, Springer International Publishing, Cham, (2015), 3-51.

[6] N. Altawell, 3 - Crude Oil, in: N. Altawell (Ed.) Rural Electrification, Academic Press, (2021), 39-80.

[7] M. Ramirez-Corredores, The Science and Technology of Unconventional Oils, Elsevier, (2017).

[8] N. Muradov, How to Produce Hydrogen from Fossil Fuels without CO_2 Emission, International Journal of Hydrogen Energy, 18 (1993) 211-215.

[9] J. Rissman, C. Bataille, E. Masanet, N. Aden, W. Morrow, N. Zhou, N. Elliott, R. Dell, N. Heeren, B. Huckestein, J. Cresko, S.A. Miller, J. Roy, P. Fennell, B. Cremmins, T. Blank, D. Hone, E. Williams, S. du Can, B. Sisson, M. Williams, J. Katzenberger, D. Burtraw, G. Sethi, H. Ping, D. Danielson, H.Y. Lu, T. Lorber, J. Dinkel, J. Helseth, Technologies and Policies to Decarbonize Global Industry: Review and Assessment of Mitigation Drivers Through 2070, Applied Energy, 266 (2020), 114848.

[10] T. Abbasi, S. Abbasi, Decarbonization of Fossil Fuels as A Strategy to Control Global Warming, Renewable & Sustainable Energy Reviews, 15 (2011) 1828-1834.

[11] S. Gonzalez-Cortes, D.R. Slocombe, T. Xiao, A. Aldawsari, B. Yao, V.L. Kuznetsov, E. Liberti, A.I. Kirkland, M.S. Alkinani, H.A. Al-Megren, J.M. Thomas, P.P. Edwards, Wax: A Benign Hydrogen-Storage Material that Rapidly Releases H_2-Rich Gases Through Microwave-Assisted Catalytic Decomposition, Scientific Reports, 6 (2016), 35315.

[12] X.Y. Jie, S. Gonzalez-Cortes, T.C. Xiao, B.Z. Yao, J.L. Wang, D.R. Slocombe, Y.W. Fang, N. Miller, H.A. Al-Megren, J.R. Dilworth, J.M. Thomas, P.P. Edwards, The Decarbonisation of Petroleum and other Fossil Hydrocarbon Fuels for the Facile Production and Safe Storage of Hydrogen, Energy & Environmental Science, 12 (2019) 238-249.

[13] Y. Yan, S. Gonzalez-Cortes, H. Al-Megren, P.P. Edwards, F. Cao, T. Xiao, Hydrogen Production from Crude Oil with Fine Iron Particles through Microwave-Initiated Catalytic Dehydrogenation Promoted by Emulsified Feed, International Journal of Hydrogen Energy, 43 (2018) 23201-23208.

[14] J. Krummenacher, K.N. West, L.D. Schmidt, Catalytic Partial Oxidation of Higher Hydrocarbons at Millisecond Contact Times: Decane, Hexadecane, and Diesel Fuel, Journal of Catalysis, 215 (2003) 332-343.

[15] N. Muradov, Emission-Free Fuel Reformers for Mobile and Portable Fuel Cell Applications, Journal of Power Sources, 118 (2003) 320-324.

[16] S. Takenaka, Y. Kobayashi, K. Otsuka, Formation of Hydrogen through the Decomposition of Kerosene over Nickel-Based Catalysts, Energy & Fuels, 18 (2004) 1775-1783.

[17] S. Takenaka, K. Kawashima, H. Matsune, M. Kishida, Production of CO-Free Hydrogen through the Decomposition of LPG and Kerosene over Ni-Based Catalysts, Applied Catalysis A: General, 321 (2007) 165-174.

[18] N. Muradov, CO_2-Free Production of Hydrogen by Catalytic Pyrolysis of Hydrocarbon Fuel, Energy & Fuels, 12 (1998) 41-48.

[19] N. Muradov, Thermocatalytic CO_2-Free Production of Hydrogen from Hydrocarbon Fuels, United States Department of Energy, (2003).

[20] D. Cohn, A. Rabinovich, C. Titus, L. Bromberg, Near-Term Possibilities for Extremely Low Emission Vehicles using Onboard Plasmatron Generation of Hydrogen, International Journal of Hydrogen Energy, 22 (1997) 715-723.

[21] T. Kim, S. Song, K. Chun, S. Lee, An Experimental Study of Syn-gas Production Via Microwave Plasma Reforming of Methane, Iso-Octane and Gasoline, Energy, 35 (2010) 2734-2743.

[22] J. Rollier, J. Gonzalez-Aguilar, G. Petitpas, A. Darmon, L. Fulcheri, R. Metkemeijer, Experimental Study on Gasoline Reforming Assisted by Nonthermal Arc Discharge, Energy & Fuels, 22 (2008) 556-560.

[23] M. Boot, A. Nikipelov, G. Correale, A. Rakitin, S. Pancheshnyi, I. Popov, A. Starikovskii, On-Board Plasma Assisted Fuel Reforming, SAE Technical Paper, (2011).

[24] Y. Matsui, S. Kawakami, K. Takashima, S. Katsura, A. Mizuno, Liquid-Phase Fuel Re-forming at Room Temperature Using Nonthermal Plasma, Energy & Fuels, 19 (2005) 1561-1565.

[25] D.H. Lee, J.-O. Lee, K.-T. Kim, Y.-H. Song, E. Kim, H.-S. Han, Characteristics of Plasma-Assisted Hydrocarbon SCR System, International Journal of Hydrogen Energy, 36 (2011) 11718-11726.

[26] C. Park, C. Kim, K. Kim, D. Lee, Y. Song, Y. Moriyoshi, The Influence of Hydrogen-Enriched Gas on the Performance of Lean NO_x Trap Catalyst for A Light-duty Diesel Engine, International Journal of Hydrogen Energy, 35 (2010) 1789-1796.

[27] B.K. Cho, J.-H. Lee, C.C. Crellin, K.L. Olson, D.L. Hilden, M.K. Kim, P.S. Kim, I. Heo, S.H. Oh, I.-S. Nam, Selective Catalytic Reduction of NOx by Diesel Fuel: Plasma-Assisted HC/SCR System, Catalysis Today, 191 (2012) 20-24.

[28] A. Lebouvier, F. Fresnet, F. Fabry, V. Boch, V. Rohani, F. Cauneau, L. Fulcheri, Exhaust Gas Fuel Reforming of Diesel Fuel by Nonthermal Arc Discharge for NOx Trap Regeneration Application, Energy & Fuels, 25 (2011) 1034-1044.

[29] V.D. Rusanov, A.I. Babaritskii, I.E. Baranov, M.B. Bibikov, M.A. Deminskii, S.A. Demkin, V.K. Zhivotov, G.M. Konovalov, G.V. Lysov, A.S. Moskovskii, B.V. Potapkin, R.V. Smirnov, F.N. Cheban'kov, Nonequilibrium Effect of Atmospheric-Pressure Microwave-Discharge Plasma on Methane and Kerosene Conversion into Synthesis Gas, Doklady Chemistry, 395 (2004) 82-85.

[30] N.I. Kuskova, A.P. Malyushevskaya, S.V. Petrichenko, A.N. Yushchishchina, Comparative Analysis of Various Schemes of Electrodischarge Processing of Kerosene to Synthesize Carbon Nanomaterials, Surface Engineering and Applied Electrochemistry, 47 (2011) 446-449.

[31] J. Hartvigsen, S. Elangovan, M. Hollist, P. Czernichowski, L. Frost, Non-Thermal Plasma Reformation of Liquid Fuels, ECS Transactions, 35 (2011), 2525-2833.

[32] A. Jahanmiri, M.R. Rahimpour, M. mohamadzadeh shirazi, N. Hooshmand, H. Taghvaei, Naphtha Cracking Through A Pulsed Dbd Plasma Reactor: Effect of Applied Voltage, Pulse Repetition Frequency and Electrode Material, Chemical Engineering Journal, 191 (2012) 416–425.

[33] S. Nomura, H. Toyota, M. Tawara, H. Yamashita, K. Matsumoto, Fuel Gas Production by Microwave Plasma in Liquid, Applied Physics Letters, 88 (2006) 231502.

[34] J.L. Hueso, V.J. Rico, J. Cotrino, J.M. Jiménez-Mateos, A.R. González-Elipe, Water Plasmas for the Revalorisation of Heavy Oils and Cokes from Petroleum Refining, Environmental Science & Technology, 43 (2009) 2557-2562.

[35] S. Horikoshi, N. Serpone, Microwaves in Catalysis: Methodology and Applications, Wiley-VCH, (2016).

[36] N.E. Leadbeater, Microwave Heating as a Tool for Sustainable Chemistry, CRC Press, (2010).

[37] S.C. Motshekga, S.K. Pillai, S.S. Ray, K. Jalama, R.W.M. Krause, Recent Trends in the Microwave-Assisted Synthesis of Metal Oxide Nanoparticles Supported on Carbon Nanotubes and their Applications, Journal of Nanomaterials, 2012 (2012), 691503.

[38] M.B. Gawande, S.N. Shelke, R. Zboril, R.S. Varma, Microwave-Assisted Chemistry: Synthetic Applications for Rapid Assembly of Nanomaterials and Organics, Accounts of Chemical Research, 47 (2014) 1338-1348.

[39] R.R. Mishra, A.K. Sharma, Microwave–Material Interaction Phenomena: Heating Mechanisms, Challenges and Opportunities in Material Processing, Composites Part A: Applied Science and Manufacturing, 81 (2016) 78-97.

[40] E.T. Thostenson, T.W. Chou, Microwave Processing: Fundamentals and Applications, Composites Part A: Applied Science and Manufacturing, 30 (1999) 1055-1071.

[41] X.Y. Jie, S. Gonzalez-Cortes, T.C. Xiao, J.L. Wang, B.Z. Yao, D.R. Slocombe, H.A. Al-Megren, J.R. Dilworth, J.M. Thomas, P.P. Edwards, Rapid Production of High-Purity Hydrogen Fuel through Microwave-Promoted Deep Catalytic Dehydrogenation of Liquid Alkanes with Abundant Metals, Angewandte Chemie-International Edition, 56 (2017) 10170-10173.

[42] A. Bayu, A. Yoshida, S. Karnjanakom, K. Kusakabe, X. Hao, T. Prakoso, A. Abudula, G. Guan, Catalytic Conversion of Biomass Derivatives to Lactic Acid with Increased Selectivity in an Aqueous Tin(II) Chloride/Choline Chloride System, Green Chemistry, 20 (2018) 4112-4119.

[43] P. Edwards, R. Johnston, C.N.R. Rao, On the Size-Induced Metal-Insulator Transition in Clusters and Small Particles, in: P. Braunstein, L. A. Oro, P. R. Raithby (Eds.), Metal Clusters in Chemistry, Wiley-VCH, (2008), 1454-1481.

[44] K.M. Szykuła, C. Wicking, S. Whitmarsh, C.S. Creaser, J.C. Reynolds, Characterization of Crude Oil and its Saturate, Aromatic, and Resin Fractions by High-Field Asymmetric Waveform Ion Mobility Spectrometry–High-Resolution Mass Spectrometry, Energy & Fuels, 32 (2018) 11310-11316.

[45] F.A. Fernandez-Lima, C. Becker, A.M. McKenna, R.P. Rodgers, A.G. Marshall, D.H. Russell, Petroleum Crude Oil Characterization by IMS-MS and FTICR MS, Analytical Chemistry, 81 (2009) 9941-9947.

[46] Y. Zhang, Re: Crude Oil Characterization. Retrieved from: https://www.researchgate.net/post/Crude-Oil-Characterization/60a4844bb9fb1c55516b49c6/citation/download, (2021).

[47] I.Z. Rakhmatullin, S.V. Efimov, B.Y. Margulis, V.V. Klochkov, Qualitative and Quantitative Analysis of Oil Samples Extracted from Some Bashkortostan and Tatarstan Oilfields Based on NMR Spectroscopy Data, Journal of Petroleum Science and Engineering, 156 (2017), 12-18.

[48] F. Ferreira, D. Flumignan, M. Lopes, E. Flumignan, J.E. de Oliveira, Determination of Saturates, Aromatics and Ethanol in Brazilian Commercial Gasoline with Low Olefin Content using ^{1}H NMR Spectroscopy, Brazilian Journal of Analytical Chemistry, 1 (2010), 29-35.

[49] A.G. Abdul Jameel, Identification and Quantification of Hydrocarbon Functional Groups in Gasoline Using ^{1}H-NMR Spectroscopy for Property Prediction, Molecules (Basel, Switzerland), 26 (2021) ,6989.

[50] I. Rakhmatullin, S. Efimov, M. Varfolomeev, V. Klochkov, High-Resolution NMR Study of Light and Heavy Crude Oils: “Structure-Property” Analysis, IOP Conference Series: Earth and Environmental Science, 155 (2018), 012014.

[51] C.S. Clendinen, G.S. Stupp, R. Ajredini, B. Lee-McMullen, C. Beecher, A.S. Edison, An Overview of Methods Using ^{13}C For Improved Compound Identification in Metabolomics and Natural Products, Frontiers in Plant Science, 6 (2015), 611-611.

[52] S. Akmaz, O. Iscan, M.A. Gurkaynak, M. Yasar, The Structural Characterization of Saturate, Aromatic, Resin, and Asphaltene Fractions of Batiraman Crude Oil, Petroleum Science and Technology, 29 (2011) 160-171.

[53] A.B.D. Nandiyanto, R. Oktiani, R. Ragadhita, How to Read and Interpret FTIR Spectroscope of Organic Material, 2019, 4 (2019) 22.

[54] J. Coates, Interpretation of Infrared Spectra, A Practical Approach, Encyclopedia of Analytical Chemistry, (2006).

[55] A. Samanta, K. Ojha, A. Mandal, Interactions between Acidic Crude Oil and Alkali and their Effects on Enhanced Oil Recovery, Energy & Fuels, 25 (2011), 1642-1649.

[56] M.A. Ali, M. Siddiqui, J. Zaidi, Thermal Analysis of Crude Oils and Comparison with SIMDIST and TBP Distillation Data, Journal of Thermal Analysis and Calorimetry, 51 (1998), 307-319.

[57] R. Parameshwaran, A. Sarı, N. Jalaiah, R. Karunakaran, Chapter 13 - Applications of Thermal Analysis to the Study of Phase-Change Materials, in: S. Vyazovkin, N. Koga, C. Schick (Eds.) Handbook of Thermal Analysis and Calorimetry, Elsevier Science, (2018), 519-572.

[58] A.I. McKay, A.J. Bukvic, B.E. Tegner, A.L. Burnage, A.J. Martı Nez-Martı Nez, N.H. Rees, S.A. Macgregor, A.S. Weller, Room Temperature Acceptorless Alkane Dehydrogenation from Molecular σ-Alkane Complexes, Journal of the American Chemical Society, 141 (2019), 11700-11712.

[59] X. Jie, J. Wang, S. Gonzalez-Cortes, B. Yao, W. Li, Y. Gao, J.R. Dilworth, T. Xiao, P.P. Edwards, Catalytic Activity of Various Carbons during the Microwave-Initiated Deep Dehydrogenation of Hexadecane, JACS Au, 1 (2021) 2021-2032.

[60] D.E. Clark, D.C. Folz, J.K. West, Processing Materials with Microwave Energy, Materials Science and Engineering: A, 287 (2000), 153-158.

[61] A. de la Hoz, Á. Díaz-Ortiz, A. Moreno, Microwaves in Organic Synthesis. Thermal and Non-Thermal Microwave Effects, Chemical Society Reviews, 34 (2005), 164-178.

[62] X. Jie, S. Gonzalez-Cortes, T. Xiao, B. Yao, J. Wang, D.R. Slocombe, Y. Fang, N. Miller, H.A. Al-Megren, J.R. Dilworth, J.M. Thomas, P.P. Edwards, The Decarbonisation of Petroleum and other Fossil Hydrocarbon Fuels for the Facile Production and Safe Storage of Hydrogen, Energy & Environmental Science, 12 (2019) 238-249.

[63] V. Palma, D. Barba, M. Cortese, M. Martino, S. Renda, E. Meloni, Microwaves and Heterogeneous Catalysis: A Review on Selected Catalytic Processes, Catalysts, 10 (2020), 246.

[64] C. Antonio, R.T. Deam, Can “Microwave Effects” be Explained by Enhanced Diffusion?, Physical Chemistry Chemical Physics, 9 (2007), 2976-2982.

[65] S. Sharifvaghefi, B. Shirani, M. Eic, Y. Zheng, Application of Microwave in Hydrogen Production from Methane Dry Reforming: Comparison Between the Conventional and Microwave-Assisted Catalytic Reforming on Improving the Energy Efficiency, Catalysts, 9 (2019), 618.

[66] A. de la Hoz, A. Díaz-Ortiz, P. Prieto, Chapter 1 Microwave-Assisted Green Organic Synthesis, Alternative Energy Sources for Green Chemistry, The Royal Society of Chemistry, (2016), 1-33.

[67] V. Gayakhe, S. Bhilare, A. Yashmeen, I.J.S. Fairlamb, A.R. Kapdi, Chapter 6 - Transition-Metal Catalyzed Modification of Nucleosides, in: A.R. Kapdi, D. Maiti, Y.S. Sanghvi (Eds.) Palladium-Catalyzed Modification of Nucleosides, Nucleotides and Oligonucleotides, Elsevier, (2018), 167-195.

[68] International Union of Pure and Applied Chemistry (IUPAC), Compendium of Chemical Terminology - Gold Book, (2014).

[69] Y. Dai, X. Gao, Q. Wang, X. Wan, C. Zhou, Y. Yang, Recent Progress in Heterogeneous Metal and Metal Oxide Catalysts for Direct Dehydrogenation of Ethane and Propane, Chemical Society Reviews, 50 (2021), 5590-5630.

[70] Z.-P. Hu, D. Yang, Z. Wang, Z.-Y. Yuan, State-Of-The-Art Catalysts for Direct Dehydrogenation of Propane to Propylene, Chinese Journal of Catalysis, 40 (2019), 1233-1254.

[71] A. Porch, D. Slocombe, P.P. Edwards, Microwave Absorption in Powders of Small Conducting Particles For Heating Applications, Physical Chemistry Chemical Physics, 15 (2013), 2757-2763.

[72] L. Liu, A. Corma, Metal Catalysts for Heterogeneous Catalysis: From Single Atoms to Nanoclusters and Nanoparticles, Chemical Reviews, 118 (2018), 4981-5079.

[73] P. Marquardt, G. Nimtz, G. Heite, H. Peters, Microwave Evidence for a Size-Induced Metal-Insulator Transition in Mesoscopic Conductors, MRS Online Proceedings Library, 124 (1988), 155-160.

[74] X. Jie, R. Chen, T. Biddle, D.R. Slocombe, J.R. Dilworth, T. Xiao, P.P. Edwards, Size-Dependent Microwave Heating and Catalytic Activity of Fine Iron Particles in the Deep Dehydrogenation of Hexadecane, Chemistry of Materials, 34 (2022), 4682-4693.

[75] P. Marquardt, L. Börngen, G. Nimtz, R. Sonnberger, H. Gleiter, J. Zhu, Microwave Absorption by Small Metal Particles, Physics Letters A, 114 (1986) 39-42.

[76] P. Marquardt, G. Nimtz, Size-Dependent Dielectric Response of Small Metal Particles, Physical Review B, 43 (1991), 14245-14247.

[77] T. Ano, S. Tsubaki, S. Fujii, Y. Wada, Designing Local Microwave Heating of Metal Nanoparticles/Metal Oxide Substrate Composites, The Journal of Physical Chemistry C, 125 (2021) 23720-23728.

[78] T.C. Schmidt, P. Kleinert, C. Stengel, K.-U. Goss, S.B. Haderlein, Polar Fuel Constituents: Compound Identification and Equilibrium Partitioning between Nonaqueous Phase Liquids and Water, Environmental Science & Technology, 36 (2002), 4074-4080.

[79] Skin Depth Calculator, MUST Online Calculator for Electronics, http://mustcalculate.com/electronics/skindepth.php.

[80] H. Wang, X. Kou, J. Zhang, J. Li, Large Scale Synthesis and Characterization of Ni Nanoparticles by Solution Reduction Method, Bulletin of Materials Science, 31 (2008), 97-100.

[81] K.S. Dijith, R. Aiswarya, M. Praveen, S. Pillai, K.P. Surendran, Polyol Derived Ni and NiFe Alloys for Effective Shielding of Electromagnetic Interference, Materials Chemistry Frontiers, 2 (2018), 1829-1841.

[82] P. Gurunathan, P.M. Ette, N. Lakshminarasimhan, K. Ramesha, A Convenient Synthesis Route for Co_3O_4 Hollow Microspheres and Their Application as a High Performing Anode in Li-Ion Batteries, ACS Omega, 2 (2017), 7647-7657.

[83] M. Manjunatha, G.S. Reddy, K.J. Mallikarjunaiah, R. Damle, K.P. Ramesh, Determination of Phase Composition of Cobalt Nanoparticles Using 59 Co Internal Field Nuclear Magnetic Resonance, Journal of Superconductivity and Novel Magnetism, 32 (2019), 3201-3209.

[84] K. Zhu, C. Jin, Z. Klencsár, A.S. Ganeshraja, J. Wang, Cobalt-iron Oxide, Alloy and Nitride: Synthesis, Characterization and Application in Catalytic Peroxymonosulfate Activation for Orange II Degradation, Catalysts, 7 (2017), 138.

Chapter5

Effective Conversion of Light Crude Oil to Syngas through Microwave-Initiated Catalysis

The conversion of crude oil to basic and intermediate chemicals is a process of utmost importance in the petroleum and petrochemical industries. However, it now requires technological innovations to address understandable and pressing environmental concerns. In this regard, an interesting alternative to the conventional conversion of crude oil into high-value chemicals is microwave technology whose rapid and selective heating alongside an advanced catalyst system has the real potential to bring significant environmental advantages to the upgrading of crude oil. This chapter presents the effective conversion of Saudi light crude oil (LCO) to syngas (H_2 + CO), through microwave-initiated catalysis using an iron (Fe) catalyst supported on gamma-alumina (γ-Al_2O_3). High selectivity for syngas formation which encourage further exploration and process optimisation as an effective means of producing syngas directly from the LCO without significant levels of CO_2 emissions.

5.1 Introduction

Synthesis gas (syngas) is a mixture comprising hydrogen, carbon monoxide (CO:H_2) in various ratios ranging from 1 to 2, and other components such as CO_2 and methane may also be present. Syngas is the main product of reformer units in most of the hydrogen industry processes [1, 2]. It is an essential industrial feedstock in several catalytic processes and is considered as a fundamental building block and a versatile basic reactant and intermediate in most of the myriad of products produced from crude oil or natural gas.

The major application areas are shown in **Figure 5.1**, and include:

1. Methanol to produce: Dimethyl ether (DME), acetic acid, formaldehyde, polyolefins … etc.
2. Synthetic Fuels such as petrol, diesel, and wax through the Fisher-Tropsch process.
3. Hydrogen through the water-gas-shift reaction.

Syngas can also be used as a primary energy source [3-5].

Syngas can be produced from a variety of renewable and non-renewable sources [5]. Thus, it can be produced from natural gas, biomass, steam and dry reforming of light hydrocarbons or the gasification of hydrocarbons or coal. A thermochemical combination of H_2O and CO_2 to give H_2 and CO is also an alternative technology to produce syngas from renewable sources [6]. The production of syngas with different compositions requires careful control of process conditions, the kind of feedstock and the technology used [7-9]. Due to these benefits, the global syngas market is projected to rise during the forthcoming years. A recent report published by Research Dive[10] states that the global syngas market was valued at $43.6 billion in 2019 and is projected to reach $66.5 billion by 2027, growing at a CAGR (Compound Annual Growth Rate) of 6.1% from 2020 to 2027.

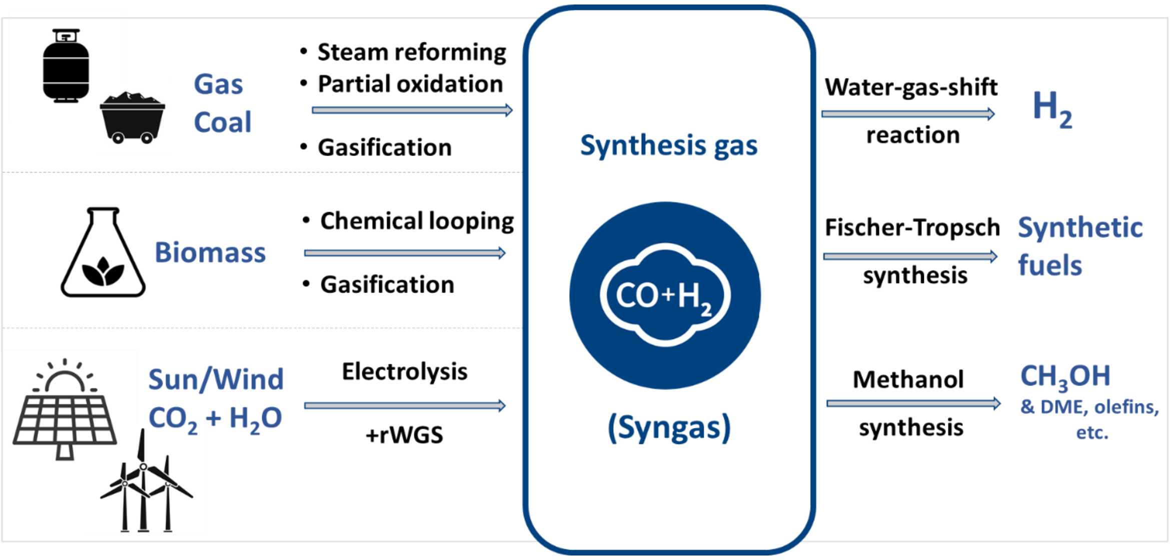

Figure 5.1 Syngas production and utilisation technologies. (Adapted from Ref. [6]).

In the last few years, there has been a noticeable growth in research and studies related to the production of syngas from hydrocarbon feedstocks via heterogeneous catalysts, as shown by the increasing number of publications in **Figure 5.2** [11, 12]. The big challenges in commercialising and scaling up any of these processes are the low catalytic activity and the inevitable coke deposition associated with the high reaction temperature (above 600 °C). Therefore, developing a catalyst and optimising a system that minimises carbon formation could be a unique and promising approach to improve the activity and the stability of the catalyst.

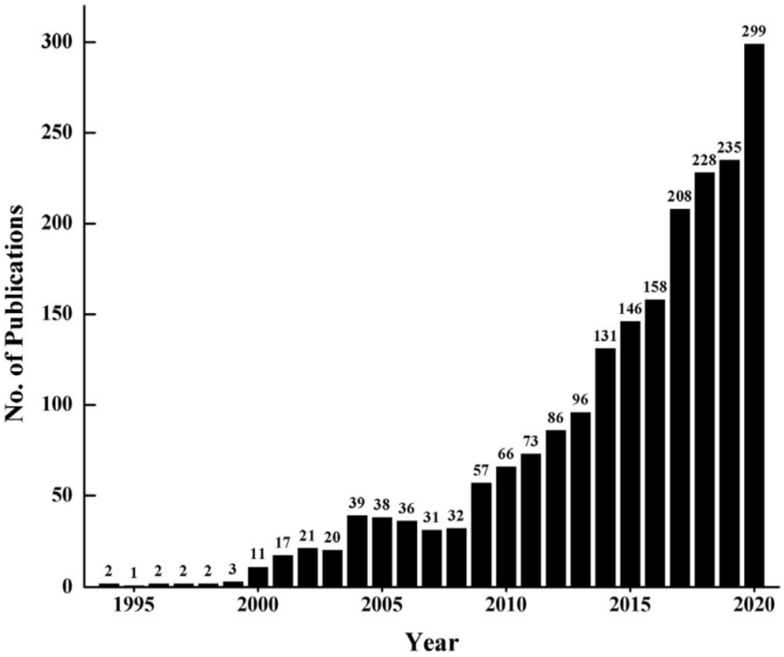

Figure 5.2 Number of publications versus years (1994-2020) extracted from citation database of Scopus retrieved using the keywords “dry reforming of methane” and limited to keywords “Synthesis Gas, Catalysts”. (Reproduced from Ref. [12]).

Nowadays, conventional electrical heating is widely used in syngas production technologies despite its (recognised) negative environmental impact. Microwave-initiated catalytic technology could be an ideal alternative due to its high selective heating and efficiency which can reduce energy consumption and any undesirable products [13, 14].

In the past decade, several researchers have reported the development and optimisation of microwave-initiated catalytic processes for syngas production.

Recently, García and his co-authors concluded that the microwave-assisted dry reforming of methane over Ni/SiC can compete with the traditional steam reforming process when conversion reaches up to 90% at a microwave power input of 45-60 W [13]. Fidalgo *et. al.* investigated activated carbon as a catalyst and microwave receptor in the microwave-assisted dry reforming of methane. Higher conversions of CH_4 and CO_2 were achieved (~100%) at lower space velocity (0.32 $Lg^{-1}h^{-1}$) for a long time period (i.e., 5 h) [15]. In the same group, they observed that higher conversion to syngas was achieved in a microwave reactor compared to conventional heating using a mixture of carbon and Ni/Al_2O_3 catalysts for the microwave-assisted CO_2 reforming of methane [16]. Dominguez *et. al.* have also studied activated carbon as a catalyst for the same process, higher conversions and the formation of carbon nanofibers as by-products were observed. [17]. Nguyen *et al*. reported that 81% CH_4 and 86% CO_2 were converted to syngas with a H_2/CO ratio of 0.9 through the microwave-assisted dry reforming of methane over bimetallic catalysts [18].

Table 5.1 summarises the performance of different catalysts reported in the literature for syngas production in microwave-assisted dry reforming of hydrocarbons. It is noticeable that Ni- and Al_2O_3-containing catalysts have been extensively examined in the dry reforming of hydrocarbons using the application of microwave energy; however, an Fe catalyst has not been examined in the microwave-assisted reforming of crude oil. Therefore, the aim of this chapter is to investigate the catalytic performance of a $Fe/\gamma\text{-}Al_2O_3$ catalyst in the reforming of LCO into syngas using microwave heating.

Table 5.1 Summary of various catalysts with different hydrocarbon feedstock for dry (CO_2) reforming process.

Catalyst	**Feedstock**	**Temperature (°C)**	**TOS (h)**	**Conversion (%)**		**Yield (%)**		**H_2/CO ratio**	**References**
				HC	**CO_2**	**H_2**	**CO**		
1%Ir/Al_2O_3	Methane	850	10	95	65	95	60	0.98	[19]
3%Ru/$ZnLaAlO_4$	Methane	800	30	89	89	99.8	-	2.1	[20]
1%Rh/9.6%Zr-γ -Al_2O_3	Methane	700	4	88	-	69	75.8	0.91	[21]
1%Rh/3%La_2O_3 -γ -Al_2O_3	Methane	850	5	-	~100	~100	-	-	[22]
3%Ce-10%Ni/Al_2O_3	Ethanol	700	5-7	35	18	~23	~14	1.7	[23]
10%NiO/SiO_2 –Al_2O_3	Ethanol	750	10	~100	76	100	36	-	[24]
2%Ir/CeO_2	Ethanol	700	70	100	-	43	48	-	[25]
15%Cu/$Ce_{0.8}Zr_{0.2}O$	Ethanol	700	90	~100	-	42.2	38.9	1.15	[26]
20%Ni-cement clinker	Glycerol	750	4	76	-	66	59	1.8	[27]
3%La–Ni/Al_2O_3	Glycerol	750	4	96	-	97	100	2	[28]

5.2 Experimental

5.2.1 Preparation of Catalysts

5.2.1.1 Iron Metal Supported on Gamma-Alumina (Fe/ γ-Al_2O_3) Catalyst Preparation

In this chapter, a series of Fe catalysts supported on γ-Al_2O_3 was synthesised with different Fe loadings ranging between 5 and 50 wt. % as described in **Figure 5.3** The Fe/ γ-Al_2O_3 catalysts were prepared using the so-called impregnation method [29]. Iron nitrate, $Fe(NO_3)_3 \cdot 9H_2O$ (Iron (III) nitrate nonahydrate, 99%, Sigma-Aldrich) was used as the iron precursor and γ-Al_2O_3 (Aluminium oxide, γ-phase, 1/8″ pellets, bimodal, Alfa Aesar) was used as catalyst support. The support was crushed to 20 mesh powder size then slowly added into an aqueous solution of iron nitrate with the concentration determined to produce the required Fe loading on the support. The mixture was stirred and heated at 100 °C for 5 hours until it became a slurry and was then dried overnight in a drying oven at 110 °C. The targeted metal-catalysts were obtained by a careful reduction process in flowing 10 vol.% H_2/Ar gaseous mixtures at 750 °C for 8 h using tubular furnace with a heating rate of 5 °C/min.

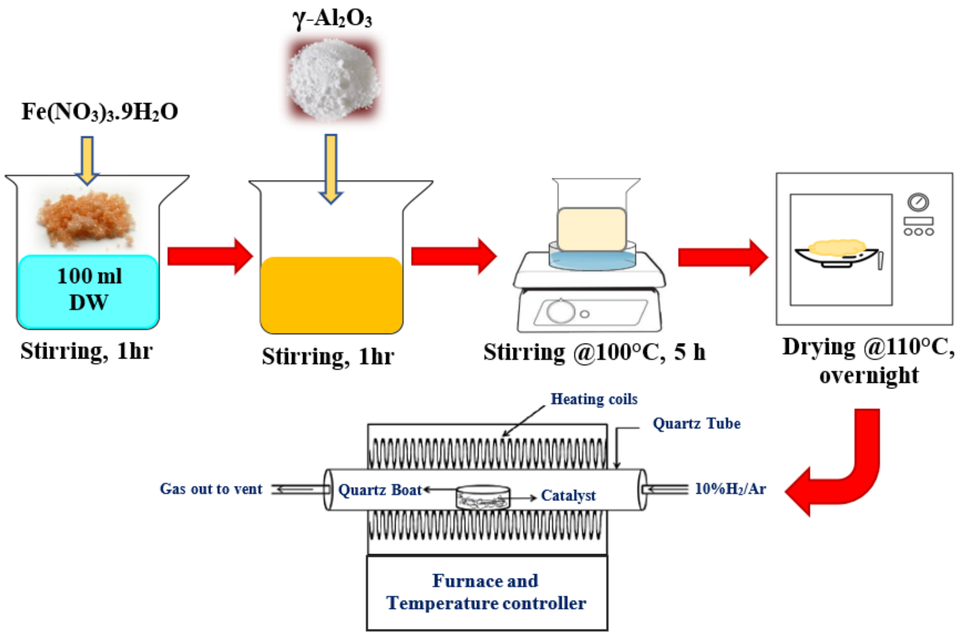

Figure 5.3 Schematic preparation of Fe/ γ-Al_2O_3 catalysts by the impregnation method.

5.2.1.2 Iron Aluminate ($FeAl_2O_4$) Catalyst Preparation

The $FeAl_2O_4$ catalyst was successfully prepared using a sol-gel method [30], as described in **Figure 5.4**. The appropriate amounts (with a Fe: Al molar ratio of 1:2) of $Fe(NO_3)_3.9H_2O$ (Iron (III) nitrate nonahydrate, 99 %, Sigma-Aldrich) and $Al(NO_3)_3 \cdot 9H_2O$ (Aluminum nitrate nonahydrate, ≥ 98%, Sigma-Aldrich) were individually dissolved in deionised water. Then, these two solutions were added to melted stearic acid (99 %, pure, anhydrous, Acros organics) (with a Fe: stearic acid molar ratio of 1.5:1) and stirred to form a homogeneous mixture, which was subsequently heated overnight in an oven at 120 °C. The gel was then calcined in three stages to obtain $FeAl_2O_4$. Firstly, the dried gel was heated at 3 °C min^{-1} up to 230 °C. At this temperature the heating was continued for 12 h constantly. In the second stage, the temperature was increased up to 372 °C and held constant for 1 h, until the stearic acid had evaporated. In the last stage, the temperature was increased up to 700 °C and held constant for 4 h to obtain $FeAl_2O_4$ powder sample.

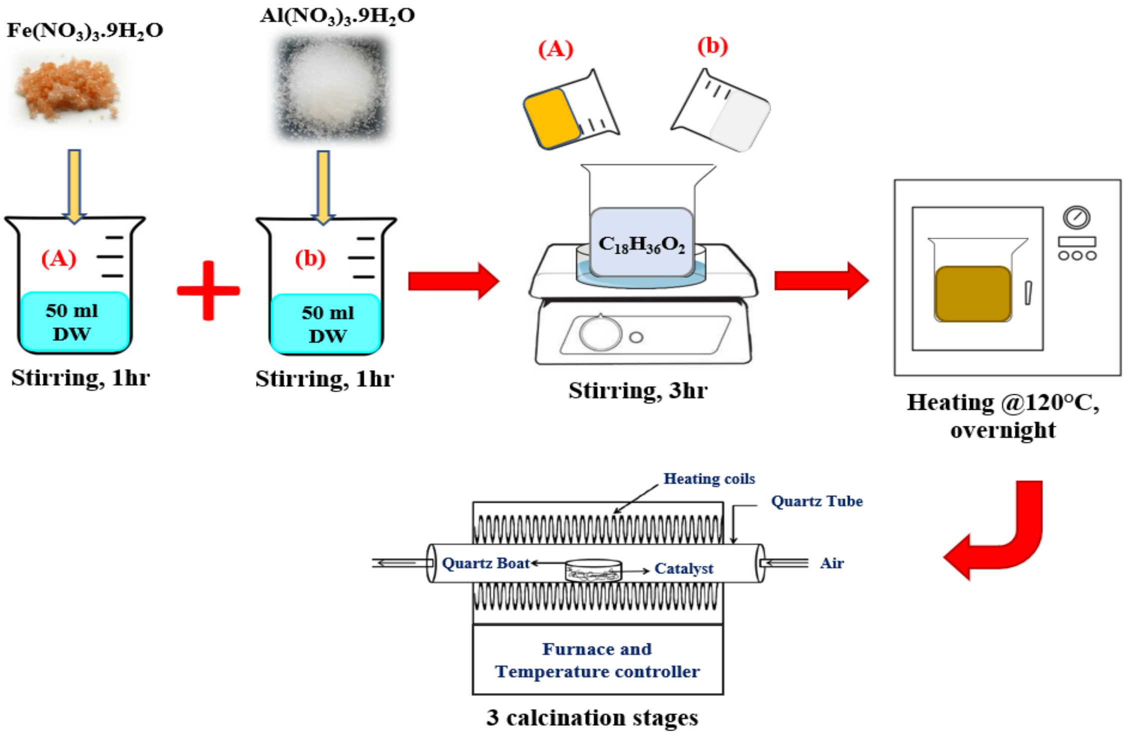

Figure 5.4 Schematic preparation of $FeAl_2O_4$ catalysts by the sol-gel method.

5.2.2 Characterisation of Catalysts

Samples were characterised before and after the experiments using different physical analytical techniques including, Powder X-ray diffraction (XRD), thermogravimetric analysis (TGA), scanning electron microscopy (SEM), Energy-dispersive X-ray spectroscopy (EDS), transmission electron microscopy (TEM), and BET surface area analysis.

5.2.3 Microwave-initiated Catalytic Decomposition of LCO

Before starting the experiment, 30 wt.% of LCO (0.3 g) was mixed with 70 wt.% of catalyst (0.7 g), and placed in a quartz (silica) tubular fixed-bed reactor. The microwave experimental set up used in this investigation is similar to that which has previously been reported in chapter 2 (**Figure 2.1**). Once the tube was placed axially in the microwave cavity, argon purging was carried out at a flow rate of 20 ml.min^{-1} for 10 minutes. The microwave irradiation was carried out at a frequency of 2.45 GHz, with input power of 200 W. After 10 minutes of irradiation, the microwave source was switched off and the temperature monitoring was switched off once the sample reached 50 °C. The collected gaseous products were analysed quantitively by gas chromatography (GC) using a Perkin-Elmer, Clarus 580 GC.

In order to study the catalytic activity in the continuously operated system, a separate experiment was performed, and the same apparatus was used as described in chapter 2. In this setup, the LCO flow into the system was regulated using a syringe pump at a flow rate of 0.05 ml.min^{-1}. The experiment was carried out at microwave power input of 200 W and for 3 hours irradiation time.

In this chapter, three experiments were conducted for the optimal system to ensure the reproducibility and the accuracy of the results. (Appendix A).

5.2.4 Conventional (Thermal) Catalytic Decomposition of LCO

In this set-up, the quartz (silica) reactor tube preparation was the same as described in chapter 2 **(Figure 2.3)**. A catalyst pre-loaded with 30 wt.% LCO was loaded into a pre-heated electric tubular furnace. Dry argon gas was used to purge the reactor tube and the reactor tube was then placed into a tube furnace, which was preheated to the reaction temperature (800 °C). The collected gaseous products - if any - were analysed using the Perkin-Elmer (Clarus 580) gas chromatograph.

In this chapter, the LCO conversion and the syngas selectivity were calculated based on **Equation 3.6** and **Equation 3.7**. But it was very critical to calculate the yield of the syngas (H_2+CO), because of the difficulties in performing the carbon balancing for the outlet carbon of by-products and due to formation of iron carbide and the carbon deposited on the surface and in the pores of the catalysts. In this regard, the process needs intensive variable techniques and investigation to perform the net carbon balance and then the yield of syngas. This matter could be resolved in the future work.

5.3 Results and Discussions

5.3.1 Syngas Production from LCO Through the Microwave-initiated Catalysis of γ-Alumina-Supported Fe Catalysts

In this work, it was found that a catalyst consisting of Fe-supported on gamma-alumina (γ-Al_2O_3) is highly efficient in the conversion of LCO to syngas with high selectivity. **Figure 5.5** shows the results of the examination of a range of catalysts with different Fe loadings between 0 and 50 wt. % using LCO as a feedstock and γ-Al_2O_3 as a support material.

Initially, and as a control experiment, the pristine γ-alumina support alone was tested to investigate its activity toward hydrogen and/or syngas production. The microwave power input was set at 200 W for 10 minutes and it was observed that no gases were released, thus, there was no LCO conversion. This is attributed to the fact that alumina is not a very good microwave absorber, so the catalyst bed is not heated enough to reach the reaction temperature, and this also applies even with the addition of 5 wt.% Fe on this support.

The dependence of the reaction temperature with time is given in **Figure 5.5a**, and, importantly, shows that the alumina support alone and even with the 5 wt.% Fe, was not heated sufficiently by microwave irradiation with the temperature reaching only 53 °C and 130 °C respectively. On the contrary, it was seen in chapter 4 how activated carbon support is an excellent microwave absorber and heated the catalyst bed to around 580 °C, and this explains its high activity for the deep-dehydrogenation of LCO. It is also observed that increasing the Fe content on the alumina support (i.e. 10, 20, 30, 40, and 50 wt.%) led to the increase of the catalyst bed temperature, and therefore, released large quantities of syngas-rich gases (98 vol.%) with very low concentration of undesirable products (**Figure 5.5b**).

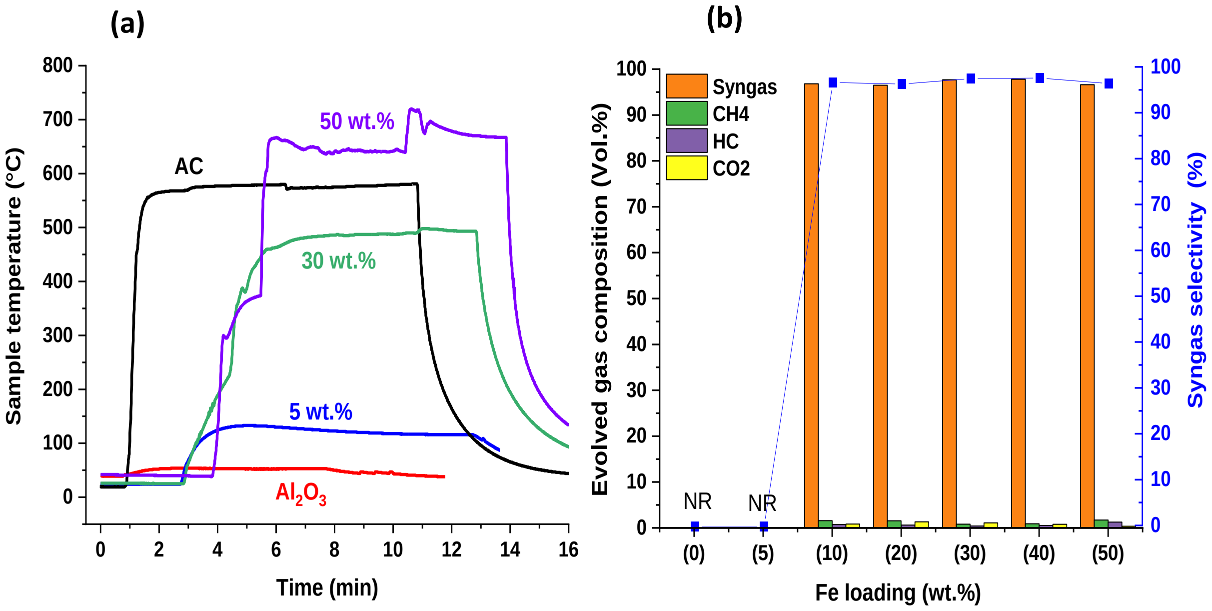

Figure 5.5 Microwave-initiated deep-dehydrogenation of 0.3 g LCO sample mixed with 0.7g of Fe/ γ-Al_2O_3 catalysts at different Fe loadings, (a) The dependence of the reaction temperature profile with time when the input of the microwave power is switched off the bed temperature decrease, (b) evolved gas volume composition and syngas selectivity at a microwave input power of 200 W for 10 min irradiation time. 'NR' indicates no observable reaction under microwave treatment.

The results in **Figure 5.6** show the catalytic performance of a range of Fe/Al_2O_3 catalysts at different Fe loading levels, under microwave heating. As a general observation, both the H_2 and CO concentrations (i.e. the syngas constituents) increase as the Fe content in the catalyst increases and reach their highest values at 30 wt. % Fe. This catalyst shows H_2 and CO selectivity at 49.2 and 47.7 % respectively, and maximum LCO conversion around 51 %, whilst the catalyst containing 40 and 50 wt.% Fe on γ-Al_2O_3 shows a diminution in syngas concentration and LCO conversion.

In addition, it can be seen in **Table 5.2**, interestingly, that the H_2/CO ratio is inversely proportional to the Fe loading, and ranges from 2 to 0.9 as the Fe loading increases from 10 to 50 wt.% Fe respectively. As mentioned earlier in this chapter, there are several factors that can affect the syngas composition and this study presents the fact that metal content in the catalyst can play important roles in controlling the H_2/CO ratio in the syngas products.

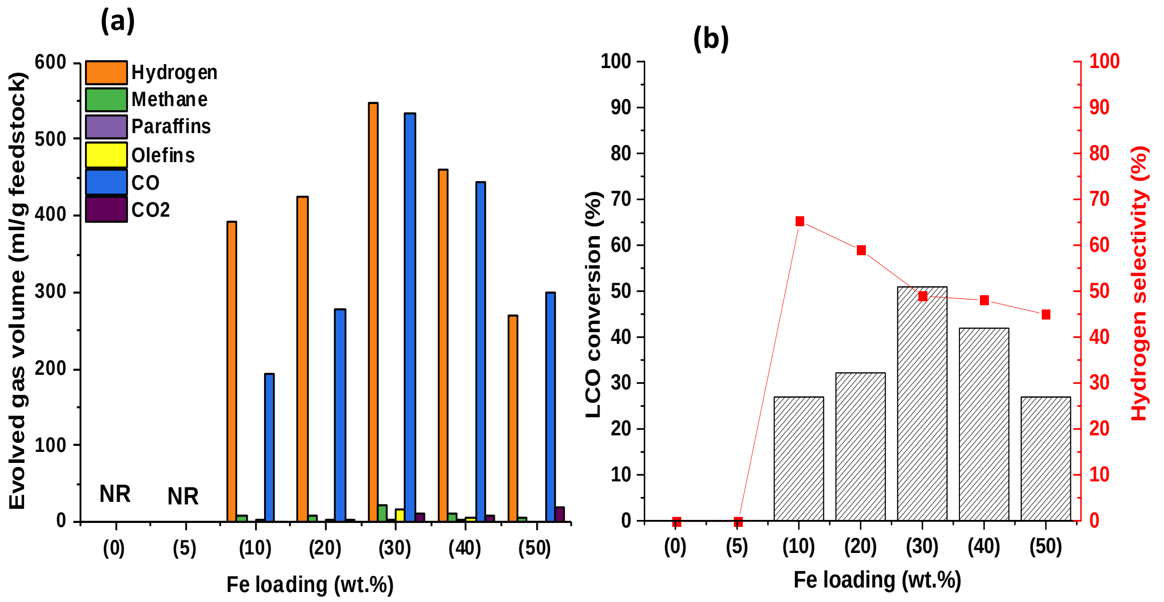

Figure 5.6 Microwave-initiated decomposition of a 0.3 g LCO mixed with 0.7g Fe/ γ-Al_2O_3 catalysts at different Fe loadings, (a) the total evolved gas volume, and (b) LCO conversion and hydrogen selectivity at a microwave input power of 200 W for 10 min irradiation time.

Table 5.2 The evolved gases composition of microwave-initiated decomposition of a 30 wt.% LCO mixed with Fe/γ-Al_2O_3 catalysts at different Fe loadings.

Fe /Al_2O_3 loading (wt.%)	**LCO conversion (%)**	**Products selectivity (%)**						**H_2/CO ratio**
		CH_4	**Paraffins**	**Olefins**	**CO_2**	**CO**	**H_2**	
0	0	0	0	0	0	0	0	0
5	0	0	0	0	0	0	0	0
10	27	1.4	0.2	0.5	0.2	32.1	65.5	2
20	32.2	1.0	0.1	0.5	0.2	38.8	59.2	1.5
30	51	1.2	0.2	0.6	1.0	47.7	49.2	1
40	42	1.8	0.3	1.4	0.9	47.2	48.3	1
50	27	0.7	0.1	0.3	3.5	50.2	45.2	0.9

5.3.2 Continuous Operation of a 30 wt.% Fe/ γ-Al_2O_3 Catalyst System Under Microwave Heating of LCO

In order to study the catalytic performance of the Fe/ γ-Al_2O_3 catalyst under continuous operation, LCO was pumped into the system at a constant flowrate of 0.05 ml.min^{-1} for 3 hours. It can be seen in **Figure 5.7**, that there is a decrease in the catalytic activity after 10 min of irradiation time. The cumulative syngas volume with H_2/CO ratio of 1.25 was at the highest level at 10 min of reaction time with hydrogen selectivity and LCO conversion of around 60%. Subsequently, the syngas concentration decreased while the olefins and CO_2 relatively increased and the effect of carbon deposition on the catalyst deactivation became clear by the strong diminution of syngas selectivity and LCO conversion. A detailed composition analysis of products is given in **Table E1** (Appendix E).

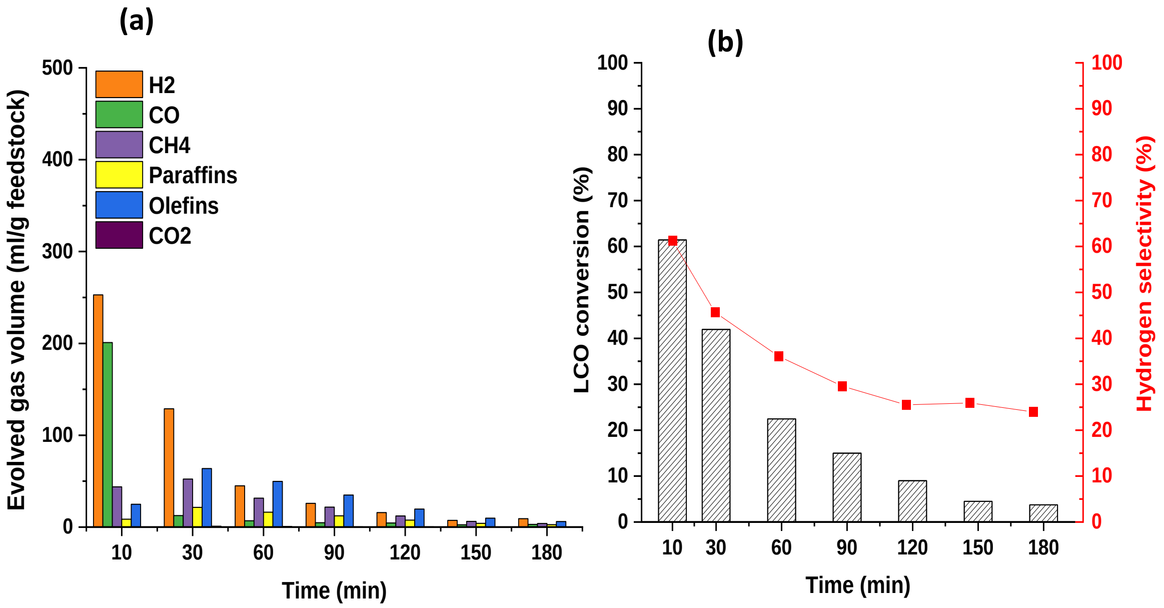

Figure 5.7 The continuous operation of microwave-initiated deep-dehydrogenation of LCO in Fe/γ-Al_2O_3 catalyst. (a) the evolved gas volume of LCO at a different time on stream, (b) LCO conversion, hydrogen selectivity at microwave power input of 200 W and for 3 h irradiation time.

The comparison of the batch and continuous experiments on the dependency of the sample temperature with time in **Figure 5.8** shows, interestingly, the effect of the continuous operation on the catalyst bed temperature. While the temperature in **Figure 5.8a** for the batch process was around 400 °C and the corresponding microwave-absorbed power was steady at 18 W (i.e. 9% of the input power), the continuous flow of LCO fed to the system can cool down the catalyst bed and keep the temperature constant at 250 °C whilst the resulting microwave-absorbed power was fairly constant at around 15 W (**Figure 5.8b**).

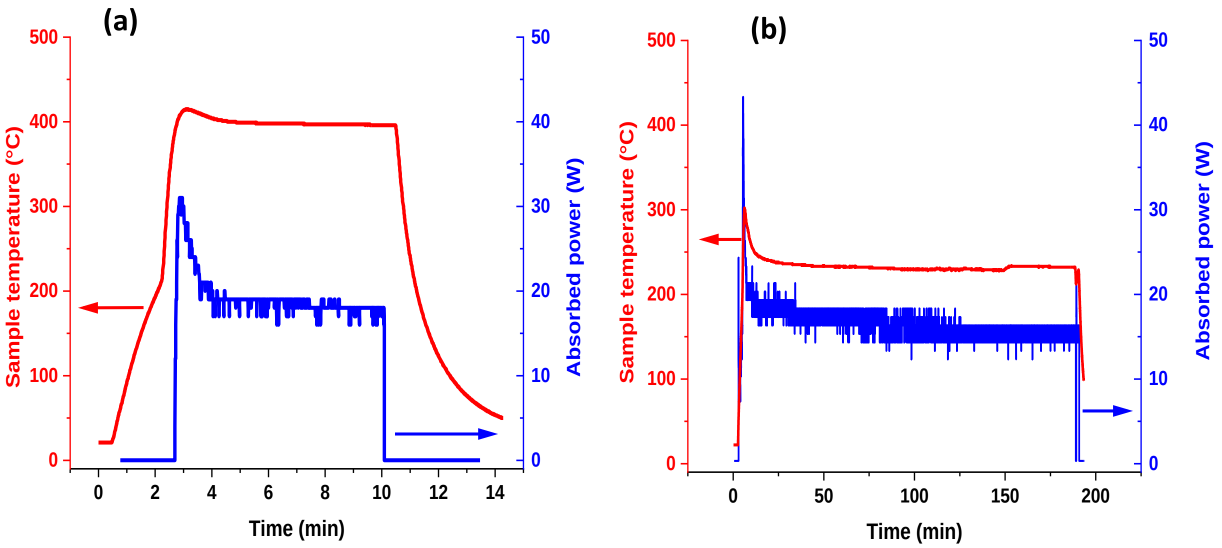

Figure 5.8 The sample (bed) temperature and corresponding microwave-absorbed power of (a) 30 wt.% Fe/ γ-Al_2O_3 catalyst at 10 min irradiation time, (b) 30 wt.% Fe/ γ-Al_2O_3 catalyst at continuous operation for 3 h irradiation time. At microwave power input of 200 W.

5.3.3 Study of the Catalytic Performance of 30 wt.% Fe/ γ-Al_2O_3 Sample of LCO Under Conventional Thermal Heating

This section is to outline the comparison between the microwave and the thermal heating on the catalyst performance. As described earlier in this chapter, the thermal heating experiment was conducted in an electric tubular furnace. The 30 wt.% Fe/ γ-Al_2O_3 catalyst was tested at constant temperature of 800 °C for 10 minutes. Importantly, there were no gases produced and this indicates that the desired catalytic reaction did not occur under these conditions. This result is a striking indication that that microwave energy (through dielectric heating) is highly effective in the conversion of LCO into syngas.

5.3.4 Iron Aluminate: A Catalyst for Syngas Production from LCO Through A Microwave- initiated Process

In general, transition-metal aluminates possess magnetic and chemical properties which make them favourable for various applications [30]. Zhou *et. al* [31] reported that the fabrication of a catalyst consisting of a Fe/$FeAl_2O_4$ formulation with 41 wt.% Fe loading resulted in both good catalytic activity and stability for methane decomposition to produce CO_x-free hydrogen. $FeAl_2O_4$ has also been proved to be a suitable catalyst for the production of hydrogen and carbon nanotubes (CNTs) [32]. Besides the accepted catalytic activity, the relevant characteristics that the $FeAl_2O_4$ material possesses are its high electrical conductivity and the fact that it is recognised as an oxygen carrier for chemical looping (process for the combustion of fuel with an intrinsic capability of highly efficient CO_2 separation) [33, 34].

Due to the high reduction temperature (750 °C) used in preparing the Fe/ γ-Al_2O_3 catalyst in this study, a spinel iron aluminate ($FeAl_2O_4$) was formed as will be discussed later in this chapter. A comparison of the catalytic activity between Fe/γ-Al_2O_3 and pure $FeAl_2O_4$ under microwave heating is shown in **Figure 5.9** and **Table 5.3** . Both catalysts showed good ability to produce syngas from LCO with high selectivity (~ 97 %). It is also observed that the Fe/ γ-Al_2O_3 catalyst has higher LCO conversion (51%) than the $FeAl_2O_4$ catalyst (34.5%), and this explains the difference in the total evolved gas volume shown in **Figure 5.9a**.

A large amount of CO is released during the process using pure $FeAl_2O_4$ as a catalyst indicating that at the high reaction temperature achieved by microwave-initiated heating may cause a decomposition of the catalyst releasing oxygen that interacts with the amorphous carbon, generated from the hydrogen production reaction from LCO, to produce CO as following:

$$\mathrm{FeAl_2O_4} \rightarrow \mathrm{Al_2O_3} + \mathrm{Fe} + \frac{1}{2}\,\mathrm{O_2}$$ **(Equation 5.1)**

$$\mathrm{C}_{amorphous} + \frac{1}{2}\,\mathrm{O_2} \rightarrow \mathrm{CO}$$ **(Equation 5.2)**

And the overall reaction could be viewed as carbothermal reduction of $FeAl_2O_4$

$$\mathrm{FeAl_2O_4} + \mathrm{C} \rightarrow \mathrm{Al_2O_3} + \mathrm{Fe} + \mathrm{CO}$$ **(Equation 5.3)**

Alternatively, the oxygen in the CO may originate from the LCO or the alumina support. Further work will be required to elucidate the precise mechanism of these reactions. It is noticeable that the H_2/CO ratio and the evolved CO_2 volume both significantly increased in the gaseous product concentration from $FeAl_2O_4$ as compared to the Fe/γ-Al_2O_3 formulation, owing to the catalytic contribution of the spinel phase to the water-gas shift reaction $(\mathrm{i.e.}, \mathrm{CO} + \mathrm{H_2O} \leftrightarrow \mathrm{CO_2} + \mathrm{H_2})$.

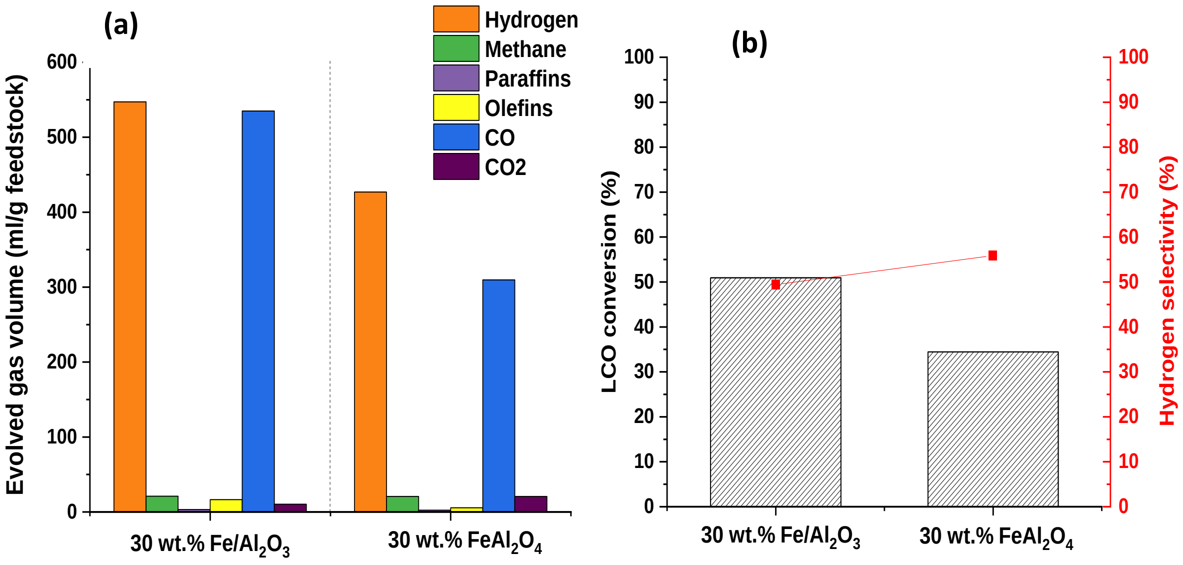

Figure 5.9 Comparison of Fe/ γ-Al_2O_3 and $FeAl_2O_4$ catalysts with 30 wt.% LCO in the microwave-initiated deep-dehydrogenation process (a) the total evolved gas volume, (b) LCO conversion and hydrogen selectivity at a microwave input power of 200 W for 10 min irradiation time.

Table 5.3 Comparison of the catalytic activity of Fe/γ-Al_2O_3 and $FeAl_2O_4$ catalysts in the microwave-initiated deep-dehydrogenation of LCO.

Catalyst	LCO Conversion (%)	Products selectivity (%)						H_2/CO ratio
		CH_4	Paraffins	Olefins	CO_2	CO	H_2	
Fe/ γ-Al_2O_3	51	1.2	0.2	0.6	1.0	47.7	49.2	1
$FeAl_2O_4$	34.5	2.7	0.3	0.7	0.2	40.4	55.7	1.4

The data in **Figure 5.10** show that during microwave heating the temperature of the sample and the absorbed power are fairly similar for both Fe/γ-Al_2O_3 and $FeAl_2O_4$ catalysts, i.e., around 400 °C and 18 W. It was also found that the temperatures remain constant during the microwave heating, giving a good indication of the high thermal stability of these catalysts during the microwave-initiated process.

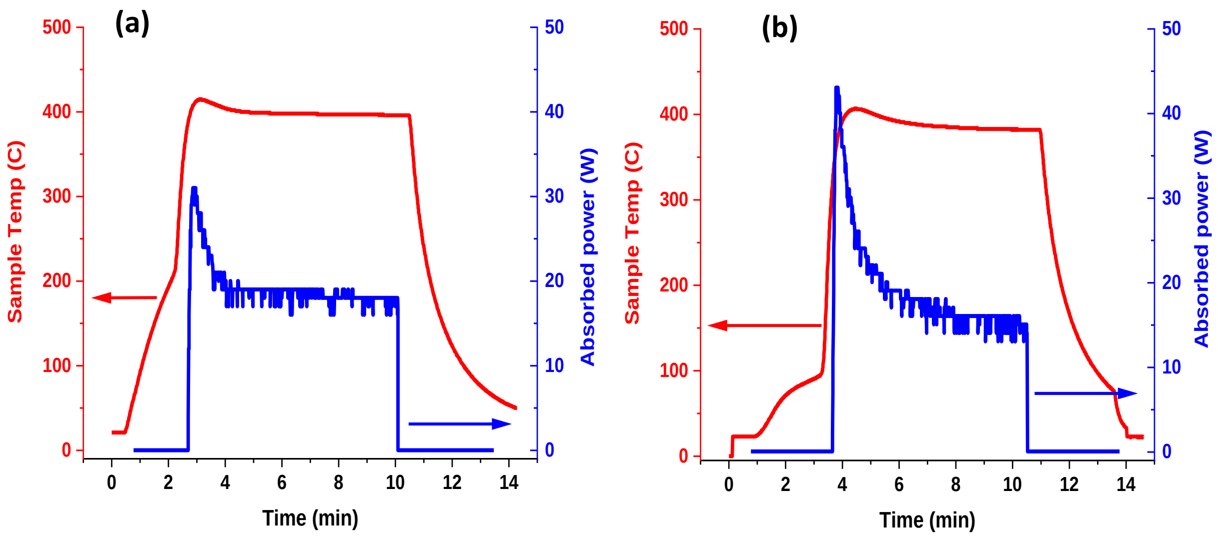

Figure 5.10 The sample (bed) temperature and corresponding microwave-absorbed power of (a) 30 wt.% Fe/γ-Al_2O_3 and (b) $FeAl_2O_4$ catalysts, at a microwave input power of 200 W and 10 min irradiation time. When the input of the microwave power is zero the bed temperature decreases.

5.3.5 Characterisation of Fresh and Spent Catalysts

The identification of the crystalline phases in the fresh catalysts was determined by XRD (**Figure 5.11**). The XRD patterns in **Figure 5.11a** show that the phase composition of each catalyst was Fe and $FeAl_2O_4$ phase. The peaks for Fe metal at 45°and 66° were detected but overlapped with $FeAl_2O_4$ peaks which are also detected at 31°, 36.7°, 44.9°, 55.5°, 59°, and 65° as the diffraction shown in **Figure 5.11b** [35]. As expected, there was no formation of Fe_3C in the fresh catalysts and this is due to using γ-Al_2O_3 as support and the absence of carbon in the catalyst body. Additionally, there is no γ-Al_2O_3 phase in the fresh Fe/Al_2O_3 catalyst [35].

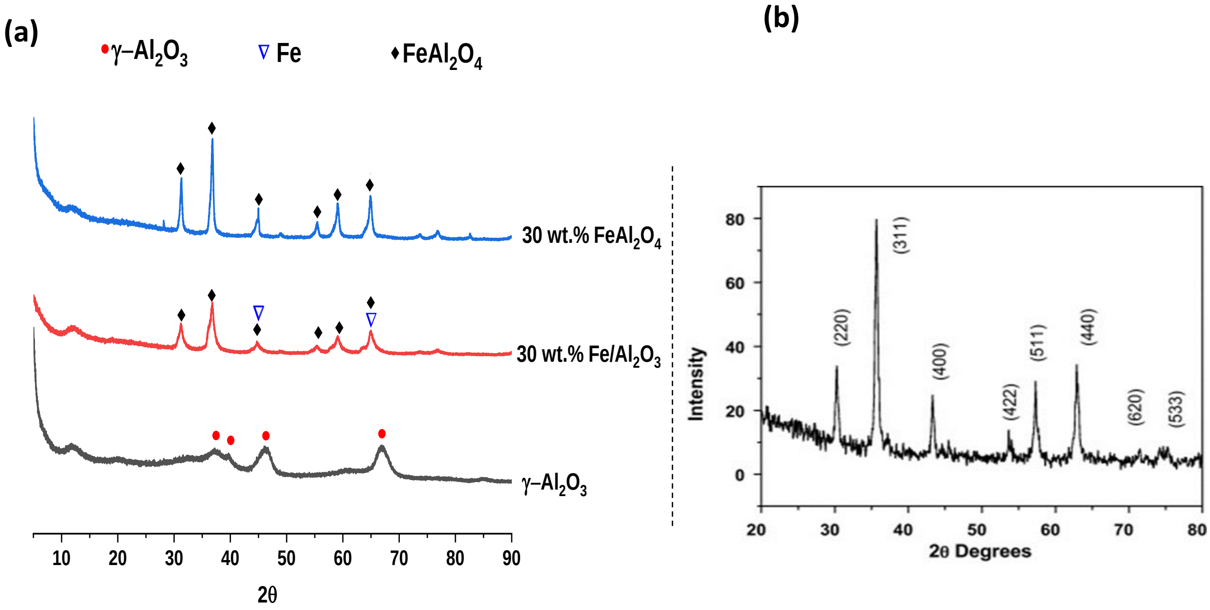

Figure 5.11 X-ray diffraction patterns of (a) Fresh catalysts and γ -alumina support (b) Iron aluminates phase. (Reproduced from Ref. [35]).

A comparison of XRD patterns of both spent samples is shown in **Figure 5.12**. It can be seen that Fe metal peaks still exist only in the spent Fe/ γ-Al_2O_3 sample at 45° and 66°. The Fe/ γ-Al_2O_3 spent sample patterns exhibit α-Al_2O_3 as the main phase [36], and this confirms the formation of a new alumina phase ($\gamma - Al_2O_3 \rightarrow \alpha - Al_2O_3$) after the samples were exposed to microwave heating. However, the $FeAl_2O_4$ spent sample patterns confirms a very high thermal stability for the aluminate since only a small fraction of α-Al_2O_3 was produced.

In addition, the presence of a graphite peak at around 26° and Fe_3C peaks were due to coke deposition during the microwave reaction leading to the dissolution of carbon into the iron- ultimately forming the carbides.

To confirm the presence of Fe metal in the fresh and spent Fe/γ-Al_2O_3, a simple experiment was conducted by using a permanent magnet. Whereas both fresh and spent Fe/Al_2O_3 samples were attracted to the magnet, samples of $FeAl_2O_4$ were not.

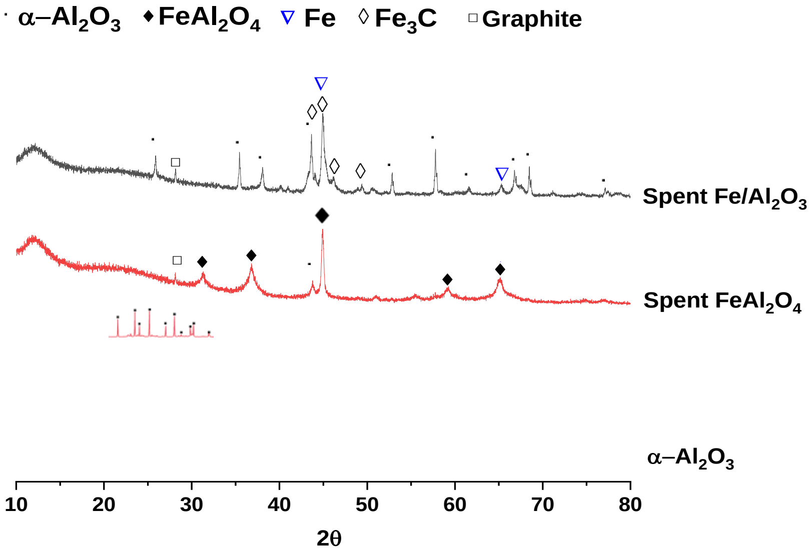

Figure 5.12 A comparison of XRD patterns of spent Fe/γ-Al_2O_3 and $FeAl_2O_4$ samples with a pure alpha-alumina sample.

Scanning electron microscopy/energy-dispersive X-ray spectroscopy (SEM/EDS) images in **Figure 5.13** show both the morphology and elemental content of fresh and spent Fe/γ-Al_2O_3 catalyst. The micrograph shows that the surface structures of the catalysts are composed of many irregular particles. It was also observed that the nanoparticles have polycrystalline $FeAl_2O_4$, and the diameters of the particles are between 50 and 80 nm. The EDX spectrum of the fresh catalyst confirms the presence of Al, Fe and O, and reveals that the Fe content in the catalyst is about 32 wt.%, as anticipated (**Figure 5.13a**). There was no carbon in the fresh catalyst in good agreement with the XRD patterns where there were no Fe_3C peaks detected. The SEM image of the spent sample in **Figure 5.13b** shows the change in the particles shape after 10 min of microwave heating. Some growth of amorphous (and graphitic) carbon due to the dehydrogenation of the LCO hydrocarbon feedstock assisted by the $FeAlO_x$ catalyst can be seen, and this was confirmed by the presence of 14.8 wt.% carbon in the EDX spectrum of the spent sample. The decrease in oxygen content from 39.8 wt.% in the fresh catalyst to 30.7 wt.% in the spent sample gives additional evidence of the contribution of the oxygen in $FeAl_2O_4$ to CO gas formation.

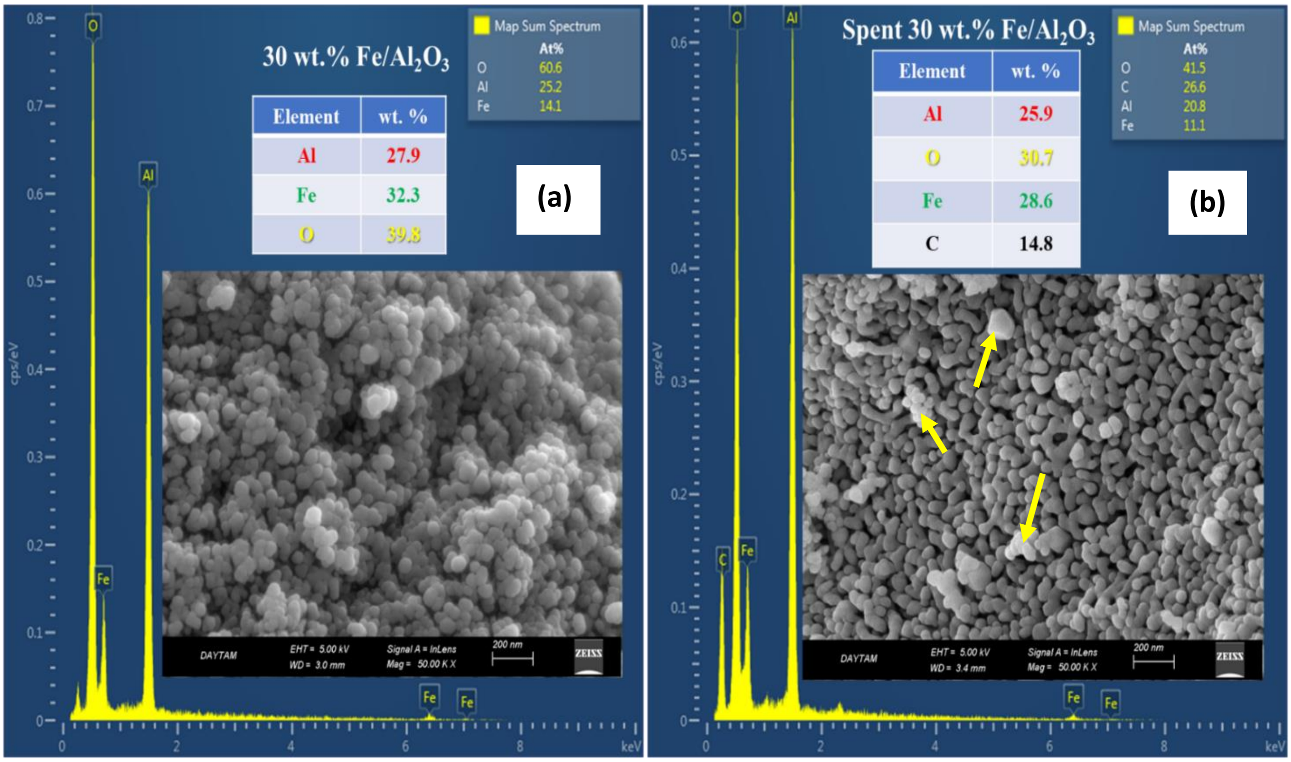

30 wt.% Fe/Al_2O_3

Element	wt. %
Al	27.9
Fe	32.3
O	39.8

Map Sum Spectrum

	At%
O	60.6
Al	25.2
Fe	14.1

Spent 30 wt.% Fe/Al_2O_3

Element	wt. %
Al	25.9
O	30.7
Fe	28.6
C	14.8

Map Sum Spectrum

	At%
O	41.5
C	26.6
Al	20.8
Fe	11.1

Figure 5.13 SEM and EDX analysis of 30 wt.% Fe/ γ-Al_2O_3 catalyst (a) fresh, and (b) spent sample after 10 min irradiation time of microwave heating. Yellow arrows indicate some growth of amorphous (and graphitic) carbon.

As shown in **Table 5.4**, the textural analysis of the samples reveals that the surface area and the total pore volume decreased significantly in the fresh sample because the γ-Al_2O_3 pellets had been sintered at 750 °C for 8 hours during the catalyst preparation. The severe effects of carbon deposit and possible high local temperatures during the reaction on the surface area and pore volume of the spent sample are also noticeable.

Table 5.4 BET surface area and pore volume of 30 wt.% Fe/ γ-Al_2O_3 catalyst.

Sample	**Surface area (m^2 g^{-1})**	**Pore volume (cm^3 g^{-1})**
γ-Al_2O_3	245	0.79
Fresh Fe/ γ-Al_2O_3	46	0.44
Spent Fe/ γ-Al_2O_3	24	0.13

5.3.6 Characterisation of the Spent Catalyst After Continuous Microwave-initiated Catalysis

The continuous microwave operation experiment was conducted as previously described in this chapter, and the resultant spent sample was characterised as described below in **Figure 5.14**.

The XRD patterns in **Figure 5.14a** show the effect of continuous operation on the catalyst structure. After 3 hours of microwave irradiation, the loss of crystallinity can be observed with broad and low intensities of the $FeAl_2O_4$ and Fe_3C peaks. There was no peak attributed to any crystalline carbons or CNTs, and this is confirmed by the temperature-programmed oxidation (TPO) in **Figure 5.14b** where the carbon deposited was largely amorphous.

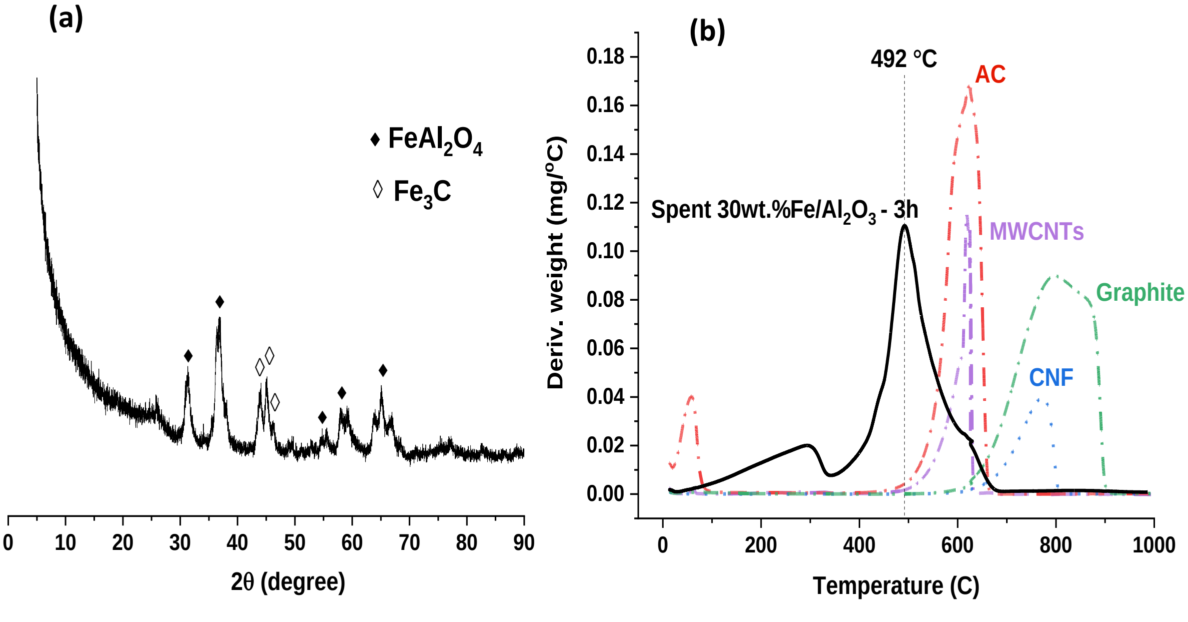

Figure 5.14 Characterisation of spent $Fe/\gamma\text{-}Al_2O_3$ sample after 3 hours of microwave continuous irradiation of 200 W, (a) X-ray diffraction patterns, (b) Derivative plots of TPO of representative spent sample compared with different carbon samples: activated carbon, multi-wall carbon nanotubes, graphite, and carbon nanofiber.

Figure 5.15a displays a representative surface morphology of a $Fe/\gamma\text{-}Al_2O_3$ spent sample after 3 hours of microwave irradiation. It can be seen the upper surface of the sample is dense and has no open pores. This result is in good agreement with XRD and BET surface area analysis which confirm the clear loss of crystallinity due to the formation of the amorphous carbon phase, and the decrease in surface area due to the formation of α-Al_2O_3 through decomposition of $FeAl_2O_4$

TEM analysis of the spent catalyst was also carried out and is shown in **Figure 5.15b**. There are small spherical/elliptical Fe_3C nanoparticles 200 nm in size can be seen. While Amorphous carbon and α-Al_2O_3 are dominant phases due to the deposit of coke and the transformation of γ-Al_2O_3 into α-Al_2O_3 during the continuous operation.

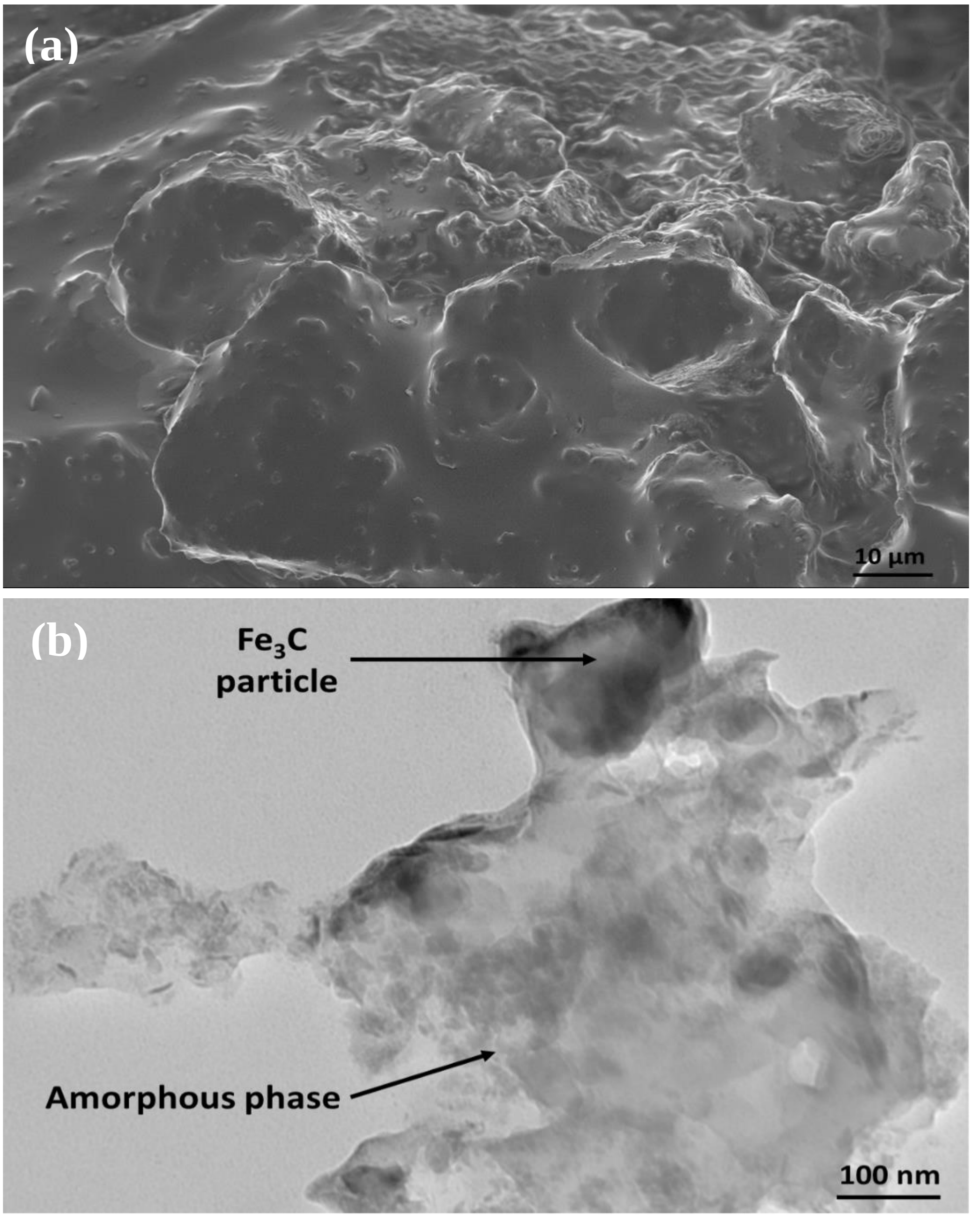

Figure 5.15 (a) SEM and (b) TEM images of 30 wt.% Fe/γ-Al_2O_3 spent sample after 3 hours of microwave continuous irradiation of 200 W.

5.4 Conclusions

A schematic representation of the primary results obtained in this study are presented in **Figure 5.16**. In summary, 30 wt. % Fe/ γ-Al_2O_3 was shown to be a highly effective catalyst in the microwave-initiated process for converting LCO to syngas, exhibiting high selectivity (98 %) and very low concentrations of CO_2 and other undesirable hydrocarbon products. Moreover, the (striking) low microwave power input (200W) gives this process an additional advantage in terms of energy saving. This work has also revealed the attractive controllability of the H_2/CO ratio in the syngas gases via the Fe metal content in the catalyst.

It was also concluded that the high microwave absorption of the catalyst during the LCO decomposition was due to the presence of $FeAl_2O_4$ as a main phase of the prepared catalyst.

The pure iron aluminate ($FeAl_2O_4$) catalyst has also been prepared for comparison purpose. The catalyst showed fairly similar catalytic performance with Fe/ γ-Al_2O_3 catalyst, and good ability to produce syngas from LCO with high selectivity.

The continuous operation of the microwave-initiated LCO decomposition showed the syngas diminution after 10 minutes of microwave irradiation due to advancing coke formation and catalyst deactivation and this gives a general idea of the lifetime of the catalyst. Moreover, there was no evidence for the formation of any high-value carbonaceous materials (i.e., graphite and CNTs) with amorphous carbon being the major co-product.

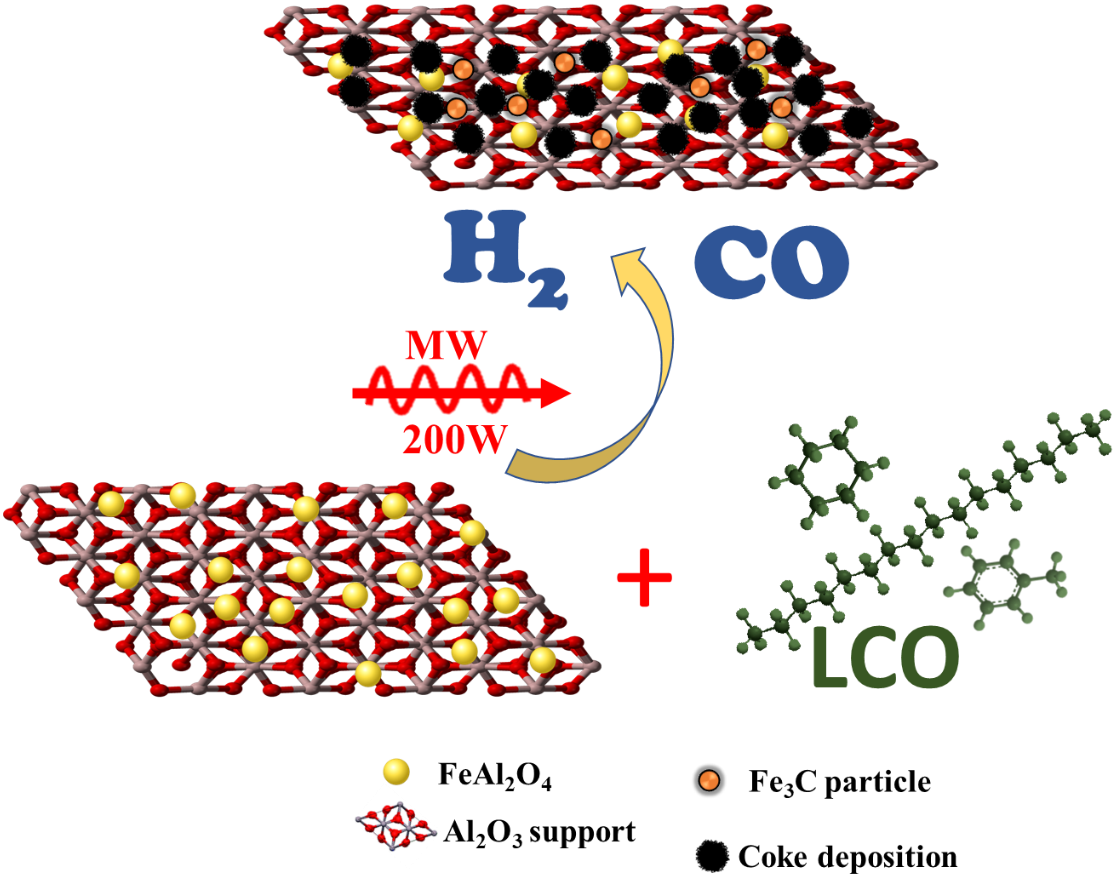

Figure 5.16 A representative diagram of syngas production using Fe/Al_2O_3 catalyst.

References

[1] M.M. Martín, Chapter 5 - Syngas, in: M.M. Martín (Ed.) Industrial Chemical Process Analysis and Design, Elsevier, Boston, (2016), 199-297.

[2] Y. Cao, Z. Gao, J. Jin, H. Zhou, M. Cohron, H. Zhao, H. Liu, W. Pan, Synthesis Gas Production with an Adjustable H_2/CO Ratio through the Coal Gasification Process: Effects of Coal Ranks and Methane Addition, Energy & Fuels, 22 (2008), 1720-1730.

[3] J.G. Speight, 3-Unconventional Gas, in: J.G. Speight (Ed.) Natural Gas (2nd Edition), Gulf Professional Publishing, Boston, (2019), 59-98.

[4] R. El-Nagar, A. Ghanem, Syngas Production, Properties, and Its Importance, Sustainable Alternative Syngas Fuel, (2019).

[5] J. Gao, J. Guo, D. Liang, Z. Hou, J. Fei, X. Zheng, Production of Syngas via Autothermal Reforming of Methane in A Fluidized-Bed Reactor over the Combined CeO_2–ZrO_2/SiO_2 Supported Ni Catalysts, International Journal of Hydrogen Energy, 33 (2008) 5493-5500.

[6] Synthesis Gas Chemistry and Synthetic Fuels, Syngaschem BV, www.syngaschem.com.

[7] R.N. Kumar, V. Aarthi, From Biomass to Syngas, Fuels and Chemicals – A review, AIP Conference Proceedings, 2225 (2020).

[8] B. Ayodele, S.I. Mustapa, T.A.R. Tuan Abdullah, S.F. Salleh, A Mini-Review on Hydrogen-Rich Syngas Production by Thermo-Catalytic and Bioconversion of Biomass and Its Environmental Implications, Frontiers in Energy Research, 7 (2019).

[9] J.v.d. Loosdrecht, J.W. Niemantsverdriet, 5.4 Synthesis Gas to Hydrogen, Methanol, and Synthetic Fuels, in: S. Robert (Ed.), Chemical Energy Storage, Walter De Gruyter GmbH, (2012), 443-458.

[10] Syngas Market Report, Global Syngas Market Analysis, (2021).

[11] M.A.A. Aziz, H.D. Setiabudi, L.P. Teh, N.H.R. Annuar, A.A. Jalil, A Review of Heterogeneous Catalysts for Syngas Production via Dry Reforming, Journal of the Taiwan Institute of Chemical Engineers, 101 (2019), 139-158.

[12] A.M. Ranjekar, G.D. Yadav, Dry Reforming of Methane for Syngas Production: A Review and Assessment of Catalyst Development and Efficacy, Journal of the Indian Chemical Society, 98 (2021), 100002.

[13] I. de Dios García, A. Stankiewicz, H. Nigar, Syngas Production via Microwave-Assisted Dry Reforming of Methane, Catalysis Today, 362 (2021) 72-80.

[14] A. Ramirez, J.L. Hueso, M. Abian, M.U. Alzueta, R. Mallada, J. Santamaria, Escaping Undesired Gas-Phase Chemistry: Microwave-Driven Selectivity Enhancement in Heterogeneous Catalytic Reactors, Science Advances, 5 (2019).

[15] B. Fidalgo, A. Domínguez, J.J. Pis, J.A. Menéndez, Microwave-Assisted Dry Reforming of Methane, International Journal of Hydrogen Energy, 33 (2008), 4337-4344.

[16] B. Fidalgo, A. Arenillas, J.A. Menéndez, Mixtures of Carbon and Ni/Al_2O_3 as Catalysts for the Microwave-Assisted CO_2 Reforming of CH_4, Fuel Processing Technology, 92 (2011), 1531-1536.

[17] A. Domínguez, Y. Fernández, B. Fidalgo, J.J. Pis, J.A. Menéndez, Biogas to Syngas by Microwave-Assisted Dry Reforming in the Presence of Char, Energy & Fuels, 21 (2007), 2066-2071.

[18] H.M. Nguyen, G.H. Pham, M. Tade, C. Phan, R. Vagnoni, S. Liu, Microwave-Assisted Dry and Bi-Reforming of Methane over M–Mo/TiO_2 (M = Co, Cu) Bimetallic Catalysts, Energy & Fuels, 34 (2020), 7284-7294.

[19] F. Wang, L. Xu, W. Shi, J. Zhang, K. Wu, Y. Zhao, H. Li, H.X. Li, G.Q. Xu, W. Chen, Thermally Stable Ir/$Ce_{0.9}La_{0.1}O_2$ Catalyst for High Temperature Methane Dry Reforming Reaction, Nano Research, 10 (2017) 364-380.

[20] Y. Khani, Z. Shariatinia, F. Bahadoran, High Catalytic Activity and Stability of $ZnLaAlO_4$ Supported Ni, Pt and Ru Nanocatalysts Applied in The Dry, Steam and Combined Dry-Steam Reforming of Methane, Chemical Engineering Journal, 299 (2016) 353-366.

[21] C. Fernández, N. Miranda, X. García, P. Eloy, P. Ruiz, A. Gordon, R. Jiménez, Insights into Dynamic Surface Processes Occurring in Rh Supported on Zr-grafted γ-Al_2O_3 During Dry Reforming of Methane, Applied Catalysis B: Environmental, 156-157 (2014), 202-212.

[22] S. Cimino, L. Lisi, G. Mancino, Effect of Phosphorous Addition to Rh-Supported Catalysts for the Dry Reforming of Methane, International Journal of Hydrogen Energy, 42 (2017) 23587-23598.

[23] M.B. Bahari, N.H.H. Phuc, B. Abdullah, F. Alenazey, D.-V.N. Vo, Ethanol Dry Reforming for Syngas Production Over Ce-Promoted Ni/Al_2O_3 Catalyst, Journal of Environmental Chemical Engineering, 4 (2016), 4830-4838.

[24] B. Bej, S. Bepari, N.C. Pradhan, S. Neogi, Production of Hydrogen by Dry Reforming of Ethanol over Alumina Supported Nano-NiO/SiO_2 Catalyst, Catalysis Today, 291 (2017), 58-66.

[25] T. Hou, Y. Lei, S. Zhang, J. Zhang, W. Cai, Ethanol Dry Reforming for Syngas Production Over Ir/CeO_2 Catalyst, Journal of Rare Earths, 33 (2015), 42-45.

[26] D. Cao, W. Cai, Y. Li, C. Li, H. Yu, S. Zhang, F. Qu, Syngas Production from Ethanol Dry Reforming over Cu/$Ce_{0.8}Zr_{0.2}O_2$ Catalyst, Catalysis Letters, 147 (2017), 2929-2939.

[27] H.C. Lee, K.W. Siew, M.R. Khan, S.Y. Chin, J. Gimbun, C.K. Cheng, Catalytic Performance of Cement Clinker Supported Nickel Catalyst in Glycerol Dry Reforming, Journal of Energy Chemistry, 23 (2014), 645-656.

[28] K.W. Siew, H.C. Lee, J. Gimbun, C.K. Cheng, Production of CO-Rich Hydrogen Gas from Glycerol Dry Reforming over La-Promoted Ni/Al_2O_3 Catalyst, International Journal of Hydrogen Energy, 39 (2014), 6927-6936.

[29] J.A. Schwarz, C. Contescu, A. Contescu, Methods for Preparation of Catalytic Materials, Chemical Reviews, 95 (1995), 477-510.

[30] M. Enhessari, $FeAl_2O_4$ Nanopowders; Structural Analysis and Band Gap Energy, High Temperature Materials and Processes, 36 (2017), 789-793.

[31] L. Zhou, L.R. Enakonda, Y. Saih, S. Loptain, D. Gary, P. Del-Gallo, J.-M. Basset, Catalytic Methane Decomposition over Fe-Al_2O_3, ChemSusChem, 9 (2016), 1243-1248.

[32] L. Zhou, L.R. Enakonda, M. Harb, Y. Saih, A. Aguilar-Tapia, S. Ould-Chikh, J.-l. Hazemann, J. Li, N. Wei, D. Gary, P. Del-Gallo, J.-M. Basset, Fe Catalysts for Methane Decomposition to Produce Hydrogen and Carbon Nano Materials, Applied Catalysis B: Environmental, 208 (2017), 44-59.

[33] K. Zhang, Y. Li, H. Yan, C. Wang, H. Li, J. Liang, J. Dang, Effect of Sintering Temperature on Microstructure and Mechanical Properties of Hot-Pressed Fe/$FeAl_2O_4$ Composite, Crystals, 11 (2021).

[34] P.-C. Chiu, Y. Ku, Y.-L. Wu, H.-C. Wu, Y.-L. Kuo, Y.-H. Tseng, Characterization and Evaluation of Prepared Fe_2O_3/Al_2O_3 Oxygen Carriers for Chemical Looping Process, Aerosol and Air Quality Research, 14 (2014) 981-990.

[35] D.P. Dutta, G. Sharma, Synthesis and Magnetic Behavior of Spinel $FeAl_2O_4$ Nanoparticles, Materials Science and Engineering: B, 176 (2011) 177-180.

[36] H. Zhang, Y. Wang, Y. Wang, J. Cao, P. Kang, Q. Tang, M. Ma, Highly Dispersed PdNPs/α-Al_2O_3 Catalyst for the Selective Hydrogenation of Acetylene Prepared with Monodispersed Pd Nanoparticles, Catalysts, 7 (2017), 128.

Chapter6

Conclusions and Future Work

6.1 Thesis Conclusions

The aim of the work described in this thesis was to demonstrate the direct conversion of Saudi Arabian Light Crude Oil (LCO) through a microwave-initiated, catalytic deep-dehydrogenation process, into clean hydrogen fuel and valuable solid carbonaceous materials. The CO_2-free hydrogen produced by this process offers an effective solution to the environmental issues related to the use of fossil fuels in the current industrial technologies reviewed in chapter 1.

At the beginning of the experimental work in chapter 3, and before using LCO as feedstock, three different hydrocarbons were selected as model compounds to simulate the paraffins, naphthenes, and aromatics present in crude oil. As expected from the molecular formula, paraffinic feedstock produced more hydrogen compared to other hydrocarbons. This gives, in general, a good indication that paraffin-rich crude oil can produce more hydrogen than naphthene- or aromatic-rich crude oil.

In addition, the data in **Figure 6.1** shows the results of the catalytic dehydrogenation of the synthetic crude oil (hexadecane+cyclohexane+BTX) and LCO under a microwave-initiated process. The hydrogen yields in both feedstocks were similar. Importantly, this reveals that the presence of impurities such as nitrogen and sulphur, and metals such as iron and nickel in the LCO do not significantly inhibit the production of hydrogen. However, unlike authentic LCO the synthetic analogue did not produce any olefins or CO_2.

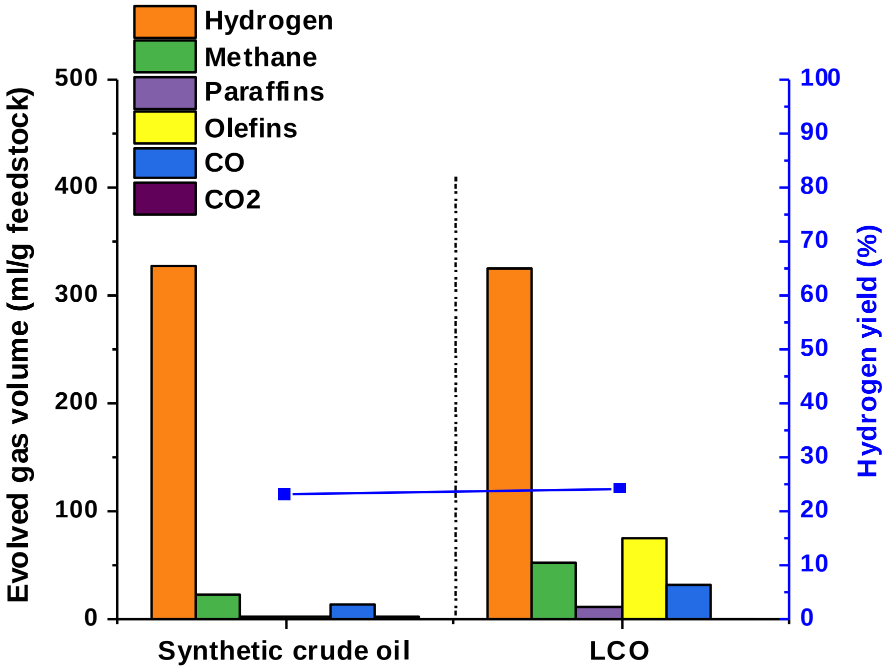

Figure 6.1 Comparison of synthetic crude oil and LCO with 30 wt.% Fe/AC at a microwave power input of 1000 W and for 10 min irradiation time. The total evolved gas volume on the left axis, and hydrogen yield on the right axis.

The microwave-initiated deep-dehydrogenation of LCO was studied in chapter 4. A series of metallic and bimetallic catalysts were prepared and investigated for hydrogen production. Microwave heating was shown to be beneficial for hydrogen production over a conventional thermal process. 30 wt. % iron supported on activated carbon was identified as the best catalyst. The microwave power input (W) and the metal loading on the catalyst (wt.%) were identified as important factors for the production of a higher gas volume but had little effect on the composition of the emitted gas.

Although the microwave-initiated catalytic deep-dehydrogenation of liquid hydrocarbons has been widely investigated, most of the research studies have been focused on comparison with conventional processes in terms of feedstock conversion and/or product yield and selectivity. However, not much information has been published on how the nature of feedstocks and/or catalyst particle size under microwave irradiation affects the course of the reaction. In this context, a systematic investigation of the microwave interaction with LCO, different wt.% loading of Fe/AC catalysts, particle sizes, and supports was performed. The experimental results showed that LCO itself contributes to the heating of the catalyst bed due to the presence of water (0.05 vol.%) and the large variety of organic molecules and other inorganic elements. It was also demonstrated that changes in the sizes of the nanoparticles of Fe as a consequence of the different Fe loadings also affect the temperature profiles. The smaller Fe nanoparticles have improved microwave heating, and consequently, lager yields of hydrogen.

The production of syngas from LCO was then investigated in chapter 5. This work showed that microwave heating converts LCO into syngas more effectively than conventional (thermal) heating. The remarkable properties of gamma-alumina-supported Fe catalysts have allowed the production of syngas with 98 % selectivity with very low CO_2 or hydrocarbon emissions. Attention has also been paid in this chapter to studying the use of iron aluminate ($FeAl_2O_4$) as a catalyst and this is shown to have both high microwave absorption and good catalytic activity toward syngas production.

Despite the complexities in the crude oil composition and in the overall interaction between the LCO and microwave irradiation with the catalytic system, these systems displayed excellent syngas production from LCO using inexpensive and obtainable components. Further studies are required in order to optimise the system and scale up the technology from the bench to the industrial level by developing an integrated environmentally-friendly plant for large scale syngas preparation. It will also be necessary to improve the catalyst lifetime by minimising carbon deposition.

6.2 Future Work

6.2.1 Energy Balance and Efficiency for Hydrogen Production

The concept of energy balance is based on the fundamental thermodynamic principle which states that energy can be transformed from one form to another but can be neither created nor destroyed. It helps to present the total amount of energy used and the relative contribution of each different source and assess the energy performance and the efficiency of the system [1, 2]. One key metric often considered in evaluating the efficiency of hydrogen production is net energy balance (NEB), which is defined as the difference between the energy value of the output fuel and the total primary energy consumed in producing the fuel. As such, a positive NEB is one important criterion for environmentally sustainable fuel, because it indicates that more energy is produced than is consumed via the system [3].

In previous works, the Edwards group reported that the NEB is the ratio of chemical energy (Energy Out) as the enthalpy of combustion of only the hydrogen produced from the fossil fuels neglecting the chemical energy of co-product solid carbon, to the energy invested (Energy In) as the electricity power consumption in the microwave system [4, 5].

Equation 6.1

$$NEB\ (\%) = \frac{Enthalpy\ of\ combustion\ of\ produced\ hydrogen\ (Energy\ Out)}{Electricity\ consumption\ (Energy\ In)}\ X\ 100$$

Therefore, it will be important to study the thermodynamics of the whole system and calculate the complete energy balance and – particularly- how much energy is required to generate 1 mole of H_2. In addition, optimising the system to meet the requirements of operation at a large scale for high efficiency of hydrogen production.

6.2.2 The Catalyst Selectivity Index (CSI)

In 2015, the Edwards group, in association with the group of Sir David King, developed a new concept “The Catalyst Selectivity Index (CSI)” which allows a route to correlate the industrial process energy input and CO_2 emission saving with a measurable improvement in catalyst efficiency. It can be defined as the average value of the efficiency of a catalyst for a specific conversion process, as compared to the best ‘‘bench mark’’ catalysts; which is representing the (current) best-performing heterogeneous catalyst to-date [6].

The long-term objective is not only to develop manufacturing processes using new sources of energy, but also to decrease the energy/carbon footprint of existing chemical processes. The CSI as set out in reference [6] is a simple metric; one increases the effectiveness of a particular catalyst in a chemical manufacturing process in terms of its performance or efficiency, and then observes the subsequent impact on total energy consumption and resulting Green House Gas emissions for that entire process.

Applying the CSI concept to this research work will give an overall picture of the efficiency and feasibility of this process by calculating the catalyst efficiency (CE). It can be applied to different kinds of catalysts such as Fe/AC, Fe/Al_2O_3, and their optimised successors.

Catalyst efficiency is given by the following expression [6]:

$$\mathrm{CE} = \frac{\frac{C_n}{C_o} + \frac{S_n}{S_o} + \frac{L_n}{L_o}}{3}$$

Equation 6.2

Where, C_n is the conversion of the new or improved catalyst, C_o is the conversion of the benchmark catalyst (CE=1.0), S_n is the new or improved catalyst selectivity, S_o is the benchmark catalyst selectivity, L_n is the lifetime of the catalyst, and L_o is the benchmark catalyst lifetime.

Then, the performance of the optimal catalyst can be illustrated by calculating the CSI factor as:

$$\text{CSI \#} = \frac{\Delta \text{gCO}_2/\text{MJ}_{\text{fuel}}}{\Delta \text{Catalyst Efficiency}} \qquad \textbf{Equation 6.3}$$

For a given change in g CO_2/MJfuel or corresponding change in CE.

Where, MJ_{fuel} is the total energy, and gCO_2 is the total CO_2 emissions.

6.2.3 Carbon Separation Technology and Using Different Support Materials

In this thesis, there was evidence of the formation of carbon nanotubes (CNT) and/or graphite during the hydrogen production process. The separation of these high-quality carbons will create a high added value to the process. Other supports such as Zeolites and Silicates should also be investigated as metal bearing catalysts in order to determine if any catalytic activities are shown. Also, the investigation of silicon carbide (SiC) as a support with its excellent microwave absorption properties may make the separation process easier than using activated carbon.

6.2.4 Iron Carbide (Fe_3C) Catalyst and Catalysts Regeneration

Future work on this topic should continue to investigate the use of an iron carbide (Fe_3C) catalyst for the microwave-initiated deep-dehydrogenation of LCO and study its activity with other support materials. Regeneration of spent catalysts extends the lifetime of the catalyst material and eliminates the need for catalyst disposal. So, it is important to study the detailed mechanism of catalytic activity and the manner in which the catalyst activity can be regenerated.

References

[1] International Energy Agency (IEA), Understanding and using the Energy Balance, (2017).

[2] E. Fraga, Process Analysis - The Importance of Mass and Energy Balances, (2022).

[3] G.G. Zaimes, V. Khanna, Chapter 8 - Life Cycle Sustainability Aspects of Microalgal Biofuels, in: J.J. Klemeš (Ed.) Assessing and Measuring Environmental Impact and Sustainability, Butterworth-Heinemann, Oxford, (2015), 255-276.

[4] S. Gonzalez-Cortes, D.R. Slocombe, T. Xiao, A. Aldawsari, B. Yao, V.L. Kuznetsov, E. Liberti, A.I. Kirkland, M.S. Alkinani, H.A. Al-Megren, J.M. Thomas, P.P. Edwards, Wax: A Benign Hydrogen-Storage Material That Rapidly Releases H_2-Rich Gases Through Microwave-Assisted Catalytic Decomposition, Scientific Reports, 6 (2016) 35315.

[5] X. Jie, Microwave-initiated Catalytic Dehydrogenation of Fossil Fuels for the Facile Production and Safe Storage of Hydrogen, Ph.D Thesis, University of Oxford, (2020).

[6] T. Xiao, T. Shirvani, O. Inderwildi, S. Gonzalez-Cortes, H. AlMegren, D. King, P.P. Edwards, The Catalyst Selectivity Index (CSI): A Framework and Metric to Assess the Impact of Catalyst Efficiency Enhancements upon Energy and CO_2 Footprints, Topics in Catalysis, 58 (2015), 682-695.

Appendix A

Estimation of Errors[1]

The assessment of the possible error in all measured quantities is of course fundamental figure in all studies. If only a single measurement is conducted any estimate of the error may be widely wrong. There may be a large personal or a large accidental error, as well as that due to the intrinsic precision of the particular instrument used. To help reduce, or reveal accidental errors, repeated measurements of the same quantities were made during development of the study.

For example, if a quantity X_0 units are measured in times and recorded as $X_1, X_2, X_3 \ldots X_n$ units, one can write:

$$X_r = X_0 + e_r$$

Where e_r is the error in the measurement X_r

The arithmetic mean $\overline{X}$ of the n measurements is then

$$\overline{x} = \frac{X_1 + X_2 + X_3 \ldots . + X_n}{n} = X_0 + \frac{e_1 + e_2 + e_3 \ldots . + e_n}{n}$$

Now, some of the errors $e_1, e_2, e_3 \ldots e_n$ may be positive and some negative and hence the value of $\frac{e_1 + e_2 + e_3 \ldots . + e_n}{n}$ may be very small.

In any case $\frac{e_1 + e_2 + e_3 \ldots . + e_n}{n}$ must be smaller numerically than the greatest value of the separate error. Thus, if e is the largest numerical error in any of the measurements, we have

$$\left| \frac{e_1 + e_2 + e_3 \ldots . + e_n}{n} \right| \leq e$$

And consequently $|\overline{x} - x_0| \leq e$

Hence in general will be near to and may be taken on the “best” value of the measured quantity which the measurements provide. Thus, in general, the number of measurements or value of n (the number of times a measurement is done) gives the average (the arithmetic mean), which approaches to the “best” value of the measured quantity.

Note that by repeated measurements of the same quantity accidental errors of the measurements may be corrected in some degree, but systematic errors cannot be kept out (since they are related to the accuracy in the instrument itself).

Hence, we can draw a distinction between the definition of accuracy and precision:

- Accuracy refers to the closeness of the measurements to the “actual” or the “real” value of any physical quantity, whereas
- Precision is used to indicate the closeness with which the measurements agree with one another value independently of any systematic error involved.

In summary, our approach is that the mean of a set of measurements (taken over, usually, 3 independents, or repeat measurements) whilst the standard deviation (if applied) provides the best estimate of the accuracy of a set of repeated values.

For instance, in **Table 4.6**, for 5 wt. % Fe/AC, there were three measurements of crystallite size before reaction: X_1= 20.5, X_2= 19.7, and X_3= 20.8 nm

$$\bar{x} = \frac{20.5+19.7+20.8}{3} = 20.3$$

$$e_1 = 20.5 - 20.3 = 0.2 \text{ , } e_2 = 19.7 - 20.3 = -0.6 \text{ , } e_3 = 20.8 - 20.3 = 0.5$$

$$\bar{e} = \frac{0.2 + 0.6 + 0.5}{3} = 0.42$$

$$\%\ e = \frac{0.42}{20.3} * 100 = 2.1\ \%$$

Table A1. Measurements of crystallite size in **Table 4.6** before reaction.

Wt. % Fe/AC	X_1	X_2	X_3	$\bar{x}$	e_1	e_2	e_3	$\bar{e}$	**e (%)**
5	20.5	19.7	20.8	20.3	0.2	0.6	0.5	0.42	2.1
10	78.2	77.5	75.3	77.0	1.2	0.5	1.7	1.13	1.5
20	90.1	84.3	88.3	87.6	2.5	3.3	0.7	2.18	2.5
30	103	95	90.2	96.1	6.9	1.1	5.9	4.62	4.8
40	112	105.5	106.7	108.1	3.9	2.6	1.4	2.62	2.4
50	123.3	118.7	122.2	121.4	2.3	2.9	0.6	1.93	1.6

Table A2. Measurements of crystallite size in **Table 4.6** after reaction.

Wt. % Fe/AC	X_1	X_2	X_3	$\bar{x}$	e_1	e_2	e_3	$\bar{e}$	**e (%)**
5	17.7	18.3	16.2	17.4	0.3	0.9	1.2	0.80	4.6
10	85.1	82.6	78.9	82.2	2.9	0.4	3.3	2.20	2.7
20	108.4	109.6	105.3	107.8	0.6	1.8	2.5	1.64	1.5
30	111.2	109.6	104.9	108.6	2.6	1.0	3.7	2.44	2.3
40	123.1	115.4	122.7	120.4	2.7	5.0	2.3	3.33	2.8
50	124.9	117.2	118.9	120.3	4.6	3.1	1.4	3.04	2.5

Thus, the value of the average crystallite size in **Table 4.6** (± 5% error) as follow:

Wt. %Fe/AC	**Crystallite size [nm] (Before reaction)**	**Crystallite size [nm] (After reaction)**
5	20 (±0.42)	17 (±0.8)
10	77 (±1.2)	82 (±2.2)
20	88 (±2.2)	108 (±1.6)
30	90 (±4.3)	109 (±2.5)
40	109 (±2.6)	120 (±3.4)
50	120 (±1.9)	120 (±3)

---

[1]. J. Topping, Errors of observation and their treatment, 4th Edition, Chapman and Hall, (1972), Great Britain.

Appendix B

The Detailed Composition Analysis of Products Distribution by GC for Microwave-Initiated Deep-dehydrogenation of Hydrocarbon Model Compounds for Hydrogen Production

Table B1. The composition of evolved gases in microwave-initiated dehydrogenation of 0.5 g hexadecane mixed with 0.5 g Fe/AC catalysts at different Fe loadings.

Fe /AC loading (wt.%)	Hexadecane conversion	(vol. %)						
		H_2		CH_4	Paraffins	Olefins	CO	CO_2
	(wt. %)	Yield	Selectivity					
0	19.0	10.0	53.0	21.4	7.8	3.5	1.4	12.9
5	20.8	12.3	59.3	21.6	3.3	10.2	5.6	1.0
10	20.2	14.1	70.0	10.2	1.3	5.7	11.3	1.5
20	23.8	18.8	79.0	8.3	1.8	7.3	2.4	1.3
30	29.1	25.9	88.8	15.8	1.7	17	7.0	1.4
40	20.2	13.6	67.5	10.4	2.9	5.0	6.5	7.6
50	17.8	10.2	57.2	7.4	2.0	4.9	13.8	14.7

Table B2. The composition of evolved gases in microwave-initiated dehydrogenation of 0.5 g hexadecane mixed with 0.5 g of 30 wt.% Fe/AC catalyst at different microwave input power.

MW input power (W)	Hexadecane conversion	(vol. %)						
		H_2		CH_4	Paraffins	Olefins	CO	CO_2
	(wt. %)	Yield	Selectivity					
500	21.4	18.2	84.8	3.3	2.2	2.3	4.6	2.9
750	26.7	23.3	87.0	6.2	1.4	2.7	1.9	0.9
1000	29.1	25.9	88.8	5.6	1.1	2.7	1.5	0.3
1250	27.4	22.3	81.6	9.1	0.9	4.0	2.9	1.5

Table B3. The composition of evolved gases in microwave-initiated dehydrogenation of a recharging catalytic cycle for a 0.5 g hexadecane mixed with 30 wt.% Fe/AC catalyst.

Number of cycles	**Hexadecane conversion (%)**	**(vol. %)**						
		H_2		**CH_4**	**Paraffins**	**Olefins**	**CO**	**CO_2**
		Yield	**Selectivity**					
1	29.1	25.9	88.8	5.6	5.5	1.3	1.5	0.3
2	17.8	13.6	76.1	8.1	1.1	2.7	1.5	1.8
3	17.2	13.2	76.5	8.8	9.6	2.4	0.7	2.0
4	19.0	10.8	56.6	17.8	17.9	5.2	1.2	1.3
5	5.9	3.0	51.4	18.0	24.8	3.3	0.6	1.8

Table B4. The composition of evolved gases in microwave-initiated dehydrogenation of a 0.5 g hexadecane mixed with 0.5 g of 30 wt.% Fe/AC and Fe_3C/AC catalysts.

Catalyst	**Hexadecane conversion (wt. %)**	**(vol. %)**						
		H_2		**CH4**	**Paraffins**	**Olefins**	**CO**	**CO_2**
		Yield	**Selectivity**					
30 wt.% Fe/AC	27.4	25.9	88.8	5.6	2.7	8.6	1.5	0.3
Fe3C/AC	29.2	24.4	89.2	3.8	0.5	1.3	3.9	1.2

Table B5. The composition of evolved gases in microwave-initiated dehydrogenation of a 0.5 g hexadecane, cyclohexane, and BTX mixed with 0.5 g of 30 wt.% of Fe/AC catalyst.

Feedstock	**Conversion (wt. %)**	**(vol. %)**						
		H_2		**CH_4**	**Paraffins**	**Olefins**	**CO**	**CO_2**
		Yield	**Selectivity**					
Hexadecane	29.1	25.9	88.8	5.6	1.1	2.7	1.5	0.3
Cyclohexane	30	20.7	68.9	1.8	0.1	4.1	24.8	0.3
BTX	29.3	15.9	65.9	8.9	0.9	1.3	22.8	0.2

Table B6. The composition of evolved gases in microwave-initiated dehydrogenation of 0.5 g of feedstock sample mixed with 0.5 g of 30 wt.% Fe/AC catalyst.

Feedstock (wt.%)	**Conversion (wt. %)**	**(vol. %)**						
		H_2						
		Yield	**Selectivity**	**CH_4**	**Paraffins**	**Olefins**	**CO**	**CO_2**
(75)Hexadecane+(25)cyclohexane	21.4	18.2	71.8	9.7	1.0	3.2	13.5	0.8
(55)Hexadecane+(45)BTX	26.8	23.3	76.5	6.3	0.4	1.5	15.1	0.9
(70)BTX+(30)cyclohexane	29.1	25.9	63.4	2.8	0.1	0.4	32.8	0.3
(46)Hexadecane+(17)cyclohexane +(37)BTX	27.4	22.3	74.2	5.1	0.4	0.7	19.1	1.5

Appendix C

The Detailed Composition Analysis of Products Distribution by GC for Microwave-initiated Deep-dehydrogenation of LCO for Hydrogen Production

Table C1. The composition of evolved gases in microwave-initiated dehydrogenation of 0.5 g LCO sample mixed with 0.5 g Fe/AC catalysts at different Fe loadings.

Fe /AC loading (wt.%)	LCO conversion (%)	(vol. %)						
		H_2						
		Yield	Selectivity	CH_4	Paraffins	Olefins	CO	CO_2
0	22.5	12.4	55.3	11.8	10.5	16.9	4.5	0.9
5	29.2	16.3	55.6	10.6	5.1	14.3	13.4	0.9
10	29.9	17.3	57.7	11.9	3.6	16.4	10	0.3
20	34.5	20.8	60.3					
30	38.9	24.3	62.5	11.4	2.5	16.3	7.2	0.0
40	26.1	13.7	52.4					
50	24.7	12.4	50.4	16	2.8	20.5	9	1.3

Table C2. The composition of evolved gases in microwave-initiated dehydrogenation of 0.5 g LCO sample mixed with 0.5 g of 30 wt.% Fe/AC catalyst at different microwave input power.

MW input power (W)	LCO conversion (%)	(vol. %)						
		H_2						
		Yield	Selectivity	CH_4	Paraffins	Olefins	CO	CO_2
250	13.5	7.6	56.2	19.3	3.3	8.3	11.9	1
500	31.5	16.6	52.9	17.2	2.3	11	15.7	0.9
750	40.4	20.1	53.4	18.7	2.9	11.9	12.6	0.5
1000	38.9	23.7	59.4	11.7	2.7	14.2	11.3	0.7
1250	32.9	15.1	45.8	18.9	3.4	16.7	14.6	0.6

Table C3. The composition of evolved gases in the continuous operation of microwave-initiated dehydrogenation of LCO sample mixed with 0.5 g of 30 wt.% Fe/AC catalyst at a microwave power input of 1000 W at different time on stream.

Time on stream (min)	**LCO conversion (%)**	**(vol. %)**						
		H_2		**CH_4**	**Paraffins**	**Olefins**	**CO**	**CO_2**
		Yield	**Selectivity**					
10	59.9	21.6	35.9	22.9	6.6	29.8	4.4	0.4
30	41.9	11.5	27.6	25.3	6.5	35.9	4.3	0.39
60	22.5	4.1	18.5	25.3	8.9	42.9	4.1	0.30
90	15.0	2.6	17.1	26.3	10.6	43.1	2.6	0.31
120	8.9	1.4	15.8	25.2	10.2	45.1	3.1	0.6
150	4.5	1.0	12.7	21.5	7.7	50.2	7.7	0.24
180	3.7	1.2	11.5	14.6	3.9	48.7	20.2	1.1
210	3.0	1.2	10.1	15.1	7.3	28.9	36.8	1.8
240	2.2	0.9	10.3	11.4	8.6	23.6	42.6	3.5

Table C4. The Comparison of microwave and conventional thermal process of LCO sample with 30 wt.% Fe/AC.

Temperature /Input power	**LCO conversion (%)**	**(vol. %)**						
		H_2		**CH_4**	**Paraffins**	**Olefins**	**CO**	**CO_2**
		Yield	**Selectivity**					
500 °C	7.7	4.2	70.9	1.4	0.37	0.24	27.1	0.1
800 °C	9.5	5.7	76.4	5.1	1.4	1.4	12.3	3.4
1000 °C	20.1	8.9	46.1	18.8	5.8	12.2	14.5	2.6
1000 W	38.9	23.7	59.4	11.7	2.7	14.2	11.3	0.7

Table C5. The composition of evolved gases in microwave-initiated dehydrogenation of 0.5 g LCO sample mixed with 0.5 g Ni/AC catalysts at different Ni loadings.

Ni /AC loading (wt.%)	**LCO conversion (%)**	**(vol. %)**						
		H_2		**CH_4**	**Paraffins**	**Olefins**	**CO**	**CO_2**
		Yield	**Selectivity**					
5	26.2	12	45.9	30.9	2.8	6.4	13.3	0.7
10	25.4	13.7	53.9	24.6	3.6	12.2	4.6	1.1
20	32.9	20.6	62.6	17.3	2.1	11.4	5.9	0.7
30	28.5	15.6	54.7	17.1	1.9	9.7	14.8	1.8
40	25.4	12.2	48	14.4	2.2	7.9	7.4	0.8
50	27	10.5	38.8	13.2	1.8	14.3	18.6	3.2

Table C6. The composition of evolved gases in microwave-initiated dehydrogenation of 0.5 g LCO sample mixed with 0.5 g of Co/AC catalysts at different Co loadings.

Co/AC loading (wt.%)	**LCO conversion (%)**	**(vol. %)**						
		H_2		**CH_4**	**Paraffins**	**Olefins**	**CO**	**CO_2**
		Yield	**Selectivity**					
5	21.4	15.4	71.9	16.9	2.1	2.9	5.8	0.4
10	28.8	18.3	63.8	18.2	2.6	9.3	5.7	0.4
20	36.9	23.8	64.4	14.6	1.6	7.9	10.9	0.3
30	35.4	22.1	62.2	13.5	1.3	6.1	16.1	0.6
40	25.8	16.5	64.1	14.8	2.5	10.3	6.9	1.4
50	19.9	10.6	53.2	20.2	4.5	17.1	4.6	0.3

Table C7. The composition of evolved gases in microwave-initiated dehydrogenation of 0.5 g LCO sample mixed with 0.5 g of Ni-Fe/AC bimetallic catalysts at different Ni and Fe loadings.

Bimetallic Ni-Fe/AC loading (wt.%)	**LCO conversion (%)**	**(vol. %)**						
		H_2		**CH_4**	**Paraffins**	**Olefins**	**CO**	**CO_2**
		Yield	**Selectivity**					
5Ni25Fe	35.4	19.8	56.1	14.6	1.7	10.8	15.1	1.7
10Ni20Fe	30.9	18.1	58.5	16.7	1.5	9.8	12.8	0.7
15Ni15Fe	36.1	19.9	55.2	16.8	1.6	11.9	13.7	0.8
20Ni10Fe	33.9	21.6	63.7	15.6	1.6	7.4	11.2	0.5
25Ni5Fe	25.8	17.3	67.3	15.7	1.7	5.4	9.3	0.6

Table C8. The composition of evolved gases in microwave-initiated dehydrogenation of 0.5 g LCO sample mixed with 0.5 g of Co-Fe/AC bimetallic catalysts at different Co and Fe loadings.

Bimetallic Co-Fe/AC loading (wt.%)	**LCO conversion (%)**	**(vol. %)**						
		H_2		**CH_4**	**Paraffins**	**Olefins**	**CO**	**CO_2**
		Yield	**Selectivity**					
5Co15Fe	31.4	20.1	64.9	14.6	1.5	6.7	12.2	0.0
10Co10Fe	38.9	22.1	57.7	16.5	1.7	11.9	12.1	0.0
15Co5Fe	31.5	20.1	65.1	13.9	1.3	5.9	13.1	0.0

Appendix D

Enthalpy calculations for the reaction of different model hydrocarbons compounds used in Chapter 3

1. Hexadecane

$$C_{16}\,H_{34}(liquid) + 48\;Fe\;(solid) \rightarrow 16\;Fe_3C(solid) + 17H_2(gas)$$

$\Delta H° = \;\Sigma\;\Delta H°_f(products) - \;\Sigma\;\Delta H°_f(reactants)$

$\Delta H°_f(C_{16}H_{34})(l)$ = - 447.97 kJ mol^{-1}

$\Delta H°_f(Fe_3C)(s)$ = 21 kJ mol^{-1}

$\Rightarrow \Delta H° = \;\left[16\;\Delta H°_f(Fe_3C) + 17\Delta H°_f(H_2)\right] - \left[\Delta H°_f(C_{16}H_{34}) + 48\Delta H°_f(Fe)\right]$

$\Rightarrow \Delta H° = \;[16\;(21) + 17(0)] - [(-447.97) + 48(0)]$

$\Rightarrow \Delta H° = (336) + (447.97) = 783.97$ kJ mol^{-1}

2. Cyclohexane

$$C_6\,H_{12}(liquid) + 18\;Fe\;(solid) \rightarrow 6\;Fe_3C(solid) + 6H_2(gas)$$

$\Delta H°_f(C_6H_{12})(l)$ = - 156 kJ mol^{-1}

$\Rightarrow \Delta H° = \;\left[6\;\Delta H°_f(Fe_3C) + 6\Delta H°_f(H_2)\right] - \left[\Delta H°_f(C_6H_{12}) + 18\Delta H°_f(Fe)\right]$

$\Rightarrow \Delta H° = \;[6\;(21) + 6(0)] - [(-156) + 18(0)]$

$\Rightarrow \Delta H° = (126) + (156) = 282$ kJ mol^{-1}

3. Benzene, xylene, and toluene

	ΔH°_{f} (kJ mol^{-1})
Fe_3C (solid)	21
C_6H_6 (liquid)	49
C_7H_8 (liquid)	12
o-C_8H_{10} (liquid)	-24.4
p- C_8H_{10} (liquid)	-24.4
m- C_8H_{10} (liquid)	-25.4
H_2 (gas)	0
Fe (solid)	0

$$C_6H_6 + C_7H_8 + o - C_8H_{10} + p - C_8H_{10} + m - C_8H_{10} + 111Fe \rightarrow 37F_3C + 22H_2$$

As the above calculation:

$\Rightarrow \Delta H^{\circ} = 790.2$ kJ mol^{-1}

Appendix E

The Detailed Composition Analysis of Products Distribution by GC for Microwave-Initiated Decomposition of LCO for Syngas Production

Table E1. The composition of evolved gases in the continuous operation of microwave-initiated dehydrogenation of 0.3 g LCO sample mixed with 0.7 g of Fe/ γ-Al_2O_3 catalysts at a microwave power input of 200W at different time on stream.

Time on stream (min)	**LCO conversion (%)**	**(vol. %)**							
		H_2							
		Yield	**Selectivity**	**CH_4**	**Paraffins**	**Olefins**	**CO**	**CO_2**
10	61.4	37.9	61.6	6.1	1.2	3.3	27.7	0.1
30	41.9	19.3	46.1	18.6	8.9	21.5	4.6	0.3
60	22.5	8.2	36.5	17.3	10.8	25.2	9.8	0.4
90	14.9	4.5	29.9	20.6	12.1	32.9	4.3	0.2
120	8.9	2.3	25.8	21.1	13.1	34.2	5.3	0.5
150	4.5	1.2	26.3	20.5	13.4	32.3	7.4	0.1
180	3.7	0.9	24.3	19.8	13.4	30.9	10.8	0.8